Plasma Physics Reports, Vol. 29, No. 1, 2003, pp. 1–30. From Fizika Plazmy, Vol. 29, No. 1, 2003, pp. 3–36.

DUSTY PLASMA

Complex Plasmas: II. Elementary Processes in Complex Plasmas[1]

G. E. Morfill*, V. N. Tsytovich, and H. Thomas***

**Max-Planck Institute fur Extraterrestrische Physik, 85740 Garching, Postfach 1312, Germany*
e-mail: gem@mpe.mpg.de
***Institute of General Physics, Russian Academy of Sciences, ul. Vavilova 38, Moscow, 119991 Russia*
e-mail: tsytov@lpi.ac.ru

Received December 19, 2001; in final form, April 10, 2002

Abstract—This paper continues a series of review papers devoted to the physics of complex plasmas. The review contains a description of elementary processes in complex plasmas. The elementary processes are described in the simplest way and in a form useful for applications and estimates for existing experiments. The paper describes (i) the processes related to the charging process, including the dust charge fluctuations, absorption of plasma particles on dust grains, and friction of ions in collisions with grains; (ii) the forces acting on dust grains in complex plasmas, including ion drag force, thermophoretic force, and dust friction on neutral gas; (iii) dust–dust noncollective interactions, including the attraction related to the nonlinearity of screening and the shadow attraction related to ion and neutral particle bombardment; and (iv) dust–dust collective attraction in the absence and presence of an ion flow and a strong magnetic field. First experiments on the detection of dust–dust interactions are described. Elementary processes in complex plasmas can be used to explain existing experiments on dust-plasma crystals, dust clusters, and waves and instabilities in complex plasmas, as well as to discuss the trends in theoretical research, laboratory experiments, and in astrophysical and industrial applications. © *2003 MAIK "Nauka/Interperiodica".*

1. INTRODUCTION

In our previous paper [1], we demonstrated the newly observed phenomenon of condensation [2–67] of a system of highly charged dust grains in plasmas in a state of complex plasma, where the dust grains are strongly correlated, and in a plasma crystal state [2–7]. This strongly correlated state of matter is used in industrial and technological applications, such as material coating and etching [8–11], and in thermonuclear fusion devices [12]. The physics of a system of highly charged dust grains in a plasma is shown to be different from both a pure Coulomb system [13, 14] and a system of Yukawa screened charged particles [15] due to strong nonlinearities [16, 17] in screening and the presence of a long-range and nonscreened part of the potential [18, 19] (see also [1]). Different models of grain charging proposed so far, including the orbit motion limited (OML) approach [20], radial drift (RD) approach [21, 22], and diffusion limited (DL) approach [1], predict large grain charges with nonlinear screening and a weak nonscreened part of the potential [1]. The values of grain charges are sufficiently large for plasma condensation to occur. The phenomenon of plasma condensation was observed in many laboratory experiments [2–7]. The interpretation of observations of complex plasmas includes elementary processes related to large dust charges, absorption of plasma particles on dust grains, collective phenomena, and dust–dust interactions. In this paper, we describe elementary processes in complex plasmas using a simple model and give exact values for the coefficients determining the strength of the elementary processes. These results can be used not only to estimate the existing experiments or those being planned, but also to formulate the simplest force balance relations that can describe the structures often formed and observed in complex plasmas.

2. PROCESSES RELATED TO THE CHARGING OF DUST GRAINS

There are several processes related to dust charging, including time-varying charging, charge fluctuations, the friction of ions and electrons on dust, and the absorption of ions and electrons by dust distributed with a certain average dust density in a complex system. Speaking about the collection of dust grains and the effects that appear for a certain dust density, we will consider only the effects that appear when summing the effects existing on individual dust grains. The collective effects mean that one of the grain influences the processes on other grains. The effects that we will consider here are more simple; we will assume that such a mutual influence can be neglected and the effects on many grains can be summed up. The collective effects will be discussed in detail later.

[1] This article was submitted by the authors in English.

1063-780X/03/2901-0001$24.00 © 2003 MAIK "Nauka/Interperiodica"

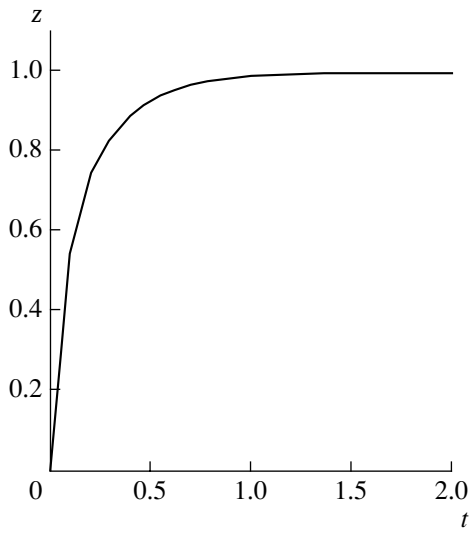

Fig. 1. Charging of a grain in time (here, z is the grain charge normalized to the equilibrium charge). The charging time corresponds to the rate of charging in its final stage where the electron and ion currents becomes almost equal to each other.

2.1. Charging Time and Charging Frequency

Equation (16) of [1] (below, references to formulas of [1] are given as (1.*N*), where *N* is the number of a formula; i.e., in the case at hand, we have (1.16)) for grain charging describes the dynamics of grain charges. It can be used to investigate the time scales of charging in different charging models. For the simplest OML model, it can be used in the general form. We multiply (1.16) by e^2/aT_e and use OML charging currents to write the equation for the time evolution of the dimensionless grain charge $z = Z_d e^2/aT_e$:

$$\frac{dz}{dt} = -\frac{1}{\sqrt{2\pi}}\frac{v_{Ti}a}{\lambda_{Di}^2}(z + \tau - \sqrt{m\tau}\exp(-z)). \qquad (1)$$

Here, a is the grain size, T_e is the electron temperature, Z_d is the grain charge (in units of the electron charge), $\tau = T_i/T_e$, $m = m_i/m_e$, and λ_{Di} is the ion Debye length.

For small deviations δz from the equilibrium dust charge z_{eq} ($\delta z \ll z_{eq}$), we find

$$\frac{\partial \delta z}{\partial t} = -\frac{1}{\tau_{ch}}\delta z = -\nu_{ch}\delta z, \qquad (2)$$

where τ_{ch} is the characteristic time of charging and ν_{ch} is the charging frequency;

$$\nu_{ch} = \frac{1}{\sqrt{2\pi}}\frac{v_{Ti}a}{\lambda_{Di}^2}(1 + z_{eq} + \tau). \qquad (3)$$

The charging frequency is proportional to the dust size, which means that the charging is faster for larger dust grains. When the charging process starts with charges that are far from equilibrium, one can distinguish two stage of charging: the first, faster stage is determined by the electron capture by a grain and is simply related to the time needed for electrons to reach the grain and the second, longer stage is determined by ion capture and the time needed to reach the equilibrium charge value (it is on the order of $t_{ch} = 1/\nu_{ch}$). Figure 1 shows the solution to the charging equation; here, time is normalized to $(v_{Ti}a/\sqrt{2\pi}\lambda_{Di}^2)^{-1}$ ($t \longrightarrow t\sqrt{2\pi}\lambda_{Di}^2/v_{Ti}a$) and z is normalized to z_{eq} ($z \longrightarrow z/z_{eq}$). The calculations were performed for argon at $\tau = 0.02$, $T_i = 300$ K, and $n_i = 10^9$ cm^{-3}; in this case, $z_{eq} = 2.63$.

Estimates of the charging frequency in typical experiments show that it is very short; i.e., the charging is extremely fast. For example, for $T_i \approx 300$ K, $n_i \approx 10^9$ cm^{-3}, $a = 10$ μm, and $z = 3$, we have $\nu_{ch} \approx 1$ MHz. A consequence of the charging process is very drastic: all the modes with frequencies less than the charging frequency are modified by charging (this problem will be considered in more detail in our subsequent paper devoted to collective effects in complex plasmas).

An important quantity is the charging length λ_{ch}, which is defined as the distance traveled by a thermal ion during the charging time,

$$\lambda_{ch} = \frac{v_{Ti}}{\nu_{ch}} \approx \frac{\lambda_{Di}^2}{a}, \qquad (4)$$

and which is always larger than the ion Debye screening length for $a \ll \lambda_{Di}$.

In the presence of superthermal ion drift, the charging frequency can be expressed through the Mach number M; for $\tau \ll 1$, it is

$$\nu_{ch} = \frac{a v_{Ti}\sqrt{\tau}}{4\sqrt{2}\lambda_{Di}^2}(z + 1)\left(\frac{z}{M} + \frac{M}{2}\right). \qquad (5)$$

For $\tau \ll 1$ and M on the order of unity (as is in the plasma sheath), the charging time is $\tau^{-1/2}$ times longer than for subthermal drift.

2.2. Fluctuations of Dust Charges

It is well known that phase transitions are accompanied by large fluctuations of all the parameters. Such fluctuations should also be present and measured during plasma condensation in complex dusty plasmas. The new effect for complex plasmas is the variability of dust charges, which will lead to fluctuations of charges. Obviously, these fluctuations should be taken into account in any approach to phase transitions in complex plasmas. Also, it is probable that these fluctuations can play a dominant role in phase transitions for a certain range of parameters. The dust charge fluctuations are of a collective nature, being in the first approximation proportional to the dust density. They were investigated only recently, and there are still some problems concerning noncollective dust fluctuations. Collective

fluctuations should exceed noncollective ones in phase transitions, and one needs to know the conditions at which collective fluctuations dominate noncollective fluctuations. We will start with noncollective fluctuations and, then, will give only the result and a reference to the collective fluctuations. This field is now fast developing, and we will able to touch only the first results on collective fluctuations. So far, different approaches have been used to describe noncollective fluctuations, and this point should also be clarified, because the links with very developed usual plasma fluctuation approaches (in the absence of dust) can be established and the methods of plasma fluctuations can be used to further develop the theory of dust fluctuations.

Noncollective dust charge fluctuations can be treated as a result of the discreteness of the charging process, i.e., as being due to the fact that the change in the dust charge is discrete: it is equal either to the electron charge $-e$ for the absorption of a single electron or to $+e$ for the absorption of a singly ionized ion. In plasma physics, the discreteness is usually treated as fluctuations of the electron and ion distribution function. These fluctuations should lead to fluctuations of the currents on dust grains and, therefore, should lead to fluctuations of the dust charges. An important question is whether these two possible treatments of dust charge fluctuations are identical or not. The answer is that the treatment of dust charge fluctuations as due to fluctuations of currents on a dust grain is more general and includes, in a certain limit, the effect of the discreteness of the charging process. In the available literature, the discreteness of the charging process was first considered in [23] (see also [24]), and the fluctuations of currents on dust grains were first treated in [25]. We intend to show here that the result of [24] coincides with a result that can be obtained from the fluctuations of the electron and ion distributions due to their discreteness [25] only in the limit where the electron and ion fluctuations can be regarded as independent particle fluctuations, i.e., as a part of noncollective fluctuations. In plasma physics, this type of fluctuations is known as free particle fluctuations, and another important type of plasma particle fluctuation is known as induced fluctuations [26]. The role of induced electron and ion fluctuations in dust charging has not yet been investigated in detail, but the role of fluctuations induced by dust (collective dust component of fluctuations, which is the most important for the problem of condensation in complex plasmas) was considered in [27]. The importance of the latter process is obvious, because the electron and ion fluctuations in the charging process can be induced by dust grains, which absorb electrons and ions, and therefore can depend on dust fluctuations. Thus, such a more detailed treatment [27] allows one to consider the problem self-consistently, which in turn can allow one to treat collective dust fluctuations as related to long-range correlations in strongly correlated states. At the end of this section, we will give the main results of [27]. Here, we start with the problem of electron and ion fluctuations as fluctuations of independent particles and neglect induced fluctuations related to both plasma particles and dust. Note that this problem was considered in [24, 28]; here, we compare the results obtained by the method of fluctuations of currents on dust grains [25] with that given in [24]. The distribution of fluctuations considered in [24] is a Gaussian distribution with the spectral width equal to the charging frequency. Induced fluctuations can have frequencies much higher or much lower than the charging frequency. In the low-frequency range, the spectral width of these fluctuations depend on the dust density [27]. The appearance of long-range correlations leading to strong coupling is related to low-frequency fluctuations and collective processes of dust grain charging. Giving here, for the first time, proof that the results of an analysis of charge fluctuations due to the discreteness of the charging process [24] coincide with those for current fluctuations due to the discreteness of electron and ion distributions [25], we hope that such an approach can be used to further develop the theory of dust charge fluctuation using the known results from plasma physics [26] or the results of the kinetic theory of dusty plasmas, which have been developed recently [27, 29, 30].

We start here with noncollective fluctuations of dust charges. When the collective effects are neglected, the charge of each dust grain is considered to fluctuate independently. The dust density affects these fluctuations via the quasineutrality condition. First, we will consider an approach treating fluctuations as being due to the discreteness of the charging process. Then, we will consider the effects related to the discreteness of the electron and ion distributions leading to current fluctuations caused by electron and ion fluctuations.

2.2.1. Charge fluctuations due to the discreteness of the charging process. Dust grains embedded in a plasma are generally multiply charged with $Z_d \gg 1$. Due to normal statistical fluctuations associated with discrete impacts of individual electrons and ions, the charge Q and, in turn, the surface potential ϕ_s of the dust grain will fluctuate.

A Fokker–Planck description of grain charging due to the discreteness of the charging process was developed in [24], where charge fluctuations resemble a Markov process: the charge varies in steps of $\pm e$ with the probability per unit time for a positive change given by I_i and, for negative change, by I_e (remember that, by definition, I_i and I_e are, respectively, the ion and electron currents on the total dust surface per the absolute value of the electron charge $e > 0$). The probability f_Q of the grain to have the charge Q at time t is then given by [24]

$$\frac{\partial f_Q}{\partial t} = I_i f|_{Q-e} - I_e f|_{Q+e} - (I_i - I_e) f|_Q. \qquad (6)$$

Equation (6) assumes that both the charging currents and the probability depend on the instantaneous charge ($Q-e$, Q, $Q+e$), but not on the previous history of charging. This is reasonable, provided that plasma fluctuations occurs on much longer time scales than dust charge fluctuations.

Treating Q as a continuous variable and using the normalization condition

$$\int f_Q dQ = 1, \tag{7}$$

we linearize the charging current around the steady state $\langle I_e\rangle + \langle I_i\rangle = 0$,

$$I_e + I_i = \delta Q(\langle I_e'\rangle + \langle I_i'\rangle) + \delta I_i + \delta I_e, \tag{8}$$

and neglect the fluctuating currents δI_e and δI_i. This yields the diffusion–convection equation

$$\frac{\partial f_Q}{\partial \tau} = \frac{\partial}{\partial Q}(\delta Q f_Q) + \langle(\delta Q)^2\rangle\frac{\partial^2 f_Q}{\partial Q^2}, \tag{9}$$

where $\delta Q = Q - \langle Q\rangle$;

$$\tau = \frac{t}{\tau_{ch}} = -te(\langle I_e'\rangle + \langle I_i'\rangle); \tag{10}$$

τ_{ch} is the steady-state charging time, coinciding with Eq. (1.82) for the OML model; and

$$\langle(\delta Q)^2\rangle = \frac{e}{2}\frac{\langle I_e\rangle - \langle I_i\rangle}{\langle I_e'\rangle + \langle I_i'\rangle} \tag{11}$$

is the mean square of dust charge fluctuations, as can be seen from a stationary solution to Eq. (9):

$$f(\delta Q) = \frac{1}{\sqrt{2\pi}\langle(\delta Q)^2\rangle}\exp\left(-\frac{(\delta Q)^2}{2\langle(\delta Q)^2\rangle}\right). \tag{12}$$

For the OML model, a simple substitution of currents in the last expression yields

$$\frac{\delta Z_d^2}{Z_d} = \frac{\tau + z}{z(1+\tau+z)} \approx \frac{1}{1+z}, \tag{13}$$

where Z_d, as previously, is the equilibrium dust charge in units of the electron charge and the last approximate equality is written in the limit $\tau \ll 1$. As could be expected, the root mean square fluctuation of the dust charge is on the order of the equilibrium dust charge, although lower than it.

The temporal evolution of the dust grain charge can also be written as a Langeven equation

$$\frac{\partial Q}{\partial t} = -eI_e + eI_i + g(t), \tag{14}$$

where $eI_i - eI_e = -(Q - \langle Q\rangle)/\tau_{ch}$ + (higher order terms) is the linearized net current on the grain and $g(t)$ is a stochastic forcing function with zero mean. For noncorrelated fluctuations, as is assumed in Eq. (6), the forcing function should satisfy the relationship

$$\langle g(t)g(t+t')\rangle = 2\tau_{ch}\langle(\delta Q)^2\rangle\delta(t-t'), \tag{15}$$

where $\delta(t)$ is the Dirac delta function.

In this approach, it is possible to calculate the "lifetime" of a given charge fluctuation $|\delta Q|$ (i.e., the growth and dissipation times), as well as the charge autocorrelation function, power spectrum, etc. For instance, the autocorrelation function of charge fluctuations is

$$\langle Q(t)Q(t+t')\rangle \propto \exp\left(-\frac{t'}{\tau_{ch}}\right), \tag{16}$$

and the power spectrum is Lorentzian with the characteristic frequency $1/\tau_{ch}$.

The time required for a charge fluctuation to grow from $\langle Q\rangle$ to $\langle Q\rangle + |\delta Q|$ is given by

$$t_{grow}(\delta Q) = \tau_{ch}\sqrt{\frac{\pi}{2}}\int_0^{|\delta Q|/\sqrt{\langle(\delta Q)^2\rangle}}\exp(x^2/2)\mathrm{erf}\left(\frac{x}{\sqrt{2}}\right)dx, \tag{17}$$

accordingly, the time required for a charge fluctuation to dissipate back from $\langle Q\rangle + |\delta Q|$ to $\langle Q\rangle$ is

$$t_{diss}(\delta Q) = \tau_{ch}\sqrt{\frac{\pi}{2}}\int_0^{|\delta Q|/\sqrt{\langle(\delta Q)^2\rangle}}\exp(x^2/2)\left(1-\mathrm{erf}\left(\frac{x}{\sqrt{2}}\right)\right)dx. \tag{18}$$

This kind of theoretical derivation can be compared with Monte Carlo simulations (see [28]) and compared with OML result (13) for Maxwellian (nonfluctuating) distributions of electrons and ions. The result of such a comparison shows good agreement between the Monte Carlo calculations and the theoretical fits based on the Fokker–Plank model. The numerical values were obtained for argon at $T_e = 1$ eV, $T_i = 500$ K, and $n_i = n_e = 10^9$ cm^{-3}. Note that both the theory and the simulations take into account only the discreteness of the charging process.

2.2.2. Charge fluctuations due to the discreteness of the electron and ion distributions. In principle, it is obvious that if the electron and ion distributions fluctuate, the current on a dust grain will also fluctuate. For instance, in the OML approach, the fluctuating currents $\delta I_{i,e}$ are given by

$$\delta I_{i,e} = \int \sigma v \delta f_{i,e} d\mathbf{v}, \tag{19}$$

where $\delta f_{i,e}$ is the fluctuating distribution function of ions or electrons. Nevertheless, the direct use the OML approach to calculate dust charge fluctuations is questionable. As will be shown, the OML approach needs to be generalized to properly treat the fluctuation currents. Indeed, one can use Eq. (19) to estimate characteristic spatial scales that will contribute to the current fluctua-

tions if the electrons and ions fluctuate as independent noncorrelated particles. Present-day plasma theory provides a simple relation for noncorrelated fluctuations, which mathematically expresses the known statistical relation for the independent fluctuations of the number of particles N in a volume V, namely,

$$\langle (\delta N)^2 \rangle = \langle N \rangle. \tag{20}$$

Applying this expression to particles with a momentum $\mathbf{p}$ in an interval $d\mathbf{p}$ leads to an expression for the mean square fluctuation of the particle distribution function $\langle (\delta f_\mathbf{p})^2 \rangle$. Since the fluctuations describe the time and space variations of the particle distributions, $\delta f_\mathbf{p}$ depends both on $\mathbf{r}$ and t. The best way to find spatial and time scales that contribute to these fluctuations is to expand the fluctuation function in Fourier components,

$$\delta f_\mathbf{p} = \int \delta f_{\mathbf{p},\mathbf{k},\omega} \exp(\mathbf{k}\cdot\mathbf{r} - \omega t) d\mathbf{k} dt. \tag{21}$$

Then, Eq. (20) reads (see [26])

$$\begin{aligned} &\langle \delta f_{\mathbf{p},\mathbf{k},\omega} \delta f_{\mathbf{p}',\mathbf{k}',\omega'} \rangle \\ &= \langle f_\mathbf{p} \rangle \delta(\mathbf{p} - \mathbf{p}') \delta(\mathbf{k} + \mathbf{k}') \delta(\omega + \omega') \delta(\omega - \mathbf{k}\cdot\mathbf{v}). \end{aligned} \tag{22}$$

Delta function $\delta(\mathbf{k} + \mathbf{k}')$ expresses that the correlation function of fluctuations depends only on the difference between the spatial coordinates, $\delta(\omega + \omega')$ expresses that the correlation function depends only on the difference between the times, and $\delta(\omega - \mathbf{k}\cdot\mathbf{v})$ expresses that the independent free particles move along straight lines.

Then, an important question arises as to whether we can use this simple expression for independent particle fluctuations in the expression for the flux on dust grains obtained from the OML model. For the following reasons, the answer is that it is impossible. The OML model relates the electron and ion distributions at the grain surface to those at infinity, and the expressions for $f_{e,i}$ in Eq. (19) are the distributions at infinity. "Infinity" physically means sufficiently far from the grain, namely, at distances much larger than the charging distance $\lambda_{ch} \approx \lambda_{Di}^2/a$. In the OML approach, the ion and electron densities can depend on the local position, but they should be almost homogeneous at distances on the order of the charging distance (only in this case, the electron and ion densities at distances on the order of the charging distance can be attributed to the grain position, being almost the same as those at the position of the grain). Applying expression (22) to Eq. (19), we can find the mean square of the OML fluctuation current. As a result, we obtain that the corresponding equation is described as an integral with respect to k ($2\pi/k$ is the characteristic fluctuation scalelength) and that this integral diverges at large k as $\int k dk$, which shows that the size of the fluctuations that give the largest contribution is much less than the charging length, in contradiction with the assumption used in the OML approach.

Thus, we cannot use the OML approach in the existing form and need to calculate the currents taking into account the inhomogeneity of fluctuations of the electron and ion distributions. We will use the expansion in Fourier series and find the cross section for each spectral harmonic (see the Appendix of [27]):

$$\begin{aligned} \sigma_{e,i}(\mathbf{k}) &= \int_0^{2\pi} d\phi \int_0^{p_{\max}} \exp(i\mathbf{k}_\perp \cdot \mathbf{r}_\perp) r_\perp dr_\perp \\ &= 2\pi \frac{p_{\max}}{k_\perp} J_1(p_{\max} k_\perp), \end{aligned} \tag{23}$$

where $p_{\max}$ is the maximum impact parameter,

$$p_{\max} = a\sqrt{1 \pm \frac{Z_d e^2 2}{m v^2}}, \tag{24}$$

and $k_\perp$ is the absolute value of the component of $\mathbf{k}$ perpendicular to $\mathbf{v}$. With this cross section, the fluctuating current is found to be

$$\delta I_{e,i,\omega} = \int \sigma_{e,i}(\mathbf{k}) \exp(i\mathbf{k}\cdot\mathbf{r}) v \delta f_{e,i,\mathbf{k},\omega} d\mathbf{k}. \tag{25}$$

Further, we take into account only the plasma particle fluctuations related to the discreteness of their distributions. Therefore, we will write the linearized charging equation for the time Fourier components in the form

$$(\omega + i\nu_{ch}) \delta Z_{d,\omega} = \delta I_{i,\omega} - \delta I_{i,\omega}. \tag{26}$$

Both the mean square of dust charge fluctuations and the autocorrelation function can be easily found from this expression through the Fourier component of the current correlation function $|I_{e,i,\omega}|^2$ defined by the relation

$$\langle \delta I_{e,i,\omega} \delta I_{e,i,\omega'} \rangle = |I_{e,i,\omega}|^2 \delta(\omega + \omega'). \tag{27}$$

Taking into account that the electrons and ions fluctuate independently yields

$$\begin{aligned} &\langle \delta Z_d(t) \delta Z_d(t+\tau) \rangle \\ &= \int \frac{\exp(-i\omega\tau)}{\omega^2 + \nu_{ch}^2} (|I_{e,\omega}|^2 + |I_{i,\omega}|^2) d\omega. \end{aligned} \tag{28}$$

Substituting here expression (25) for the fluctuating current and using formula (22) to find its mean square value, we obtain for the fluctuations related to the ion discreteness

$$\begin{aligned} \frac{\langle (\delta Z_d)^2 \rangle|_i}{Z_d} &= \frac{\tau}{\pi z(1+\tau+z)} \int \frac{\nu_{ch} d\omega}{\omega^2 + \nu_{ch}^2} \left(y + \frac{z}{\tau}\right) \\ &\times \exp(-y) dy J_1^2\left(k_\perp a \sqrt{1 + \frac{z}{\tau y}}\right) \frac{dk_\perp}{k_\perp} = \frac{\tau + z}{2z(1+\tau+z)}. \end{aligned} \tag{29}$$

In obtaining this result, we used the relationship

$$\int_0^\infty J_1^2(k)\frac{dk}{k} = \frac{1}{2}. \tag{30}$$

The first equality in expression (29) shows that the frequency spectrum is of the Lorentz type, $\propto 1/(\omega^2 + \nu_{ch}^2)$. Although the cross sections for electrons and ions differ from each other, the contribution from the electron discreteness to dust charge fluctuations is equal to the contribution from ion fluctuations (29). Indeed, we find

$$\frac{\langle(\delta Z_d)^2\rangle\big|_e}{Z_d} = \frac{\tau}{\pi z}\frac{n_e v_{Te}}{n_i v_{Ti}}\exp(-z)\int\frac{\nu_{ch}d\omega}{\omega^2+\nu_{ch}^2}\int_z^\infty dyy$$
$$\times \exp(-y)J_1^2\left(k_\perp a\sqrt{1-\frac{z}{y}}\right)\frac{dk_\perp}{k_\perp} = \frac{\tau+z}{2z(1+\tau+z)}. \tag{31}$$

To obtain final expression (31), we used the balance of average currents described by the dust charging equation.

The sum of expressions (29) and (31) coincides with result (13), obtained in [24] by a quite different method exploiting the discreteness of the charging process (although the final result in form (13) was not given in [24], one can easily obtain it from expression (32) of [24] by using relations from the OML charging equation). The coincidence seems to be natural because the method of fluctuating current also uses the discreteness of the electron and ion distributions. The new result that cannot be seen so clearly from the previous approach is that the contributions from electrons and ions to dust charge fluctuations are equal to each other. However, more important is the possibility of generalizing current fluctuation by taking into account induced fluctuations through the plasma and dust responses and the possibility of a self-consistent treatment of dust charge fluctuations taking into account the dependence of electron and ion fluctuations on dust charge fluctuation and other dust and plasma parameters, such as induced fluctuations of both dust and plasma particle densities. This way makes it possible to find the role of dust fluctuations both in long-range interactions in strongly correlated systems and in transitions to and from strong correlated states.

2.3. Collective Dust Fluctuations

Collective dust fluctuations were obtained only recently by using a new kinetic theory of dusty plasma, which we are not able to present here in short terms. Here, we will give only the final result in which all noncollective fluctuations and also the effects of induced fluctuations of electrons and ions are neglected (estimates show that these effects are small when the numbers of electrons and ions in their Debye spheres are large) [27]:

$$\frac{\langle\delta Z_d\rangle^2}{Z_d^2} \approx n_d a^2 \lambda_{Di}\frac{z^2}{\tau^2(1+z)^2}. \tag{32}$$

Let us take some typical data of existing experiments: $a = 3$ μm, $\lambda_{Di} = 30$ μm, $n_d = 3\times10^3$, and $\tau/z = 10^2$. Then, for collective fluctuations, we find $\langle(\delta Z_d)^2\rangle/Z_d^2 \approx 4\times10^{-3}$, while for noncollective fluctuations, we have $\langle(\delta Z_d)^2\rangle/Z_d^2 = Z_d^{-1}(1+z)^{-1} = 3\times10^{-5}$; i.e., the latter is two orders of magnitude lower, which means that under laboratory conditions, collective dust charge fluctuations can be much larger than were expected earlier for noncollective fluctuations. This is an important point for further developments related to dust charge fluctuations in the course of plasma condensation to a strongly coupled state.

2.4. Absorption of Ions and Electrons on Grains

We consider here only the noncollective absorption of ions and electrons on dust grains with the grain number density n_d. The term noncollective means that each grain absorbs independently of the presence of other grains and the total absorption is a sum of absorptions on individual grains. Since any ion on its path through a dust-containing region subsequently reaches other grains and has a probability to be absorbed by one of them, the average ion density will decrease. To calculate this effect, we can sum the absorption on individual grains and find the corresponding dissipation term in the ion continuity equation. The flux of ions onto an individual grain is determined by the current I_i (remember that above we introduced I_i as the current on an individual grain per unit charge $e > 0$ and, therefore, I_i coincides with the ion flux onto the grain). We can write this flux for the general case in the presence of ion drift (this case, which was regarded in [1] as anisotropic charging, is of practical interest in sheath regions). We introduce the charging coefficient α_{ch} given by expression (1.75). Then the ion flux onto an individual grain can be written as

$$I_i = 4\pi\sqrt{2}\,v_{Ti}n_i\frac{z}{\tau}\alpha_{ch}. \tag{33}$$

In the limit of low ion drift velocities, $u \ll 1$, where

$$\mathbf{u} \equiv \frac{\mathbf{v}_i}{\sqrt{2}\,v_{Ti}}, \quad v_{Ti} = \sqrt{\frac{T_i}{m_i}}, \tag{34}$$

$$\alpha_{ch} \approx \frac{1}{2\sqrt{\pi}}\left(1+\frac{\tau}{z}\right), \tag{35}$$

we return to expression (1.24) for the ion flux. With expression (33), we will be able to find the absorption of ions on grains for any ion drift velocity. The continu-

ity equation for ions that takes into account the effect of absorption of ions on grains will be

$$\frac{\partial n_i}{\partial t_{\rm ac}} + \frac{\partial n_i \mathbf{v}_i}{\partial \mathbf{r}_{\rm ac}} = -n_d I_i. \quad (36)$$

Here, the subscript "ac" is introduced to distinguish the actual spatial coordinates and time from their normalized values, for which it is convenient to use notation without any subscript. Equation (36) takes a very simple form if we write it in a dimensionless form, using for the normalization of distances and time the characteristic charging length and the characteristic charging time, respectively. More exactly, for normalization we will use these quantities, excluding the parameters that can, in fact, be time or space dependent. Instead of $\lambda_{\rm ch} = \lambda_{Di}^2\sqrt{2\pi}/a(1+\tau+z)$ for the normalization of distances, we will use simply

$$L = \frac{\lambda_{Di}^2}{a} = \frac{T_i}{4\pi n_0 e^2 a}, \quad (37)$$

and for the normalization of time, we will use L/v_{Ti}. Here, n_0 is a constant density that can naturally be the plasma density outside the dust-containing region or some other density relevant to the problem under consideration. This density should be constant in order to exclude time or space dependent coefficients from normalization. For the same reason, we excluded the factor $1 + z + \tau$ from normalization because the dust charge can vary in space and time. Thus, we have

$$\mathbf{r} \equiv \frac{\mathbf{r}_{\rm ac}}{L}, \quad t \equiv \frac{t_{\rm ac} v_{Ti}}{L}. \quad (38)$$

For the ion density and drift velocity, we use the natural normalization

$$n \equiv \frac{n_i}{n_0}, \quad \mathbf{u} \equiv \frac{\mathbf{v}_i}{\sqrt{2} v_{Ti}}. \quad (39)$$

Multiplying Eq. (36) by $\lambda_{Di}^2/an_0\sqrt{2}\,v_{Ti}$, we convert it to a very simple dimensionless form

$$\frac{\partial n}{\partial t} + \frac{\partial n\mathbf{u}}{\partial \mathbf{r}} = -Pn\alpha_{\rm ch}, \quad (40)$$

where $P = n_d Z_d/n_0$ is the parameter characterizing the relative dust charge density [see expression (1.2)]. Here, we normalize the dust charge density to a constant ion charge density (e.g., to the ion density outside the dust region).

Equation (40) has no small parameters and shows that, for P on the order of unity, complex plasma will disappear on the time scale of the charging process if there is no source supporting the ion density. In experiments, such a source is often volume ionization. A reasonable model for this source is one where the number of the ions created is proportional to the electron density. For instance, this can be expressed as an additional term on the right-hand side of Eq. (40):

$$Q_i = n_e/\tau_i, \quad (41)$$

where $n_e = n_{e,\,\rm ac}/n_0$ is the normalized electron density and τ_i is the characteristic time of creating an ion by ionization (in units of L/v_{Ti}). Equation (40) with additional term (41) will have a steady-state solution when ionization is balanced by absorption on dust grains.

As concerns electron dissipation, we note that the electron flux should be almost equal to the ion flux and the sink term in the electron continuity equation is the same as the source term because the electrons and ions are created by an ionization source in pairs (for usual weakly ionized laboratory plasma). On the other hand, the behavior of electrons and ions is usually different because, in most cases of interest, the electron drift velocity is small as compared to the electron thermal velocity and often does not enter in the equations for the electron component. Therefore, one does not need to consider the electron continuity equation to find the electron drift velocity. The electron density can be determined from the distribution of the electrostatic potential because the electrons behave almost adiabatically. Models different from the OML charging model give another value for the charging coefficient $\alpha_{\rm ch}$; therefore, the theoretical description of the mentioned balance is model dependent. We note that experiments on this balance for a known ionization source can check different models of charging. This may be important issue for future experiments.

2.5. Noncollective Friction of Ions in a Gas of Grains

The ions are not only absorbed by grains but also transfer their momentum to the grains. There are two mechanisms for this transfer: one is related to ion absorption by grains and another is related to the scattering of ions by the Coulomb field of the grains. The second mechanism conserves the number of ions and does not contribute to the continuity equation. Under the condition $z/\tau \gg 1$, the second mechanism is dominant for low ion drift velocities, while for superthermal velocities and Mach numbers on the order of unity, both mechanisms are comparable and neither of them is negligible. As in the previous section, we will consider here only noncollective effects, by summing the momentum transferred in the interactions with individual grains. In the limit of low drift velocities, the friction of ions in the interaction with grains is proportional only to the drift velocity. An estimate of the capturing friction force $\mathbf{F}_{\rm c}$ and the capturing friction frequency $\nu_{\rm c}$ related to ion absorption (capture) for small drift velocities is very simple:

$$\mathbf{F}_{\rm c} = -\nu_{\rm c} m_i \mathbf{v}_i, \quad \nu_{\rm c} \approx n_d v_{Ti} \sigma_i \approx n_d v_{Ti} \pi a^2 \frac{Z}{\tau}. \quad (42)$$

The last approximate equality in the second of expressions (42) is found from the OML approach in the limit $z/\tau \gg 1$. We note that the last formula can be also expressed through the parameter P if we use as a unit for the friction force the value of the force that decreases the energy of ions by T_i on the distance $L = \lambda_{Di}^2/a$, which is on the order of the charging length λ_{ch}; i.e., we extract from expression (42) the factor T_i/L,

$$\mathbf{F}_c = -\frac{T_i}{2\sqrt{2}L}P\mathbf{u}. \tag{43}$$

For P on the order of unity and for an ion drift velocity on the order of the ion thermal velocity, this force decreases the ion momentum by the thermal ion momentum on the distance equal to the charging length and, since this force is completely inelastic, it decreases the directed ion energy by the ion thermal energy. The other force F_{sc}, related to elastic scattering of ions in the dust Coulomb field can be estimated as follows:

$$\mathbf{F}_{sc} = -\nu_{sc} m_i \mathbf{v}_i,$$
$$\nu_{sc} \approx n_d v_{Ti} \sigma_{sc} \approx n_d v_{Ti} \pi r_{eff}^2 \approx n_d v_{Ti} \frac{Z_d^2 e^4}{T_i^2}. \tag{44}$$

The last estimate is found by assuming that

$$\frac{Z_d e^2}{r_{eff}} \approx T_i. \tag{45}$$

Scattering force (44) can be expressed through P by extracting the factor T_i/L:

$$\mathbf{F}_{sc} - \frac{z}{\tau}\frac{T_i a}{2\sqrt{2}\lambda_{Di}^2}P\mathbf{u} = -\frac{T_e}{2\sqrt{2}L}zP\mathbf{u}. \tag{46}$$

The last expression shows explicitly that the scattering force is z/τ times larger than the capture force if $z/\tau \gg 1$. This force changes the energy by an amount on the order of electron thermal energy on the distance equal to the charging length.

To find the general expression for the friction force for any values of the ion drift velocity due to both Coulomb scattering and the capturing of ions, one can integrate the change of the ion momentum described by both the known Coulomb collision integral and the capturing OML cross section over the drifting Maxwellian distribution and express the result through the so-called drag coefficient α_{dr}:

$$\mathbf{F}_{fr} = \mathbf{F}_c + \mathbf{F}_{sc} = -\frac{T_e a}{\lambda_{Di}^2}zP\alpha_{dr}\mathbf{u}. \tag{47}$$

It is natural to normalize the friction force to $F_0 = T_e a/\lambda_{Di}^2$,

$$\mathbf{F} \equiv \frac{\mathbf{F}_{fr}}{F_0} = -zP\alpha_{dr}\mathbf{u}. \tag{48}$$

In the general case, the coefficient α_{dr} can be expressed through the error function

$$\alpha_{dr} = \frac{\mathrm{erf}(u)}{8u^3}\left[\frac{\tau}{z}(-1 + 4u^2 + 4u^4) + 2\frac{\tau^2}{z^2}(-1 + 2u^2) + 4\ln\Lambda\right] + \frac{\exp(-u^2)}{4\sqrt{\pi}u^2}\left[\frac{\tau}{z}\left(\frac{\tau}{z}(1 + 2u^2) + 2\right) - 4\ln\Lambda\right], \tag{49}$$

where $\ln\Lambda$ is the Coulomb logarithm equal in the first approximation to $\ln(\lambda_{Di}/a)$. In the drag coefficient, one can easily distinguish between the terms that appear due to the ion capture by the grain and the terms that appear due to Coulomb scattering by the grains: all terms containing the Coulomb logarithm are due to Coulomb scattering, while all terms that do not contain the Coulomb logarithm are due to capturing. In the limit $z/\tau \gg 1$, the effect of Coulomb scattering is dominant if the drift velocities are low as compared to the ion thermal velocity. In this case, we find

$$\alpha_{dr} = \frac{2}{3\sqrt{\pi}}\ln\Lambda. \tag{50}$$

For superthermal ion drift velocities, it is possible to express the drag coefficient through the Mach number M:

$$\alpha_{dr} u \approx \frac{\tau}{M^2}\left[\ln\Lambda + \frac{M^2}{2z} + \frac{M^4}{4z^2}\right]. \tag{51}$$

The coefficient τ on the right-hand side of this expression is usually included in the normalized length; therefore, in this case, the effective drag depends only on the Mach number. For M on the order of unity, the terms with the Coulomb logarithm and the terms without it are of the same order of magnitude, which means that the contributions from Coulomb scattering and capturing are of the same order of magnitude. Expression (51) is important for treating dusty plasma in sheaths.

The question then arises as to why we called the total friction coefficient the drag coefficient. The reason is simple: due to momentum conservation, the loss of the ion momentum is transferred to dust grains and any ion drift creates the drag force for grains. The ion drag force is one of the most important forces acting on dust grains. In a similar way, it can be also shown that friction on electrons is always small as compared to other forces acting on electrons if $\tau \ll m^{1/3}$, which is always

satisfied when $\tau \ll 1$. Because of the small electron mass, the drag of electrons on grains is of minor importance.

The ion momentum losses are also model dependent, because both the absorption on grains and the scattering are model dependent (here, we used only the OML model for estimates) and because we assumed a multiple scattering approach (estimates show that taking into account the scattering by large angles gives nearly the same contribution as the multiple scattering by small angles). Both models can be checked by experiments on injecting ions into a dusty plasma and measuring the depletion of the ion density (these experiments are being developed now).

2.6. Characteristic Electric Fields in Complex Plasmas

High dissipation rates in complex plasma can create rather large fields even in quasineutral regions. These fields can easily be estimated in the case where ion–neutral collisions are negligible and in the case where they are dominant. In the first case, we can equate the friction force acting on ions to the electric field force. If the drift velocity is on the order of the thermal velocity and P is on the order of unity, then we obtain the following estimate for the effective electric field:

$$E_{0,id} \approx \frac{T_e a}{e\lambda_{Di}^2}. \tag{52}$$

For typical ion densities on the order of $n_i \approx 10^9$ cm^{-3}, $a \approx 30$ μm, and $T_e \approx 2$ eV, we obtain $E \approx 10^3$ V/cm. When the ion friction is determined by ion–neutral collisions, in this estimate, we should use the mean free path for ion–neutral collisions λ_{in} instead the charging length λ_{Di}^2/a. In this case, estimates also give a large value of the electric field.

When the characteristic length is determined by the charging length, the usual estimate obtained from the quasineutrality condition changes. In this case, we normalize the length to $L = \lambda_{Di}^2/a$ and introduce the dimensionless field as

$$E \equiv \frac{E_{\rm ac}}{E_{0,id}}. \tag{53}$$

Then, Poisson's equation takes the form

$$\frac{\partial \mathbf{E}}{\partial \mathbf{r}} = \tau\frac{\lambda_{Di}^2}{a^2}(n - n_e - P). \tag{54}$$

The quasineutrality condition means that we can neglect the left-hand side of Eq. (54) and equate the right-hand side to zero. When the dimensionless electric field is on the order of unity and its gradient (or the characteristic dimensionless length) is also on the order of unity, this condition is determined by the relation

$$a \ll \lambda_{Di}\sqrt{\tau}. \tag{55}$$

This relation is a consequence of the large influence of dust on electrostatic phenomena in a complex plasma. It is unusual only at first glance and follows from Poisson's equation. Note that, in ordinary plasmas, the quasineutrality condition means that the characteristic inhomogeneity length should be larger than the Debye length. There is no contradiction between these two statements because the latter condition is usually obtained from linearized Poisson's equation, whereas the condition in which the characteristic length is the charging mean free path (or the mean free path for ion–dust collisions) it is related to the self-consistent nonlinear behavior of the total complex system. Numerical solution of the set of self-consistent nonlinear balance equations confirms that, in dust-containing regions, relation (55) is really the quasineutrality condition [31]. In regions where dust does not play a crucial role, the quasineutrality condition takes the usual form. The only important restriction to apply relation (55) is that the ion–neutral friction force is negligible as compared to the friction on dust grains. When ion–neutral collisions dominate and the electric field in a quasineutral plasma is determined by self-consistent nonlinear interaction with dust, we find the following estimate for the characteristic electric field $E_{0,in}$:

$$E_{0,in} \approx \frac{T_i}{e\lambda_{in}} \approx E_{0,id}\tau\frac{\lambda_{\rm ch}}{\lambda_{in}} = E_{0,id}R, \tag{56}$$

where

$$R = \tau\frac{\lambda_{\rm ch}}{\lambda_{in}}. \tag{57}$$

Estimate (56) is obtained by equating the ion–neutral collision friction force to the electric field force. In this case, the characteristic length differs from that introduced above by the same factor R; i.e., it is equal to the ion–neutral mean free path divided by τ. The dimensionless ion and electron densities and the parameter P should be defined in this case by dividing not by n_0 as above but by the product n_0R, which does not in fact depend on n_0 because $\lambda_{Di}^2 \propto 1/n_0$. This follows from the normalization of the whole set of balance equations and is confirmed by many numerical results. Under conditions where the ion–neutral collisions are dominant, instead of quasineutrality condition (55), we obtain

$$a \ll \lambda_{in}. \tag{58}$$

This condition seems to be quite natural and is also confirmed by self-consistent numerical simulations of dust structures [69–71]. Remember that expression (56) is correct only when, due to self-consistent nonlinear

behavior of the complex system, the characteristic length turns out to be λ_{in}/τ.

3. FORCES ACTING ON GRAINS IN COMPLEX PLASMAS

The most important forces acting on dust grains are the drag force created by an ion flow, the electric field force, the dust pressure force, the thermophoretic force, the friction force in a neutral nonmoving gas or a neutral drag force in a moving neutral gas, and the dust inertia force. We will describe all these forces and estimate their values under conditions of existing experiments.

3.1. Ion Drag and Electric Field Forces

The drag force was first addressed in [32, 33]. The drag by an ion flow exists for both low and high ion drift velocities (much lower and much higher than the ion thermal velocity). In existing experiments, the ion drift velocity can be on the order or somewhat higher than the ion sound velocity (the Mach number is on the order of unity); it is, however, always still lower than the electron thermal velocity. Physically, dust drag by an ion flow appears due to the loss of the ion momentum in the interaction with dust grains and is a direct consequence of momentum conservation. One can obtain the same estimate as formula (42) for the momentum transfer due to the capturing process in a subthermal ion flow. In this case, the collision frequency should be determined by the ion number density, rather than the dust number density as in formula (42). The same change should be made in estimate (44) for the drag force due to Coulomb scattering. Certainly, the force will be determined by the difference between the ion and dust velocities; however, the dust velocity in the expression for the drag force can usually be neglected because, almost in all cases of interest, it is much smaller than the ion drift velocity. As a result, instead of the parameter P entering into formula (46), we have $Z_d n_i/n_0$. In the general case of an arbitrary ion drift velocity, we find the same coefficient α_{dr} but multiplied by $Z_d n$ instead of P. If we use the same normalization as in expression (48), then for the drag force we obtain

$$\mathbf{F}_{dr} = \frac{\mathbf{F}_{dr,ac}}{F_0} = Z_d z n \alpha_{dr} \mathbf{u}, \tag{59}$$

where $\mathbf{F}_{dr,ac}$ is the actual (nonnormalized) drag force. Note that, as could be expected, the drag force is proportional to the square of the dust charge [one factor, Z_d, enters into normalized dust charge z, and the other factor Z_d enters directly into expression (59)].

The presence of the large factor Z_d is also a consequence of the momentum conservation law. Indeed, expression (59) is written for a single dust grain. To find the momentum transferred per unit volume, we should multiply expression (59) by n_d; as a result, the additional factor Pn_0 appears. On the other hand, to find the momentum lost by ions per unit volume, we should multiply expression (48) by $n_i = n_0$. If we sum these expressions for the change of the momentum per unit volume, we will obtain exactly zero.

The presence of the large factor Z_d in front of the expression for the drag force is very important because all other dimensionless parameters are usually on the order of unity and the presence of the large factor Z_d in expression (59) shows that the drag force is usually large. However, due to the large value of Z_d, the electric field force $\mathbf{F}_{el}$ acting on dust grains is also large. Normalizing the electric field in the same manner as when deriving expression (53) for the force acting on ions, we obtain

$$\mathbf{F}_{el} = -eZ_d\mathbf{E}. \tag{60}$$

For the sum of the electric field force and the drag force, we have

$$\mathbf{F}_{el} + \mathbf{F}_{dr} = -Z_d(e\mathbf{E} - nz\alpha_{dr}\mathbf{u}), \tag{61}$$

i.e., the factor Z_d appears as a common factor in the expression for the total force. Thus, if we find the force balance of these two forces by equating the left-hand side of Eq. (61) to zero, then the balance condition will not be determined by the common factor Z_d [34–36]. This, however, does not mean that the presence of Z_d in the expressions for the electric field force and the drag force has no physical consequences. In fact, it has a very important consequences if other forces are added in the total force and if these forces do not contain the large factor Z_d. In this case, these other forces can be neglected. For instance, the normalized dust pressure force $\mathbf{F}_{pr,ac} = -(T_d/n_d)(\partial n_d/\partial \mathbf{r}_{ac})$ is equal to

$$\mathbf{F}_{pr} = \frac{\mathbf{F}_{pr,ac}}{F_0} = -\frac{T_d}{T_e}\frac{z}{P}\frac{\partial}{\partial \mathbf{r}}\left(\frac{P}{z}\right) = -Z_d\tau_d\frac{z}{P}\frac{\partial}{\partial \mathbf{r}}\left(\frac{P}{z}\right), \tag{62}$$

where τ_d is the effective dimensionless dust temperature,

$$\tau_d = \frac{T_d}{T_e Z_d}, \tag{63}$$

which, for any real experiment, is very small ($\tau_d \ll 1$) due to the presence of the factor Z_d in the denominator. Then, the total force $\mathbf{F}_{tot}$, including the electric force, the drag force, and the pressure force, can be written as

$$\mathbf{F}_{tot} = -\frac{Z_d}{P}\left(\tau_d z\frac{\partial}{\partial \mathbf{r}}\left(\frac{P}{z}\right) + P(e\mathbf{E} - \alpha_{dr}nz\mathbf{u})\right). \tag{64}$$

If we neglect the term with a very small parameter τ_d in the force balance equation, we get

$$P(e\mathbf{E} - \alpha_{dr}nz\mathbf{u}) = 0. \tag{65}$$

This equation has two solutions. One of them corresponds to the balance between the electric field force

and the drag force, and the other one is $P = 0$. In a spatial region where the electric field force is balanced by the drag force, P is usually nonzero. This means that there should be a boundary with a jump in the parameter P. Since z is continuous, the dust density should have a jump at this boundary. The term with the dust gas pressure allows one to describe the fine structure of this jump as a continuous but steep change in the dust density, probably with small oscillations on spatial scales that are τ_d^{-1} times smaller than the other characteristic spatial scales of the problem.

Thus, we can conclude that, due to the presence of the large factor Z_d in both the electric field force and the drag force (which allows one to neglect the dust pressure force, proportional to the small parameter τ_d), a new type of boundary can be created with all the parameters being continuous, except for the dust density. Note that this is not only a theoretical possibility. In the experiments of [37, 38], dust distributions with sharp boundaries were observed (see also theoretical papers [39, 40]). In [37], the boundary observed was very sharp and, outside the dust cloud, the dust was practically absent. In [38], several interesting structures with sharp dust boundaries separating regions with dust grains of different size (grains with the sizes a and $2a$ were injected simultaneously) were observed. This phenomenon requires future detailed investigations. Also, the convection of dust was observed in [38].

The above relationships were obtained under the assumption that ion–dust collisions are the most important. Formally, these expressions survive in the case where ion–neutral collision are dominant. In this case, it is only necessary to change the normalization according to the expressions given in the previous section.

3.2. Temperature Gradients and the Themophoretic Force

The thermophoretic force is proportional to the temperature gradient of a neutral gas and becomes important when ion–neutral collisions dominate over ion–dust collisions. This well-known phenomenon was considered for dust grains in [41, 42]. The ratio of the corresponding friction forces depends on the gas pressure. In experiments, this ratio is often on the order of unity.

The thermophoretic force $\mathbf{F}_{\text{tp, ac}}$ is determined by the neutral gas density n_n and by the gradient of the neutral gas temperature T_n [41],

$$\mathbf{F}_{\text{tp, ac}} = 2.4 n_n \pi a^2 \lambda_{nn} \frac{\partial T_n}{\partial \mathbf{r}_{\text{ac}}}. \quad (66)$$

The main problem is the question of what processes in a neutral gas determine the temperature gradient. It can be some external heat sources or the difference in the electrode temperatures in a particular experimental device. A question we need to answer is what kind of temperature gradients in a neutral gas can be created by the presence of dust. We exclude from consideration externally created temperature gradients, because in this case, the thermophoretic force is completely determined by Eq. (66). In the general case, the temperature gradient is determined by heat conduction, which, under conditions where ion–neutral collisions are dominant, is described by a diffusion equation with heat sources. We consider only sources related to the presence of dust and steady-state heat transfer.

Let us first consider the heat balance at the surface of a dust grain. The flux of electrons and ions related to the charging process continuously supply the surface with the energy that is the energy of the captured ions and electrons. This energy flux onto the grain surface can easily be calculated using the OML cross sections. Each ion is accelerated by the dust field almost to the energy corresponding to the electron temperature. Therefore, the electron and ion contributions to the heat flux onto the dust surface are almost equal to each other (the direct calculations show that these fluxes differ by only a factor of $z/2$). The energy deposited on the dust surface cannot stay there because, for a low degree of ionization, the neutral density is much higher than the ion density (in typical experiments, $n_n/n_i \approx 10^6$) and the rate of dust collisions with neutral gas atoms is $(n_n/n_i)(\tau/z) \approx 10^4$ times larger than the rate of collisions with ions (the ion and neutral thermal energies in this estimate are assumed to be approximately the same). In this estimate, the factor τ/z is the ratio of the cross section for neutral–dust collision (which is the geometrical cross section πa^2) to the cross section for ion–dust collisions $(z/\tau)\pi a^2$. In neutral dust collisions, the neutral atoms are attached to the dust surface for a rather short time (called the resident time), which is sufficient to equalize the thermal energy of the attached neutral atoms to the dust surface temperature. Then, the neutral atoms take the excess of energy that was deposited by ions and reemitted from the dust grain. As a result, the surface dust temperature becomes almost equal to the neutral gas temperature. Heat transfer from the dust surface to the neutral atoms is very fast, and the surface temperature of the dust grain is larger than the temperature of the neutral gas (this determines the direction of heat transfer); however, this difference is very small. In the above numerical example, the relative difference between the dust surface temperature and the neutral gas temperature is as low as [36]

$$\frac{T_s - T_n}{T_n} \approx \frac{n_i}{n_n}\frac{z}{\tau} \approx 10^{-4}. \quad (67)$$

Thus, the energy deposited on the dust grain in the charging process is a source of the local heating of neutral atoms (the heat source q_d), which produces the temperature gradient and thus creates a self-consistent thermophoretic force that is not related to external heating. Of course, the external source creates the ion flow which also deposits energy in the neutral gas (the heat

source q_i) via ion–neutral collisions and ion–neutral friction.

The best way to write the heat conduction equation with these heat sources on the right-hand side is to normalize the distance to $\lambda_{nn}/\tau \approx \lambda_{in}\tau$ and the thermophoretic force to T_n/λ_{nn} (note that, above, the force was normalized to T_i/λ_{in}):

$$Z_d\mathbf{F}_{\rm tp} = \frac{\mathbf{F}_{\rm tp,\,ac}\lambda_{nn}}{T_n}, \quad (68)$$

where $\mathbf{F}_{\rm tp}$ is the thermophoretic force divided by Z_d in order to extract the factor Z_d, which is common for all forces acting on a dust grain (this simplifies the comparison of different forces). Then, according to expression (66) for the thermophoretic force, which contains the first derivative with the respect to the neutral temperature, we obtain the heat conduction equation for a neutral gas in a form containing only the first derivative of the thermophoretic force with respect to the dimensionless distance. For simplicity, we will write this equation in the one-dimensional form, assuming that the temperature depends only on the x coordinate [36]:

$$\alpha_{\rm tp}\frac{z\partial F_{\rm tp}}{\partial x} = \tau(q_d + q_i), \quad (69)$$

where $\alpha_{\rm tp}$ is a numerical coefficient on the order of unity (when ion–neutral collisions are dominant, it is 0.8). The OML approach gives

$$q_d = \frac{1}{2\sqrt{\pi}}Pn(z+2)\alpha_{\rm ch}, \quad (70)$$

and simple calculations with the friction force determined by ion–neutral collisions give for $u \ll 1$ (in this case, the friction force is proportional to u and the ion mobility is proportional to the electric field)

$$q_i = \frac{nu^2}{4\sqrt{2\pi}}. \quad (71)$$

For $u \gg 1$ (when the ion–neutral friction force is proportional to the square of the drift velocity and, correspondingly, the ion mobility is proportional to the square of the electric field), we obtain an estimate for q_i, which differs from expression (71) by the additional factor u.

The appearance of the small factor τ in Eq. (69) for the thermophoretic force is very important. When all the dimensionless parameters are on the order of unity, the presence of the factor τ on the right-hand side of Eq. (69) shows that, in most cases of interest, the self-consistent thermophoretic force is fairly small and can be neglected. The only exception is the case of high ion drift velocities, where the heat source (71) can be large. This can occur only if the ion drift velocity substantially exceeds the ion thermal velocity, namely, if τu^3 is on the order of unity or if $M > \tau^{1/6}$, which means $M > 0.5$ for existing experiments, where $\tau \approx 0.02$. Thus, the thermophoretic force can be important in sheaths, where M is on the order of unity. However, this also requires high pressures in order that the characteristic length of the problem be determined by ion–neutral (or neutral–neutral) collisions, when the above expression for the thermophoretic force is valid. In existing experiments, where ion–neutral collisions are dominant, u is on the order of unity and $M \ll \tau^{1/6}$. Under these conditions, the thermophoretic force is small. The possible presence of sharp dust boundaries does not change this conclusion because Eq. (70) contains the parameter P, but not its derivatives with respect to the distance.

If the characteristic length is not determined by the nonlinear balance and is not directly related to the collisional mean free path of neutral gas atoms, then the thermophoretic force can be rather important. In particular, it is important in the interaction of two dust grains when the distance between them is larger than the collisional mean free path (below, we will consider this problem in more detail). The thermophoretic force can be used to remove dust from a system by an externally applied temperature gradient [43].

3.3. Neutral Gas Drag Force, Gravity Force, and Dust Inertia

The neutral drag (or neutral friction force) appears when a dust grain moves with a certain drift velocity $\mathbf{v}_d$ through a neutral gas. When the neutral gas is moving, this force can cause dust to move. Dust motion can also appear when the gas is not moving and when the balance of the other forces acting on dust grains require that the neutral gas drag to be included. For example, when the ion drag force and the electric field force are not acting in the same direction, they can be compensated in one direction but cannot be compensated in the other direction without taking into account the neutral drag force. Then, the electric and ion drag forces create dust motion in the direction where the force balance cannot be established without the neutral drag force. This leads to the dust convection observed in many experiments. The role of the neutral drag force in creating dust convection was first considered in [38, 44]. In the presence of gravity, the neutral drag force can balance the gravity force and can lead to a constant-velocity fall of dust grains injected in the gas discharge. The physical reason for the appearance of the neutral drag force, which is also known as the Epstein drag force [45], is that the impact rate of neutral atoms on the front side of a dust grain is larger than that on the rear side. The difference in these impact rates, multiplied by the average momentum transferred by impacts of gas atom, is equal to the momentum transferred to the grain per unit time, which is the neutral drag force:

$$\mathbf{F}_{\rm nd,\,ac} = -\frac{4}{3}n_nT_n\pi a^2\frac{\mathbf{v}_{d,\,\rm ac}}{v_{Tn}} = -m_d\nu_{\rm nd,\,Ep}\mathbf{v}_{d,\,\rm ac}, \quad (72)$$

where, as before, the index "ac" stands for the actual value and $\nu_{\rm nd,\,Ep}$ is the Epstein collision frequency of

momentum exchange between the dust and the neutral gas atoms.

We will also introduce the normalized drag force. The neutral drag force is important both when ion–dust collisions are dominant (in this case, normalization is related to ion–dust collisions) and when ion–neutral collisions are dominant (in this case, normalization is related to ion–neutral collisions). In the first case, when ion–dust collisions are dominant, we have

$$\mathbf{F}_{\rm nd} = \frac{\mathbf{F}_{\rm nd,\,ac}\lambda_{Di}^2}{T_e a} = Z_d\frac{\mathbf{v}_d^i}{z}, \tag{73}$$

where we intentionally extracted the factor Z_d, which is the common factor for all forces acting on dust grains, and $\mathbf{v}_d^i$ is the normalized dust velocity,

$$\mathbf{v}_d^i = \frac{\mathbf{v}_{\rm nd,\,ac}}{v_{d,*}}, \tag{74}$$

with

$$v_{d,*} = v_{Tn}\frac{3T_i}{T_n\tau^2}\frac{n_i}{n_n}. \tag{75}$$

This expression can be used to estimate the characteristic dust velocities that can appear due to the disbalance of other forces acting on dust grains. For $T_n = T_i$, $\tau = T_i/T_e \approx 0.02$, and $n_n/n_i \approx 10^6$, we find $v_{d,*} = 7.5\times 10^{-3} v_{Tn} \approx 120$ cm/s for krypton. Note that this characteristic velocity does not depend on the dust size.

When ion–neutral collisions are dominant, we have another normalization:

$$\mathbf{F}_{\rm nd} = \frac{\mathbf{F}_{\rm nd,\,ac}\lambda_{in}^2}{T_i} = Z_d\frac{\mathbf{v}_d^n}{z}, \tag{76}$$

where

$$\mathbf{v}_d^n = \frac{\mathbf{v}_{\rm nd,\,ac}}{v_{d,**}}, \tag{77}$$

$$v_{d,**} = v_{Tn}\frac{3Z_d T_i}{T_n}\frac{\sigma_{in}}{4\pi a^2}. \tag{78}$$

This velocity depends strongly on the dust size a ($v_{d,**} \propto 1/a$, because $Z_d \propto a$). For $Z_d \approx 10^4$, $T_n \approx T_i$, $\sigma_{in} \approx 5\times 10^{-15}$ cm^{-3}, and $a \approx 3$ μm, we find $v_{d,**} \approx 1.3\times 10^{-4} v_{Tn} = 2$ cm/s in krypton.

When the neutral drag force is taken into account in the force balance equation, we have

$$-e\mathbf{E} + \alpha_{\rm dr} z n\mathbf{u} - \frac{\mathbf{v}_d}{z} = 0. \tag{79}$$

This equation has the same form both when ion–dust collisions are dominant and when ion–neutral collisions are dominant. The only difference is in the normalization of n, $\mathbf{E}$, and $\mathbf{v}_d$. In Eq. (79), dust inertia is neglected, which is possible under steady-state conditions when the drag friction force exceeds the inertia force $m_d(\partial v_{d,\,\rm ac}^2)/2\partial x_{\rm ac}$ or when ion–dust collisions are dominant and the condition

$$m_d v_{d,i} \ll m_{d,*} \tag{80}$$

is satisfied, where

$$m_{d,*} = m_n\frac{Z_d T_n}{9zT_i}\tau^3\frac{n_n^2}{n_i^2}. \tag{81}$$

For $v_{d,i} \longrightarrow 0$, according to condition (80), dust inertia can be neglected; however, for $v_{d,i} \approx 1$, dust inertia can be neglected only for sufficiently light dust grains, $m_d \ll m_{d,*}$. For $n_n/n_i \approx 10^6$, $Z_d \approx 10^4$, $\tau \approx 0.02$, $T_n \approx T_i$, and $z \approx 3$, we find $m_{d,*}/m_n \approx 3\times 10^9$. This large value appears because all other forces, except for the inertia force, are proportional to Z_d and, therefore, Z_d appears in the expression for the critical mass. When ion–neutral collisions are dominant, we obtain a condition for neglecting dust inertia similar to condition (80) with a substitution of $v_{d,n}$ for $v_{d,i}$ and $m_{d,**}$ for $m_{d,*}$. For $v_{d,n}$ on the order of unity, we find

$$m_d \ll m_n\frac{T_n}{9Z_d T_i}\left(\frac{4\pi a^2}{\sigma_{in}}\right)^2, \tag{82}$$

which, in contrast to the previous relation, contains Z_d in the denominator. For $T_n \approx T_i$, $\sigma_{in} \approx 5\times 10^{-15}$, and $a \approx 3$ μm, we find $m_d/m_n \ll 10^{18}$. This relation is usually fulfilled in existing experiments. Note that condition (82) is independent of the dust size if $m_d \propto a^3$ and $Z_d \propto a$, which is valid when dust grains are not hollow.

If there is a potential well for dust grains, then a grain can reach the bottom of the well with a zero velocity; in this case, the neutral drag force vanishes.

In the presence of gravity, the balance equation should include the gravity force $F_{g,\,\rm ac} = gm_d$, where g is the free-fall acceleration. The neutral drag force, being balanced by the gravity force $F_g = gm_d \propto a^3$, leads to a constant dust drift velocity proportional to a.

4. NONCOLLECTIVE DUST–DUST INTERACTIONS

4.1. Electrostatic Energy of Two Charged Grains

Let us consider two charged grains of equal size embedded in a plasma with a fixed electron temperature T_e. Then, the grain charge will be a function of the distance $r_{1,2}$ between the grains. We will consider distances at which the field of each grain is a nonlinearity screened field (including the nonscreened long-range field) and the total potential is described by $Z_d eV(r_{1,2})/r_{1,2}$, where $r_{1,2} = |\mathbf{r}_1 - \mathbf{r}_2|$ is the relative distance between the two dust grains and $V(a) = 1$. Quali-

tatively, the dependence of the dust charge on the distance between the two grains follows from the condition that the total potential on each grain be approximately equal to the electron temperature, $(Z_d e^2/a) + (Z_d e^2 V(r_{1,2})/r_{1,2}) \approx T_e$ or [46]

$$Z_d = \frac{Z_{d,\infty}}{\left(1 + \frac{aV(r_{1,2})}{r_{1,2}}\right)}, \quad (83)$$

where $Z_{d,\infty}$ is the dust charge when the distance between the grains is infinite. Thus, the charge on each dust grain decreases as the intergrain distance decreases. In this case, the Coulomb interaction energy increases; however, the total electrostatic energy decreases because the Coulomb energy is added by the intrinsic energy of two dust grains, $2 \times Z_d^2/2a \approx (Z_{d,\infty}^2/2a)(1 - 2aV/r)$. The total change in the electrostatic energy when the grains are displaced from ∞ to $r_{1,2}$ will not be $Z_d^2 V/r_{1,2}$, as for the case where the dust charges does not change with distance, but it will be $-Z_d^2 V/r_{1,2}$, as if the dust grains were attracting, rather than repelling each other, as could be expected in the case of two charges with the same sign [46].

This contradiction is well known in electrostatics. The electrostatic energy of two charged conducting spheres changes its sign if the potential of the spheres is kept constant. The potential can be kept constant by external sources that under equilibrium conditions produce a work on the charges; as a result, the total force should be calculated as the derivative of the total electrostatic energy with an opposite sign [47, 49], which leads to the repulsion of charges with the same sign.

There exists a large doubt as to whether this statement, proven only for systems that are in thermal equilibrium, can be applied to a complex dusty plasma as an open system [48]. We will demonstrate by explicit calculations that it is not applicable. The openness of the system assumes the presence of not only two dust grains, but of many dust grains, which results in collective effects. These dust grains create a constant sink of energy (a homogeneous one if they are distributed randomly) and lead to a decrease in the electron energy (or the electron temperature when the distributions are approximated by thermal distributions), which should be compensated by external sources. Thus, attraction in an open system could be of collective nature: many dust grains are needed as a sink of energy to produce attraction between two probe grains (see below). The only conclusion that could be made from the present consideration is that the electrostatic energy of two dust grains decreases when they come closer to each other; as a result, electrostatic energy is gained. How this will be compensated by the work of an external source is a separate problem. However, the concept of minimum energy does not work in open systems and we cannot conclude from the decrease in the electrostatic energy that two dust grains attract each other. The presence of a reservoir of energy creates the possibility of the attraction of grains with equal-sign charges with the same sign. The realization of this possibility depends on the type of external sources that make the system open. Therefore, it is necessary to know the specific properties of the sources to explicitly find the actual forces between the grains. As we will see, these forces can be attractive starting from a certain distance depending on the type of the external source. Expression (83) [46] for the decrease in the dust charges when the grains come closer to each other was confirmed by numerical simulations [50]. For a distance source, the time during which information on the produced work reaches the source is determined by the speed of sound. In this case, the grains will be able to attract each other or even agglomerate before this information will reach the source. Thus, for open complex dusty systems, the condition of thermodynamic equilibrium cannot be used and the result of interaction depends on the external source structure. However, we will show that, even for a homogeneous external source, there exists an attraction force related to plasma production by ionization.

4.2. Dust Attraction and Nonlinear Screening

Screening is often nonlinear. Due to nonlinearity, the screenings of two dust grains cannot be superposed on each other. The simplest way to treat this nonlinearity is to consider large distances between the dust grains where the screening of each of them is approximately linear and the nonlinearity can be considered weak. Nevertheless, it can be important when the field of each grain is screened exponentially as it should be in the case of weak nonlinearity. We will show that two dust grains with charges of the same sign can create a nonscreened potential in the direction perpendicular to the line connecting their centers, i.e., to $\mathbf{r}_{1,2}$. This potential can act as a potential well for the third negatively charged dust grain. This means that, in this perpendicular direction, the nonlinearity of the fields of two dust grains can create a bunch of positive polarization charges that can serve as a well for another dust grain. This property is completely determined by nonlinearity and is absent in the linear approach. We start with the equation neglecting electron screening and electron nonlinearities:

$$\Delta\phi = -4\pi e n_i \left(e^{-\frac{e\phi}{T_i}} - 1\right) + 4\pi Z_{d,1}\delta(\mathbf{r} - \mathbf{r}_1) + 4\pi Z_{d,2}\delta(\mathbf{r} - \mathbf{r}_2). \quad (84)$$

The last two terms describe the charge densities of two point charges at positions $\mathbf{r}_1$ and $\mathbf{r}_2$. The linear potential of each of them is given by

$$\phi_{1,2} = \frac{1}{2\pi^2\lambda_{Di}} eZ_{d,1,2}\int \exp\left(i\mathbf{k}\cdot\left(\frac{\mathbf{r}-\mathbf{r}_{1,2}}{\lambda_{Di}}\right)\right)\frac{d\mathbf{k}}{k^2+1}, \quad (85)$$

which leads to the screened Coulomb interaction

$$V_{1,2} = \frac{Z_{d,1}Z_{d,2}}{r_{1,2}}\exp\left(-\frac{r_{1,2}}{\lambda_{Di}}\right). \quad (86)$$

The nonlinearity on the right-hand side of Eq. (84) can be found by expanding the exponent and taking into account the term with the product of potentials (85) of each dust grain, $\propto\phi_1\phi_2$ (the terms $\propto\phi_1^2$ or $\propto\phi_2^2$, which describe small corrections to screening, were discussed in [1] when considering the nonlinear screening of a single dust grain). We consider the line connecting two dust grains, $\mathbf{r}_{1,2}$; the distance r is counted from the center of this line or from any other point on this line. The latter makes no difference because we assume that $r \gg r_{1,2} = |\mathbf{r}_1 - \mathbf{r}_2|$. Then, simple calculations lead to an additional potential ϕ_{nonl}, created by two dust grains, and to an additional energy for the third dust grain; in contrast to expression (86), this energy appears to be negative:

$$V_3 = eZ_{d,3}\phi_{\text{nonl}} = -\frac{e^4 Z_1 Z_2}{2\pi T_i r\lambda_{Di}}\exp\left(-\frac{r_{1,2}}{\lambda_{Di}}\right). \quad (87)$$

This energy does not contain the exponential term $\exp(-r/\lambda_{Di})$; therefore, the interaction is nonscreened. Of course, the use of the linear approximation as a first approximation assumes that the distances are large as compared to λ_{Di}. Thus, the exponent with $r_{1,2}$ in expression (87) is acting; the only restriction is that the linear approximation for the potential be applicable and the nonlinearity be weak. We also assume $r \gg r_{1,2}$ and, therefore, $r \gg \lambda_{Di}$. We can therefore expect that this attraction, which increases with decreasing r, will have a maximum at $r \approx r_{1,2}$. We can estimate that, at these distances, the ratio of the attraction energy V_3 to $V_{1,3}$ (or $V_{2,3}$) will be on the order of

$$\frac{V_3}{V_{1,3}} = \frac{z_3}{2\pi}\frac{a}{\lambda_{Di}}, \quad (88)$$

where $z_3 = Z_{d,3}e^2/aT_e$. Obviously, this ratio can be larger than unity. This result seems to be important for the attraction of grains in the plane perpendicular to the line between two other grains. Therefore, nonlinear screening can be accompanied by the appearance of an "overshooting" of the screening charge and, accordingly, the creation of regions with a positive space charge. A similar effect can occur in the presence of an ion flow when the ions can be concentrated behind the grain forming the potential well for other grains, as was discussed in [1]. This effect can also appear due to the work done by an external source, as will be discussed below.

4.3. Shadow Noncollective Attraction Force Created by Ion Flux

We consider here the so-called noncollective shadow effect [50–54], which occurs in the interaction of two isolated dust grains in the absence of other grains ($P = 0$). We assume that the distance between two dust grains is larger than the ion Debye length (further, this distance is set to be on the order of λ_{Di}^2/a) and is much less than the ion–neutral mean free path λ_{in}.

The physics of shadow attraction is very simple: the plasma flux onto one of the grains is shadowed by another grain, and, therefore, the ram pressure from the outer sides of dust grains is larger than from the inner side. The force arising due to the shadowing of the ion flux can be easily estimated when the distance between the grains is large compared to the grain size, which corresponds to the case where the shadow solid angle is small, $a^2/r_{1,2}^2 \ll \tau/z$. In this case, the shadowing force $\mathbf{F}_{\text{sh},i}$ is determined by the product of the shadow solid angle [see (1.41)] and the transfer of the ion momentum $m_i v_{Ti} I_i$ through the midplane between two dust grains (here, according to [54], we take into account momentum conservation in the grain interaction); i.e., it is approximately equal to $n_i T_i\sqrt{1+\tau/z}$). The force is directed along the line connecting the two dust grains; i.e., it is aligned with $\mathbf{r}_{1,2}/r_{1,2}$:

$$\mathbf{F}_{\text{sh,i}} \approx a^2\frac{\mathbf{r}_{1,2}}{r_{1,2}^3}n_i T_i \pi a^2\left(\frac{z}{\tau}\right)^2. \quad (89)$$

The last expression corresponds to the case where $z/\tau \gg 1$. This calculation oversimplifies the problem, because it takes into account only the flux of the captured ions, whereas the flux related to ion scattering by a dust grain is ignored. In the absence of the second dust grain, the latter flux is scattered isotropically from all sides of the grain and the net momentum transferred to the grain is zero. In the presence of another grain, this symmetry is violated. Thus, the shadow effect has two parts: one is related to the capture flux and another is related to the scattering by the grain field (which can also include the effect of nonlinear screening and long-range nonscreened field). We will discuss these processes quantitatively. Nevertheless, the we will refer to the simplest expression (89) as a standard one and will find additional coefficients that mathematically describe the mentioned effects. Expression (89) has some general features:

(i) The force is attractive and has the same dependence on the intergrain distance as the nonscreened Coulomb force ($\propto 1/r_{1,2}^2$).

(ii) In contrast to the Coulomb force, this force is not screened and should be dominant at distances larger than the Coulomb field screening length.

(iii) The shadow force is smaller than the Coulomb force at distances where the Coulomb field is not screened ($r_{1,2} \ll \lambda_{scr}$). Indeed, by substituting one of the factors a^2 by $Z_d^2 e^4 / z^2 T_e^2$, we have

$$F_{sh,i} \approx -\frac{Z_d^2 e^2}{r_{1,2}^2} \frac{a^2}{\lambda_{Di}^2}. \quad (90)$$

The first factor in this expression coincides with the nonscreened Coulomb field (with the opposite sign); the estimate of the second factor should be improved by taking into account the shadow effect related to scattering. The most important factor is the last one $a^2/\lambda_{Di}^2 \ll 1$, which shows that the absolute value of the attraction force is indeed much less than the absolute value of the nonscreened Coulomb force. Thus, it can be dominant only at distances larger than the screening distance, where the Coulomb force is screened, whereas the shadow force is not screened.

(iv) The shadow attraction is proportional to a^4 and increases rather sharply with increasing dust size. In many existing experiments on etching, the grain size is continuously growing; under these conditions, the role of shadow forces increases with time.

(v) The shadow force appears only for finite-size grains and is zero for point charges. For strong coupling in complex plasmas, the grain size is not small and is even a fraction of the screening length; hence, the shadow effect is very important.

These general features are common to all attraction forces, except for the fact that under certain conditions the attraction force caused by neutral particle shadowing can exceed the Coulomb force (see below). This is related to the inequality $n_n/n_i \gg 1$. Using the above estimate, we will write the general expression for the shadow force in the form [50]

$$\mathbf{F}_{sh} = -\frac{\partial U_{sh}(r_{1,2})}{\partial \mathbf{r}_{1,2}}, \quad U_{sh}(r_{1,2}) = -\eta_{sh} \frac{Z_d^2 e^2}{r} \frac{a^2}{\lambda_{Di}^2}, \quad (91)$$

where the shadow coefficient η_{sh} is the sum of the shadow coefficients $\eta_{sh,ic}$, $\eta_{sh,is}$, and $\eta_{sh,n}$, related to ion capture, ion scattering, and neutral flux shadowing (see the next section), respectively:

$$\eta_{sh} = \eta_{sh,ic} + \eta_{sh,is} + \eta_{sh,n}. \quad (92)$$

First, we quantitatively consider the shadow effect related to ion capture. We take into account exact expressions (1.40) and (1.41) for the shadow angle. To find the shadow force related to ion capture, we invert the problem and calculate the capture force for the case where the ions are present only in the shadow angle cone, because, by virtue of zero momentum transfer in the absence of a shadow, the effect calculated in this way is just opposite in sign and equal in magnitude to the effect we are interested here. We will integrate the expression for the momentum transferred by a single ion over angles and velocities, assuming that the ion distribution far from the grain is thermal. Taking into account that the shadow flux far from the grain is almost uniform and the cross section is πa^2, we obtain

$$\eta_{sh,ic} = \frac{1}{4\sqrt{\pi}} \frac{\tau^2}{z^2} \int_{y_{min}}^{\infty} \left(y + \frac{z}{\tau}\right)^2 \exp(-y) dy, \quad (93)$$

$$y_{min} = \frac{a^2}{r_{1,2}^2} \frac{z}{\tau}.$$

For $z/\tau \gg 1$ and $r_{1,2} \gg a\sqrt{z/\tau}$, we have

$$\eta_{sh,ic} \approx \frac{1}{4\sqrt{\pi}} \approx 0.14. \quad (94)$$

Let us estimate the shadow effect related to ion scattering. Note that the advantage of the OML approach used to evaluate the shadow capturing force is that it uses simple conservation laws that do not require the knowledge of the potential distribution close to the grain (the only requirement is that the potential far from the grain should be much less than at the grain surface). For shadowing related to scattering, we need to know the potential profile. The potential is strongly nonlinear for $z/\tau \gg 1$, and the Coulomb potential can be used approximately only for z/τ on the order of unity. In the latter case, calculations with a Coulomb potential [51] showed that $\eta_{sh,is}$ is approximately on the order of $\ln(\lambda_{Di}/a)$. For existing experiments, the case where $z/\tau \gg 1$ is more appropriate. In this case, due to strong screening we can expect that $\eta_{sh,is}$ will be less than that obtained for the case of a pure Coulomb field. The exact results for $z/\tau \gg 1$ can be obtained only numerically with the use of an explicit expression for the nonlinear screened potential; in the general case, the problem has not yet been analyzed.

The shadow attraction potential is a long-range potential operating at distances larger than the screening distance, where the nonscreened long-range repulsion potential also operates (this potential was calculated and discussed in detail in [1]). We remind that the potential energy related to the latter is approximately $(Z_d^2 e^2/r_{1,2})(a^2/2r_{1,2})$, while the potential energy related to shadow attraction is on the order of $-\eta_{sh}(Z_d^2 e^2/r_{1,2})(a^2/\lambda_{Di}^2)$. It follows from here that in the long-range domain (at distances larger than the screening distance), the attraction due to the shadow effect becomes comparable with the repulsion at

$$r_{1,2} \approx \frac{1}{\eta_{sh}} \frac{\lambda_{Di}^2}{a}, \quad (95)$$

which is on the order of the charging length λ_{Di}^2/a. From the physical standpoint, the ion capturing attraction is directly related to the charging process; in this context, the last important result seems to be natural. The attraction due to neutral flux shadowing can be larger, and the distances where it can dominate can be shorter. Under conditions where the attraction due to neutral atoms can be neglected, the whole potential curve corresponding to the interaction of two dust grains becomes similar to the usual molecular potential curve: at short distances, the Coulomb repulsion dominates, and at distances larger than the screening distance, there is a potential well with the minimum value

$$V_{\text{at}} = -(\eta_{\text{sh}})^2 Z_d^2 e^2 \frac{a^3}{2\lambda_{Di}^4}. \quad (96)$$

For typical experimental conditions ($Z_d \approx 10^4$, $T_i \approx 0.02$ eV, and $a \approx 10$ μm), we find $V_{\text{at}} \approx 310\eta_{\text{sh}}^2$ eV, which corresponds to the characteristic binding energy. Thus, two dust grains with equal sizes can form a dust molecule, and several dust grains can form dust clusters. Two-dimensional dust clusters (clusters on a plane) were investigated in a number of experiments [55–57] by using a small external confining potential. Although the role of shadow attraction in the formation of these clusters has not yet been investigated, it is obvious that the attraction plays an important role if the confining potential is lower than estimate (96). The shadow-force theory predicts that clusters can exist without any external confining potential, which can be verified experimentally. Experiments can also be performed in the presence of an external transverse confining potential to measure the value of η_{sh} and to check the shadow force physics (existing and planned experiments of this type will be discussed below). The general theory of modes, oscillation frequencies, and stability of two-dimensional clusters recently developed in [58] can be used for the experimental detection of attraction forces.

4.4. Shadow Attraction Force Created by Neutral Flux

In low-temperature plasmas, the flux of neutral atoms on the dust grain surface substantially exceeds the ion flux. This flux is not related to the charging and, for the most part, is usually returned back. The neutral atoms are absorbed by the dust surface, are kept at it for a rather short resident time, and then are reinjected into plasma. Nevertheless, the resident time is sufficient to exchange energy and almost equalize it to the surface temperature. Thus, in the presence of a small difference between the temperatures of the neutral gas and the dust surface, there can exist a net transfer of energy and momentum, which can result in a shadow force. One can rigorously prove that, if the collisions of neutral atoms with the dust surface are completely elastic, then the net force due to the neutral atom flux is exactly zero. If all of the neutral atoms are absorbed by the surface, then this force can easily be calculated when the distance between the grains is less than the mean free path in the neutral gas λ_g, which is on the order of λ_{in} [52, 53]. In this case, one need to calculate the momentum transferred to the dust surface, assuming that neutral atoms reaching the grain move along straight trajectories. Then, the attraction force is [52, 53]

$$\mathbf{F}_{\text{sh, dn}} = -\frac{\mathbf{r}_{1,2}}{r_{1,2}^3}\frac{3}{4}\pi a^4 n_n T_n. \quad (97)$$

This expression corresponds to the previous qualitative estimate; however, since $n_n/n_i \approx 10^6$ in the existing experiments, force (97) is many orders of magnitude larger than that related to the ion flux. We emphasize that the attachment coefficient κ_{at} in expression (97) is taken to be equal to unity, while the detachment coefficient κ_{det} is taken to be zero, which is incorrect. Actually, the difference between them is very small ($\delta\kappa = \kappa_{\text{at}} - \kappa_{\text{det}} \ll \kappa_{\text{at}}$), and the temperature of the dust surface T_s is not equal to the neutral gas temperature T_n. Taking into account these differences, we find instead of expression (97)

$$\mathbf{F}_{\text{sh, dn}} = -\frac{\mathbf{r}_{1,2}}{r_{1,2}^3}\frac{3}{4}\pi a^4 n_n T_n\left(\kappa_{\text{at}} - \kappa_{\text{det}}\sqrt{\frac{T_s}{T_n}}\right). \quad (98)$$

As was already noted, the dust surface temperature is usually higher than the neutral temperature and when the they differ substantially force (98) describes the repulsion. However, under certain conditions, the dust can be cooled quickly (this happens under astrophysical conditions where the radiative cooling is very efficient). Under laboratory conditions, both the temperature difference and the difference between the attachment and detachment coefficients is very small. Thus, the sign of the force is determined by the interplay of two small parameters, $\delta\kappa/\kappa$ and $\delta T/T$. The latter, as was discussed above, is on the order of 10^{-3}. The relative difference between the attachment and detachment coefficients [59, 60] can be larger than this value, especially for rough dust surfaces (e.g., for fractal dust). In this case, an attraction appears that depends on the structure of the dust surface and other delicate problems of surface physics; however, the attraction force will be two to three orders of magnitude weaker than that described by estimate (97). Since estimate (97) is larger than the ion capturing shadow force by the large factor n_n/n_i, the neutral shadow force can exceed the ion shadow force by several orders of magnitude. Neglecting the temperature difference, we obtain the estimate [53]

$$\eta_{\text{sh, nd}} \approx \frac{3}{16}\frac{\tau^2}{z^2}\frac{n_n}{n_i}\delta\kappa. \quad (99)$$

When the temperature of the dust surface is substantially lower than the neutral gas temperature and, accordingly, $\delta T/T$ is on the order of unity, the attraction force is much larger because, in this case, the small factor $\delta\kappa/\kappa$ is absent.

When the distance between the grains is larger than the mean free path of atoms in the gas, the physics of interaction changes and the main role is played by the thermal flux q equal to the difference between the thermal fluxes onto and from the dust surface. The thermal flux created by one dust grain at the position of another dust grain is

$$\mathbf{q} = -\frac{\mathbf{r}_{1,2}}{r_{1,2}^3} n_n a^2 \sqrt{\frac{2}{\pi}} v_{Tn} (\kappa_{at} T_n - \kappa_{det} T_s). \quad (100)$$

This leads to a temperature gradient in the place of the other dust grain,

$$\frac{\partial T_n}{\partial \mathbf{r}_{1,2}} = \frac{\mathbf{q}}{\kappa_T}, \quad (101)$$

where κ_T is the thermal conductivity of the gas. A dust grain situated in this temperature gradient experiences a thermophoretic force, which can be expressed through the thermal conductivity as

$$\mathbf{F}_{tp} = -\frac{16}{15}\sqrt{\frac{\pi}{2}} v_{Tn} a^2 \kappa_T \frac{\partial T_n}{\partial \mathbf{r}_{1,2}}. \quad (102)$$

Thus, the thermal conductivity cancels and we again find expression (98) for the neutral flux shadow force with the additional numerical coefficient $64/45\pi \approx 0.45$ [53].

For high gas pressures or large dust sizes, the neutral shadow attraction can obviously be stronger than the Coulomb repulsion even at distances shorter than the Coulomb field screening length. This means that if the grains are continuously growing in a gas discharge, then they should eventually reach the stage at which they will only attract each other and, therefore, will agglomerate. The phenomenon of dust agglomeration is the common phenomenon in most etching devices operating for a long time sufficient for dust grains to grow [8–12]. Observations show that dust grains grow up to sizes on the order of few fractions of a millimeter [8] and that many of them finally take the form of cauliflower agglomerates. Theoretically, the criterion for dust agglomeration due to neutral shadow attraction was first obtained in [12, 59, 60]. Dust grain agglomerates that were observed in tokamak plasmas [12] are a big issue in fusion research (see [61, 62]). This phenomenon can also be applied to interpret new observations of fast dust creation in H-stars and behind supernova shocks [63].

It is expected that the further development of the physics of shadow forces can provide a natural explanation of the observed phenomenon of dust agglomeration in both space and laboratory plasmas.

5. COLLECTIVE DUST ATTRACTION

In this section, we consider collective dust attraction in a simple model, assuming that at large distances between the grains (such that the collective effects are important), the linear approximation for the responses is valid. We will self-consistently consider the basic state in which many dust grains are present with the dust number density n_d. We will find the electrostatic potential created by a test grain and the pair interaction of two test grains at large distances. This linear assumption is reasonable because, as we have already demonstrated, the attraction mainly occurs at large distances between the grains. The assumption that the collective effects also occur at large distances can be checked from the final result, assuming that the parameter P_0 is not extremely small (see below). Denoting by $\phi_1(r)$ the potential of one of the two test grains (grain 1) in the presence of many others grains, the potential of the interaction of the two grains can be written as $eZ_2\phi_1(r_{1,2})$. Since, in the linear approximation, the potential of grain 1 can be described by a static dielectric constant $\epsilon_{\mathbf{k}}$, we have

$$V_{1,2} = \frac{Z_d^2 e^2}{2\pi^2}\int \frac{\exp(i\mathbf{k}\cdot\mathbf{r})}{k^2 \epsilon_{\mathbf{k}}} d\mathbf{k}. \quad (103)$$

The collective effects change the usual interactions and open the possibility of the existence of new collective attraction forces. The possibility of attraction appears when the dielectric constant ϵ_k is negative in a certain range of wavenumbers k, which denotes the possibility of changing the sign of $V_{1,2}$. As was discussed at the beginning of the previous section, such a possibility exists in an open system in which the energy is gained with decreasing distance between two grains, which can result in their attraction. The openness of the system can be provided by the presence of many dust grains that create a plasma sink balanced by ionization. Thus, we assume that many grains are present in the unperturbed state with a certain average dust charge density P equal to P_0. The two grains that we will consider here can be any two probe grains in the "sea" of dust grains; in this sense, we will consider collective effects in the dust–dust interaction as functions of the parameter P_0. The latter will be considered constant (a homogeneous distribution of the "sea" grains), and the two probe dust grains will be considered at rest, so that their interaction is described only by the static dielectric constant. Ionization will also be assumed to be homogeneous. Thus, in the ground state, there is a balance between plasma production by ionization and plasma absorption by dust grains. This balance creates a difference in the basic state of a complex dusty plasma from the basic plasma state in the absence of dust, when only the condition of charge neutrality is used. In the perturbation of the basic state, both the ionization source and the "sea" of dust grains are perturbed. These perturbations are reflected in the dielec-

tric response, which creates the possibility of attraction between two test dust grains. The presence of ionization is an important property of complex dusty plasmas because, in the absence of ionization, the dusty plasma disappears due to the absorption of plasma particles by the grains on the time scale of dust charging. Experiment proves the latter statement. Thus, collective interaction can be quite different from the interaction of two individual grains in the absence of the "sea" of other grains. Of course, such an approach is a rather rough approximation of the more realistic conditions where the interaction of all the grains should be considered. However, this approach gives certain information about collective interactions and the new physics introduced by them in complex plasmas.

5.1. Collective Attraction (Isotropic Case)

First, we will consider the case of a completely isotropic basic state and will show that there exists collective attraction between the grains. For sufficiently large P_0 values, this attraction can be substantially stronger than noncollective attraction and can substantially affect screening [64]. For the first time, collective attraction was studied in [27] for a source that was assumed to be independent of the plasma parameters. Here, we consider the case that is closer to the conditions of the existing experiments; namely, we assume that the ionization source power is proportional to the electron density [64]. This is the case in most of the existing experiments with RF plasmas, where ionization is permanently produced by an RF source. The case where the ionization power is proportional to the electron density turns out to be simpler for consideration than that with a constant source [27].

First, we consider the case where the distance between the two dust grains is shorter than the ion–neutral mean free path. Remember that, in this case, the friction of ions is determined by ion–dust collisions. The rate of ion–dust collisions is on the order of $\nu_{ch}P_0 \approx v_{Ti}P_0 a/\lambda_{Di}^2$, and the characteristic mean free path for ion–dust collisions is on the order of $\lambda_{id} \approx \lambda_{Di}^2/aP_0$. The latter estimate is of importance because one can expect that the attraction will be somehow related to this mean free path, which differs by a factor of $1/P_0$ from that previously obtained for noncollective attraction. For $P_0 \ll 1$, this mean free path is much longer than the previously found distance λ_{Di}^2/a, at which noncollective attraction can be found. For P_0 on the order of unity, one should take into account collective effects even at distances on the order of λ_{Di}^2/a.

Then, we can define the basic state as a state in which the ionization the balances plasma absorption by dust. In this case, the dimensionless electron density [see Eqs. (40) and (41)] is

$$n_{e,0} = \frac{n_{e,ac}}{n_{i,ac}} = \tau_i P_0 \alpha_{ch}, \tag{104}$$

where τ_i is the ionization time in units of the characteristic charging time λ_{Di}^2/av_{Ti}. For given ratio (104), the charging equation determines the dust charge z_0 in the basic state. The dielectric constant describes the response of the system to linear perturbations of the basic state. We use the static balance equations to determine the static dielectric constant; continuity equation (40) with ionization source (41); and the ion force balance equation with the electric field force $e\mathbf{E}$, friction force (48), and ion pressure force $(T_i/n_i)(\partial/\partial\mathbf{r})$, which, in the dimensionless units used in Eq. (48), is $\tau(\partial/\partial\mathbf{r})$. We also use the electron force balance equation with the electric field force balanced by the electron pressure. Then, in dimensionless units, the linearized system of equations takes a simple form:

$$i\mathbf{k}\cdot\mathbf{u} = \frac{1}{\tau_i}\delta n_e - p_0\alpha_{ch}\delta n - \frac{P_0}{z_0}\alpha_{ch}\delta z, \tag{105}$$

$$e\mathbf{E} = -\frac{1}{n_{e0}} i\mathbf{k}\delta n_e, \quad e\mathbf{E} = \tau i\mathbf{k}\delta n + \alpha_{dr}P_0 z_0 \mathbf{u}, \tag{106}$$

where the drag force and charging coefficients are taken for $u = 0$ and, in Eq. (105), an account is made of dust charge variations δz, which depend on the wavenumber k (i.e., it is taken into account that the dust charge changes with the intergrain distance). To make the description as simple as possible, we will first consider only the changes of the ion and electron densities by the two probe charges. Of course, in this case, we also take into account variations in the dust charges. The dust charge density also changes; however, this effect affects the final result only slightly (by a factor on the order of unity). Later, we will also give the result that takes into account the changes in the dust charge density. Variations in the dust charge when varying the electron and ion densities are taken into account exactly. We will see that the openness of the system due to the charging effect is the most important and that the change of the dust charge with the intergrain distance quantitatively (but not qualitatively) changes the attraction forces. From Eq. (106), we obtain for the dielectric constant

$$\epsilon_{\mathbf{k}} = 1 + \frac{\tau}{\lambda_{Di}^2 k^2}\left[1 - P_0 + \frac{\left(1 - \dfrac{P_0^2 a^2 \alpha_{dr}\alpha_{ch} z_0^2}{k^2\lambda_{Di}^4(1+z_0)}\right)}{\left(\tau + \dfrac{P_0^2 a^2 \alpha_{dr}\alpha_{ch} z_0^2}{k^2\lambda_{Di}^4(1+z_0)}\right)}\right]. \tag{107}$$

We note that dielectric constant (107) can indeed be negative for $k \ll aP_0 z_0/\lambda_{Di}^2(1+z_0) \approx 1/\lambda_{in}$. In the limit

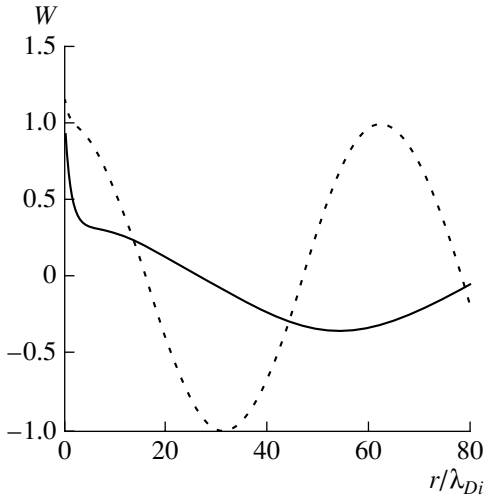

Fig. 2. Screening factors for collective dust attraction. The regions where the screening factors are negative correspond to dust attraction. The solid line describes the case of the relatively small value of the collective parameter ($\eta_{coll} = 1/3$), and the dotted line describes the case of the relatively large value of the collective parameter ($\eta_{coll} = 3$). The Debye screening can be seen at the beginning of the solid line and is less pronounced at the beginning of the dotted line.

$P_0 \longrightarrow 0$, expression (107) corresponds to the usual sum of the permittivity of a vacuum (unity) and two terms corresponding to electron screening (the first term in parentheses) and ion screening (the second term in parentheses). We note that, according to the quasineutrality condition, $(1 - P_0) = n_{e0,\,ac}/n_{i0,\,ac}$. Taking into account variations in the dust charge density gives a contribution proportional to the electron density; in this case, one should substitute into Eq. (107) $1 - P_0 + P_0/(1 + z_0)$ for $1 - P_0$ and, in front of the second term in parentheses in Eq. (107), one should introduce the coefficient $1 + P_0/(1 + z_0)$. For P_0 on the order of unity, these changes result in a factor on order of unity, and, for $P_0 \ll 1$, they are negligible. Therefore, keeping in mind these corrections, we will still analyze the simplest expression (107).

Integration of expression (103) with respect to k can easily be performed by calculating the residues of the poles determined by the quadratic equation for k^2. The result contains two terms with the factor $1/r_{1,2}$ in front of them. One of them corresponds to the exponential screening and another one corresponds to cosinusoidal variations of the potential energy, which changes its sign with distance (i.e., the potential contains a series of attraction minima). In a general form, the interaction energy can be written as

$$V_{1,2} = \frac{Z_d^2 e^2}{r_{1,2}}\left[\nu_a \exp\left(-s_a\frac{r_{1,2}}{\lambda_{Di}}\right) + \nu_b \cos\left(s_b\frac{r_{1,2}}{\lambda_{Di}}\right)\right] \quad (108)$$

with the coefficients ν_a, s_a, ν_b, and s_b depending on τ, P_0, and η_{coll},

$$\eta_{coll} = \frac{a^2 P_0^2 z_0^2 \alpha_{dr}\alpha_{ch}}{\tau(1 + z_0)\lambda_{Di}^2}. \quad (109)$$

We will consider here only the limiting cases that seem to be the most interesting, namely, the limits $\eta_{coll} \ll 1$ and $\eta_{coll} \gg 1$. Note that both the numerator and the denominator of η_{coll} are small: the denominator is small because $\tau \ll 1$, and the numerator is small because the ratio a/λ_{Di} is small. Of course, for very small values of P_0, the second limit is not possible to satisfy. We assume here that $P_0 a/\lambda_{Di} > \sqrt{\tau}$, which is the case of experiments with large dust grains and is almost satisfied in existing experiments, where $\tau \approx 0.02$, $P_0 \approx 0.5$, and $a/\lambda \approx 1/5$. It is clear that for complex plasma condensation experiments, it is desirable to operate with largest available dust size in order to satisfy the condition $\eta_{coll} > 1$, which is the case where the collective effects are the largest. For $\eta_{coll} \ll 1$, we obtain

$$V_{1,2} \approx \frac{Z_d^2 e^2}{r_{1,2}}\left[\exp\left(-\frac{r_{1,2}}{\lambda_{Di}}\right) + \eta_{coll}\cos\left(\sqrt{\eta_{coll}P_0}\tau\frac{r_{1,2}}{\lambda_{Di}}\right)\right], \quad (110)$$

and for $\eta_{coll} \gg 1$, we have

$$V_{1,2} \approx \frac{Z_d^2 e^2}{r_{1,2}}\left[\frac{1}{\eta_{coll}}\exp\left(-\sqrt{\eta_{coll}}\frac{r_{1,2}}{\lambda_{Di}}\right) + \cos\left(\sqrt{\tau P_0}\frac{r_{1,2}}{\lambda_{Di}}\right)\right]. \quad (111)$$

We see that the collective attraction changes substantially from expression (110), where it plays a relatively marginal role, to expression (111), where collective effects are large. In expression (110), the collective attraction is similar to the noncollective one, for which the usual Coulomb screening is dominant at small distances and the attraction begins to be dominant at large distances at which the Coulomb repulsion is screened. The difference is that the collective attraction coefficient is proportional to P_0 and is absent as $P_0 \longrightarrow 0$. However, in real experiments, P_0 is often on the order of unity. The other factor, a^2/λ_{Di}^2, is the same as in noncollective attraction. The coefficient η_{coll} depends also on the product of the drag and charging coefficients, as well as on z_0. This dependence is also important; however, in the absence of ion drift, these coefficients are on the order of unity (in the presence of ion drift, the above expressions are not valid because, in this case, additional terms proportional to the ion drift velocity and derivatives of the drag coefficient appear). An important feature of the collective attraction term is the appearance of the small parameter τ in the denominator in front of the cosinusoidal term, which is absent for noncollective attraction. This makes the amplitude of collective attraction larger (provided of course that P_0 is on the order of unity). The parameter τ in expression

(110) also determines the distance corresponding to the first attraction minimum; for P_0 on the order of unity, this distance is shorter than that for noncollective attraction. Due to the condition $\eta_{coll} \ll 1$, the coefficient in front of the collective term in expression (110) is small and the attraction operates only at distances at which the Coulomb potential is screened, as is the case of noncollective attraction. Thus, we see that, in the limit $\eta_{coll} \ll 1$, collective attraction has some similarities with noncollective attraction. Figure 2 shows the screening factor $W = V_{1,2}/(Z_d^2 e^2/r_{1,2})$ as a function of the distance normalized to the ion Debye length, $r = r_{1,2}/\lambda_{Di}$, for $\tau = 0.2$ and $P_0 = 0.5$ for two cases: $\eta_{coll} = 1/3$ [solid curve calculated from expression (110)] and $\eta_{coll} = 3$ [dotted curve calculated from expression (111)].

An opposite situation occurs in the limit where the collective effects are large and $\eta_{coll} \gg 1$. In this case, the screened part of the potential is much smaller in amplitude than the Coulomb potential and the screening length is much shorter than in the previous case; however, the amplitude of the cosinusoidal part becomes equal to the Coulomb potential amplitude, and the first attraction minimum appears at much shorter distances. At small distances, the cosinusoidal part still describes repulsion. The cosinusoidal-type attraction force was first found in [27] for a plasma source independent of the electron density; therefore, the results of [27] differ in the attraction length and the strength of attraction force from that given here. No substantial change in the shape of the potential was found in [27]. According to [64], our model, in which the ionization source is proportional to the electron density, is the most appropriate one for the RF plasma used in the existing experiments. In this case, collective effects substantially change screening and lead to the enhancement of collective attraction.

A similar type of attraction can be obtained when the distance between the two dust grains is larger than the ion–neutral mean free path. In this case, ion–neutral friction should be substituted for ion–dust friction and the effect of diffusion should be taken into account in the continuity equation [36]. It appears that, for $\tau \ll 1$, diffusion can be neglected (it contributes τ^{-1} times less than the ion pressure); in this case, the balance between the plasma sink and ionization is determined by the charging process, as was described in [1]. Then, the only difference is the change of the value of the collective parameter η_{coll}, which now depends on the ion–neutral mean free path λ_{in}. We denote the new parameter $\eta_{coll,\,in}$. Simple calculations yield

$$\eta_{coll,\,in} = \frac{P_0 \alpha_{ch} z_0}{1 + z_0} \frac{a}{\lambda_{in}}. \tag{112}$$

Since $a \ll \lambda_{in}$, the coefficient $\eta_{coll,\,in}$ is always less than unity. This means that in the case where ion–neutral collisions are dominant, the collective effects are described by expression (110) and the attraction occurs at distances where the screened part of the potential is small. Since $\eta_{coll,\,in}$ does not depend on τ, the attraction can dominate for $\exp(-r_{1,2}/\lambda_{Di}) \ll aP_0/\lambda_{in}$, although the distance corresponding to the first minimum ($\approx \lambda_{Di}\lambda_{in}/aP_0\tau$) depends strongly on τ.

5.2. Role of Dust Pressure

In the previous simplified consideration, we neglected the effect of dust density perturbation. Here, we briefly discuss the dust pressure effects. We present here the final result in the form of an additional term in dielectric function (107) that appears when we take into account the change in the dust charge density. We also assume $P_0 \gg \tau$. As a result, we find

$$\epsilon_{\mathbf{k}} = 1 + \frac{\tau}{\lambda_{Di}^2 k^2}\left[1 - \frac{P_0 z_0}{1 + z_0}\right.$$

$$+ \left(1 + \frac{P_0}{1 + z_0}\right)\frac{\left(1 - \dfrac{P_0^2 a^2 \alpha_{dr}\alpha_{ch} z_0^2}{k^2 \lambda_{Di}^4 (1 + z_0)}\right)}{\left(\tau + \dfrac{P_0^2 a^2 \alpha_{dr}\alpha_{ch} z_0^2}{k^2 \lambda_{Di}^4 (1 + z_0)}\right)} \tag{113}$$

$$\left. + P_0 \frac{\left(\tau + \dfrac{\alpha_{dr}\alpha_{ch} P_0 z_0 (1 + P_0)}{k^2}\right)}{\left(\tau_d + \dfrac{\alpha_{dr}\alpha_{ch} P_0^2 z_0^2}{k^2 (1 + z_0)}\right)}\right],$$

where

$$\tau_d = \frac{T_d}{T_e Z_{d,0}} = \frac{T_d e^2}{T_e^2 a z_0}.$$

For high dust pressures, the role of the dust pressure is negligible; however, for low pressures, it plays a stabilizing role. Note that, in the general case, it is necessary to take into account the effects of ion–neutral and dust–neutral collisions.

5.3. Collective Attraction in the Presence of an Ion Flow

In the presence of ion drift, which usually exists in the plasma sheath, the distribution of all the parameters is inhomogeneous and the definition of the basic state is much more complicated. We will consider here a homogeneous state with ion drift in a model approach.

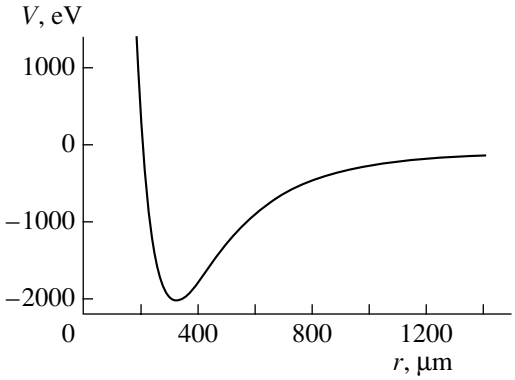

Fig. 3. Numerical results for the attraction well in the downstream direction in the presence of an ion flow with $M = 1$.

When the friction of ions on dust is balanced by other forces (e.g., by some neutral flux), a homogeneous ion drift can arise. If the external force that creates the drift does not depend on the plasma parameters, then this force will not appear in the responses. Of course, such a model can serve only for the qualitative illustration of the problem. In this case, the static dielectric constant can be found by taking into account small perturbations of the basic state, as was done in the previous section. Here, we note a very important point, namely, the large rate of dissipation in complex dusty plasmas will eventually destroy the Mach cone and will destroy the wake in the form in which it is usually expected to be present, although the asymmetry of the interaction forces with respect to the direction of the flow is naturally conserved. As a result, we obtain the rather cumbersome expression

$$\epsilon_{\mathbf{k}} = 1 + \frac{\tau}{\lambda_{Di}^2 k^2}\left[1 - \frac{P_0 z_0}{1+z_0} + \left(1 + \frac{P_0}{1+z_0}\right)\frac{\left(1 - \frac{A}{k^2\lambda_{Di}^2}\frac{a^2}{\lambda_{Di}^2}\right)}{\left(\tau + \frac{B}{k^2\lambda_{Di}^2}\frac{a^2}{\lambda_{Di}^2}\right)}\right], \tag{114}$$

where

$$A = \frac{P_0 z_0}{\left(\frac{k_z^2}{k^2} f + \frac{k_\perp^2}{k^2} g\right)(1+z_0)}[\alpha_{ch}(u_0)h + 2u_0\alpha_{dr}(u_0)s], \tag{115}$$

$$B = \frac{1}{\left(\frac{k_z^2}{k^2} f + \frac{k_\perp^2}{k^2} g\right)} \times \left[\left(\frac{P_0 z_0 \alpha_{ch}(u_0)}{1+z_0} + iu_0\right)h + \frac{P_0 z_0 u_0 \alpha_{dr}(u_0)}{1+z_0}s\right], \tag{116}$$

$$h = \left(P_0 z_0 \frac{\partial}{\partial u_0}(u_0\alpha_{dr}(u_0)) + 2iu_0 k_z\right), \quad s = \left(P_0 \frac{\partial}{\partial u_0}\alpha_{ch}(u_0) + ik_z\right), \tag{117}$$

$$f = 1 - iP_0 \frac{\partial}{\partial u_0}\alpha_{ch}(u_0), \quad g = \frac{\left(P_0 z_0 \frac{\partial}{\partial u_0}(u_0\alpha_{dr}(u_0)) + 2iu_0 k_z\right)}{\alpha_{dr}(u_0) z_0 P_0 + 2ik_z u_0}. \tag{118}$$

Here, k_z is the component of the wave vector along the ion flow and $k_\perp$ is the absolute value of the component of the wave vector perpendicular to the flow. The structure of the dielectric function is the same as before but the coefficients have large imaginary parts, which makes the response highly dissipative. This means that the oscillations in the screening factor are decaying and under certain conditions, only one attraction minimum is even possible. This dissipation substantially smoothes the Mach cone and modifies the interaction. Although the attraction in the downstream direction is maximum, there are still large attraction minima at large angles to the downstream direction and also in the upstream direction. For $k \ll 1 \ll 1/\sqrt{\tau}$, when the last term in formula (114) has a negative sign, the terms with f and g are canceled and for Mach numbers on the order of unity, one can use the asymptotic expressions for α_{dr} and α_{ch}:

$$\alpha_{dr} \approx \frac{1}{2|u_0|^3}\left(\ln\Lambda + \frac{M^2}{2z} + \frac{M^4}{4z^2}\right), \quad \alpha_{ch} \approx \frac{1}{2|u_0|}(1 + M^2 2z), \quad M = \sqrt{2\tau}u_0. \tag{119}$$

The derivatives of the coefficients are negative for Mach numbers somewhat less than unity and positive for Mach numbers somewhat larger than unity. Estimates show that, for M on the order of unity, α_{dr} is on the order of $\tau^{3/2}$ and α_{ch} is on the order of $\sqrt{\tau}$. In the range τ, $\tau^{3/2} \ll k \ll 1 < 1/\sqrt{\tau}$, we have $A/B \approx 1$ and the attraction more weakly depends on the direction, as it did in the previous case. Nevertheless, such a depen-

dence exists, and detailed numerical calculations [65] show that the attraction in the downstream direction substantially exceeds the attraction in other directions.

We illustrate the result obtained by numerically calculating the potential energy of a grain in the downstream direction, where the attraction is the strongest. The computations were performed for the following parameters: the grain size is 7 μm, the ion density is 10^9 cm^{-3}, the electron temperature is 5 eV, $\tau = 0.02$, $P_0 = 0.6$, and the Mach number is $M = 1$, which gives $Z_d = 8 \times 10^4$. The results are presented in Fig. 3, which shows the presence of a deep attraction potential well for the other dust grain. Similar potential wells are observed for rather large angles to the stream velocity; however, the potential wells in the perpendicular direction and in the upstream direction are not so deep.

5.4. Dust Attraction in the Presence of a Magnetic Field

Recent experiments with a complex plasma in a magnetic field showed interesting structures, dust rotation, and the modification of dust motion [66, 67]. We consider here the simplest effects of the influence of a magnetic field on the collective dust–dust interaction; namely, we assume that the basic state is the same as in the absence of both a magnetic field and an externally excited ion drift. Since, in the existing experiments, the magnetic field is not so strong as to change the charging and drag coefficients, we consider only the disturbances of the basic state related to the influence of the magnetic field on the ion motion, while at the same time the dust grains move according to the forces exerted on them by ions. Since we are interested in the electrostatic forces acting between two test dust grains in the presence of a magnetic field, we should take into account that disturbances of the basic state should lead to the appearance of ion drift caused by the grain field. This drift will be changed by the magnetic field, which in turn will affect the dust–dust interaction. In the presence of a magnetic field, the equilibrium conditions of the force balance and quasineutrality are the same as in the absence of a magnetic field because the Lorentz force is zero in the absence of ion drift in the basic state. A straightforward calculation of the static dielectric constant is similar to that performed above; the only additional term is the Lorentz force acting on ions. As for electrons, the magnetic field changes their motion, but does not change their contribution to the static dielectric constant because, as in the absence of a magnetic field, they only contribute to Debye screening. We introduce the dimensionless magnetic field $\mathbf{H}$ and the dimensionless Lorentz force $\mathbf{F}_L$:

$$\mathbf{H} = \frac{\mathbf{H}_{\rm ac}\sqrt{2}ev_{Ti}\lambda_{Di}^2}{acT_e}, \quad \mathbf{F}_L = \mathbf{u}\times\mathbf{H}, \tag{120}$$

where, as before, the index "ac" stands for the actual magnetic field strength. Straightforward calculations give the following expression for the static dielectric constant in the form corresponding to formula (114):

$$\epsilon_{\mathbf{k}} = 1 + \frac{\tau}{\lambda_{Di}^2 k^2}\left\{1 - \frac{P_0 z_0}{1+z_0} + \left(1+\frac{P_0}{1+z_0}\right)\frac{\left(R_H - \dfrac{P_0^2 z_0^2 \alpha_{\rm ch}\alpha_{\rm dr}}{k^2(1+z_0)}\right)}{\left(\tau R_H + \dfrac{P_0^2 z_0^2 \alpha_{\rm ch}\alpha_{\rm dr}}{k^2(1+z_0)}\right)}\right\}, \tag{121}$$

where

$$R_H = \frac{k_z^2}{k^2} + \frac{k_\perp^2}{k^2}\frac{P_0^2 z_0^2 \alpha_{\rm dr}^2}{P_0^2 z_0^2 \alpha_{\rm dr}^2 + H^2}. \tag{122}$$

For $H \longrightarrow 0$, we obtain the previous result. Therefore, the critical magnetic field strength at which the magnetic field starts to influence the dust–dust interaction corresponds to the value at which the Lorentz force is equal to the force of ion friction on dust, which in turn is completely determined by the drag coefficient. Since both forces are proportional to the ion drift velocity, the latter does not enter into the expression for the critical magnetic field. In dimensional units, we have

$$\frac{H_{\rm cr}^2}{2\pi n_0 m_i c^2} = \frac{a^2}{\lambda_{Di}^2 \tau^2} P_0^2 z_0^2 \alpha_{\rm dr}^2. \tag{123}$$

For practical applications, we can write the critical field in Gauss units

$$H\ [\mathrm{G}] = 9.4\times 10^4 \left(\frac{0.02}{\tau}\right)\sqrt{\left(\frac{n_0}{10^9\ \mathrm{cm}^{-3}}\right)} P_0 z_0 \frac{a}{\lambda_{Di}} \ln\Lambda, \tag{124}$$

where $\ln\Lambda$ is the Coulomb logarithm. Note that this criterion depends strongly on the dust size a. Expression (122) shows that the magnetic field introduces an anisotropy in the attraction: as the magnetic field increases, the attraction is enhanced both in the direction perpendicular to the magnetic field and along the magnetic field. In the direction perpendicular to the magnetic field, the distance to the first minimum of the potential decreases with increasing magnetic field.

We conclude this section with the following remarks:

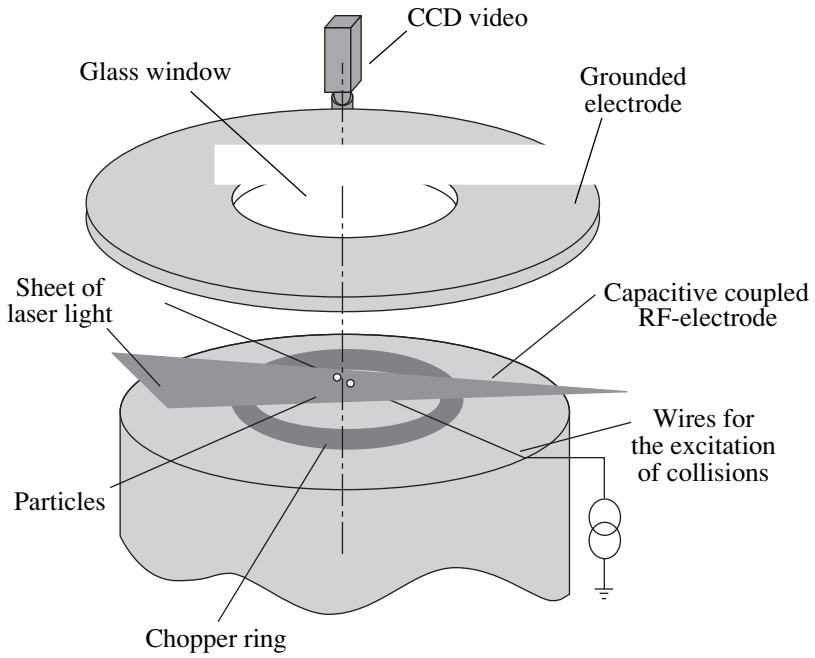

Fig. 4. Sketch of an experimental setup for measuring the dust–dust interaction potential in the dust collision experiments.

(i) The attraction of dust grains is a natural phenomena in complex dusty plasmas and is related to the shadowing of the collective action produced by many dust grains.

(ii) Noncollective attraction can serve for the demonstration of the shadow effect; however, in complex plasmas with many dust grains, the main attraction effect is collective attraction.

(iii) The attraction force strongly increases with the dust size, which is typical of all the shadow effects.

(iv) Ion–neutral collisions affect collective attraction for $\lambda_{in} \ll \lambda_{Di}^2/a$. The latter condition depends on the gas pressure and the size of the grains. In the existing experiments, it is satisfied for $a \ll 1$ μm.

(v) The presence of an attraction force is rather important for the problem of transition to a strongly correlated state. Although the attraction potential wells usually appear at distances larger than the dust size and on the order of or even much larger than the screening length, the depth of the attraction potential well can be relatively large because it is proportional to Z_d^2.

(vi) The presence of a molecular-type potential that is repulsive at small distances, while attractive at large distances, opens the real physical possibility of forming a strongly correlated state with nonrigid requirements on the coupling coefficient Γ.

(vii) Neutral–grain collisions cause only noncollective attraction, which can exceed Coulomb repulsion even at small distances between the grains. It can cause dust agglomeration and serves as one of the most probable explanation for the observed agglomeration of large-size grains.

(viii) In order to reach a strongly coupled state, it is desirable to operate in the range of parameters where the agglomeration is inefficient. Therefore, a deeper understanding of the phenomenon of dust agglomeration (where the attraction force can exceed the Coulomb force) is rather important for the problems of plasma condensation.

6. MEASUREMENTS OF THE SCREENED POTENTIAL IN DUST–DUST COLLISIONS

The potential distribution around a charged grain in a plasma can be measured by performing scattering experiments similar to those already used many years ago to determine nuclear potentials and by deriving the force field from the measured trajectories of the interacting grains. Such experiments were performed for the first time in [68–70].

6.1. Experimental Technique

Scattering experiments conducted so far use RF discharge plasmas. The plasma chamber is basically a GEC reference cell [68–70], modified so that it is possible to view its interior from the side and from the top through the upper (grounded) electrode (Fig. 4).

Depending on the research requirements, the working gases are helium, argon, or krypton. An RF discharge is ignited using a 13.56-MHz signal applied to the lower (powered) electrode. Previously, this experimental technique was used in complex-plasma experi-

ments that were not intended to take measurements of the screened potential. The requirements for the studies of complex plasmas in the strong coupling limit (especially to the investigations of phase transitions to the liquid and crystalline states) imply the use of low RF power and, hence, a low degree of ionization (typically, from 10^{-7} to 10^{-6}). This ensures that both ions and neutral atoms are in collisional equilibrium at room temperature. Let us briefly review this requirement. In order to ignite an RF discharge with a 13.56-MHz signal, the electron–neutral collision time should be longer than the time needed to accelerate an electron from zero velocity to the first ionization potential of the working gas (typically, about 10 eV). In practice, it is sufficient that some electrons in the distribution reach the ionization potential. The condition for this can be easily calculated. We assume that the RF potential varies as $V(t) = V_0 \sin \omega t$, where $\omega = 2\pi f$ and $f = 13.56$ MHz is the signal frequency used. We also assume that the instantaneous electron energy is $E_e(t) = eV(t)$ and consider only the initial (linear) phase of the cycle, at which $E_e(t) \approx eV_0 \omega t$. This assumes $\omega t \ll 1$; however, in any case, calculations can easily be repeated for the sinusoidal dependence $\sin(\omega t)$. Writing the kinetic energy in the form $E_e(t) = (m_e/2)(dx/dt)^2$ and integrating

$$\int_0^{\lambda_{en}} dx = \int_0^{t_{\mathrm{coll},\,en}} \left(\frac{2eV_0\omega t}{m_e}\right)^{1/2} dt \qquad (125)$$

yields

$$t_{\mathrm{coll}} = \left(\frac{3m_e}{4eV_0\omega n_n^2 \sigma_{en}^2}\right)^{1/3} \qquad (126)$$

for the electron–neutral collision time, where the electron–neutral collisional mean free path is $\lambda_{en} = 1/n_n\sigma_{en}$ with n_n being the neutral gas density and σ_{en} being the electron–neutral collision cross section. After some algebra, the condition $E_e(t_{\mathrm{coll,\,en}}) > \bar{E}_e$ yields

$$\frac{eV_0}{\bar{E}_e} > \left(\frac{4\bar{E}_e n_n^2 \sigma_{en}^2}{3m_e\omega^2}\right)^{1/2}. \qquad (127)$$

For the frequency ω used and typical values of the gas density (10^{16} cm^{-3}) and cross section (10^{-15} cm^2), we obtain

$$eV_0 > 36.7\bar{E}_e; \qquad (128)$$

in other words, a typical peak voltage on the order 100 V is sufficient to initiate the discharge. This also implies that low-power RF devices can be used; in this case, the gas and ion temperatures are essentially the environment (room) temperatures, as is desired for many applications.

6.2. Collision Experiments

An advantage of using microsphere grains for collision experiments is the possibility of visualizing their trajectories by fast microscopy; a disadvantage is that not all regions of the plasma are accessible for such experiments because the microspheres have to be electrically suspended against gravity. For instance, the electrostatic field required to support a typical microsphere of mass 10^{-10} g carrying a surface charge $Q = eZ_d \approx 10^4 e$ is about 10 V/cm, as can be calculated from the force balance

$$QE = mg. \qquad (129)$$

This means that only the sheath regions of a plasma [71] or striations in a DC discharge [2] (in other words, substantially inhomogeneous plasma regions) can be investigated in this way. Fortunately, the sheath regions themselves are of great interest to plasma physicists, because they mark a transition from subsonic to supersonic ion flow. From the standpoint of applications, the sheath regions are important because they are sites for many types of plasma processing, deposition, and etching.

The collision experiment proceeds in two stages:

(i) In the first stage, a single grain is injected into the plasma. Its trajectory is mainly governed by gravity, electrostatic forces, and neutral drag and ion drag forces. Under the low-pressure and low-power conditions used in the pioneering experiments by Konopka *et al.* [68], other forces related to thermophoresis, photophoresis, pressure gradients, neutral convection, etc., were negligible. The neutral gas was at rest and provided the damping of grain motion. From the grain trajectory, it is possible to derive the form of the electrostatic trapping potential $\phi_T(\mathbf{R})$ as a function of the distance R from the axis of the axisymmetric plasma chamber.

(ii) In the second stage, a binary-collision experiment is performed. From the trajectories of two colliding grains, which both move in the known confining potential $\phi_W(R)$, it is possible to derive their interaction potential $\phi_I(r)$. The total potential is $\phi_T = \phi_W + \phi_I$.

The mathematical derivation is the following. Since in the first approximation the grain motion takes place only in the horizontal plane, the vertical force balance is assumed to be permanently satisfied. Grain observations taken from the side confirm this assumption. Then, the equation of motion is

$$m\frac{d\mathbf{v}_d}{dt} = -Q\nabla\phi_T - \mathbf{F}_D, \qquad (130)$$

where the drag force by neutral atoms, $\mathbf{F}_D$, is given by the Epstein drag law [see (72), (74)]. This description is applicable when the neutral–neutral collisional mean free path is much larger than the grain size. The force $\mathbf{F}_D$ is linearly proportional to the grain velocity $\mathbf{v}_d$. It is also implicitly assumed in Eq. (130) that the charge of

the microsphere does not vary either systematically or stochastically. There are two possibilities of such variations: independent collisional variations of the charges of each microsphere and the dependence of the charge on the intergrain distance. The absence of the first type of variation implies homogeneous plasma conditions on the trajectory of each grain. The absence of the second type of variation implies that the distance between the colliding grains should be at least larger than their size. From our previous discussion on charge fluctuations, we may conclude that the constancy of charge is a good assumption for micron-sized grains. Also, because of the rapid charging that microspheres experience in a discharge, it is reasonable to assume that the equilibrium charge is attained instantaneously as compared to the dynamic scales involved. This means that the experiments should be conducted with grains moving with velocities substantially lower than the ion thermal velocity.

The experiments were performed with equal-size grains; hence, both of them should experience nonlinear screening, which does not obey the law of linear superposition. Therefore, this experiment is dealing with a new phenomenon that has been poorly investigated theoretically. In experiments in which one of the microspheres serves as a test grain with linear screening, it is necessary that this grain be small; in this case, the detection of its trajectory can require methods other than fast microscopy used in this experiment.

In the first stage of the experiment, it was found that the grains injected without initial angular momentum oscillate radially through the center of axial symmetry.

This fact considerably simplifies calculations because, in this case, the one-dimensional equation of motion can be used; i.e.,

$$m_d \frac{d^2x}{dt^2} = -Q\frac{\partial \phi_T}{\partial x} - \eta \frac{dx}{dt}. \qquad (131)$$

Expanding the confining potential in powers series and fitting the theoretical grain trajectory to the measurements allows one to determine ϕ_T and the friction constant η. It turns out that in almost all applications the potential is fairly accurately described by a parabolic function

$$\phi_T = \phi_0 + b(x - x_0)^2,$$

where x_0 is the position of the center and b and ϕ_0 are constants.

At the second stage, experiments on collisions between two grains showed the following. Without angular momentum and in the case of central collisions, both grains move purely radially and their motion, as with single grains, is again described by the one-dimensional equation

$$m_j \frac{d^2x_j}{dt^2} = -Q_j \left.\frac{\partial \phi_I}{\partial x}\right|_{x_j - x_i} - Q_j \left.\frac{\partial \phi_W}{\partial x}\right|_{x_j} - \eta \frac{dx_j}{dt} \qquad (132)$$

for the jth grain interacting with the ith grain and a similar equation for the ith grain interacting with the jth grain. Using two identical grains ($m_i = m_j = m$ and $Q_i = Q_j = Q$), we can write the difference equation by subtracting the equation for the ith grain from the equation for the jth grain:

$$m\frac{d^2x_r}{dt^2} + \eta \frac{dx_r}{dt} + 2bx_r + 2Q \left.\frac{\partial \phi_L}{\partial x}\right|_{x_r} = 0, \qquad (133)$$

where $x_r = x_i - x_j$. The sum of the ith and jth equations leads to the differential equation for the center of mass, $x_c = x_i + x_j$:

$$m\frac{d^2x_c}{dt^2} + \eta \frac{dx_c}{dt} + 2b(x_c - x_0) = 0. \qquad (134)$$

Measuring the trajectories of both grains, we can determine b and η from the last equation (the obtained values can be compared with the corresponding values determined using a single grain), and from Eq. (133), it is possible to obtain the interaction potential between the two grains as a function of the separation distance x_r.

Figure 5 shows the trajectory of the center of mass of two colliding microspheres. The solid line is the calculated trajectory for a parabolic potential with allowance for the friction damping due to collisions with neutral gas atoms. The fitted values are in agreement with the Epstein drag calculated from the known gas pressure and temperature.

Figure 6 gives the derived interaction potential between the grains. The solid line is calculated from the grain motion in a parabolic potential and a Debye–Hueckel interaction potential. Note that the grains finally come to an equilibrium state corresponding to the separation between them $\langle x_r \rangle = 2.2\lambda_D$, where λ_D is the screening length fitted to the measurements.

Figure 7 shows that the screening length depends weakly on the pressure of the neutral gas (neutral particle density).

Summarizing the results of the experimental determination of the screened grain potential ϕ_I, we may conclude the following:

(i) The experiments performed so far have probed a region $0.5\lambda_D < r < 3\lambda_D$, in which the interaction potential is described very well by the Debye–Hueckel potential; no attraction potential is observed in this region. According to the above theory, the screening is still nonlinear in this region because $r \ll \sqrt{\tau/z}\lambda_{Di} \approx 16\lambda_{Di}$. The screening potential predicted by nonlinear screening in the investigated range of distances can be

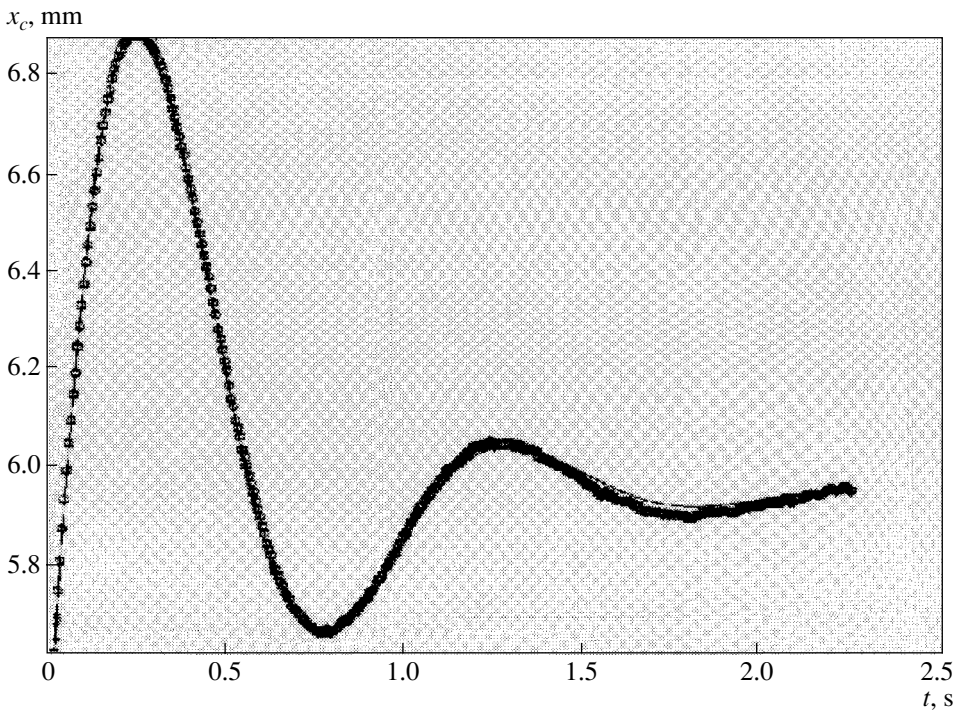

Fig. 5. Trajectories of the center of mass x_c of two colliding dust grains in the plasma sheath in an argon RF discharge at a pressure of 2.1 Pa and a voltage of 145 V. The solid line is calculated for a harmonic oscillator with the damping constant $\eta = 2.5 \times 10^{-12}$ kg/s and $b = 1.1 \times 10^{-11}$ kg/s^2.

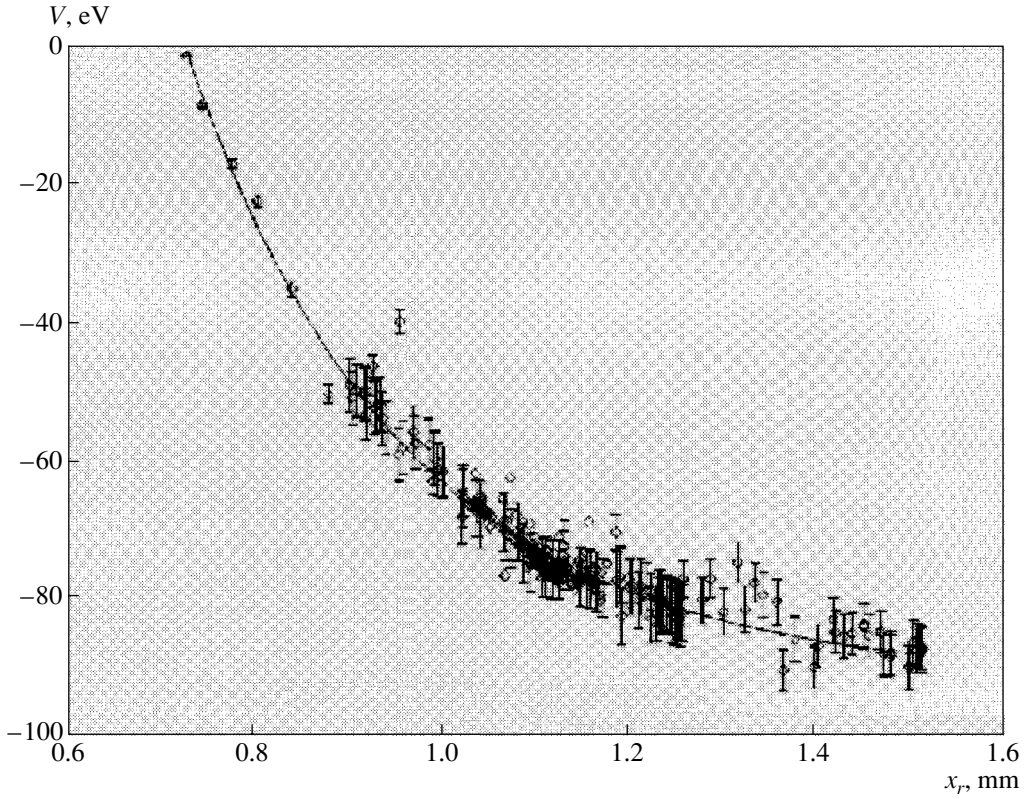

Fig. 6. Interaction potential between two charged dust grains in a plasma sheath. The solid line shows the fit with an exponentially screened Coulomb potential.

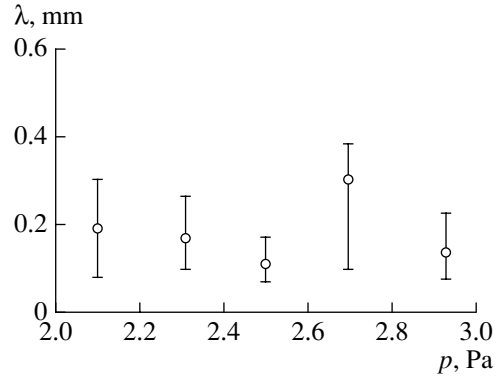

Fig. 7. Evaluated screening length of the grain field as a function of the neutral gas pressure for a grain size of 6.9 ± 0.2 μm.

approximated by an exponential dependence (Debye–Hueckel potential), but with the screening length $\lambda_D < \lambda_{Di}$. Experiments were performed for equal-size grains. In this case, it is impossible to distinguish the nonlinear screening of each grain, and new theoretical investigations are required to quantitatively compare the calculated screening length with experiments. The measured value of λ_D is likely to be closer to the electron Debye length.

(ii) The ratio λ_D/a in these experiments was large (on the order of 100); in this case, the long-range attraction is weak. The relative value of the shadow attraction potential is on the order of $a^2/\lambda_{Di}^2 \approx 10^{-3}$. This means that the long-range shadow attraction should be very weak and the associated attractive forces related to ion flux are hard to detect. On other hand, the detection of these forces at least needs $r > 5\lambda_D$, which was not the case in those experiments. The shadow forces due to neutral flux can be appreciable at higher gas pressures. Experiments with bigger grains, larger distances, and higher gas pressure are required to detect these new forces.

(iii) The intergrain distance for closest collisions was much larger than the grain size. Under these conditions, it is hardly possible to detect the change in the grain charges in collisions. Experiments with bigger grains or smaller distances between colliding grains are required.

(iv) The experiments have to be performed in a plasma sheath. Being accelerated in the vertical direction in the sheath electric field, the ions acquire superthermal drift velocities. This means that the shielding is quite different from that in the absence of ion drift (in the linear approximation, it is determined by the electron Debye radius, rather than the ion Debye radius). Nonlinear screening in this case is poorly investigated both numerically and analytically. As was discussed in the previous sections, ion drift also changes the shadow attraction. Experiments with vertically interacting grains could be designed to investigate the wake field and flow shadowing effects.

(v) So far, the estimates of the grain charge have not been compared with the charging theories. Such a comparison is not simple due to the mutual influence of charging and screening. This should be a task for future experiments performed under different conditions and with different plasmas (e.g., electronegative or photoemission plasmas).

(vi) The binary collision technique is a novel tool for investigating the basic physics of dust–plasma interactions. This technique can be extended to answer a number of important questions, including the questions of the absence of nonlinear interference in the interaction of two grains with substantially different sizes, the asymmetry of shielding in the presence of an ion flow, and the existence of a long-range attractive potential predicted by the theory.

(vii) It is rather important to investigate the interaction of two grains in the presence of many other grains in a complex plasma, e.g., the interaction of two dust grains which differ from other grains by their size (being smaller or larger than the "sea" grains). This seems to be the way to investigate the collective interactions in complex plasmas, which can be very important for creating strongly correlated states.

7. CONCLUSIONS

Some points were already emphasized in each section. Here we will only stress that the aim of this paper was to present the main tools to be used in current research in this very rapidly developed field, to list simple physical arguments and simple elementary physical processes in complex plasmas, and to introduce the reader to the atmosphere and new physical intuition appearing in this field of research.

In summary, we can draw the following conclusions:

(i) The material presented here for elementary processes in complex plasmas can be used to analyze the conditions for strong coupling and strong correlations, to consider the transitions to a complex dusty plasma state, and to discuss the effect of different types of dust–dust interactions on the criteria for phase transitions.

(ii) The understanding of elementary processes in complex plasmas is important for estimates in experiments on strong coupling (including experiments in which the plasma–dust crystals were observed), experiments on melting and phase transitions, and experimental investigations of waves and instabilities in the crystalline and disordered states of a complex plasma.

(iii) The knowledge of elementary processes in complex plasmas is important for technological, industrial, environmental, and astrophysical applications.

ACKNOWLEDGMENTS

V.N. Tsytovich appreciates the hospitality during his stay at the Max Plank Institute for Extraterrestrial Physics in Garching when this review was started.

REFERENCES

1. V. N. Tsytovich, G. E. Morfill, and H. Thomas, Fiz. Plazmy **28**, 675 (2002) [Plasma Phys. Rep. **28**, 623 (2002)].
2. H. Thomas, G. Morfill, V. Demmel, and J. Goree, Phys. Rev. Lett. **73**, 652 (1994).
3. J. H. Chu and I. Lin, Physica A (Amsterdam) **205**, 183 (1994).
4. A. Melzer, T. Trottenberg, and A. Piel, Phys. Lett. A **191**, 301 (1994).
5. Y. Hayashi and K. Tachibana, Jpn. Appl. Phys. **33**, 804 (1994).
6. N. Sato, T. Mieno, T. Hirata, *et al.*, Phys. Plasmas **1**, 3480 (1994).
7. V. E. Fortov, A. P. Nefedov, O. F. Petrov, *et al.*, Phys. Lett. A **219**, 89 (1996).
8. G. Selwyn, J. Heidenrich, and K. Haller, Appl. Phys. Lett. **57**, 1867 (1990).
9. A. Boushoule, A. Plain, L. Boufendi, *et al.*, J. Appl. Phys. **70**, 1991 (1991).
10. A. Gasgarden, B. N. Ganguly, P. D. Haaland, and J. Williams, Plasma Sources Sci. Technol. **3**, 329 (1994).
11. L. Boufendi and A. Boushoule, Plasma Sources Sci. Technol. **3**, 262 (1994).
12. V. N. Tsytovich and J. Winter, Usp. Fiz. Nauk **168**, 899 (1998) [Phys. Usp. **41**, 815 (1998)].
13. J. J. Bollinger, D. J. Wineland, and D. H. Dubin, Phys. Plasmas **1**, 1403 (1994).
14. H. Ikezi, Phys. Fluids **29**, 1764 (1986).
15. S. Hamaguchi and R. T. Faruoki, J. Chem. Phys. **101**, 9876 (1994); J. Chem. Phys. **101**, 9885 (1994).
16. Ya. L. Al'pert, A. V. Gurevich, and L. P. Pitaevskiĭ, *Satellites in a Rarefied Plasma* (Nauka, Moscow, 1964); J. Lafranbose and L. Parker, Phys. Fluids **16**, 629 (1973).
17. V. Tsytovich, U. de Angelis, and R. Bingham, J. Plasma Phys. **42**, 429 (1989).
18. I. B. Bernstein and I. N. Rabinovich, Phys. Fluids **2**, 112 (1959).
19. L. P. Pitaevskiĭ, Zh. Éksp. Teor. Fiz. **43**, 27 (1963) [Sov. Phys. JETP **16**, 40 (1963)].
20. J. E. Allen, Phys. Scr. **45**, 447 (1992).
21. J. E. Allen, Plasma Sources Sci. Technol. **4**, 234 (1995).
22. J. E. Allen, B. M. Annaratone, and U. de Angelis, J. Plasma Phys. **63**, 299 (2000).
23. Ciu. Chunshi and J. Goree, IEEE Trans. Plasma Sci. **22**, 151 (1994); J. Goree, Sci. Technol. **3**, 400 (1994).
24. N. Matsuokas and M. Russel, J. Appl. Phys. **77**, 4285 (1995).
25. A. G. Sitenko, A. G. Zagorodny, and V. N. Tsytovich, AIP Conf. Proc. **345**, 311 (1995).
26. V. N. Tsytovich, *Lectures on Nonlinear Plasma Kinetics* (Springer-Verlag, New York, 1995).
27. V. N. Tsytovich and U. de Angelis, Phys. Plasmas **9** (2002) (in press).
28. T. K. Aslaksen, J. Plasma Phys. **54**, 373 (1995).
29. V. N. Tsytovich and U. de Angelis, Phys. Plasmas **6**, 1093 (2000); Phys. Plasmas **7**, 554 (2002).
30. P. Ricci, G. Lapenta, U. de Angelis, and V. N. Tsytovich, Phys. Plasmas **8**, 769 (2001).
31. V. N. Tsytovich, Fiz. Plazmy **26**, 712 (2000) [Plasma Phys. Rep. **26**, 668 (2000)].
32. M. Barnes, J. Keller, J. Forster, *et al.*, Phys. Rev. Lett. **68**, 313 (1992).
33. N. Kilgore, J. Daugherty, R. Porteous, and D. Graves, J. Appl. Phys. **73**, 7195 (1993).
34. V. N. Tsytovich, S. V. Vladimirov, G. E. Morfill, and J. Goree, Phys. Rev. E **63**, 056609 (2001).
35. V. N. Tsytovich, Phys. Scr. **89**, 89 (2001).
36. G. Morfill and V. N. Tsytovich, Phys. Plasmas **7**, 235 (2001).
37. D. Samsonov and J. Goree, Phys. Rev. E **59**, 1047 (1999).
38. H. M. Thomas, D. D. Goldbeck, T. Hagi, *et al.*, Phys. Scr. **89**, 16 (2001); G. Morfill, U. Thomas, U. Konopka, and M. Zusic, Phys. Plasmas **6**, 1769 (1999).
39. J. Goree, G. E. Morfill, V. N. Tsytovich, and S. V. Vladimirov, Phys. Rev. E **59**, 7055 (1999).
40. A. Nefedov, G. Morfill, V. Fortov, *et al.*, Phys. Rev. Lett. (2002) (in press).
41. R. Talbot, J. Cheng, D. Schefer, and A. Willis, Fluid Mech. **101**, 737 (1980).
42. O. Havnes, T. Nitter, V. N. Tsytovich, *et al.*, Plasma Sources Sci. Technol. **3**, 448 (1994).
43. H. Rotharnmel, H. Thomas, and M. Zusic, Phys. Rev. Lett. (in press).
44. D. A. Law, W. N. Steel, B. M. Annaratone, and J. E. Allen, in *Proceedings of the XXIII International Conference on Phenomena in Ionized Gases, Toulose, 1997*, Vol. 1, p. 192; E. B. Tomme, B. M. Annaratone, and J. E. Allen, Plasma Sources Sci. Technol. **9**, 87 (2000).
45. L. D. Landau and E. M. Lifshitz, *Course of Theoretical Physics*, Vol. 5: *Statistical Physics* (Nauka, Moscow, 1976; Pergamon Press, Oxford, 1980).
46. V. N. Tsytovich, Comm. Plasma Phys. Controlled Fusion **15**, 349 (1994).
47. S. Hamaguchi, Comm. Plasma Phys. Controlled Fusion **17**, 311 (1999).
48. V. Tsytovich and S. Vladimirov, Comm. Modern Phys. E **2**, 17 (2001).
49. L. D. Landau and E. M. Lifshchits, *Electrodynamics of Continuous Media* (Nauka, Moscow, 1970; Pergamon Press, New York, 1984).
50. Ya. L. Khodataev, R. Bingham, V. P. Tarakanov, and V. N. Tsytovich, Fiz. Plazmy **22**, 1028 (1996) [Plasma Phys. Rep. **22**, 932 (1996)].
51. V. N. Tsytovich, Y. Khodataev, and R. Bingham, Comm. Plasma Phys. Controlled Fusion **17**, 249 (1996).
52. A. M. Ignatov, Kratk. Soobshch. Fiz. FIAN, Nos. 1–2, 58 (1995).
53. Ya. K. Khodataev, G. Morfill, and V. N. Tsytovich, J. Plasma Phys. **65**, 257 (2001).

54. M. Lampe, M. Joyce, and G. Ganguli, Phys. Scr. **89**, 106 (2001); M. Lampe, M. Gavrishchaka, V. Ganguli, and G. Joyce, Phys. Rev. Lett. **86**, 5278 (2001).
55. I. Lin, Lai Yin-Ju, Juan Wen-Tau, Chen Ming-Heng, in *Proceedings of the 2nd Internatoinal Conference on Physics of Dusty Plasmas, Hakone (Japan), 1999*, p. 75.
56. A. Meltzer, V. A. Schweigert, and A. Piel, in *Proceedings of the 2nd Internatoinal Conference on Physics of Dusty Plasmas, Hakone (Japan), 1999*, p. 115.
57. Sh. Amiranashvili, N. Gusein-zade, and V. Tsytovich, Phys. Rev. E **64**, 016407 (2001).
58. R. Bingham, V. N. Tsytovich, V. P. Tarakanov, and Ya. K. Khodataev, IEEE Trans. Plasma Sci. **4**, 3 (1998).
59. V. N. Tsytovich, Ya. K. Khodataev, G. E. Morfill, *et al.*, Comm. Plasma Phys. Controlled Fusion **8**, 281 (1998).
60. R. Bingham and V. N. Tsytovich, IEEE Trans. Plasma Sci. **29**, 158 (2001).
61. J. Winter, Plasma Phys. Controlled Fusion **40**, 1201 (1998).
62. J. Winter, Phys. Plasmas **7**, 3862 (2000).
63. R. Bingham and V. N. Tsytovich, Astron. Astrophys. Lett. **376**, 43 (2001).
64. V. N. Tsytovich and G. E. Morfill, Fiz. Plazmy **28**, 195 (2002) [Plasma Phys. Rep. **28**, 171 (2002)].
65. R. Kompaneetz and V. Tsytovich, Contib. Plasma Phys. (2002) (in press).
66. O. Ishihara and N. Sato, IEEE Trans. Plasma Sci. **29**, 179 (2001).
67. U. Konopka, D. Samsonov, A. V. Ivlev, *et al.*, Phys. Rev. E **61**, 1890 (2000).
68. U. Konopka, L. Ratke, and H. M. Thomas, Phys. Rev. Lett. **79**, 1269 (1997).
69. U. Konopka, G. E. Morfill, H. M. Thomas, and L. Ratke, AIP Conf. Proc. **446**, 53 (1998).
70. U. Konopka, G. E. Morfill, and L. Ratke, Phys. Rev. Lett. **84**, 891 (2000).
71. A. V. Ivlev, U. Konopka, and G. E. Morfill, Phys. Rev. E **62**, 2739 (2000).

Plasma Physics Reports, Vol. 29, No. 1, 2003, pp. 31–41. Translated from Fizika Plazmy, Vol. 29, No. 1, 2003, pp. 37–48.

DUSTY PLASMA

Dynamics of Dust Grains in a Two-Component Dusty Plasma Induced by Solar Radiation under Microgravity Conditions

A. P. Nefedov†, O. S. Vaulina, O. F. Petrov, V. E. Fortov, I. E. Dranzhevskiĭ, and A. M. Lipaev

Institute for High Energy Densities, Russian Academy of Sciences, Izhorskaya ul. 13/19, Moscow, 127412 Russia

Received April 29, 2002

Abstract—Results are presented from experimental studies of the dynamics of dust grains charged via photoemission under microgravity conditions. The experiments are performed with bronze grains exposed to solar radiation on board the *Mir* space station. The velocity distribution, temperature, mean charge, and friction and diffusion coefficients of dust grains are determined. An analysis of the data obtained shows that the polarization caused by the separation of opposite charges can significantly affect the transport processes in a two-component dusty plasma consisting of dust grains and the electrons emitted by them. © *2003 MAIK "Nauka/Interperiodica".*

1. INTRODUCTION

The dusty plasma is an ionized gas containing micron-sized charged condensed grains (dust). The combined action of the interaction between dust grains and dissipative processes in a dusty plasma can lead to the formation of both steady-state dusty structures (similar to fluid or solid) and complex vibrational or dynamic configurations associated with large-scale transport processes [1–10].

Plasma–dust structures play an important role in the processes occurring in the upper atmosphere, where the main ionization agents are cosmic rays and solar radiation [11–13]. Under these conditions, the charging of atmospheric aerosols is governed by the two competing processes: the absorption of the atmospheric ions and electrons by grains and the emission of electrons from the grain surface. Under the action of intense solar radiation, the grains are mainly charged via photoemission. Micron-size grains can acquire a positive charge of 10^2–10^5 elementary charges, which can result in the formation of ordered structures [6, 14]. Moreover, the emission processes make it possible for two-component system consisting of positively charged grains and the electrons emitted by them to exist.

Recently, experimental studies of dusty plasmas under microgravity conditions have attracted great attention [6–10]. These experiments allow one to investigate various phenomena (such as the charging of atmospheric aerosols and the dynamics of large dust grains ~100 μm in size) that cannot be studied on Earth [6–8]. In recent experiments performed by the Russian–German scientific team on board the International Space Station, a number of new phenomena (dust beating, the formation of complex lattices, the opposite-sign charging of dust grains, etc.) were observed in RF-discharge dusty plasmas [10]. Note that analogous phenomena cannot be observed under ordinary laboratory conditions.

The main process responsible for dust mass transfer is diffusion, which determines the dynamic characteristics of dust systems (such as the phase state, wave propagation conditions, and instabilities) and governs the energy losses (dissipation) in them. Both the dust grains suspended in the buffer gas and the gas molecules or charged plasma particles can undergo diffusion (Brownian motion and self-diffusion, respectively). The transport properties of a plasma–dust cloud consisting of charged dust grains, ions, and electrons can be significantly affected by the concurrent diffusion of the oppositely charged particles (ambipolar diffusion). A simple case of ambipolar diffusion in the absence of a magnetic field was investigated by W. Schottky (1924). However, direct experimental observations of this phenomenon without attendant processes, like ionization or eddy currents under the Earth's gravity conditions, are still lacking. The first results on the polarization effects related to the separation of opposite charges in a two-component system consisting of dust grains and photoelectrons under microgravity conditions are presented in [7, 8].

Most experimental methods for determining the diffusion coefficients of ions and electrons are based on indirect measurements of the particle mobilities in an external electric field [15]. However, these methods introduce significant perturbations in the system under study and hence are inappropriate for diagnosing particles in a plasma. In order to determine the transport properties of dust grains, spectroscopy and photon correlation methods are traditionally used. The range of

† Deceased.

1063-780X/03/2901-0031$24.00 © 2003 MAIK "Nauka/Interperiodica"

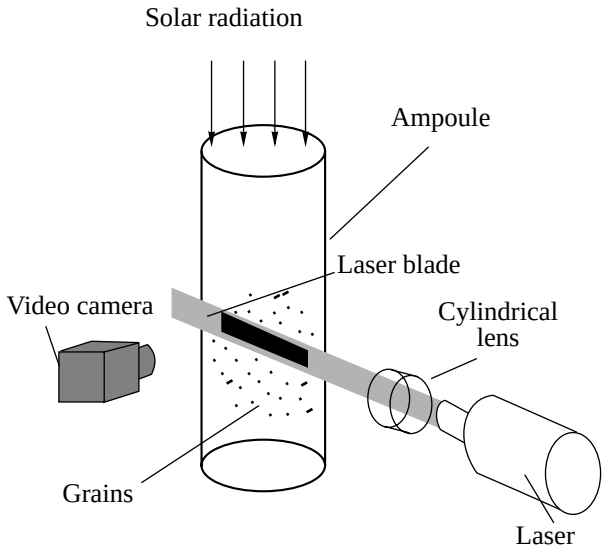

Fig. 1. Schematic of the experimental facility.

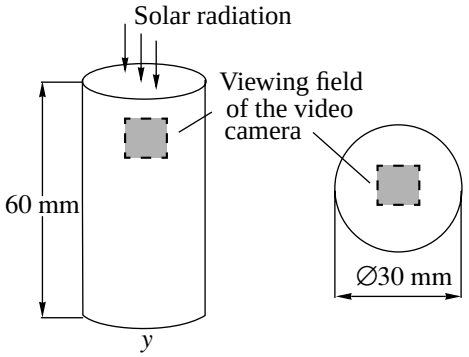

Fig. 2. Working ampoule.

applicability of these methods is limited by the short-range ordering related to the interaction between grains [16]. The methods rely on different hydrodynamic models; thus, the main problem is determining the conditions under which these models are applicable.

Dusty plasma is a good object for experimentally studying transport phenomena in a system of interacting particles because dust grains can be shot with a video camera, which greatly simplifies the use of perturbative and nonperturbative diagnostics. A weakly ionized dusty plasma can be regarded as a dissipative system of grains with the Yukawa interaction potential $\varphi = eZ_d\exp(-l/\lambda)/l$, where eZ_d is the dust grain charge, λ is the screening length, and l is the intergrain distance. In such systems, the correlation between grains is governed by the dimensionless coupling parameter $\Gamma_n = (1 + \kappa + \kappa^2/2)\exp(-\kappa)\Gamma$, where $\Gamma = (eZ)^2 n_d^{1/3}/T_d$, T_d is the kinetic temperature of the grains in energy units, n_d is their number density, and $\kappa = n_d^{-1/3}/\lambda$. Numerical simulations show that at $\Gamma_n > 1$, short-range ordering arises in Yukawa systems, the critical value of the coupling parameter Γ_n at the melting point being close to 106 [17, 18].

In this paper, we report the results of the first experiments on the grain dynamics in a dusty plasma induced by solar radiation under microgravity conditions. The experiments were performed on board the *Mir* space station. The photoemission charge, velocity distribution, and friction and diffusion coefficients of dust grains, as well as the coupling parameter of the dust system, are determined. The polarization effects related to the separation of opposite charges in a two-component system consisting of positively charged dust grains and the electrons emitted by them are observed. The experiments were briefly described in [7, 8]. Most of the results reported here are being published for the first time.

2. EXPERIMENTAL SETUP

A schematic of the experimental facility is shown in Fig. 1. The main component of the working chamber was a glass ampoule with bronze grains (with a specific mass density of 8.2 g/cm^3 and diameters of 50–100 μm, the average radius being a_d = 37.5 μm) covered with a cesium monolayer (with a work function of W = 1.5 eV). The grains resided in a buffer gas (neon) at a pressure of P = 40 torr. The ampoule was a cylinder, one end of which was a flat uviol window for illuminating the grains with solar radiation (Fig. 2). The grains in the ampoule were additionally illuminated with a ribbon laser beam ("laser blade") with a thickness of ~500 μm. For this purpose, a 0.67-μm semiconductor laser was used. The image recorded with a CCD video camera was stored on a magnetic tape (with a frame frequency of 25 s^{-1}). The viewing field of the camera was a rectangle 8×9 mm in size. The camera was focused on the ampoule center. The depth of focus (at a chosen iris value of 16) was ~9 mm (Fig. 2). The video recording was treated with a special computer code enabling the identification of the displacements of the individual grains that reside in the viewing field of the video camera. Under intense solar radiation, the number of the observed grains was determined by the depth of focus of the video system, which allowed one to monitor the grain positions during the time $t > 5\nu_{fr}^{-1}$ (where ν_{fr} is the friction coefficient, determined by the collision frequency of the dust grains with the buffer gas molecules), long enough to analyze the transport properties of the system. The number of the identified grains was less than 40% of the total number of grains initially recorded with the video camera.

3. EXPERIMENT

At the first stage of the experiment, the grain behavior under microgravity conditions in the absence of solar radiation (dark regime) was investigated. The aim of the experiment was to evaluate the characteristic time it takes for the grains to lose the velocity acquired with the initial shaking of the ampoule. Since direct measurements of the damping rate of the initial perturbations in the narrow cross section of the laser beam were unfeasible, the grain dynamics was analyzed by measuring the dependence of the grain number density n_d (determined by the number of grains inside the laser blade) on time t. These measurements showed that 2–4 s after shaking the ampoule, the grain density n_d sharply decreased from ~10^3 to ~250–350 cm^{-3}. One can assume that the fast loss of grains is related to their deposition onto the ampoule wall due to the high adhesion coefficient. Then, for time ~20 min, the number of grains in the viewing field of the video camera changed only slightly ($n_d \approx$ const).

At the second stage of the experiment, the shaken ampoule was exposed to solar radiation. During the first 10 s, the grain density remained almost equal to the initial density $n_d^0 = n_d(0) \sim 900$ cm^{-3}. The time it took for the grains to depart to the ampoule wall was ~5 min. Comparing with the dark regime, it is reasonable to assume that the electric field arising due to the irradiation of the system somehow impedes the grain adhesion on the ampoule wall. The time behavior of the grain velocity V after the dynamic action on the system is shown in Fig. 3 for different regions of the viewing field. It can be seen that over the time $t \approx$ 5–10 s after the dynamic action, the grains are involved in the vibrational motion with a frequency $\omega \sim 4.5$–5.2 s^{-1} (a period of ~1.2–1.4 s) against the background of their translational motion toward the wall.

At the third stage of the experiment, the dynamics of grains under the action of solar radiation was investigated. Initially, the bronze grains resided on the ampoule wall; hence, the experiments were carried out as follows: (i) dynamic action (kick) upon the system at the closed porthole curtain; (ii) aging in darkness for the time $t \approx 4$ s $\gg \nu_{fr}^{-1}$ in order to reduce the grain velocities acquired with the initial kick; (iii) exposure to solar radiation; and (iv) the relaxation of grains to the initial state (return to the wall), after which the porthole curtain was closed again. This procedure was repeated several times. The kinetic temperature and the degree of correlation of the dust grains increased for the first 3–5 s after the beginning of solar illumination. The pair correlation functions for the illuminated dust cloud obtained by exclusion of the intergrain distances shorter than $l_d/2$ (where $l_d = n_d^{-1/3}$) are shown in Fig. 4. Although these functions cannot be used for the quantitative analysis of the degree of grain correlation in a dusty structure, they reflect the qualitative changes in the system under study.

At the initial stage of illumination, the grain velocities are randomly directed. 1–3 s after the beginning of illumination, the grain motion evidently develops into ordered motion toward the ampoule wall. The time of the grain migration to the ampoule wall is 3–4 min, which is nearly five orders of magnitude shorter than the characteristic time of the total diffusion losses due to Brownian motion at room temperature. The grain parameters measured at the instant ~5 s after the beginning of illumination are shown in Figs. 5–9. Figure 5 shows the trajectories of 40 grains, and Fig. 6 demonstrates the time behavior of the relative grain density $n_d(t)/n_d^0$. The initial grain density n_d^0 varied in the range 195–300 cm^{-3}, which corresponded to the results obtained at the first stage of the experiment. The spatial distributions of the drift and thermal grain velocities, the velocity distributions of dust grains, and the self-diffusion coefficients during the first 10–15 s of the experiment are shown in Figs. 7–9. An analysis of the experimental results is presented in the next section; it is mainly based on the data from the third stage of experiments, which were repeated several times and demonstrate the necessary repeatability.

4. DISCUSSION OF THE MEASUREMENT RESULTS

4.1. Temperature and Velocity Distribution of Dust Grains

Irregular variations in the magnitude and direction of the velocities of individual grains against the background of their general drift motion (Fig. 5) can be associated with the grain kinetic temperature, which in the case of a Maxwellian distribution over the velocities V_x and V_y can be expressed as

$$T_{x(y)} = m_d(\langle V_{x(y)}^2\rangle - \langle V_{x(y)}\rangle^2), \quad (1)$$

where the angular brackets stand for averaging over the ensemble and time. During the first 10–15 s, the spatial distributions of the mean (drift) velocities $\langle V_{x(y)}\rangle$ of dust grains toward the ampoule wall and the thermal velocities $V_{x(y)}^T = (\langle V_{x(y)}^2\rangle - \langle V_{x(y)}\rangle^2)^{1/2}$ changed only slightly (Fig. 7). The recorded grain distributions over the V_x and V_y velocity components turned out to be close to Maxwellian with the temperatures calculated by formula (1) (Fig. 8). At n_d^0 = 195–300 cm^{-3}, the temperatures obtained by formula (1) for different regions of the ampoule are $T_x \simeq (51 \pm 5)$ eV and $T_y \simeq (22 \pm 2)$ eV; i.e., they are much higher than room temperature ($T \simeq$ 0.03 eV). We note that the kinetic energy of random grain motion in plasma can be nonuniformly distributed over the degrees of freedom (i.e., Maxwellian distributions with $T_x \neq T_y$ can occur) and the kinetic grain tem-

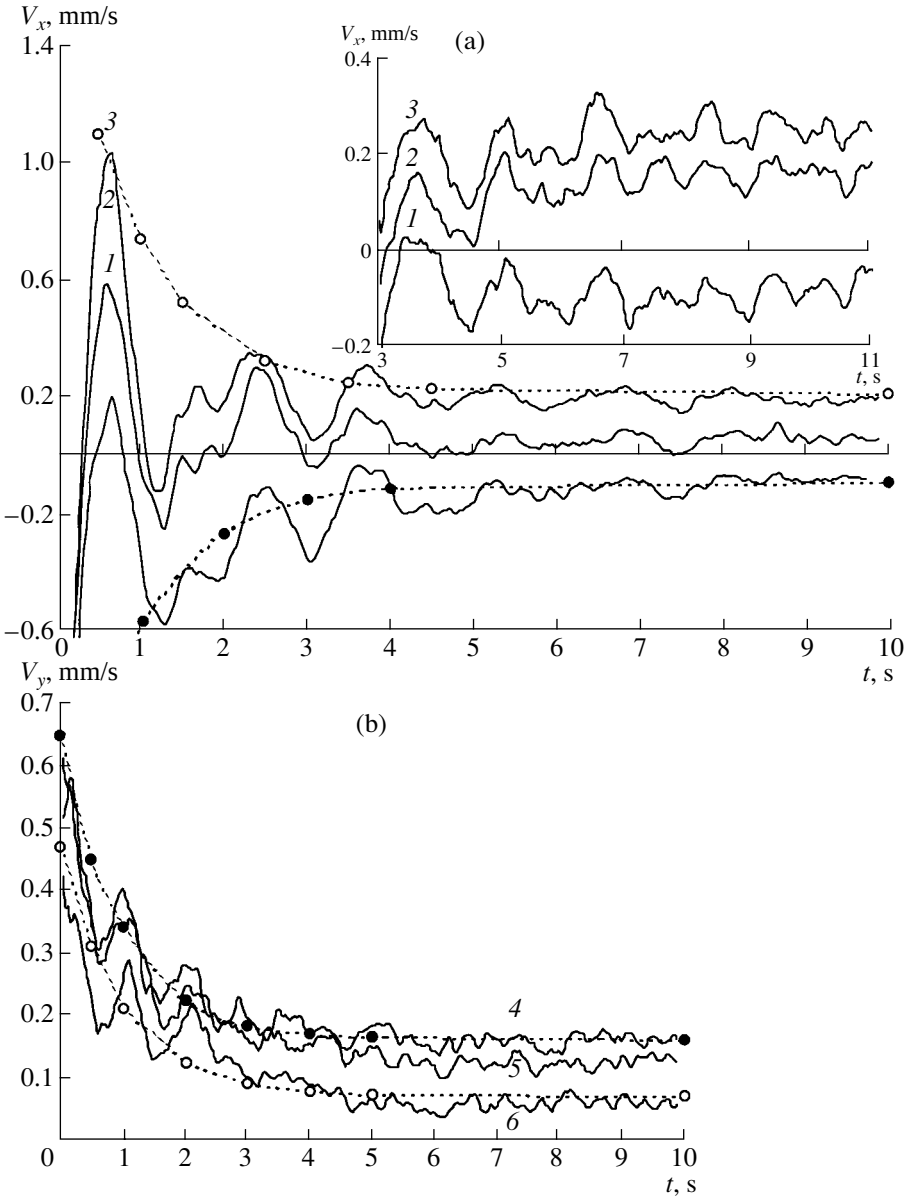

Fig. 3. Grain velocities V_x and V_y along the (a) x-axis and (b) y-axis vs. time for different viewing-field sections: x = (*1*) 0–1, (*2*) 4–5, and (*3*) 7–8 mm at y = 0–8 mm and y = (*4*) 0–1, (*5*) 1–2, and (*6*) 6–7 mm at x = 0–9 mm. The dashed line shows the approximation $V(t) = V(0)\exp(-t/\tau_{Maxw})$, where $\tau_{Maxw} = 1$ s.

perature can substantially exceed the temperature of the surrounding gas. These effects can be related, for example, to the grain charge fluctuations or the spatial inhomogeneity of the plasma–dust system [3, 5, 19, 20]. The anomalous heating of grains was repeatedly observed in experiments on dusty structures in laboratory plasmas [3, 20–22].

4.2. Friction and Self-Diffusion Coefficients of Dust Grains

In the system under study, the grains reside in a viscous medium; hence, dissipation due to collisions with the buffer gas neutrals significantly affects the grain motion. At room temperature, the mean free path of neon atoms is determined by the relationship $l_n[\mu m] \approx 50/P[\text{torr}]$ [15] and, under the given experimental conditions (P = 40 torr), it is $l_n \approx 1.25$ μm, which is much less than the minimum radius of the bronze grains a_d (25 μm). In this case ($a_d \gg l_n$), the friction coefficient ν_{fr} for a round grain in the Stokes approximation [23] can be written as

$$\nu_{fr} = 6\pi\eta a_d/m_d \equiv 4.5\eta(\rho a_d^2)^{-1}, \qquad (2)$$

where ρ is the specific mass density of the grain material and $\eta \approx 10^{-4}$ g/(cm s) is the neon viscosity at room

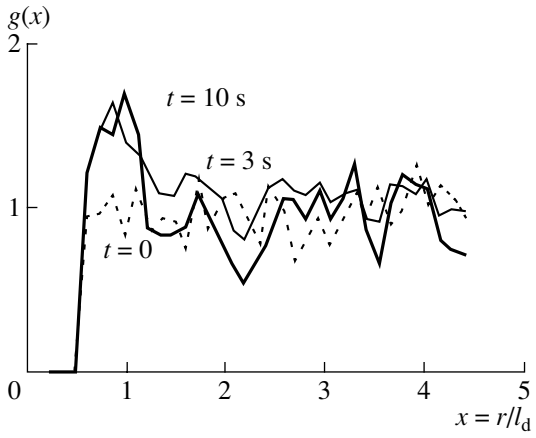

Fig. 4. Pair correlation functions $g(x = r/l_d)$ for an illuminated dust cloud at different times t.

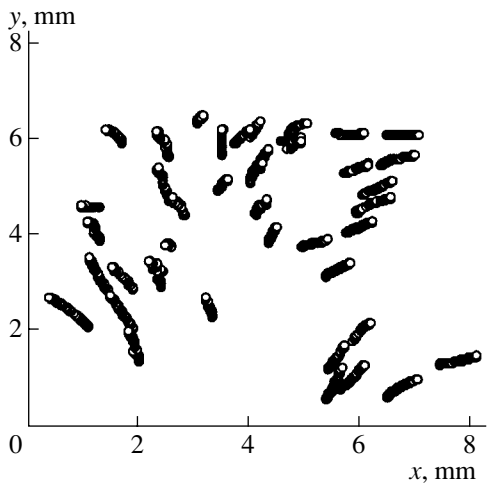

Fig. 5. Grain trajectories after irradiation.

temperature. Thus, for bronze grains with the radius $a_d = 37.5$ μm, we have $\nu_{fr} \approx 4$ s^{-1}.

The diffusion coefficient of the noninteracting (Brownian) grains can be calculated by the measured grain temperature as

$$D_0^{x(y)} = T_d^{x(y)}/\nu_{fr} m_d. \quad (3)$$

Then, for $\nu_{fr} = 4$ s^{-1}, $T_x \simeq 51$ eV, and $T_y \simeq 22$ eV, we have $D_0^x \simeq 10^{-5}$ cm^2/s and $D_0^y \simeq 4.4 \times 10^{-6}$ cm^2/s.

The grain self-diffusion coefficients $D_d^{x(y)}$ can be directly determined from the experimental data, taking into account the regular grain drift velocities $\langle V_{x(y)} \rangle$ (see Section 4.1):

$$D_d^{x(y)}(t) = [\langle \Delta r(t)^2 \rangle - (\langle V_{x(y)} \rangle t)^2]/2t, \quad (4)$$

where $\langle \Delta r(t)^2 \rangle$ is the mean square displacement of an individual grain along either the x- or y-axis. When the interaction between grains is negligible, the self-diffusion coefficient $D_d^{x(y)}$ at $t \longrightarrow \infty$ should obey Einstein relation (3); i.e., $D_d^{x(y)}(t \longrightarrow \infty) = D_0^{x(y)}$. Figure 9 illustrates the dependences $D_d^{x(y)}(t)$ measured in some regions of the ampoule and the results of averaging these dependences over all the experiments. At $t = 4$ s, the measured $D_d^{x(y)}(t)$ values are equal to $D_d^x \approx 1.3 \times 10^{-5}$ cm^2/s and $D_d^y \simeq 5.7 \times 10^{-6}$ cm^2/s; i.e., they are higher than those obtained by formula (3) by ~30%. We note that the value $\nu_{fr} \approx 4$ s^{-1}, obtained for the grain mean radius $a_d = 37.5$ μm, may not correspond to the effective friction coefficient for a polydisperse dusty system. We also note that in the preliminary dark regime, the probability of a grain departing to the wall is higher for smaller and, hence, more mobile grains (i.e., grains with relatively small values of $\nu_{fr} m_d$).

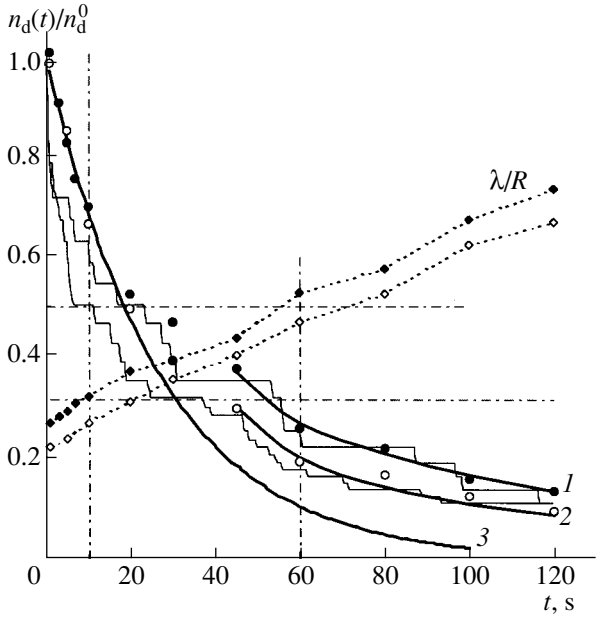

Fig. 6. Measured time dependences of the relative density n_d/n_d^0 for $n_d^0 = 195$ and 300 cm^{-3} (closed and open circles, respectively). The light curves show the calculations by method of molecular dynamics, curves *1* and *2* correspond to approximation (15), and curve *3* shows the function $n_d/n_d^0 = \exp(-\nu_{dif} t)$. Closed and open diamonds show the time behavior of λ/R for $n_d^0 = 195$ and 300 cm^{-3}, respectively.

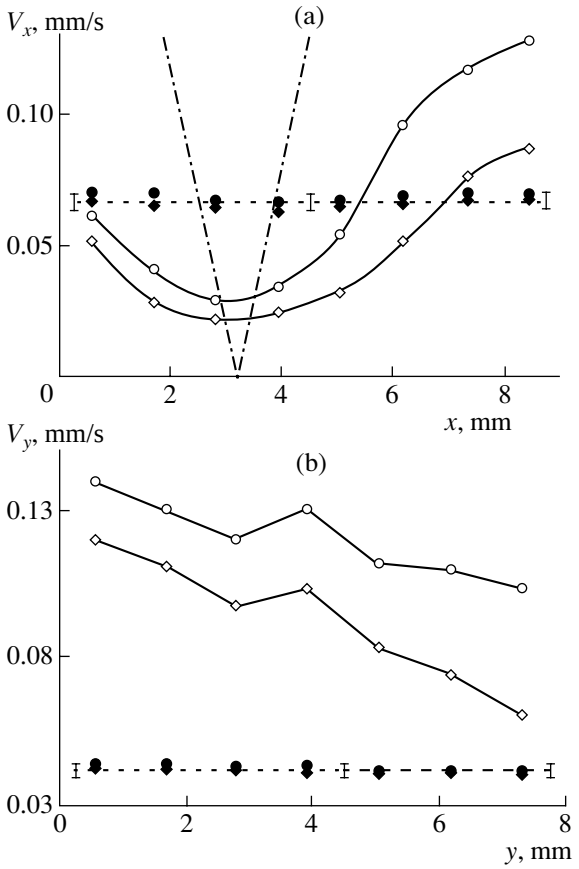

Fig.7. Spatial distributions of the drift velocity $\langle V \rangle$ (open diamonds and circles) and thermal velocity V^T (closed diamonds and circles) of dust grains over the (a) x- and (b) y-axes for n_d^0 = 195 and 300 cm^{-3} (diamonds and circles, respectively). The dashed-and-dotted line shows the minimum radial grain velocity for a dust cloud transparent to the emitted electrons.

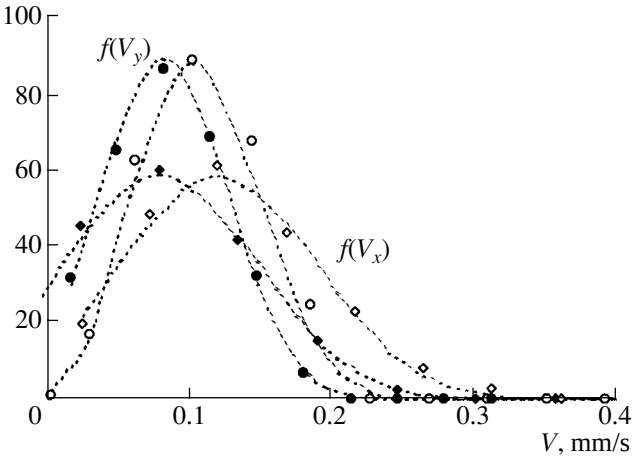

Fig. 8. Grain distributions over the V_x velocity component (diamonds) in the region (x = 7–8 mm, y = 0–8 mm) and the V_y velocity component (circles) in the region (y = 5–6 mm, x = 0–9 mm) for n_d^0 = 300 and 195 cm^{-3} (open and closed symbols, respectively). The dashed lines show the approximation of the experimental data by Maxwellian distributions with temperatures $T_x \simeq 51$ eV and $T_y \simeq 22$ eV.

The time dependence of the self-diffusion coefficient for noninteracting grains can be represented as [18]

$$D_d^{x(y)}(t) = D_0^{x(y)}[1 - (1 - \exp(-\nu_{fr}t))/\nu_{fr}t]. \quad (5)$$

Thus, one can evaluate both the friction coefficient ν_{fr} and the diffusion coefficient $D_0^{x(y)} = D_d^{x(y)}$ ($t \longrightarrow \infty$) from the measured $D_d^{x(y)}(t)$ values. The approximation of the experimental $D_d^{x(y)}(t)$ dependences by formula (5) for $T_x \simeq 51$ eV and $T_y \simeq 22$ eV (Fig. 9) gives the friction coefficient $\nu_{fr} \simeq 3.1$ s^{-1} and the diffusion coefficients $D_0^x \simeq 1.4 \times 10^{-5}$ cm^2/s and $D_0^y \simeq 6.2 \times 10^{-6}$ cm^2/s. It can be easily seen that the measured behavior of $D_d^{x(y)}(t)$ is in good agreement with formula (5) for noninteracting (Brownian) grains. Note that for grains in strongly correlated dusty systems (Γ_n > 40–50), the time dependence of the self-diffusion coefficient D_d is nonmonotonic; in contrast to the experimental data shown in Fig. 9, it has a pronounced maximum [18].

4.3. Grain Charge

Photoemission charging plays an important role when irradiating grains with photons with energy $h\nu$ exceeding the photoelectron work function from the grain surface. The number of the emitted electrons (photocurrent) is proportional to the intensity of the incident radiation. The maximum kinetic energy of photoelectrons $K_{max} = h\nu - W$ increases linearly with the incident radiation frequency ν and does not depend on the radiation intensity. Thus, the maximum photoemission grain charge Z_{max} can be found by equating the surface potential $\phi_s = eZ_{max}/a_d$ to the quantity K_{max}/e [14]:

$$Z_{max} = (h\nu_{max} - W)a_d/e^2, \quad (6)$$

where $h\nu_{max}$ is the maximum photon energy, which, in our case, is determined by the transmission coefficient of the experimental chamber and corresponds to the wavelength $\lambda_{min} \simeq 0.35$ μm [11]. Thus, for a_d = 37.5 μm, we have $Z_{max} \approx 53000$. Generally, the photoelectron flux depends on the radiation source properties, the efficiency of radiation absorption Q, and the quantum yield Y and temperature T_{pe} of the emitted electrons. Moreover, the grain charge is affected by the thermoemission properties of grains and the presence

of photoelectrons that return back to the grain surface. The latter circumstance can significantly decrease the equilibrium grain charge Z_d as compared to its limiting value Z_{max} [14].

Let us evaluate the charge of bronze grains exposed to solar radiation. To calculate the photon flux J, the solar radiation can be considered blackbody radiation with the temperature T_c = 5800 K [13]:

$$J = \int_{\lambda_{min}}^{\lambda_0} f_{tr} c_1 \lambda^{-4} / [\{\exp(c_2/\lambda T_c) - 1\} hc] d\lambda, \quad (7)$$

where $f_{tr} \approx 0.85$ is the transmission coefficient of the experimental chamber, λ_{min} = 0.35 μm, and λ_0 is the boundary wavelength for the photoeffect. Thus, we have $J \approx 3.4 \times 10^{17}$ photon/(s cm^2). Since the photons with energies of ≤4 eV are incapable of ionizing the buffer gas, the positive grain potential will be determined by the balance between the electron recombination on the grain surface and the flux of the emitted photoelectrons. Assuming that the system is opaque to the emitted electrons, their density n_e in a dust cloud will obey the quasineutrality condition $n_e = Z_d n_d$. When the electron mean free path l_{ne} in collisions with neutrals is comparable with or exceeds the grain radius a_d ($l_{ne} > a_d$), the electron balance equation can be written in the form [24, 25]

$$Z_d n_d \left(\frac{8T_e}{\pi m_e}\right)^{1/2} = JY \exp\left(\frac{h\nu - W - e\phi_s}{T_{pe}}\right)$$
$$\approx JY^* \frac{T_{pe}}{h\nu_{max} - W} \exp\left(\frac{h\nu_{max} - W - e\phi_s}{T_{pe}}\right), \quad (8)$$

where m_e is the electron mass, T_e is the plasma electron temperature, and Y^* is the mean quantum yield of cesium-covered bronze in the spectral range under study. The temperature T_{pe} of the photoemission electrons depends on the grain material and, in most cases, lies in the range 1–2 eV [12, 13]. Then, under the assumption $T_e \approx T_{pe}$ = 1.5 eV, we obtain from Eq. (8) that for the grain radius a_d = 37.5 μm, the limiting charge $Z_{max} \approx 53000$ is attained at the densities $n_d \approx$ 400–2000 cm^{-3} (which corresponds to $Y^* \approx (0.8–4) \times 10^{-2}$). Thus, at n_d < 400 cm^{-3}, the electrons returning to the grain surface will not significantly affect the equilibrium grain charge. The higher n_d, the lower the equilibrium charge; thus, at $n_d \approx$ 900 cm^{-3} ($Y^* \approx 8 \times 10^{-3}$), we have $Z_d \approx 40000$.

The electron temperature in the system under study may be different from the temperature T_{pe} of the photoelectrons leaving the grain surface. Thus, in the absence of an electric field, the characteristic time of the electron energy relaxation (the time during which the electron energy falls by a factor of ~2.7) is determined as

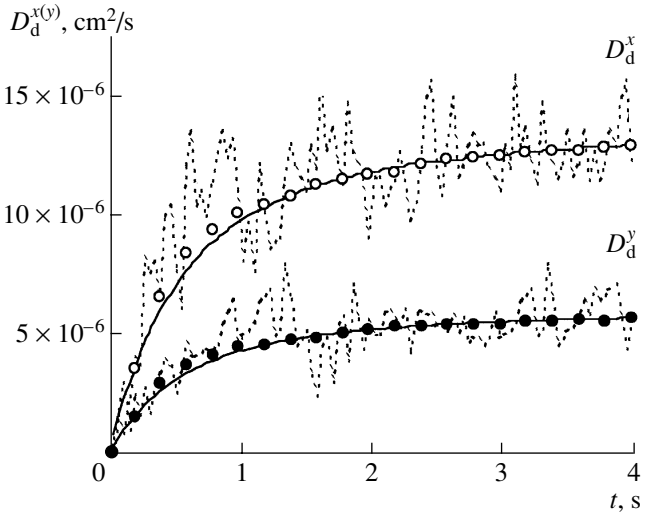

Fig. 9. Time dependences of the diffusion coefficients D_d^x and D_d^y (dashed curves) measured in one experiment in the regions (x = 7–8 mm, y = 0–8 mm) and (y = 5–6 mm, x = 0–9 mm), respectively, and the values of $D_d^{x(y)}$ averaged over several experiments (circles) and their fits by formula (7) (solid curves).

$\tau_u \approx \tau\delta^{-1}$ (where $\tau = \nu_{ne}^{-1}$, ν_{ne} is the electron–neutral collision frequency, and δ^{-1} is the number of effective collisions for electron–neutral energy transfer) and the effective relaxation length is $\Lambda_u \approx l_{ne}\delta^{-1/2}$ [15]. For neon, $\delta \approx 10^{-4}$ and the relaxation length is Λ_u[cm] ≈ 12/P[torr]. At the given pressure, this length is ~0.3 cm; i.e., it is longer than the mean distance l_d ~ 0.15–0.18 cm between the dust grains, which are the sources of background electrons. Hence, the emitted electrons loose about 30% of their initial energy over a distance of ~l_d/2. Such an insignificant energy loss can readily be balanced by the stochastic energy input due to the presence of electric fields in the system [15].

The electron energy loss can be estimated by comparing the electron–neutral thermal equilibration rate $\nu_E \approx (V_e/l_{ne})m_e/m_n$ with the electron–dust grain collision rate $\nu_{ed} \approx 2\pi a_d^2 n_d V_e$ (at $e\phi_s \approx T_e$), where V_e is the electron velocity [14]. If $\nu_{ed} \gg \nu_E$ (i.e., $2\pi a_d^2 n_d l_{ne} m_n/m_e \gg 1$), then the rate of electron recombination at the grains is much higher than the rate of thermal losses due to electron–neutral collisions; consequently, the electron temperature T_e in the system should be equal to the temperature T_{pe} of the emitted electrons. For neon, we have $m_e/m_n \approx 2.7 \times 10^{-5}$ and $l_{ne} \approx 30$ μm (at P = 40 torr); hence, for a_d = 37.5 μm and n_d > 200 cm^{-3}, we obtain $\nu_{ed}/\nu_E > 2$. It should also be taken into account that for the electrons with energies T_e = 0.5–2 eV, the electron mean free path is 2–4 times longer than the table value

l_e[cm] ≈ 0.12/P[torr], which is commonly used for theoretical estimates. This is because at energies of ~1 eV, the cross section for the electron–neutral collisions in neon has a pronounced minimum (Ramsauer effect) [15]. Accordingly, in further calculations, we assume that $T_{pe} \simeq T_e$.

The theoretical estimates of Z_d by formulas (6) and (8) can only provide the order of magnitude of the photoemission charge acquired by a grain because they strongly depend on the accuracy with which the grain parameters and the spectrum of inducing radiation are determined; in turn, this accuracy depends on the specific experimental conditions. To measure the charges of individual grains moving with velocity V in the known electric field E, one can use the equation of motion [6]

$$dV/dt = -\nu_{fr}V + EeZ_d/m_d. \quad (9)$$

To solve Eq. (9), one needs a priori data on the electric field E, which (as well as theoretical estimates of the grain charge) depends on the transparency of the dust cloud to the emitted photoelectrons. Let us suppose that at $t > 100$ s, all the emitted electrons have already left the dust cloud and the electric field E is equal to the field of a uniformly charged cylinder: $E \approx 2\pi eZ_d n_d x_R$, where x_R is the distance from the tube axis. In this case, estimating the grain charge from Eq. (9) with the use of the measured values of dV/dt and V for individual grains [6] gives charges ranging from $Z_d \approx 4 \times 10^4$ ($\nu_{fr} = 3$ s^{-1}) to $Z_d \approx 3 \times 10^4$ ($\nu_{fr} = 4$ s^{-1}), depending on the chosen value of the friction coefficient ν_{fr}.

In a cloud transparent to photoelectrons ($n_e = 0$), the grain charge Z_d can also be evaluated from the measured time dependence of the grain density $n_d(t)$, which characterizes the rate with which like-charged dust grains escape from the measurement volume due to electrostatic repulsion. If the electric forces acting on an individual grain from all the other grains are balanced by the friction forces, then the dependence $n_d(t)$ can be approximated by the function [6]

$$n_d(\Delta t) = n_d^{t_0}(1 + 3\omega_0^2\Delta t/\nu_{fr})^{-1}, \quad (10)$$

where $\omega_0 = eZ_d\{n_d^{t_0}/m_d\}^{1/2}$, $n_d^{t_0}$ is the dust grain density at a certain time $t = t_0$, and $\Delta t = (t - t_0)$. Approximation (10) allows one to determine ω_0 by fitting the calculated results to the experimental data; the result obtained makes it possible to find the grain charge. Figure 6 presents the results of approximating the experimental data by formula (10) under the assumption that the system becomes transparent as the grain density decreased to values lower than $n(t) = 90$ cm^{-3} ($t > 45$ s) and $n_d^{t_0} \equiv n_d$ ($t_0 = 45$ s). Hence, it follows that $3\omega_0^2/\nu_{fr} \approx 0.0023$ s^{-1} for $n_d^0 = 195$ cm^{-3} and $n_d^{t_0} = 0.37\,n_d^0$ and that $3\omega_0^2/\nu_{fr} \approx 0.0033$ s^{-1} for $n_d^0 = 300$ cm^{-3} and $n_d^{t_0} = 0.3\,n_d^0$. Therefore, the grain charge is $Z_d = (4.3 \pm 0.2) \times 10^4$ at $\nu_{fr} \approx 3$ s^{-1}. At $\nu_{fr} \approx 4$ s^{-1}, Z_d is larger by ~15%.

Figure 6 also presents the results of calculations of the dependence $n_d(t)/n_d^0$ by the method of molecular dynamics for the parameters close to the experimental ones under the assumption that the system is transparent to the emitted electrons. A set of three-dimensional equations of motion was solved for a cylindrical ampoule (Fig. 2) with allowance for the random (Langevin) force $\mathbf{F}_{br}$, assuming that the grains have zero initial velocities and are absorbed on the cylinder wall:

$$m_d\frac{d^2\mathbf{r}_k}{dt^2} = \sum_j \Phi(r)\Big|_{r=|\mathbf{r}_k-\mathbf{r}_j|}\frac{\mathbf{r}_k-\mathbf{r}_j}{|\mathbf{r}_k-\mathbf{r}_j|} - m_d\nu_{fr}\frac{d\mathbf{r}_k}{dt} + \mathbf{F}_{br}. \quad (11)$$

Here, $\Phi(r) \approx (eZ)^2/r^2$ and r is the distance between the two interacting grains. It can be easily seen that the assumption of the system transparency (Coulomb repulsion) allows one to describe the experimental data within the applicability range of formula (10) for $t > 45$ s. At $t < 20$ s, the rate at which grains escape from the measurement volume is significantly lower. This effect manifests itself in the magnitude of the recorded drift velocities of dust grains, which are lower than those expected for a transparent cloud: $V \approx 2\pi(eZ_d)^2 n_d x_R/(\nu_{fr}m_d)$ [see (9)]. The estimated minimum drift velocity $V \approx 0.1x_R$ s^{-1} for this case is shown in Fig. 7a by the dashed-and-dotted line for $Z_d = 4.3 \times 10^4$ and $n_d = 200$ cm^{-3}. This phenomenon can be related to the presence of the polarization electric field, whose magnitude is lower than the electric field in a transparent system of charged grains by a factor of ~$(\lambda/R)^2$, where λ is the electron Debye radius [15] ($\lambda^2 = T_e/4\pi e^2 n$). The possibility of polarization caused by the separation of opposite charges is determined by the requirement that the dust cloud is opaque to the emitted electrons (see the last section for details).

In a two-component system consisting of grains and electrons, the approximation of the dust cloud opacity corresponds to the quasineutrality condition

$$\delta n = |n_e - n_d| \ll n \approx n_e \approx Z_d n_d.$$

For a cylinder of radius R, this is true when [15]

$$\delta n/n \approx (\lambda/R)^2 \ll 1. \quad (12)$$

Thus, for a dust cloud in a 1.5-cm-radius tube, condition (10) is met at $n_e \approx Z_d n_d \gg (2.5\text{–}4.9) \times 10^5$ cm^{-3} (for $T_e \simeq 1$–2 eV).

The other limiting case is that where all the emitted electrons freely escape from the system ($n_e \approx 0$):

$$e\Delta\varphi \le T_e,$$

where $\Delta\varphi = \pi Z_d n_d R^2$ is the potential difference in the electric field of a uniformly charged cylinder of radius R. Hence, the criterion for the dust cloud to be transparent to photoelectrons can be obtained from the condition

$$\lambda_d/R > 0.5, \tag{13}$$

where $\lambda_d^2 = T_e/(4\pi e^2 Z_d n_d)$ is a quantity equivalent to the Debye radius squared of an opaque system. Thus, the condition that the system is transparent to the emitted electrons is determined by the parameter λ/R, where $\lambda^2 = T_e/(4\pi e^2 Z_d n_d)$ both in the case of $n_e \approx Zn_d$ (when this quantity can be associated with the screening length in a two-component system) and at $n_e \approx 0$. The experimental time dependence of λ/R is shown in Fig. 6 for the grain parameters (Z_d, n_d) measured at $T_e = 2$ eV. Here, the dashed-and-dotted lines show the margins $\lambda/R = 0.5$ and $\lambda/R = 0.33$ corresponding to the limiting cases of a transparent and an opaque dust clouds [see (12) and (13)]. It can be seen that the region $\lambda/R > 0.5$, in which the system can be assumed to be transparent ($t > 60$ s), approximately corresponds to the time domain in which the grain charges were measured by using this assumption.

4.4. Estimated Characteristic Times for Different Dynamic Regimes

The data on the grain charges and friction coefficients allow us to estimate the characteristic times and frequencies in a dusty system for different dynamic regimes. Since in our experiments $\omega_d = Z_d e(n_d/m_d)^{1/2} \ll \nu_{fr}$, the time τ_{Maxw} during which dynamic equilibrium in a system of charged grains is established is determined by [6, 15]

$$\tau_{Maxw} \simeq \nu_{fr}/4\pi\omega_d^2. \tag{14}$$

At $n_d = 195$–300 cm^{-3}, we have $\tau_{Maxw} \sim 4$–6 s, which is close to the relaxation times for the temperature and intergrain correlation observed in our experiments (see Section 4.1). The minimum value of the coupling parameter Γ_n^{min} in the state of dynamic equilibrium can be estimated by choosing the maximum temperature ($T_d \equiv T_x = 51$ eV) and minimum grain density ($n_d^0 = 195$ cm^{-3}). Since in our experiments $\kappa < 0.5$–0.7 ($T_e = 1$–2 eV), we have $\Gamma_n \equiv (1 + \kappa + \kappa^2/2)\exp(-\kappa)\Gamma \simeq \Gamma \equiv (eZ_d)^2/l_d T_d$. Consequently, at $Z_d \approx 4.3 \times 10^4$ ($\nu_{fr} = 3$ s^{-1}), we have $\Gamma_n^{min} \approx 32$.

In the experiments performed under solar irradiation (see Section 4.1, second stage of the experiment), the time τ_{Maxw} during which the dynamic equilibrium in a dusty system is established can be measured by monitoring the decay of the initial grain velocity $V(t)$ acquired with the shaking of the ampoule. This velocity should behave as $\sim\exp(-t/\tau_{Maxw})$ [15]. The approximation of the $V(t)$ dependence by the curves $V(t) = V(0)\exp(-t/\tau_{Maxw})$ at $\tau_{Maxw} \simeq 1$ s is shown in Fig. 3. The obtained value of τ_{Maxw} is in excellent agreement with a value of ~1 s, calculated by formula (14) for the measured parameters $n_d \approx 900$ cm^{-3}, $Z_d \approx 4.3 \times 10^4$, and $\nu_{fr} = 3$ s^{-1}.

We note that the high-frequency ($\omega \sim 4.5$–5.2 s^{-1}) dust grain oscillations (Fig. 3) during the relaxation to dynamic equilibrium can also be due to the polarization effects related to the separation of opposite charges. Thus, for charged particle oscillations with frequency ω and amplitude A, which is close to one-half of the characteristic spatial scale for charge separation ($2A = \lambda$), in the polarization electric field (which is proportional to $\sim T_e$), we can write $m_d(\omega\lambda/2)^2/2 \approx 4\pi e^2 Z_d^2 n_d \lambda^2 \equiv Z_d T_e$. Hence, at $n_d \approx 900$ cm^{-3} and $Z_d \approx 4.3 \times 10^4$, the oscillation frequency is $\omega = eZ_d(32\pi n_d/m_d)^{1/2} \approx 4.6$ s^{-1}.

4.5. Ambipolar Diffusion

Let us consider a two-component system consisting of positively charged grains and the photoelectrons emitted by them. Because of a significant difference in the electron mobility μ_e and the dust grain mobility μ_d, the components of this system will be separated in the entire ampoule volume and a negative surface charge will arise on the wall. The arising polarization electric field will impede the further separation of the charged components; consequently, the electrons will diffuse together with heavy grains with a certain effective coefficient of ambipolar diffusion D_a. The D_a value is determined by the diffusion coefficient of the less mobile component; in the absence of external magnetic and electric fields, it can be written as [15]

$$D_a = \{D_e\mu_d + D_0\mu_e\}/\{\mu_d + \mu_e\}, \tag{15}$$

where D_e is the coefficient of free diffusion,

$$D_e = T_e/\nu_{en}m_e, \tag{16}$$

and D_0 is given by formula (3). Since $\mu_e \gg \mu_d$, the coefficient of ambipolar diffusion can be written as $D_a \approx D_0 + D_e\mu_d/\mu_e$. Then, with allowance for formulas (3) and (16), we have

$$D_a \approx (1 + Z_d T_e/T_d)D_0. \tag{17}$$

We note that formulas (15)–(17) are valid only in the case of a weakly ionized plasma–dust system, in which dissipation is determined by the buffer gas neutrals, whereas the collisions between charged particles are

unimportant. On the other hand, the coefficient of ambipolar diffusion describes the polarization effects, which are absent in a rarified plasma with low densities of the charged components. In such a plasma, the particle diffusion is determined by coefficients (3) and (16). Diffusion is ambipolar when the plasma is quasineutral and condition (12) is met. Hence, the regime of ambipolar diffusion is determined by the inequality $\lambda/R < 0.33$ (i.e., $\delta n/n_e < 10$). Thus, for $t < 10$ s (Fig. 6), the polarization effects related to the separation of opposite charges are feasible in the system under study.

Assuming that at $t < 10$ s, the charge loss in our experiment is related to the ambipolar diffusion toward the wall, the mean diffusion loss rate for dust grains can be written as [15]

$$dn_d/dt = -n_d\nu_{dif}, \quad (18)$$

where ν_{dif} is the effective diffusion loss rate,

$$\nu_{dif} \equiv -D_a/\Lambda_{dif}^2, \quad (19)$$

and Λ_{dif} is a characteristic scale length. For a cylinder of radius $R = 1.5$ cm and length $L = 4R$, we have $\Lambda_{dif}^2 \approx ((2.4/R)^2 + (\pi/L)^2)^{-1} = 0.6$ cm (Fig. 2) [15]. The diffusion loss rate ν_{dif} can be estimated by the rate at which the relative grain density changes. The experimental curve $n_d(t)/n_d^0$ is in good agreement with the exponential solution $n_d = n_d^0\exp(-\nu_{dif}t)$ to Eq. (19) with $\nu_{dif} \approx 0.035$ s^{-1} at $t < 10$ s (Fig. 6). Hence, the estimated coefficient of ambipolar diffusion is $D_a = \Lambda_{dif}^2\nu_{dif} \simeq 1.3 \times 10^{-2}$ cm/s, which is much larger than the measured coefficients $D_0^{x(y)}$ of grain self-diffusion (see Section 4.2). To compare the obtained coefficient D_a with its theoretical value $D_a \approx Z_dT_eD_d/T_d$ [see Eq. (17)], we use the obtained values $Z_d \approx (4.3 \pm 0.2) \times 10^4$ and $D_d/T_d \approx 2.8 \times 10^{-7}$ cm^2/(s eV) and assume that $T_e = 1$–2 eV. Then, we have $D_a \approx (1.2$–$2.4) \times 10^{-2}$ cm^2/s, which agrees with the coefficient of ambipolar diffusion measured by the rate at which the grains depart to the wall [see Eqs. (18), (19)] to within the accuracy in determining the characteristic length Λ_{dif} and the grain parameters and the validity of the assumption $T_e = 1$–2 eV.

5. CONCLUSION

We have presented the experimental results on the dynamics of dust grains charged via photoemission under microgravity conditions. The velocity distribution, temperature, mean charge, and diffusion coefficient of the dust grains are determined. An analysis of the experimental data shows that in the initial stage ($t < 10$ s), the particles undergo ambipolar diffusion; i.e., the densities of the charges of both signs are so high that the charge separation leads to the formation of a significant space charge, which induces the polarization electric field. The polarization caused by the separation of opposite charges decreases the drift velocities of the dust grains with respect to their velocities in a system transparent to photoelectrons and affects the excitation of high-frequency oscillations observed after the dynamic action on a dust system exposed to solar radiation. We emphasize that direct experimental observations of the phenomena related to charge separation in a two-component dusty plasma are hardly possible under the Earth's gravity conditions.

To conclude, the experiments show that the interaction between dust grains only slightly affects both the grain self-diffusion coefficient, which remains close to the Brownian one (D_0), and the ambipolar dust transfer, whose theory is based on neglecting Coulomb collisions between oppositely charged particles. Thus, we can suggest that if the coupling parameter Γ is no higher than 30–35 (see Section 4.4), then the transport properties of strongly dissipative systems of dust grains ($\omega_d/\nu_{fr} \ll 1$) with a weak screening of the grain charges ($\kappa < 1$) can be described with good accuracy in the gas-dynamic approximation.

ACKNOWLEDGMENTS

This study was supported in part by the Russian Foundation for Basic Research (project no. 01-02-16658), INTAS (grant no. 2000-0522), and the Netherlands Organization for Scientific Research (NWO) (grant no. 047-008-013).

REFERENCES

1. H. Thomas, G. Morfill, V. Demmel, *et al.*, Phys. Rev. Lett. **73**, 652 (1994).
2. A. Melzer, T. Trottenberg, and A. Piel, Phys. Lett. A **191**, 301 (1994).
3. V. V. Zhakhovskiĭ, V. I. Molotkov, A. P. Nefedov, *et al.*, Pis'ma Zh. Éksp. Teor. Fiz. **66**, 392 (1997) [JETP Lett. **66**, 419 (1997)].
4. S. Nunomura, T. Misawa, N. Ohno, and S. Takamura, Phys. Rev. Lett. **83**, 1970 (1999).
5. O. Vaulina, S. Khrapak, A. Nefedov, *et al.*, Phys. Rev. E **60**, 5959 (1999).
6. V. E. Fortov, A. P. Nefedov, O. S. Vaulina, *et al.*, Zh. Éksp. Teor. Fiz. **114**, 2004 (1998) [JETP **87**, 1087 (1998)].
7. O. S. Vaulina, A. P. Nefedov, O. F. Petrov, *et al.*, Phys. Rev. Lett. **88**, 035001 (2002).
8. O. S. Vaulina, A. P. Nefedov, O. F. Petrov, *et al.*, Zh. Éksp. Teor. Fiz. **119**, 1129 (2001) [JETP **93**, 1184 (2001)].
9. G. Morfill, H. Thomas, U. Konopka, *et al.*, Phys. Rev. Lett. **83**, 1598 (1999).
10. T. Stuffler, G. Schmitt, H. Pfeuffer, *et al.*, in *Proceedings of the 52nd International Astronautical Congress, Toulouse, 2001*, paper IAF-01-J.6.02.

11. V. N. Tsytovich, Usp. Fiz. Nauk **167**, 57 (1997) [Phys. Usp. **40**, 53 (1997)].
12. C. K. Goertz, Geophys. Rev. **27**, 271 (1989).
13. V. A. Grilikhis, P. P. Orlov, and L. B. Popov, *Sun Energy and Space Flights* (Nauka, Moscow, 1986).
14. M. Rosenberg, D. A. Mendis, and D. P. Sheehan, IEEE Trans. Plasma Sci. **24**, 1422 (1996).
15. Yu. P. Raizer, *Gas Discharge Physics* (Nauka, Moscow, 1987; Springer-Verlag, Berlin, 1991).
16. H. Z. Cummins and E. R. Pike, *Photon Correlation and Light Beating Spectroscopy* (Plenum, New York, 1974; Mir, Moscow, 1978).
17. O. S. Vaulina and S. V. Vladimirov, Plasma Phys. **9**, 835 (2002).
18. O. S. Vaulina and S. A. Khrapak, Zh. Éksp. Teor. Fiz. **119**, 264 (2001) [JETP **92**, 228 (2001)].
19. O. S. Vaulina, A. P. Nefedov, O. F. Petrov, and V. E. Fortov, Zh. Éksp. Teor. Fiz. **118**, 1325 (2000) [JETP **91**, 1147 (2000)].
20. H. Thomas and G. Morfill, Nature (London) **379**, 806 (1996).
21. A. Melzer, A. Homann, and A. Piel, Phys. Rev. E **53**, 2757 (1996).
22. J. Pieper and J. Goree, Phys. Rev. Lett. **77**, 3137 (1996).
23. E. M. Lifshitz and L. P. Pitaevskiĭ, *Physical Kinetics* (Nauka, Moscow, 1979; Pergamon, Oxford, 1981).
24. M. S. Sodha and S. Guha, Adv. Plasma Phys. **4**, 219 (1971).
25. A. A. Samarian, O. S. Vaulina, A. P. Nefedov, *et al.*, Phys. Rev. E **64**, 056407 (2001).

Translated by N.N. Ustinovskiĭ

Plasma Physics Reports, Vol. 29, No. 1, 2003, pp. 42–52. Translated from Fizika Plazmy, Vol. 29, No. 1, 2003, pp. 49–59.

PLASMA DIAGNOSTICS

Microwave Enhanced-Scattering Correlation Diagnostics of a Turbulent Plasma

E. Z. Gusakov* and A. V. Surkov**

Ioffe Physicotechnical Institute, Russian Academy of Sciences, Politekhnicheskaya ul. 26, St. Petersburg, 194021 Russia

**e-mail: Evgeniy.Gusakov@mail.ioffe.ru*

***e-mail: a.surkov@mail.ioffe.ru*

Received June 27, 2002

Abstract—A study is made of the influence of large-scale plasma turbulence on the results from a diagnostic method that is based on enhanced scattering of microwaves near the upper hybrid resonance and is highly sensitive to small-scale fluctuations. The resolution in radial wavenumbers that is provided by an enhanced-scattering correlation analysis of small-scale fluctuations with allowance for multiple small-angle scatterings of the probing and scattered waves along their paths is determined. The frequency spectrum of a wave that is backscattered by the small-scale fluctuations involved in large-scale turbulent motion and undergoes multiple small-angle scatterings is analyzed. © *2003 MAIK "Nauka/Interperiodica"*.

1. INTRODUCTION

At first, the diagnostics based on measuring the signals from microwaves that undergo enhanced scattering in the vicinity of the upper hybrid resonance (UHR) was used to study small-scale oscillations and waves in quiescent plasmas of linear laboratory devices [1]. In recent years, this diagnostic technique has been widely applied to investigate plasma turbulence and the propagation of microwaves in tokamak plasmas. Thus, in experiments carried out in the FT-1 tokamak [2], in which this method was used to study spontaneous plasma density fluctuations, a substantial broadening of the frequency spectra of the backscattered signal was observed and was found to increase in proportion to the wavenumber of the fluctuations by which the probing wave is backscattered. In our recent paper [3], it was shown that such behavior of the frequency spectrum may stem from the fact that in a tokamak, a probing wave propagating in a turbulent plasma is scattered primarily by predominant large-scale plasma density fluctuations. The frequency shift and spectrum broadening may be associated not only with the frequency of the small-scale density fluctuations responsible for backscattering, but also with the effects of multiple small-angle scatterings of the probing and scattered waves by large-scale plasma turbulence along their paths. In the enhanced-scattering diagnostics, these effects may also influence the resolution in radial wavenumbers that is provided by a correlation analysis of the backscattered signals from two probing waves with different frequencies [4].

In [3], we considered the evolution of the frequency spectrum of a plane extraordinary probing wave during its multiple small-angle scatterings in a turbulent plasma. In the present paper, which is a logical continuation of [3], we examine the influence of multiple small-angle scattering on the resolution of the enhanced-scattering correlation diagnostics with allowance for the directional pattern of the antenna generating a probing wave. The analysis is performed by the eikonal method; however, in the UHR region, the problem is investigated exactly. These two approaches are shown to yield the same results in the spatial region where both of them are applicable.

In this paper, we also analyze the frequency spectrum of the backscattered wave recorded by the enhanced-scattering diagnostics. This spectrum may form as a result of multiple small-angle scatterings of the wave along its path or as a result of the Doppler broadening, when small-scale fluctuations responsible for backscattering are involved in turbulent motions.

2. CORRELATION ANALYSIS OF ENHANCED BACKSCATTERING IN THE EIKONAL APPROXIMATION

We consider a cold collisionless plasma in a magnetic field directed along the z-axis. Let an extraordinary wave be emitted by an antenna in the x direction, in which the plasma density is nonuniform, and let the signal of the same polarization, backscattered by small-scale fluctuations near the UHR, be received by the same antenna. In the eikonal approximation, the elec-

1063-780X/03/2901-0042$24.00

tric field of the emitted extraordinary wave can be written as (see, e.g., [5])

$$E_x(\mathbf{r}) = \frac{k_x^{3/2}(x)}{k_c\sqrt{k_0}}\int_{-\infty}^{+\infty}\frac{dk_y dk_z}{(2\pi)^2}E_{k_y,k_z} \times \exp\left\{i\int_0^x k_x(x')dx' + ik_y y + ik_z z\right\}.$$

In deriving this expression, we omitted the harmonic dependence on time and used the relationship $k_x^2(x) = -k_c^2/\varepsilon(x) - k_y^2 - A(x)k_z^2$ (with $A(x) \approx -\eta/\varepsilon(x)$ and $k_c = g(x_{UH})/c$), which holds near the UHR in the paraxial approximation. Here, ε, g, and η are the elements of the dielectric tensor; the plasma density profile is assumed to be linear, $\varepsilon = (x - x_{UH})/\ell$ with x_{UH} the position of the UHR; $k_0 = \omega_i/c$ is the wave vector of the probing wave in a vacuum; and E_{k_y,k_z} is the wavenumber (over k_y and k_z) spectrum of the field generated by the antenna.

Following [3], in the expression for the phase of the electric field of the probing wave, we take into account large-scale plasma density fluctuations, which give rise to the wavenumber perturbations

$$\delta k(x, y, z, t) = -k_c\frac{\delta n(x, y, z, t)}{2n[-\varepsilon(x)]^{3/2}}.$$

In this case, the fluctuation-related phase increment can be obtained by integrating the density fluctuations with the corresponding weighting factor along an unperturbed path of the ray [3]:

$$\xi = \int_0^x \delta k[x', y(x'), z(x'), t]dx',$$

where the functions $y(x')$ and $z(x')$ describe the ray trajectory. Taking into account that the ray passes in the axial region and that the main contribution to the fluctuation-related phase increment comes from the UHR region, in which the small-angle scattering is enhanced [5] and the wave propagates predominantly in the direction in which the plasma is nonuniform, we set $y(x) \approx y$ and neglect the dependence of the fluctuations on z, assuming that they are very long-wavelength in the direction of the magnetic field.

In this way, we can readily calculate the extinction of the averaged electric field by multiple small-angle scattering:

$$\langle E\rangle \propto \langle e^{i\xi}\rangle.$$

Under the assumption that the distribution of the fluctuation-related change in the eikonal ξ is normal, we obtain

$$E \propto e^{-\langle\xi^2\rangle/2},$$

which yields the following expression for the Poynting vector of the probing wave:

$$S = \text{const}\, e^{-\langle\xi^2\rangle}. \quad (1)$$

The expression for $\langle\xi^2\rangle$ was obtained in [3]:

$$\langle\xi^2\rangle = \begin{cases}\dfrac{\langle\delta n^2\rangle}{8k_c^2 n_{UH}^2}\ell\ell_c k_x^4(x), & x_{UH} - x \gg \ell_c,\\ \dfrac{\langle\delta n^2\rangle}{n_{UH}^2}\ell^2 k_x^2(x), & x_{UH} - x \ll \ell_c,\end{cases}$$

where ℓ_c is the correlation length of the large-scale plasma density fluctuations.

Note that the approach used here agrees with the approach developed in our earlier paper [5] for a description of the small-angle scattering. In that paper, using the Born approximation, we obtained the dependence of the total Poynting vector of the probing wave that had undergone multiple small-angle scatterings on the coordinate measured from the plasma boundary to the UHR. This dependence can readily be reduced to the form

$$S_s = \mathcal{A}(x)S_i,$$

$$\mathcal{A}(x) = \begin{cases}\dfrac{\langle\delta n^2\rangle}{8k_c^2 n_{UH}^2}\ell\ell_c k_x^4(x), & x_{UH} - x \gg \ell_c,\\ \dfrac{\langle\delta n^2\rangle}{n_{UH}^2}\ell^2 k_x^2(x), & x_{UH} - x \ll \ell_c,\end{cases} \quad (2)$$

where the Poynting vector S_i of the probing wave in the Born approximation is assumed to be constant. In actuality, however, small-angle scatterings weaken the probing wave; this weakening can be taken into account by means of formulas (2). In order to determine the law by which the Poynting vector of the probing wave changes, we write

$$\frac{dS_i}{dx} = -\frac{d\mathcal{A}(x)}{dx}S_i,$$

which yields

$$S_i = \text{const}\cdot\exp(-\mathcal{A}(x)). \quad (3)$$

Since formulas (1) and (3) coincide, we can conclude that a more convenient phase approach, which makes it possible to determine the spectral properties of a multiply scattered wave, does not contradict a more sophisticated energy approach.

We consider the backscattering of a probing wave with the frequency ω_i by plasma density fluctuations with the radial wavenumbers satisfying the condition

$$Q_x \ll \frac{\omega_i}{c}\sqrt{\frac{c}{v_{Te}}},$$

where v_{Te} is the electron thermal velocity. This condition indicates that the wave is backscattered far from the conversion point [6]; moreover, the probing and backscattered waves are both extraordinary modes ($X \longrightarrow X$). Following [1], we use the reciprocity theorem, according to which the power in the receiving antenna is $P_s = |A|^2$, where

$$A(\omega) = \frac{1}{4}\int \mathbf{j}_\omega(\mathbf{r})\mathbf{E}^+(\mathbf{r})d\mathbf{r}.$$

Here, the integration is performed over the entire plasma volume and $\mathbf{E}^+(\mathbf{r})$ is the electric field of the antenna for an oppositely directed magnetic field. The nonlinear current

$$\mathbf{j}_\omega(\mathbf{r}) = \frac{\delta n_\Theta}{n}\hat{\sigma}\mathbf{E}(\mathbf{r})$$

with $\hat{\sigma} = i\omega_i(\hat{\varepsilon} - \hat{I})/(4\pi)$ being the plasma conductivity tensor, is determined by small-scale plasma density fluctuations

$$\delta n(\mathbf{r}, t) = \int_{-\infty}^{+\infty}\frac{d\Theta}{2\pi}\delta n_\Theta(\mathbf{r})e^{-i\Theta t},$$

where it is assumed that $\Theta = \omega - \omega_i \ll \omega$. Here and below, Θ and $\mathbf{Q}$ denote the frequency and wave vector of small-scale fluctuations, and Ω and $\mathbf{q}$ denote the frequency and wave vector of large-scale fluctuations.

The amplitude of the backscattered signal depends parametrically on time:

$$A_s(t) = \frac{i\omega_i}{16\pi n_{UH}}\int_{-\infty}^{+\infty}d\mathbf{r}\int_{-\infty}^{+\infty}\frac{dk_y dk_z}{(2\pi)^2}E_{k_y,k_z}$$

$$\times\int_{-\infty}^{+\infty}\frac{dk_y' dk_z'}{(2\pi)^2}E_{k_y',k_z'}\int_{-\infty}^{+\infty}\frac{d\mathbf{Q}}{(2\pi)^3}\delta n_{\mathbf{Q},\Theta}\frac{k_x^3(x)}{k_c^2 k_0}$$

$$\times\exp\left\{2i\int_0^x k_x(\chi)d\chi + i(k_y + k_y')y + i(k_z + k_z')z\right.$$

$$\left. + i\mathbf{Q}\mathbf{r}\right\}\exp\left\{2i\int_0^x \delta k(\chi, y, t)d\chi\right\}.$$

In the enhanced-scattering diagnostic method, the radial-wavenumber spectrum of small-scale turbulence is determined by calculating the correlation function of the signals from two scattered probing waves with different frequencies [4]. With allowance for multiple small-angle scatterings of the probing and scattered waves along their paths, the correlation function in the eikonal approximation has the form

$$\langle A_{s1}(t)A_{s2}^*(t+\tau)\rangle = \frac{\omega_1\omega_2}{(16\pi n_{UH})^2}\int_{-\infty}^{\infty}d\mathbf{r}d\mathbf{r}'$$

$$\times\int_{-\infty}^{\infty}\frac{1}{(2\pi)^8}dk_y dk_z dk_y' dk_z' d\kappa_y d\kappa_z d\kappa_y' d\kappa_z'$$

$$\times E_{k_y,k_z}E^+_{k_y',k_z'}E^*_{\kappa_y,\kappa_y}E^{+*}_{\kappa_y',\kappa_z'}\exp[i(k_y + k_y')y + i(k_z + k_z')z$$

$$- i(\kappa_y + \kappa_y')y' - i(\kappa_z + \kappa_z')z']\frac{k_1^3(x)k_2^3(x')}{k_0^2 k_c^4}$$

$$\times\int_{-\infty}^{\infty}\frac{d\mathbf{Q}}{(2\pi)^3}|\delta n_{\mathbf{Q},\Theta}|^2 \qquad (4)$$

$$\times\exp\{iQ_x(x_1 - x_2) + iQ_y(y - y') + iQ_z(z - z')\}$$

$$\times\exp\left\{2i\int_0^x k_1(\chi)d\chi + iQ_x(x - x_1)\right.$$

$$\left. - 2i\int_0^{x'} k_2(\chi')d\chi' - iQ_x(x' - x_2)\right\}\langle\exp[2i\xi_1 - 2i\xi_2]\rangle.$$

Here, we have introduced the following notation: A_{s1} and A_{s2} are the amplitudes of the signals from the scattered probing waves with the frequencies ω_1 and ω_2, respectively,

$$\langle A_{si}\rangle = 0, \quad i = 1, 2;$$

$k_1(x)$ and $k_2(x)$ are the projections of the wave vectors of the waves with the corresponding frequencies onto the direction in which the plasma is nonuniform; and x_1 and x_2 are the positions of the UHR for waves with the corresponding frequencies. The influence of large-scale fluctuations can be described by introducing the random quantities

$$\xi_1 = \int_0^x \delta k_1(\chi, y, t)d\chi, \quad \xi_2 = \int_0^{x'}\delta k_2(\chi', y', t + \tau)d\chi',$$

in which small- and large-scale fluctuations are assumed to be statistically independent. In formula (4), the averaging over small-scale fluctuations has been carried out under the assumption that the fluctuations are statistically uniform in both space and time:

$$\langle\delta n_{\mathbf{Q},\Theta}\delta n^*_{\mathbf{Q}',\Theta'}\rangle = (2\pi)^4|\delta n_{\mathbf{Q},\Theta}|^2\delta(\mathbf{Q} - \mathbf{Q}')\delta(\Theta - \Theta').$$

In order to investigate the influence of large-scale fluctuations on the correlation function of the scattered waves, we follow the approach developed in [3]; specif-

ically, we assume that the distribution of the fluctuation-related phase increments is normal and analyze the correlation function

$$K = \langle e^{2i\xi_1 - 2i\xi_2} \rangle = \exp[4\langle \xi_1 \xi_2 \rangle - 2\langle \xi_1^2 \rangle - 2\langle \xi_2^2 \rangle]. \quad (5)$$

The integrals over dx and dx' in expression (4) can be evaluated by the stationary-phase method. This yields the Bragg condition, which determines the points of backscattering in a nonuniform plasma. Probing waves with frequencies ω_1 and ω_2 are backscattered at the points $x = x_{s1}$ and $x' = x_{s2}$, satisfying the conditions

$$2k_1(x_{s1}) = -Q_x, \quad 2k_2(x_{s2}) = -Q_x,$$

in which case we have

$$\langle \xi_1 \xi_2 \rangle = \frac{k_c^2 \ell^3}{4n_{UH}^2} \int_{-\infty}^{+\infty} \frac{dq_x dq_y d\Omega}{(2\pi)^3} |\delta n_{\mathbf{q},\Omega}|^2 \int_0^{x_{s1}} d\chi \times \int_0^{x_{s2}} d\chi' \frac{\exp[iq_x(\chi - \chi') + iq_y(y - y') + i\Omega\tau]}{(x_1 - \chi)^{3/2}(x_2 - \chi')^{3/2}}, \quad (6)$$

where $\delta n_{\mathbf{q},\Omega}$ is the spectral density of large-scale fluctuations.

Let us consider this correlation function for the case when the distances from the UHR at which the probing waves are backscattered,

$$x_1 - x_{s1} = x_2 - x_{s2} = 4k_c^2 \ell / Q_x^2, \quad (7)$$

are much longer than the correlation length of large-scale fluctuations, $|x_1 - x_{s1}| \gg \ell_c$.

To calculate the integrals, we introduce the variables $u^2 = x_1 - \chi$ and $u'^2 = x_2 - \chi'$ and make the following two assumptions. First, the small-angle scattering is nonlinear; i.e., the correlation length and time of the wave field are much longer than those of the plasma density fluctuations. Second, the distance between the resonances, $x_1 - x_2$, and the corresponding time delay τ, which are both necessary for correlation analysis, are on the order of the correlation length and time of the wave field. This latter assumption makes it possible to expand the exponentials in the integrands in formula (6). Neglecting small terms in this formula, we find

$$\ln K = -\frac{2k_c^2 \ell^3}{n_{UH}^2} \int_{-\infty}^{+\infty} \frac{dq_x dq_y d\Omega}{(2\pi)^3} |\delta n_{\mathbf{q},\Omega}|^2 \times [q_x^2 (x_1 - x_2)^2 + q_y^2 (y - y')^2 + \Omega^2 \tau^2] \left| \int_{\sqrt{x_1 - x_{s1}}}^{\sqrt{x_1}} \frac{du}{u^2} e^{iq_x u^2} \right|^2.$$

In order to obtain the sought-for asymptotic expression at $x_1 - x_{s1} \gg \ell_c$, we use the relationship $q_x(x_1 - x_{s1}) \gg 1$. The coefficient in the term with $x_1 - x_2$ can be calculated from the approximate relationship

$$\int_{\sqrt{x_1 - x_{s1}}}^{\sqrt{x_1}} \frac{du}{u^2} e^{iq_x u^2} \approx \frac{\exp[iq_x(x_1 - x_{s1})]}{2iq_x(x_1 - x_{s1})^{3/2}}.$$

To evaluate the coefficients in the terms with y–y' and Ω, we can use a simpler estimate:

$$\int_0^{x_{s1}} d\chi \int_0^{x_{s2}} d\chi' \frac{\exp[iq_x(\chi - \chi')]}{(x_1 - \chi)^{3/2}(x_2 - \chi')^{3/2}} \approx \frac{\pi \delta(q_x)}{(x_1 - x_{s1})^2}.$$

Taking into account relationship (7), we obtain

$$\ln K \approx -\frac{Q_x^4 \ell}{64 k_c^2 n_{UH}^2} \left\{ \frac{Q_x^2 \langle \delta n^2 \rangle}{2k_c^2 \ell} (x_1 - x_2)^2 + \int_{-\infty}^{+\infty} \frac{dq_y d\Omega}{(2\pi)^2} |\delta n_{0, q_y, \Omega}|^2 [q_y^2 (y - y')^2 + \Omega^2 \tau^2] \right\}. \quad (8)$$

Introducing the corresponding notation, we arrive at the following estimate:

$$\ln K \approx -\frac{Q_x^4 \ell \ell_c}{64 k_c^2} \frac{\langle \delta n^2 \rangle}{n_{UH}^2} \times \left\{ \frac{Q_x^2 \ell_c}{2k_c^2 \ell} \left(\frac{\Delta x_{UH}}{\ell_c} \right)^2 + \langle q_y^2 \rangle (y - y')^2 + \langle \Omega^2 \rangle \tau^2 \right\}.$$

In the opposite limit $x_{1,2} - x_{s1,2} \ll \ell_c$ (which indicates that the waves are backscattered near the UHR), correlation function (6) can also be simplified. In this case, we have

$$\int_0^{x_{s1}} d\chi \int_0^{x_{s2}} d\chi' \frac{\exp[iq_x(\chi - \chi')]}{(x_1 - \chi)^{3/2}(x_2 - \chi')^{3/2}} \approx \frac{4}{\sqrt{x_1 - x_{s1}}\sqrt{x_2 - x_{s2}}},$$

which yields

$$\langle \xi_1 \xi_2 \rangle = \frac{\ell^2 k_1(x_{s1}) k_2(x_{s2})}{n_{UH}^2} \times \int_{-\infty}^{+\infty} \frac{dq_x dq_y d\Omega}{(2\pi)^3} |\delta n_{\mathbf{q},\Omega}|^2 e^{iq_x \Delta x_{UH} + iq_y(y - y') + i\Omega\tau}.$$

Assuming again that $\Delta x_{UH} \ll \ell_c$ and expanding the right-hand side of the last expression in a series, we obtain

$$\ln K \approx -\frac{\ell^2 Q_x^2}{2n_{UH}^2}\int_{-\infty}^{+\infty}\frac{dq_x dq_y d\Omega}{(2\pi)^3}|\delta n_{\mathbf{q},\Omega}|^2$$
$$\times [q_x^2(\Delta x_{UH})^2 + q_y^2(y-y')^2 + \Omega^2\tau^2]. \quad (9)$$

Hence, the expression describing the breaking of correlations by multiple small-angle scatterings,

$$K = \exp\left\{-\frac{(\Delta x_{UH})^2}{L_x^{\text{eff}^2}} - \frac{(y-y')^2}{L_y^{\text{eff}^2}} - \frac{\tau^2}{T_c^{\text{eff}^2}}\right\}, \quad (10)$$

contains the effective correlation lengths and times, which can be estimated as follows:

For $Q_x^2\ell_c/(4k_c^2\ell) \ll 1$, the estimates are given by

$$L_x^{\text{eff}} = 8\sqrt{2}k_c^2/\left(Q_x^3\frac{\overline{\delta n}}{n_{UH}}\right),$$

$$L_y^{\text{eff}} = 8k_c/\left(Q_x^2\sqrt{\ell\ell_c}\bar{q}_y\frac{\overline{\delta n}}{n_{UH}}\right),$$

$$T_c^{\text{eff}} = 8k_c/\left(Q_x^2\sqrt{\ell\ell_c}\bar{\Omega}\frac{\overline{\delta n}}{n_{UH}}\right);$$

and, for $Q_x^2\ell_c/(4k_c^2\ell) \gg 1$, the estimates have the form

$$L_x^{\text{eff}} = \sqrt{2}/\left(Q_x\ell\bar{q}_x\frac{\overline{\delta n}}{n_{UH}}\right),$$

$$L_y^{\text{eff}} = \sqrt{2}/\left(Q_x\ell\bar{q}_y\frac{\overline{\delta n}}{n_{UH}}\right), \quad (11)$$

$$T_c^{\text{eff}} = \sqrt{2}/\left(Q_x\ell\bar{\Omega}\frac{\overline{\delta n}}{n_{UH}}\right).$$

Here, $\bar{q}_{x,y} = \sqrt{\langle q_{x,y}^2\rangle}$, $\bar{\Omega} = \sqrt{\langle\Omega^2\rangle}$, and $\overline{\delta n} = \sqrt{\langle\delta n^2\rangle}$.

For $k_x \sim \omega/c\sqrt{c/v_{Te}}$, an extraordinary wave converts near the UHR into a Bernstein mode [6], which propagates from the UHR toward the plasma boundary. Near the conversion point, the Wentzel–Kramers–Brillouin (WKB) approximation fails to hold, as does the cold plasma approximation, in which the dispersion relation has been derived. However, behind the conversion point, the Bernstein mode at sufficiently long distances from the UHR can be described in the eikonal approximation. Near the conversion point, the wavenumber of the mode has the form

$$k(x) = \sqrt{-\varepsilon}/\ell_T, \quad (12)$$

where the parameter ℓ_T accounts for the thermal particle motion and $\ell_T^2 = 3v_{Te}^2/(3\omega_{ce}^2 - \omega_{pe}^2)|_{x=x_{UH}}$. For a linear plasma density profile, ($\varepsilon = (x - x_{UH})/\ell$), the spatial region in which the eikonal approximation and relationship (12) are both applicable is determined by the conditions $\ell_T/\ell \ll (-\varepsilon)^{3/2} \ll 1$.

Let us consider the backscattering in the part of the region of applicability of the eikonal approximation where the probing and backscattered waves are Bernstein modes ($B \longrightarrow B$), which indicates that the following condition on the radial wavenumber of the fluctuations responsible for backscattering is satisfied:

$$Q_x > 2\frac{\omega_i}{c}\sqrt{\frac{c}{v_{Te}}}.$$

For Bernstein modes with the frequencies ω_1 and ω_2, the fluctuation-related changes in the eikonal have the form

$$\xi_1 = \frac{\sqrt{\ell}}{2n_{UH}\ell_T}\int_{x_1}^{x}\frac{\delta n(\chi, y, t)}{\sqrt{x_1-\chi}}d\chi,$$

$$\xi_2 = \frac{\sqrt{\ell}}{2n_{UH}\ell_T}\int_{x_2}^{x'}\frac{\delta n(\chi, y', t+\tau)}{\sqrt{x_2-\chi}}d\chi.$$

For a Bernstein mode backscattered at distance from the UHR that is shorter than the correlation length of large-scale fluctuations, we obtain the following expression for the exponential index in correlation function (5):

$$\ln K = 4\langle\xi_1\xi_2\rangle - 2\langle\xi_1^2\rangle - 2\langle\xi_2^2\rangle$$
$$\approx -\frac{\ell^2 Q_x^2}{2n_{UH}^2}\int_{-\infty}^{+\infty}\frac{dq_x dq_y d\Omega}{(2\pi)^3}|\delta n_{\mathbf{q},\Omega}|^2$$
$$\times [q_x^2(\Delta x_{UH})^2 + q_y^2(y-y')^2 + \Omega^2\tau^2],$$

which exactly coincides with expression (9). In this case, the effective correlation lengths and times in expression (10) for the correlation function K are given by formulas (11).

In order to evaluate correlation function (5) far from the UHR, when both of the probing waves are scattered behind the conversion point at distances from the UHR that are much larger than the correlation length of large-scale fluctuations ($x_{1,2} - x_{s1,2} \gg \ell_c$), we again introduce the variables $u^2 = x_1 - \chi$ and $u'^2 = x_2 - \chi'$. As a result, we obtain

$$\ln K = -\frac{2\ell}{n_{UH}^2\ell_T^2}\int_{-\infty}^{+\infty}\frac{dq_x dq_y d\Omega}{(2\pi)^3}|\delta n_{\mathbf{q},\Omega}|^2$$

$$\times [q_x^2(\Delta x_{UH})^2 + q_y^2(y-y')^2 + \Omega^2\tau^2] \left| \int_0^{\sqrt{x_1 - x_{s1}}} du e^{iq_x u^2} \right|^2.$$

The integral over u in this expression can be evaluated by the stationary-phase method:

$$\int_0^{\sqrt{x_1 - x_{s1}}} du e^{iq_x u^2} \approx \frac{1}{2}\sqrt{\frac{\pi}{|q_x|}} e^{i\pi/4}.$$

This yields

$$\ln K = -\frac{\pi\ell}{2n_{UH}^2\ell_T^2}\int_\Gamma \frac{dq_x}{2\pi}\int_{-\infty}^{+\infty}\frac{dq_y d\Omega}{(2\pi)^2}|\delta n_{\mathbf{q},\Omega}|^2$$

$$\times \frac{1}{|q_x|}[q_x^2(\Delta x_{UH})^2 + q_y^2(y-y')^2 + \Omega^2\tau^2].$$

The integral over q_x is taken over the region $\Gamma = (-\ell_c^{-1}, -q^*) \cup (q^*, \ell_c^{-1})$, where $q^* \sim 4/(Q_x^2\ell\ell_T) \ll \ell_c^{-1}$. In the limit in question, the contribution of the closed interval $[-q^*, q^*]$, in which the stationary-phase method fails to hold, is as small as $\ell_c q^*$. This allows us to estimate the integral over q_x with logarithmic accuracy:

$$\int_\Gamma \frac{dq_x}{2\pi|q_x|}|\delta n_{\mathbf{q},\Omega}|^2 \sim 2\int_{q^*}^{1/\ell_c}\frac{dq_x}{2\pi|q_x|}|\delta n_{\mathbf{q},\Omega}|^2$$

$$\sim -\frac{1}{\pi}|\delta n_{0,\Omega}|^2 \ln(q^*\ell_c),$$

which gives

$$\ln K \sim -\frac{\ell}{2\ell_T^2 n_{UH}^2}\left[\pi\int_{-\infty}^{+\infty}\frac{dq_x}{2\pi}|\delta n_{q_x}|^2|q_x|(\Delta x_{UH})^2\right. \quad (13)$$

$$\left. + \int_{-\infty}^{+\infty}\frac{dq_y d\Omega}{(2\pi)^2}|\delta n_{0,q_y,\Omega}|^2[q_y^2(y-y')^2 + \Omega^2\tau^2]\ln\frac{Q_x^2\ell\ell_T^2}{4\ell_c}\right].$$

In the case at hand ($Q_x^2\ell\ell_T^2/\ell_c \gg 1$), the correlation lengths and times can be estimated as

$$L_x^{\text{eff}} = \ell_T\sqrt{2}/\left(\sqrt{\pi\ell\langle|q_x|\rangle}\frac{\overline{\delta n}}{n_{UH}}\right),$$

$$L_y^{\text{eff}} = \ell_T\sqrt{2}/\left(\bar{q}_y\sqrt{\ell\ell_c}\frac{\overline{\delta n}}{n_{UH}}\ln\frac{Q_x^2\ell\ell_T^2}{4\ell_c}\right), \quad (14)$$

$$T_c^{\text{eff}} = \ell_T\sqrt{2}/\left(\bar{\Omega}\sqrt{\ell\ell_c}\frac{\overline{\delta n}}{n_{UH}}\ln\frac{Q_x^2\ell\ell_T^2}{4\ell_c}\right).$$

Under the condition

$$|Q_x| > \frac{\omega_i}{c}\sqrt{\frac{c}{v_{Te}}}$$

the backscattering of the modes in the vicinity of the UHR can be accompanied by their mutual conversion: $B \longrightarrow X$ and $X \longrightarrow B$. When such scattering occurs at distances from the UHR that are much larger than the correlation length of large-scale fluctuations, the analysis is far more complicated than for the $X \longrightarrow X$ and $B \longrightarrow B$ processes. However, it can be easily seen that in this case, the behavior of the correlation function is governed completely by the fluctuation-related increment of the phase of the Bernstein wave and is described by expression (13) under the Bragg condition $k_x(x_s) \approx -Q_x$ for backscattering. Below, the correlation function in the UHR region will be considered with allowance for all possible backscattering processes.

3. CORRELATION ANALYSIS IN THE UHR REGION

Expressions (10) and (13) describe the influence of multiple small-angle scattering on correlations between the signals from two backscattered probing waves at different frequencies in the region in which the eikonal approximation is applicable. The backscattering in the UHR region (at $Q_x \sim \omega_i/c\sqrt{c/v_{Te}}$), in which the eikonal approximation fails to hold, should be described by an exact expression for the electric field of the probing wave [1]:

$$E(\xi, y, z, t) = \sqrt{\frac{8}{\gamma^2\ell\omega}}D(y, z)\int_0^\infty \exp\left[i\left(\frac{\kappa^3}{3} - \frac{b}{\kappa} + \xi\kappa\right)\right]d\kappa,$$

where we have introduced the dimensionless parameters

$$\gamma = \left(\frac{\ell_T}{\ell}\right)^{2/3}, \quad \xi = \frac{x - x_{UH}(t)}{\gamma\ell}, \quad b = (k_c\ell)^2\gamma, \quad (15)$$

and the factor $D(y, z)$ takes into account the directional pattern of the antenna. In expressions (15), the change in the position of the UHR is determined by the influence of large-scale density fluctuations. We assume that the scales on which the plasma density fluctuates are sufficiently large for both their dependence on the coordinates and their influence on the density gradient to be neglected:

$$x_{UH}(t) = x_{UH} - \ell\frac{\delta n(t)}{n_{UH}}. \quad (16)$$

Using the reciprocity theorem, we write out the amplitude of one of the signals from the backscattered waves [1]:

$$A_{s1}(t) = \frac{i}{2\pi n_{UH}\gamma}\int_{-\infty}^{+\infty}\frac{d\mathbf{Q}}{(2\pi)^3}\delta n_{\mathbf{Q},\Theta}e^{-iQ_x x_1}$$

$$\times\int_{-\infty}^{+\infty}dydzD(y,z)D^+(y,z)e^{-iQ_y y - iQ_z z}\int_{-\infty}^{+\infty}d\xi e^{-ip\xi}$$

$$\times\int_0^\infty\exp\left\{i\left[\frac{\kappa^3}{3}-\frac{b}{\kappa}+\xi\kappa\right]\right\}d\kappa$$

$$\times\int_0^\infty\exp\left\{i\left[\frac{\kappa'^3}{3}-\frac{b}{\kappa'}+\xi\kappa'\right]\right\}d\kappa',$$

where $p \equiv \gamma\ell Q_x$. We integrate over ξ and perform the necessary manipulations to obtain

$$A_{s1}(t) = \frac{i}{\gamma n_{UH}}\int_{-\infty}^{\infty}\frac{d\mathbf{Q}}{(2\pi)^3}\delta n_{\mathbf{Q},\Theta}U(\gamma\ell Q_x)e^{-iQ_x x_1(t)}F(Q_y,Q_z), \quad (17)$$

where

$$U(p) = \frac{p}{2}e^{ip^3/12}\int_{-1}^{1}d\chi\exp\left[i\left(\frac{p^3}{4}\chi^2-\frac{4b}{p(1-\chi^2)}\right)\right],$$

$$F(Q_y,Q_z) = \int_{-\infty}^{+\infty}dydzD(y,z)D^+(y,z)e^{-iQ_y y - iQ_z z}.$$

Without allowance for large-scale density fluctuations, the asymptotics of expression (17) in the WKB approximation coincide with the corresponding expressions that were derived in [1] for the amplitudes of the signals from extraordinary and Bernstein backscattered waves.

In the approximation at hand, in expression (17) for the amplitude, the time dependence, which reflects the influence of multiple small-angle scattering, is given by the exponential factor $\exp[-iQ_x x_1(t)]$ alone. With this circumstance in mind, we can readily obtain the correlation function of the signals from backscattered probing waves at two different frequencies. Using relationship (16), we can write

$$\langle A_{s1}(t)A_{s2}^*(t+\tau)\rangle = \frac{1}{\gamma^2 n_{UH}^2}\int_{-\infty}^{\infty}\frac{d\mathbf{Q}}{(2\pi)^3}|\delta n_{\mathbf{Q},\Theta}|^2|U(\gamma\ell Q_x)|^2$$

$$\times e^{iQ_x\Delta x_{UH}}|F(Q_y,Q_z)|^2$$

$$\times\left\langle\exp\left\{iQ_x\frac{\ell}{n_{UH}}[\delta n(x_1,t)-\delta n(x_2,t+\tau)]\right\}\right\rangle. \quad (18)$$

Assuming that the distribution of the density fluctuations is normal, we find

$$\left\langle\exp\left\{iQ_x\frac{\ell}{n_{UH}}[\delta n(x_1,t)-\delta n(x_2,t+\tau)]\right\}\right\rangle$$

$$= \exp\left\{\left(\frac{Q_x\ell}{n_{UH}}\right)^2[\langle\delta n(x_1,t)\delta n(x_2,t+\tau)\rangle-\langle\delta n^2\rangle]\right\}$$

$$\approx \exp\left\{-\frac{Q_x^2\ell^2}{2n_{UH}^2}\int_{-\infty}^{\infty}\frac{dq_x dq_y d\Omega}{(2\pi)^3}|\delta n_{\mathbf{q},\Omega}|^2[q_x^2(\Delta x_{UH})^2+\Omega^2\tau^2]\right\}. \quad (19)$$

Together with expressions (8) and (9), relationship (19) is valid in the limit of intense small-angle scattering. This relationship coincides with expression (9), which was obtained for the backscattering of extraordinary and Bernstein waves near the UHR using assumptions that are far less restrictive than those made for the UHR region. It is easy to see that in the WKB approximation, asymptotic expression (18) for the correlation function of the backscattered signals can be matched with the expressions for an extraordinary wave and for a Bernstein mode.

Generally, attempts to take into account the dependence of large-scale density fluctuations on y in the UHR region run into mathematical difficulties similar to those arising when constructing the hybrid-resonance theory in a plasma that is inhomogeneous in two directions [7]. However, the approach in which large-scale fluctuations are assumed to parametrically depend on the y coordinate makes it possible to evaluate correlation function (19), and the resulting expression will be precisely the same as expression (9).

Presumably, for a weakly inhomogeneous warm tokamak plasma, for which the geometrical-optics approximation is valid up to the linear conversion point and in which, strictly speaking, the field does not grow in a resonant fashion, expression (9) exhaustively describes the influence of large-scale turbulence on the propagation and backscattering of waves in the vicinity of the UHR.

When analyzing small-angle scattering in the UHR region, we neglected the influence of large-scale plasma density fluctuations on the plasma density gradient and took into account only the change in the UHR position. Let us derive the criterion for the validity of this approximation. In the presence of large-scale fluc-

tuations, the spatial scale of the density inhomogeneity is equal to

$$\tilde{\ell} \equiv \left(\frac{\partial \varepsilon}{\partial x}\right)^{-1}\Bigg|_{x = x_{UH}} \approx \ell\left[1 + \frac{\ell}{\ell_c}\frac{\delta n}{n_{UH}}\right].$$

According to [1], the function $|U(p)|^2$, which determines the backscattering efficiency in formula (18), has a narrow peak at $p = p_* \equiv 2b^{1/4}$ in the UHR region, the peak width being about $|p - p_*| \lesssim p_*^{-1/2}$.

With allowance for large-scale plasma density fluctuations, we have

$$\tilde{p} - \tilde{p}_* \approx (p - p_*)\left[1 + \frac{1}{3}\frac{\ell}{\ell_c}\frac{\delta n}{n_{UH}}\right].$$

It is natural to write the criterion for the validity of the approximation at hand in the form

$$|\tilde{p} - \tilde{p}_* - (p - p_*)| \ll p_*^{-1/2},$$

which gives

$$\frac{1}{3}\frac{\ell}{\ell_c}\left|(\tilde{p} - \tilde{p}_*)\frac{\delta n}{n_{UH}}\right| \ll p_*^{-1/2}.$$

This criterion reduces to the inequality

$$\frac{\ell}{\ell_c}\frac{\delta n}{n_{UH}} \ll 3,$$

which ensures the existence of only one UHR point and is not too strong.

Hence, in the correlation function of the backscattered signals, large-scale turbulence is accounted for by the additional factor $K(Q_x, \Delta x_{UH}, \tau)$, which is determined by formulas (10), (11), and (14):

$$\langle A_{s1}(t)A_{s2}^*(t + \tau)\rangle$$
$$= \frac{1}{\gamma^2 n_{UH}^2}\int_{-\infty}^{\infty}\frac{d\mathbf{Q}}{(2\pi)^3}|\delta n_{\mathbf{Q},\Theta}|^2|U(\gamma\ell Q_x)|^2 \qquad (20)$$
$$\times e^{iQ_x\Delta x_{UH}}|F(Q_y, Q_z)|^2 K(Q_x, \Delta x_{UH}, \tau).$$

In the method of correlation analysis, first, the dependence of correlation function (20) on the distance Δx_{UH} between the upper hybrid resonances for two probing waves is calculated from the experimental data and, then, the inverse Fourier transform of the correlation function is taken:

$$\int_{-\infty}^{+\infty}\langle A_{s1}A_{s2}^*\rangle e^{-iq\Delta x_{UH}}d\Delta x_{UH}$$
$$= \frac{1}{\gamma^2 n_{UH}^2}\int_{-\infty}^{\infty}\frac{d\mathbf{Q}}{(2\pi)^3}|\delta n_{\mathbf{Q},\Theta}|^2|U(\gamma\ell Q_x)|^2|F(Q_y, Q_z)|^2$$
$$\times \sqrt{\pi}L_x^{\text{eff}}(Q_x)e^{-(q - Q_x)^2 L_x^{\text{eff}^2}(Q_x)/4}.$$

As may be seen, in measurements of the radial-wavenumber spectrum of small-scale plasma density fluctuations, multiple small-angle scattering limits the resolution of the correlation diagnostics to the level

$$\Delta Q_x \sim 1/L_x^{\text{eff}}(Q_x).$$

Let us turn to the case of small-scale density fluctuations with wavenumbers at which the backscattering is most intense ($\gamma\ell Q_x \sim p_*$) and compare the resolution ΔQ_x of the diagnostics with the width δQ_U of the peak of the function $|U(p)|^2$. Under the condition $p_*^{3/2}\ell\bar{q}_x\overline{\delta n}/n_{UH} \ll 1$, it is easy to obtain the relationship $\Delta Q_x \ll \delta Q_U$. When this condition holds, multiple small-angle scattering merely limits the resolution provided by the diagnostics in measurements of the radial-wavenumber spectra, while in the opposite case, the diagnostics always fails to reliably determine the radial-wavenumber spectra of small-scale plasma density fluctuations.

4. BACKSCATTERING BY SMALL-SCALE FLUCTUATIONS INVOLVED IN LARGE-SCALE TURBULENT MOTIONS

The multiple small-angle scattering of the probing and scattered waves along their paths is one of the mechanisms responsible for the broadening of the frequency spectrum of the scattered wave. For a probing wave, this mechanism was analyzed in [3]. In that paper, for the backscattered wave, we obtained expression (10), which describes the breaking of correlations (in particular, the breaking of time correlations) and, accordingly, the broadening of the frequency spectrum.

Another possible mechanism for the broadening of the frequency spectrum from collective scattering is associated with turbulent motions of the volume elements of the medium in which the wave responsible for scattering propagates [8]. When the turbulent motion in the medium occurs on a scale much larger than that of the fluctuations giving rise to scattering, the broadening of the scattering spectrum can be described in terms of the Doppler effect. Assuming that the small-scale fluctuations are completely frozen into the large-scale fluctuations in the medium and thus have to move as the large-scale fluctuations move across the magnetic field (in particular, in the radial direction), we write the plasma density perturbation in the form

$$\delta n(\mathbf{r}, t) = \delta n_0\left(\mathbf{r} - \int_{t^*}^{t}\mathbf{v}[\mathbf{r}(t'), t']dt', t\right),$$

where the time t^* is chosen to be sufficiently close to the current time. Expanding δn_0 into a Fourier integral,

$$\delta n_0(\mathbf{r}', t) = \int_{-\infty}^{+\infty} \frac{d\mathbf{Q}}{(2\pi)^3} \delta\tilde{n}_{\mathbf{Q}}(t) e^{i\mathbf{Q}\mathbf{r}'},$$

we obtain

$$\delta n(\mathbf{r}, t) = \int_{-\infty}^{+\infty} \frac{d\mathbf{Q}}{(2\pi)^3} \delta n_{\mathbf{Q}}(t) \exp\left\{ i\mathbf{Q}\mathbf{r} - i\mathbf{Q}\int_{t^*}^{t} \mathbf{v}[\mathbf{r}(t'), t']dt' \right\}.$$

As a result, in the WKB approximation, the parametric dependence of the amplitude of the backscattered signal on time is described by the expression

$$A_s(t) = \frac{i\omega_i}{16\pi n_{UH}} \int_{-\infty}^{+\infty} d\mathbf{r} \int_{-\infty}^{+\infty} \frac{dk_y dk_z}{(2\pi)^2} E_{k_y, k_z}$$

$$\times \int_{-\infty}^{+\infty} \frac{dk_y' dk_z'}{(2\pi)^2} E_{k_y', k_z'} \int_{-\infty}^{+\infty} \frac{d\mathbf{Q}}{(2\pi)^3} \delta n_{\mathbf{Q}, \Theta} \frac{k_x^3(x)}{k_c^2 k_0}$$

$$\times \exp\left\{ 2i\int_0^x k_x(\chi)d\chi + i(k_y + k_y')y + i(k_z + k_z')z + i\mathbf{Q}\mathbf{r} \right\}$$

$$\times \exp\left\{ 2i\int_0^x \delta k(\chi, y, t)d\chi - i\mathbf{Q}\int_{t_0}^{t} \mathbf{v}[\mathbf{r}(t'), t']dt' \right\}. \quad (21)$$

Let us consider the frequency spectrum of the backscattered wave. To do this, we analyze the correlation function

$$\mathcal{K} = \langle A_s(t) A_s^*(t+\tau) \rangle, \quad (22)$$

where the average is taken under the assumption that small- and large-scale fluctuations are statistically independent. We use the representation

$$\int_{t^*}^{t+\tau} \mathbf{v}[\mathbf{r}(t'), t']dt' - \int_{t^*}^{t} \mathbf{v}[\mathbf{r}(t'), t']dt'$$

$$\approx \int_{t^*}^{t} \frac{\partial \mathbf{v}}{\partial r_i}[\mathbf{r}(t'), t'](r_i - r_i')dt' + \mathbf{v}[\mathbf{r}(t), t]\tau, \quad (23)$$

which is valid under the conditions $t - t^* \ll t_c$ and $\tau \ll t_c$, where t_c is the correlation time of large-scale turbulent fluctuations. We also take into account the large-scale character of turbulent motions and on the right-hand side of expression (23), neglect the first term, which is proportional to the gradient of the fluctuation velocity and thus is small in comparison with the second term. In addition, we employ the fact that the Bragg condition determines the scattering point $x = x' = x_s$ in a nonuniform plasma and annihilates the term with $x - x'$. In order to check the validity of the approximation just described, we estimate the terms in relationship (23). The condition under which the remaining terms, which are proportional to the fluctuation velocity gradient, can be omitted has the form

$$\frac{v}{\ell_{cy}}(y - y')(t - t^*) \ll v\tau,$$

where ℓ_{cy} is the correlation length of the fluctuations along the y-axis. This condition can be satisfied for intense multiple small-angle scattering, when the correlation length of the field is $y - y' \sim L_y^{\text{eff}} \ll \ell_{cy}$. In this case, the inequalities $\tau \ll t_c$ and $t - t^* \ll t_c$, which were used to derive expression (23), can also be satisfied.

We introduce the notation

$$\xi_1 = \int_0^x \delta k(\chi, y, t)d\chi, \quad \xi_2 = \int_0^{x'} \delta k(\chi', y', t+\tau)d\chi'$$

and, taking into account the relationships $Q_x \gg Q_y, Q_z$, we also introduce the notation

$$\xi_3 = \mathbf{Q}\int_t^{t+\tau} \mathbf{v}[\mathbf{r}(t'), t']dt' \approx Q_x v[\mathbf{r}, t]\tau.$$

The contribution of the large-scale turbulence to correlation function (22) is described by the expression

$$K = \langle e^{2i\xi_1 - 2i\xi_2 + i\xi_3} \rangle.$$

Assuming that the random quantities ξ_i obey normal distributions, we obtain

$$K = \exp\left\{ -2\langle \xi_1^2 \rangle - 2\langle \xi_2^2 \rangle - \frac{1}{2}\langle \xi_3^2 \rangle \right.$$

$$\left. + 4\langle \xi_1 \xi_2 \rangle - 2\langle \xi_1 \xi_3 \rangle + 2\langle \xi_2 \xi_3 \rangle \right\}.$$

The expression $4\langle \xi_1 \xi_2 \rangle - 2\langle \xi_1^2 \rangle - 2\langle \xi_2^2 \rangle$ can be evaluated from formulas (8) and (9) by setting $\omega_1 = \omega_2$. To calculate the term $\langle \xi_2 \xi_3 \rangle$ in the correlation function, we perform integration over x in formula (21) by the stationary-phase method, which determines the scattering points $x = x' = x_s$. As a result, we arrive at the expression

$$\langle \xi_2 \xi_3 \rangle = -\frac{k_c Q_x \tau \ell^{3/2}}{2n_{UH}} \int_{-\infty}^{+\infty} \frac{dq_x dq_y d\Omega}{(2\pi)^3}$$

$$\times \int_0^{x_s} \frac{d\chi}{(x_{UH} - \chi)^{3/2}} \langle \delta n_{\mathbf{q}, \Omega} \delta v_{\mathbf{q}, \Omega}^* \rangle e^{iq_x(\chi - x_s) + iq_y(y' - y) - i\Omega\tau}.$$

We consider the case in which scattering occurs at distances from the UHR that are much less than the correlation length of large-scale fluctuations, $x_{UH} - x_s \ll \ell_c$. Assuming that the spectral density of large-scale fluctuations is symmetric in q_y and retaining terms up to second order, we get

$$\langle \xi_2 \xi_3 \rangle - \langle \xi_1 \xi_3 \rangle \approx -\frac{Q_x^2 \tau^2 \ell}{2 n_{UH}} \int_{-\infty}^{+\infty} \frac{dq_x dq_y d\Omega}{(2\pi)^3} \langle \delta n_{\mathbf{q},\Omega} \delta v^*_{\mathbf{q},\Omega} \rangle i\Omega.$$

Then, we have

$$\ln K = -\frac{\ell^2 Q_x^2}{2 n_{UH}^2} \int_{-\infty}^{+\infty} \frac{dq_y d\Omega}{(2\pi)^2} \left|\delta n_{q_y,\Omega}\right|^2 [q_y^2 (y-y')^2 + \Omega^2 \tau^2]$$

$$-\frac{1}{2} Q_x^2 \tau^2 \langle \delta v^2 \rangle - \frac{\ell Q_x^2 \tau^2}{n_{UH}} \int_{-\infty}^{+\infty} \frac{d\Omega}{2\pi} \langle \delta n_\Omega \delta v^*_\Omega \rangle i\Omega .$$

Introducing the corresponding notation, we finally obtain

$$K = \exp\left\{ -\frac{\ell^2 Q_x^2}{2} \frac{\langle \delta n^2 \rangle}{n_{UH}^2} \langle q_y^2 \rangle (y-y')^2 \right\}$$

$$\times \exp\left\{ -\frac{Q_x^2}{2} \left[\ell^2 \frac{\langle \delta n^2 \rangle}{n_{UH}^2} \langle \Omega^2 \rangle \right.\right.$$

$$\left.\left. + \frac{2\ell}{n_{UH}} \int_{-\infty}^{+\infty} \frac{d\Omega}{2\pi} \langle \delta n_\Omega \delta v^*_\Omega \rangle i\Omega + \langle \delta v^2 \rangle \right] \tau^2 \right\}. \qquad (24)$$

The density and velocity fluctuations are related by the equation

$$\frac{\partial n}{\partial t} + \operatorname{div} n\mathbf{v} = 0.$$

We consider the drift fluctuations, for which we set $\delta v = \delta v_x$ and

$$\delta v_\Omega = -i\Omega \ell \frac{\delta n_\Omega}{n}. \qquad (25)$$

By substituting this expression into formula (24), we see that for a drift-related dispersion, there is no broadening of the frequency spectrum in the approximation at hand. This stems from the fact that the probing and scattered waves undergo multiple small-angle scatterings along their paths at distances from the backscattering point that are shorter than the correlation length; i.e., they are scattered by the same fluctuations that are responsible for the Doppler effect resulting from large-scale turbulence motions.

During backscattering far from the UHR ($4k_c^2 \ell / Q_x^2 \gg \ell_c$), the frequency spectrum is always broadened. In this case, assuming that the spectral density of the plasma-density and plasma-velocity fluctuations are even in q_x and q_y, we obtain

$$K = \exp\left\{ -\frac{\ell \ell_c Q_x^4}{64 k_c^2} \frac{\langle \delta n^2 \rangle}{n_{UH}^2} \langle q_y^2 \rangle (y-y')^2 \right.$$

$$\left. - Q_x^2 \tau^2 \left[\frac{\ell \ell_c Q_x^2}{64 k_c^2} \frac{\langle \delta n^2 \rangle}{n_{UH}^2} \langle \Omega^2 \rangle + \frac{1}{2} \langle \delta v^2 \rangle \right] \right\}.$$

In the case of drift-related dispersion, the broadening of the frequency spectrum occurs primarily owing to the Doppler effect and is essentially insensitive to multiple small-angle scatterings of the probing and scattered waves along their paths.

It should be noted that during backscattering near the UHR, the broadening of the frequency spectrum may persist, at least for the following three reasons. First, there remains the spectrum broadening associated with scatterings far from the UHR. Second, the oscillations in the nonlinear stage of drift turbulence are unlikely to satisfy the dispersion relation obtained in linear theory and used in deriving formula (25). Finally, one of the assumptions used in deriving this formula, namely, the assumption that small-scale fluctuations are completely frozen into the plasma and thus have to move as the plasma moves in the radial direction, is unduly restrictive, because it does not take into account the fact that the regions where small-scale fluctuations are generated are determined by the radial structure of the magnetic configuration, in particular, by the positions of the rational magnetic surfaces.

We emphasize that according to the above formulas, the frequency spectrum behaves in different ways in the case of immobile small-scale fluctuations [3], in which we can set $v_\Omega = 0$ in expression (24), and in the case in which small-scale fluctuations are assumed to be frozen into large-scale turbulence fluctuations and thus have to move as large-scale fluctuations move in the medium. In the latter case, the broadening of the frequency spectrum of a signal backscattered far from the UHR should depend linearly on the fluctuation wave vector. This allows us to hope that the parameters of the large-scale motions can be measured experimentally from the fluctuation wavenumber.

The above analysis shows that the contribution of the Doppler effect to the spectrum broadening during backscattering near the UHR is comparable with the contribution of multiple small-angle scatterings of the probing wave along its path, whereas the contribution from the Doppler effect far from the resonance is dominant. For this reason, when using the assumption that small-scale fluctuations are entrained in large-scale turbulence motions, it is necessary to take into account the associated broadening of the frequency spectrum.

5. CONCLUSION

The correlation function of the signals from backscattered extraordinary probing waves at two different frequencies have been examined theoretically with allowance for multiple small-angle scatterings of the probing and scattered waves along their paths. We have considered the region far from the UHR (for an extraordinary wave), the UHR region, and the region behind the conversion point (for a Bernstein mode). The analysis of the region far from the UHR has been performed by the approximate eikonal method, and the UHR region has been investigated in the limit of large-scale plasma density fluctuations. We have shown that these two approaches yield the same results in the spatial region where both of them are applicable.

We have derived expressions describing the breaking of the spatial and temporal correlations by multiple small-angle scattering. For the enhanced-scattering diagnostics, we have determined the resolution in radial wavenumbers that is provided by a correlation analysis of small-scale fluctuations with allowance for the influence of large-scale plasma turbulence.

We have investigated backscattering by small-scale fluctuations involved in large-scale turbulent motion and have derived expressions describing the frequency spectrum broadening resulting from the Doppler effect. The analysis has been carried out by taking into account the influence of multiple small-angle scatterings of the probing and scattered waves along their paths on the frequency spectrum.

The results of our study will promote an adequate interpretation of the experimental data obtained from the microwave enhanced-scattering correlation diagnostics.

ACKNOWLEDGMENTS

We are grateful to A.D. Piliya for his continuing interest in this work and critical comments. This work was supported in part by the Russian Foundation for Basic Research (project nos. 02-02-17591, 01-02-17926, 00-15-96762, 02-02-06632, and 02-02-17589), INTAS (grant no. 01-2056), and the Netherlands Organization for Scientific Research (NWO) (project no. 047.009.009).

REFERENCES

1. K. M. Novik and A. D. Piliya, Plasma Phys. Controlled Fusion **36**, 357 (1993).
2. D. G. Bulyginskiy, A. D. Gurchenko, E. Z. Gusakov, *et al.*, Phys. Plasmas **8**, 2224 (2001).
3. E. Z. Gusakov and A. V. Surkov, Fiz. Plazmy **28**, 898 (2002) [Plasma Phys. Rep. **28**, 827 (2002)].
4. V. I. Arkhipenko, V. N. Budnikov, E. Z. Gusakov, *et al.*, Pis'ma Zh. Tekh. Fiz. **19** (11), 20 (1993) [Tech. Phys. Lett. **19**, 241 (1993)].
5. E. Z. Gusakov and A. V. Surkov, Fiz. Plazmy **27**, 1027 (2001) [Plasma Phys. Rep. **27**, 971 (2001)].
6. B. Brüsehaber, E. Z. Gusakov, M. Krämer, and A. D. Piliya, Plasma Phys. Controlled Fusion **36**, 997 (1994).
7. A. D. Piliya and V. I. Fedorov, Zh. Tekh. Fiz. **46**, 1532 (1976) [Sov. Phys. Tech. Phys. **21**, 873 (1976)].
8. D. Grésillon, B. Cabrit, J. P. Villain, *et al.*, Plasma Phys. Controlled Fusion **34**, 1985 (1992).

Translated by I.A. Kalabalyk

Plasma Physics Reports, Vol. 29, No. 1, 2003, pp. 53–64. Translated from Fizika Plazmy, Vol. 29, No. 1, 2003, pp. 60–71.

OSCILLATIONS AND WAVES IN PLASMA

Numerical Simulations of Tangential Microwave Launching for EC Heating in a Tokamak

M. A. Balakina, O. B. Smolyakova, and M. D. Tokman

Institute of Applied Physics, Russian Academy of Sciences, ul. Ul'yanova 46, Nizhni Novgorod, 603950 Russia

Received May 14, 2002, in final form, July 10, 2002

Abstract—A scheme of tangential microwave launching is analyzed by using a weakly relativistic ray-tracing code. The scheme makes it possible to minimize the thickness of the heated magnetic-flux tube. Numerical simulations show that with tangential launching, the attainable localization of the power deposition region well satisfies the requirements for experiments on the stabilization of tearing modes in ITER-scale devices. © *2003 MAIK "Nauka/Interperiodica".*

INTRODUCTION

It is well known that the tearing instability in tokamaks can be stabilized by modifying the temperature profile with the help of either local auxiliary heating or noninductive current drive.

Numerous investigations (see, e.g., [1, 2] and the literature cited therein) have shown that both of these methods impose strict constraints on the width of the power deposition region. For ITER-scale devices, this size must be no larger than several centimeters. The scheme of tangential microwave launching studied in this paper is one of the possible schemes satisfying this strict limitation. Note that, by tangential launching, we mean the method of microwave launching in which the rays propagate along a tangent to a chosen magnetic surface in the electron-cyclotron-resonance (ECR) region. A possibility of minimizing the heating volume is seen from Fig. 1; of course, in this case, the aperture of a microwave beam must be smaller than the characteristic size of the absorption region for a ray crossing the magnetic surface. We note that the possibility of minimizing the width of the electron-cyclotron current-drive (ECCD) profile (which is, in fact, determined by the width of the power deposition profile) for an ITER-scale tokamak in the tangential microwave launching regime was discussed, e.g., in [3]. The calculations carried out in [3] with the use of the "cold" ray-tracing code demonstrated that for beams with an angular divergence of nearly 2°, it is possible to achieve current profiles of width no less than 5–10 cm. At first glance, a further reduction of the width of the energy deposition profile would always be possible with beams focused into the tangency point on the magnetic surface. In this

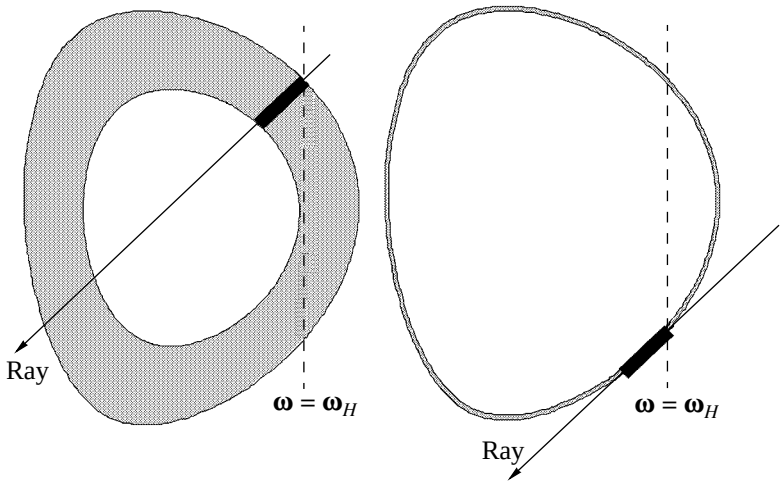

Fig. 1. Qualitative illustration of the dependence of the thickness of the heated magnetic-flux tube on the microwave propagation direction: the ray propagates along a tangent to the magnetic surface (on the right) and crosses it (on the left). The dissipation region is marked with a heavy line segment.

1063-780X/03/2901-0053$24.00 © 2003 MAIK "Nauka/Interperiodica"

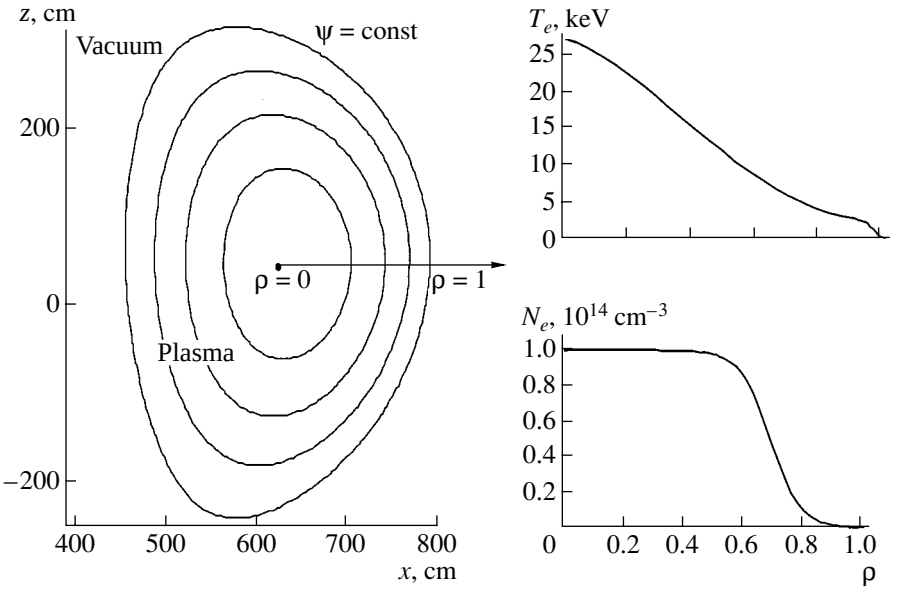

Fig. 2. Toroidal device: surfaces Ψ = const (on the left), the temperature T_e, and the density N_e (on the right).

paper, however, we will show that a substantially (several times) narrower profile can only be achieved for an optimally chosen tangency point on a given magnetic surface (we have performed such an optimization for a surface with the safety factor $q = 2$). We also use a ray-tracing code that takes into account the influence of the thermal and relativistic effects on the ray trajectories, which improves the calculation accuracy.

In this paper, we present the results from numerical simulations of the propagation and absorption of microwave radiation in a toroidal device. The calculations were performed for the ITER parameters [4]. As usual, the effective radius $\rho = 1 - \Psi/\Psi_c$ was used as a "label" of the surface of a constant magnetic poloidal flux Ψ (magnetic surface).[1] Here, Ψ is the poloidal field flux through the circular contour that is perpendicular to the symmetry axis of the torus and $\Psi_c \simeq 9.62$ is the value of the flux Ψ at the magnetic axis. Hence, we have $\rho = 0$ at the magnetic axis and $\rho = 1$ on the separatrix magnetic surface, separating the plasma from a vacuum. The temperature and density distributions [4] are also specified as functions of the effective radius ρ of the magnetic surface (Fig. 2).

The propagation of radiation in a plasma was calculated by using a ray-tracing code in a weakly relativistic approximation in which the permittivity tensor is expressed through the so-called Shkarofsky functions [5, 6]. In particular, we considered the $q = 2$ magnetic surface, in the vicinity of which one might expect the onset of the tearing instability, playing a significant role in disruptions. The results of calculations demonstrate a satisfactory efficiency of tangential launching. For instance, on this surface, we have managed to obtain a power deposition profile with a width less than one centimeter, which satisfies the present requirements fairly well.

The paper is organized as follows. In the first section, we describe the procedure of numerical ray-tracing calculations with allowance for the thermal and relativistic effects. In the second section, we discuss the features of the method proposed that should be taken into account when implementing it in practice. Finally, the third section demonstrates the computation results.

1. It is well known that the dissipation and energy transport of normal waves in the ECR region possess some specific features (see [7–9]). The dispersion relation for a plasma with the permittivity tensor ε_{pm} has the form

$$D(\omega, \mathbf{k}) = \det\left(\delta_{pm}k^2 - k_p k_m - \frac{\omega^2}{c^2}\varepsilon_{pm}\right) = 0. \quad (1)$$

For real-frequency electron-cyclotron (EC) waves propagating at a nonzero angle to the magnetic field, Eq. (1) has a solution corresponding to weakly damping waves,[2]

$$|\mathrm{Re}\,\mathbf{k}| \gg |\mathrm{Im}\,\mathbf{k}|. \quad (2)$$

In this case, however, the imaginary and real parts of the derivatives of the function $D(\omega, \mathbf{k}, \mathbf{r})$ with respect to $\mathbf{k}$ and $\mathbf{r}$ in the vicinity of the center of the cyclotron absorption line at the first and second harmonics of the

[1] In the simplest case of a cylindrical plasma column with a circular cross section, where the magnetic surfaces in the cross section constitute a set of concentric circles, the effective radius ρ is a usual magnetic surface radius, normalized to the radius of the plasma column.

[2] This is related to the character of polarization of the normal electromagnetic waves propagating at a nonzero angle to the magnetic field [7–9].

electron gyrofrequency are of the same order of magnitude:

$$\left|\mathrm{Re}\left(\frac{\partial D}{\partial \mathbf{r}}, \frac{\partial D}{\partial \mathbf{k}}\right)\right| \sim \left|\mathrm{Im}\left(\frac{\partial D}{\partial \mathbf{r}}, \frac{\partial D}{\partial \mathbf{k}}\right)\right|. \quad (3)$$

Hence, if we formally consider the function $D(\omega, \mathbf{k}, \mathbf{r})$ to be a ray Hamiltonian and take into account spatial dispersion, then, in view of relationship (3), the ray trajectories will be defined in complex space.

To avoid complexities of this kind, the ray trajectories are usually calculated in the cold-plasma approximation [7, 8]. In [10], it is shown that the influence of the thermal effects on the ray trajectories can correctly be taken into account by using the effective real Hamiltonian $H(\mathbf{r}, \mathbf{k})$ if the corresponding solution $\mathbf{k}(\mathbf{r})$ for $H = 0$ coincides with the dependence $\mathrm{Re}\,\mathbf{k}(\mathbf{r})$ obtained in solving Eq. (1). It is important (see [10] for details) that this effective Hamiltonian cannot be correctly obtained by simply omitting non-Hermitian components of the permittivity tensor.

Note that in some cases, taking into account kinetic (thermal) corrections to the cold dispersion equation is of fundamental importance. Thus, thermal corrections can be important when solving the problem of the optimum aiming of rays in the method of tangential launching. This is related to the fact that even a small difference between trajectories calculated in the cold and warm approximations may become comparable to the size of a magnetic island, which is on the order of several centimeters (see Fig. 3). When qualitatively demonstrating the advantages of tangential launching, it is quite sufficient to restrict oneself to the cold-plasma approximation (see [3]); however, in detailed calculations, taking into account thermal corrections is of crucial importance.

In this paper, we restrict ourselves to the weakly relativistic description. This is explained by the fact that gaining the computation time, the results of calculations in the weakly relativistic approximation usually (see review [11]) well coincide with the results of fully relativistic calculations (at least, in the temperature range $T_e \lesssim 30$ keV, typical of most of the existing devices).

1.1. We consider dispersion relation (1) with the permittivity tensor in the form [12]

$$\varepsilon_{xx} = \varepsilon_{yy} = 1 - \mu\frac{\omega_{pe}^2}{\omega^2}\sum_{n=-\infty}^{\infty}\frac{n^2\lambda^{|n|-1}}{2^{|n|}|n|!}\mathcal{F}_{|n|+\frac{3}{2}}(n),$$

$$\varepsilon_{xy} = -\varepsilon_{yx} = i\mu\frac{\omega_{pe}^2}{\omega^2}\sum_{n=-\infty}^{\infty}\frac{n^2\lambda^{|n|-1}}{2^{|n|}|n|!}\mathrm{sgn}(n)\mathcal{F}_{|n|+\frac{3}{2}}(n),$$

$$\varepsilon_{xz} = \varepsilon_{zx} = -\mu\frac{\omega N_\perp N_\parallel}{\omega_H}\frac{\omega_{pe}^2}{\omega^2}$$

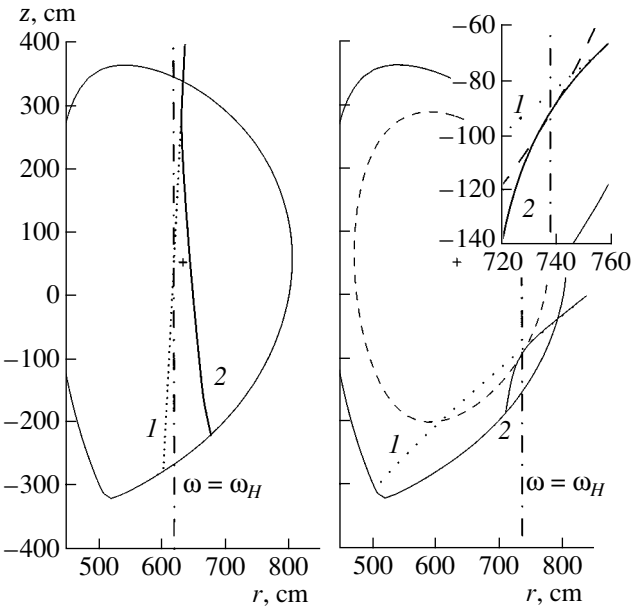

Fig. 3. The influence of the kinetic effects on the wave propagation (the fundamental harmonic of the O-mode): the launching from top at $T_e \approx 26.6$ keV and $\omega_{pe}^2/\omega^2 \approx 0.34$ (on the left) and the launching along a tangent to the $q = 2$ surface at $T_e \approx 6$ keV and $\omega_{pe}^2/\omega^2 \approx 0.2$ (on the right). Curves *1* and *2* show the results obtained with a "cold" code and a weakly relativistic code, respectively.

$$\times \sum_{n=-\infty}^{\infty}\frac{n\lambda^{|n|-1}}{2^{|n|}|n|!}\left(\mathcal{F}_{|n|+\frac{3}{2}}(n) - \mathcal{F}_{|n|+\frac{5}{2}}(n)\right),$$

$$\varepsilon_{yz} = -\varepsilon_{zy} = -i\mu\frac{\omega N_\perp N_\parallel}{\omega_H}\frac{\omega_{pe}^2}{\omega^2}$$

$$\times \sum_{n=-\infty}^{\infty}\frac{|n|\lambda^{|n|-1}}{2^{|n|}|n|!}\left(\mathcal{F}_{|n|+\frac{3}{2}}(n) - \mathcal{F}_{|n|+\frac{5}{2}}(n)\right),$$

$$\varepsilon_{zz} = 1 - \mu^2\frac{\omega_{pe}^2}{\omega^2}\sum_{n=-\infty}^{\infty}\frac{\lambda^{|n|}}{2^{|n|}|n|!}$$

$$\times\left(N_\parallel^2\left(\mathcal{F}_{|n|+\frac{7}{2}}(n) - \mathcal{F}_{|n|+\frac{5}{2}}(n)\right.\right.$$

$$\left.\left. + \mathcal{F}_{|n|+\frac{3}{2}}(n) + \mu^{-1}\mathcal{F}_{|n|+\frac{5}{2}}(n)\right)\right),$$

where

$$\begin{cases} \mathcal{F}_q(n) = -ie^{-\psi^2}\int_0^\infty dt(1-it)^{-q} \\ \times \exp[-i\phi^2 t + \psi^2/(1-it)], \\ \psi = N_\parallel c/v_T\sqrt{2}, \quad \phi^2 = \psi^2 - \mu(1 - n\omega_H/\omega \end{cases} \quad (4)$$

is the qth-order Shkarofsky function (see [5, 6, 13]) of the arguments ψ and ϕ, the z-axis is directed along the field $\mathbf{B}$, the y-axis is directed along the vector product $\mathbf{B} \times \mathbf{k}$, $N_\parallel$ and $N_\perp$ are the parallel and perpendicular (with respect to the magnetic field $\mathbf{B}$) components of the refractive index $\mathbf{N} = \mathbf{k}c/\omega$, $\mu = c^2/v_T^2$ is the squared ratio of the speed of light to the thermal electron velocity, $\omega_H = |e|B_0/mc$ is the nonrelativistic gyrofrequency, and $\lambda = N_\perp^2\omega^2/(\mu\omega_H^2)$ is the squared ratio of the Larmor radius to the wavelength. The other notation is standard.

Since the contribution from the nth harmonic to the components of the tensor ε is proportional to $\lambda^{|n|-1} \sim (v_T/c)^{2(|n|-1)}$ and $(v_T/c)^2 \ll 1$, in calculations, we restrict ourselves to considering the harmonics corresponding to $n = 0, \pm 1, \pm 2, \pm 3$.

Dispersion relation (1) can formally be considered a biquadratic equation in $N_\perp$:

$$A(N_\perp)N_\perp^4 + B(N_\perp)N_\perp^2 + C(N_\perp) = 0,$$

$$A = \varepsilon_{xx}(\varepsilon_1 - 1) - N_\parallel^2\varepsilon_1 - \check{\varepsilon}_{xz}(\check{\varepsilon}_{xz} + 2N_\parallel),$$

$$B = -N_\parallel^4\varepsilon_1 - N_\parallel^2(\chi + \varepsilon_{xx}(1 - 2\varepsilon_1)) + \varepsilon_{xx}\chi$$

$$+ (\varepsilon_{xx}^2 + \varepsilon_{xy}^2)(1 - \varepsilon_1) + 2N_\parallel(\check{\varepsilon}_{xz}(\varepsilon_{xx} - N_\parallel^2) - \varepsilon_{xy}\check{\varepsilon}_{yz}) \quad (5)$$

$$- 2\check{\varepsilon}_{yz}\check{\varepsilon}_{xz}\varepsilon_{yx},$$

$$\chi = \varepsilon_0 + \check{\varepsilon}_{xz}^2 - \check{\varepsilon}_{yz}^2, \quad \check{\varepsilon}_{xz} = \varepsilon_{xz}/N_\perp, \quad \check{\varepsilon}_{yz} = \varepsilon_{yz}/N_\perp,$$

$$C = \varepsilon_0(2N_\parallel^2\varepsilon_{xx} - N_\parallel^4 - \varepsilon_{xx}^2 - \varepsilon_{yx}^2).$$

Here, the component of the dielectric tensor ε_{zz} is represented as a sum of two terms,

$$\varepsilon_{zz} = \varepsilon_0 + \varepsilon_1 N_\perp^2,$$

where ε_0 is the component of ε_{zz} that is independent of $N_\perp$ (for the $n = 0$, it is equal to ε_{zz}) and, in the term $\varepsilon_1(N_\perp)N_\perp^2$, which is responsible for the thermal effects, the factor $N_\perp^2$ is separated out.

Near the ECR region, the factors A, B, and C in Eq. (5), as well as the wave vector $\mathbf{k}$, become complex.

The following considerations can be used to choose the real ray Hamiltonian and calculate the wave absorption. Since the plasma parameters are homogeneous along the magnetic field lines and the characteristic width of a microwave beam is smaller that the characteristic scale length of the magnetic field inhomogeneity, we can use an approximation in which the dissipative medium is considered to be locally plane-stratified. Taking into account that in this approximation, the tangential component of the wave vector is conserved, we can choose the solution for which the imaginary part of the complex vector $\mathbf{N}$ always lies in the plane perpendicular to the magnetic field. Since the problem is locally isotropic in this plane, we can assume that the imaginary part of the wave vector is directed along the real component of $\mathbf{N}_\perp$ (see [10] for details).

Then, we rewrite Eq. (5) in the form

$$A(N_\perp)(N_\perp^2 - X_1(N_\perp))(N_\perp^2 - X_2(N_\perp)) = 0. \quad (6)$$

Two solutions $X_{(1,2)}(N_\perp)$ to dispersion relation (6) correspond to eigenwaves propagating in plasma. Choosing one of these waves (with either index $j = 1$ or $j = 2$), we reduce Eq. (6) to the form

$$N_\perp^2 - X_j(N_\perp) = 0. \quad (7)$$

In the dissipation region, the values $N_\perp = N_r + iN_c$ and $X_j(N_\perp) = X_r + iX_c$ are complex; however, under conditions of weak [in the sense of inequality (2)] absorption, the following approximation can be used:

$$X_j(N_\perp) \approx X_j(N_r).$$

Then, Eq. (7) takes the form

$$N_\perp^2 \approx X_j(N_r). \quad (8)$$

In view of Eq. (7) and approximate equality (8), the real Hamiltonian discussed in Section 1 should have the form

$$H = N^2 - N_\parallel^2 - (\mathrm{Re}(\tilde{N}_\perp)_j)^2; \quad (9)$$

where $N_\parallel = \mathbf{N} \cdot \mathbf{B}/|\mathbf{B}|$ is the projection of the refractive index $\mathbf{N}$ onto the $\mathbf{B}$ field direction and $(\tilde{N}_\perp)_j = \sqrt{X_j(N_r)}$ is the approximate solution to dispersion relation (1) for the real-frequency eigenwave under consideration.

Hamiltonian (9) was considered in [10], where the corresponding ray trajectories were compared with the propagation of wave beams in a layer medium. Numerical analysis performed in [10, 14] showed that the beam trajectories in a plane-stratified medium can indeed be represented by a ray Hamiltonian in form (9), in which case the trajectory direction coincides with the direction of the energy flux. (We note that, in order to obtain this result, one should take into account the fact that in the case of a dissipative dispersive medium, the standard expression for the wave energy flux is somewhat modified; see [14, 15] for details.)

For the imaginary part of the refractive index N_c, we use the standard expression obtained under the assumption that absorption is weak [7]:

$$N_c = \frac{X_c(N_r)}{2N_r}. \quad (10)$$

The calculations show that the numerical values of the absorption coefficient N_c coincide well with its values calculated by well-known analytical formulas (see, e.g., [7]). A comparison of the computation results with analytical estimates from [7] is made in Appendix.

1.2. As a characteristic of the spatial distribution of the absorbed power, it is convenient to use the quantity

$$U(\rho) = \partial \exp(-\tau)/\partial\rho, \quad \tau(\rho) = \int_{s_0}^{s(\rho)} 2(\mathrm{Im}\,\mathbf{k}\cdot d\mathbf{s}), \quad (11)$$

where τ is the plasma optical depth measured from the entry into the plasma column to the running point s (where $\mathbf{s}$ is the coordinate along the ray trajectory).

As an illustration, Fig. 4 presents several projections (onto the xz plane) of ray trajectories (on the left) with the corresponding calculated dependences $U(\rho)$ (on the right). We note that the broadening of the power deposition profile for trajectories passing at smaller angles to the vertical direction is explained by the longer path of these trajectories along the z-axis; as a result, the thickness of the heated magnetic-flux tube increases.

As a characteristic half-width of the function $U(\rho)$, we consider the quantity

$$\Delta = \sqrt{\overline{(\rho-\bar{\rho})^2}} = \sqrt{\overline{\rho^2}-\bar{\rho}^2}, \quad (12)$$

where

$$\overline{\rho^k} = \frac{\int \rho^k U(\rho)\,d\rho}{\int U(\rho)\,d\rho}.$$

2. The direction in which the microwaves are launched into the plasma is optimized with respect of minimizing the volume of the heated plasma layer. In the first step, we choose the EC cutoff point $\mathbf{r}_0$ (which, at the same time, is the ray tangency point on a magnetic surface) lying on the surface $\Psi = \Psi_0$ inside the plasma. At this point, we find the initial values of the wave vector $\mathbf{k}_0$ by solving the set of nonlinear equations

$$H(\mathbf{r}_0, \mathbf{k}_0) = 0, \quad (13)$$

$$\mathbf{k}_0 \cdot \mathbf{N}_\Psi = 0, \quad (14)$$

$$N_\parallel^2/2 = 1 - n\frac{\omega_H}{\omega}. \quad (15)$$

We note that the solution $\mathbf{k}(\mathbf{r})$ to Eq. (13) coincides with the dependence $\mathrm{Re}\,\mathbf{k}(\mathbf{r})$ given by Eq. (1). Equation (14) is the condition for a ray trajectory to be tangent to the magnetic surface Ψ_0 at the point $\mathbf{r}_0$ (here, $\mathbf{N}_\Psi$ is the normal to the chosen magnetic surface Ψ_0 at the point $\mathbf{r}_0$). Note that in this condition, it would be more correct to use the scalar product of the group velocity by the normal. However, since the poloidal magnetic field component is smaller than the toroidal one, the angle between the projections of the group velocity and the wave vector onto the poloidal cross section of the torus is small (under our conditions, this difference is on the order of 10^{-8} rad); hence, condition (14) is satisfied to a high accuracy.

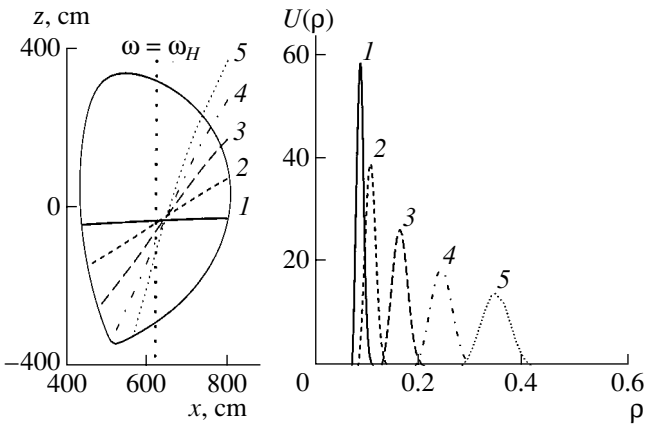

Fig. 4. Projections of ray trajectories onto the xz plane and the corresponding power deposition profiles $U(\rho)$ (for all the trajectories, $N_\parallel \approx 0$ in the ECR region).

Equation (15) is the condition of the EC cutoff in the weakly relativistic approximation. Since it is the anti-Hermitian part of the dielectric tensor that is responsible for absorption, the onset of absorption is characterized by the appearance of a nonzero anti-Hermitian part in the tensor. In the case of a weakly relativistic tensor, the equivalent condition is the appearance of imaginary parts in the Shkarofsky functions [5, 6].

In the next step, we calculate the ray trajectory with the initial conditions ($\mathbf{r}_0$, $\mathbf{k}_0$) up to the plasma–vacuum boundary from the low-field side. After the trajectory has passed through this boundary, we fix the coordinates and wave vector of this test beam ($\mathbf{r}_{\mathrm{vac}}$, $\mathbf{k}_{\mathrm{vac}}$) at an arbitrary point on the outside of the boundary. Then, a ray with the wave vector $-\mathbf{k}_{\mathrm{vac}}$ is launched from the point $\mathbf{r}_{\mathrm{vac}}$ back in the plasma. In this case, simultaneously with the ray trajectory, we calculate the absorption power, construct the profile $U(\rho)$, and determine its half-width Δ.

Because of errors in determining the initial value of the wave vector $\mathbf{k}_0$ and in calculating the trajectory itself, the ray returns into the close vicinity of the starting point $\mathbf{r}_0$. The size of this region is smaller than one millimeter. The relative error in the flux coordinate is no larger than 10^{-3}. A further improvement of the computation accuracy (at the expense of a longer computation time) allows one to reduce this error, which, however, is not of fundamental importance in our case.

Let us return to relativistic cutoff condition (15). This condition imposes a constraint on the parameters ω and $N_\parallel$. Hence, two calculation versions of the scheme with tangential launching can be proposed. In the first version, for a given initial point $\mathbf{r}_0$, the frequency ω in the ratio $\omega_H(\mathbf{r}_0)/\omega$ can be chosen such that condition (15) is satisfied for a certain specified value of $N_\parallel$. And vice versa, for a fixed frequency $\omega = \omega_0$ (which is invariant at any choice of $\mathbf{r}_0$), the correspond-

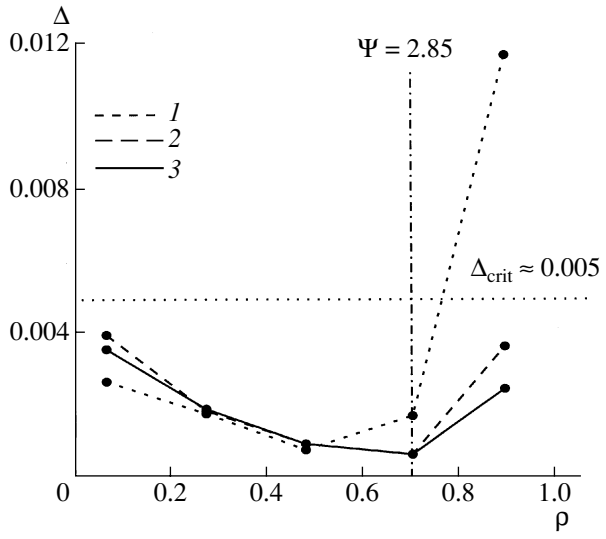

Fig. 5. Minimum width of the energy deposition region Δ vs. parameter ρ for the heated magnetic surface at three different values of $N_\parallel$ at the tangency point: (*1*) $N_\parallel = 0.3$, (*2*) $N_\parallel \approx \beta_T \approx 0.1$, and (*3*) $N_\parallel \approx 0$.

ing values of $N_\parallel$, which are determined by condition (15) and are unknown in advance, depend on the choice of the point $\mathbf{r}_0$ and the value of $\mathbf{k}_0$.

In the subsequent discussion of the results obtained, the first version will be referred to as the matched-frequency scheme, whereas the second version will be called the fixed-frequency scheme.

3. Let us consider the results of calculations by the matched-frequency scheme (Fig. 5). The tangency point $\mathbf{r}_0$ on different magnetic surfaces with the parameter ρ in the range from 0 to 1 is chosen such that the characteristic half-width of the power deposition profile Δ is smallest among all possible values (i.e., the values of the half-width Δ) obtained for any of the points lying on this magnetic surface and chosen to be the tangency point $\mathbf{r}_0$).

To examine the efficiency of the tangential launching scheme, it is convenient to choose a certain criterion (the upper bound) for the Δ values. If the half-width of the power deposition profile exceeds this bound, the profile will be considered broad. As such a bound, we use the quantity $\Delta_{crit} = 0.005$ ($\lesssim$1 cm); according to the calculations of [1], this is a maximum permissible half-width of the power deposition profile for the tearing mode to be stabilized by correcting the temperature profile with the use of an auxiliary local EC plasma heating at magnetic surfaces[3] corresponding to the safety factor $q \approx 2$. The effective radius of the $q = 2$ surface is $\rho \simeq 0.7$, and the value of the corresponding magnetic flux is $\Psi \simeq 2.85$. In Fig. 5, the effective radius corresponding to $\Psi \simeq 2.85$ ($\rho \simeq 0.7$) is shown by the vertical dashed-and-dotted line.

As can be seen in Fig. 5, over a broad range of $N_\parallel$ values and over almost the entire plasma volume (up to $\Psi \sim 2$, depending on the value of $N_\parallel$), tangential launching does ensure the highly localized power deposition with characteristic half-widths that are less than the bound value Δ_{crit}. For $N_\parallel \lesssim \beta_t = v_T/c$ ($N_\parallel$ at the tangency point), the scattering in the half-widths Δ is insignificant. For large $N_\parallel$ values, the power deposition profiles are broader; i.e., Δ increases. We note that the large $N_\parallel$ values are of interest because the ECCD efficiency increases with increasing $N_\parallel$ [16–18]. For further calculations, we chose an intermediate value of the longitudinal wavenumber: $N_\parallel \approx \beta_T$.

A certain increase in Δ near the magnetic axis ($\rho = 0$) is explained by the fact that, here, the radii of the magnetic surfaces become comparable to the width of the power deposition region.

The increase in Δ near the plasma boundary ($\rho \longrightarrow 1$) is explained by the fact that the optical depth falls at the periphery. If the dissipation region lies at the periphery of the plasma column, where the optical depth is small ($\tau_{max} < 1$, where τ_{max} is the maximum optical depth on a given trajectory), then the width of the power deposition region is determined, in fact, by the spatial distribution of the absorption coefficient $d\tau(\rho)/d\rho \sim \mathrm{Im}\mathbf{k}$ [see (11)]. And vice versa, if absorption begins in the high-temperature region (lying not too close to the plasma boundary), then we have $\tau_{max} \gg 1$, and the width Δ depends on how rapidly the optical depth approaches the value $\tau = 1$.

Both these cases are presented in Fig. 6, where the left plot compares the dependences $d\tau/d\rho$ (dashed line) and $U(\rho)$ (solid line) for a trajectory passing through the periphery of the plasma column. The right plot shows the same dependences for a trajectory passing through the plasma core.

Let us again consider the $q = 2$ magnetic surface. We examine how the width of the power deposition region depends on the choice of the tangency point $\mathbf{r}_0$ on this surface. For this purpose, we calculate several trajectories with the tangency points $\mathbf{r}_0$ on the $q = 2$ surface that are chosen as is shown in Fig. 7. As a label of each trajectory (which characterizes the position of the point $\mathbf{r}_0$ on the magnetic surface), we use the angle $\theta = \arccos(k_z/|k|)$ between the *z*-axis and the ray trajectory at the chosen tangency point $\mathbf{r}_0$. Actually, the angle θ is the deviation of the ray trajectory from the vertical near the tangency point ($\theta = 90°$ corresponds to the horizontal line, and $\theta = 0°$ corresponds to the vertical line). The value of the longitudinal wavenumber at the tangency point on each trajectory is taken as $N_\parallel \simeq \beta_T \simeq 0.1$.

[3] This stabilization scheme [1] imposes rigid constrains on the localization of the power deposition region. For comparison, in the scheme of tearing-mode stabilization by correcting the current profile via ECCD, the allowable values of the half-width of the power deposition region are one order of magnitude greater: $\Delta_{crit} \simeq 0.03$ ($\lesssim$6 cm).

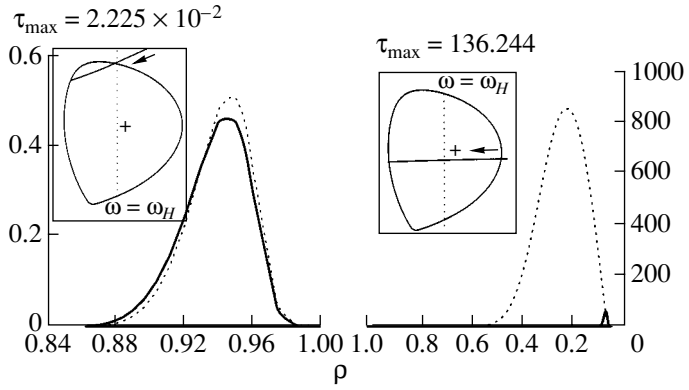

Fig. 6. Influence of the position of the dissipation region with respect to the axis of the plasma column on the width of the power deposition region for ray trajectories passing through the plasma periphery (on the left) and through the plasma core (on the right). The dashed lines show the profiles of $d\tau/d\rho$, and the solid lines show the profiles of $U(\rho)$. The corresponding trajectories, the boundary of the ECR region, and the value of τ_{max} are shown in the insets. Arrows indicate the microwave propagation direction, and the crosses indicate the position of the magnetic axis ($\rho = 0$).

The results of this calculation are presented in Fig. 8. On the left, the characteristic half-widths Δ are plotted versus the angle θ. On the right, the values of the frequency ω satisfying condition (15) (the relativistic-cutoff condition) at the point $\mathbf{r}_0$ (for given θ and $N_\parallel$) are shown. The numerical simulations were performed for both an individual ray and a parallel microwave beam 1 cm in diameter.

The beam was modeled by a set of rays with a Gaussian power distribution over the distance from the beam axis. It should be taken into account that in a real experiment, the initially broad beam should be focused in a small region near the tangency point (Fig. 9). We note that for a transversely launched horizontal ray crossing the $q = 2$ magnetic surface in the equatorial plane (in this case, we assume $T_e \approx 6$ keV and $\omega_{pe}^2/\omega^2 \approx 0.2$ in the absorption region), the size of the power deposition region along the ray amounts to ~6 cm. Hence, in the case of tangential launching, the beam waist should be no larger than 2 cm; otherwise, the use of tangential launching make no sense.[4] To estimate the role of diffraction, we use the following expressions[5] for the Gaussian beam parameters (the width D and the radius of curvature R of the beam phase front) at the distance z (see [20]):

$$D = D_0\sqrt{1 + \frac{4z^2}{k^2 D_0^4}}, \quad \frac{1}{R} = \frac{z}{z^2 + k^2 D_0^2/4}. \qquad (16)$$

[4] For a beam width of nearly 2 cm, we have $\Delta \approx \Delta_{crit}$.

[5] For more accurate estimates of the beam parameters until the beam reaches the ECR region, it is possible, in principle, to use the method of [19], which allows one to take into account diffraction and, thus, to go beyond the limits of vacuum estimates (16).

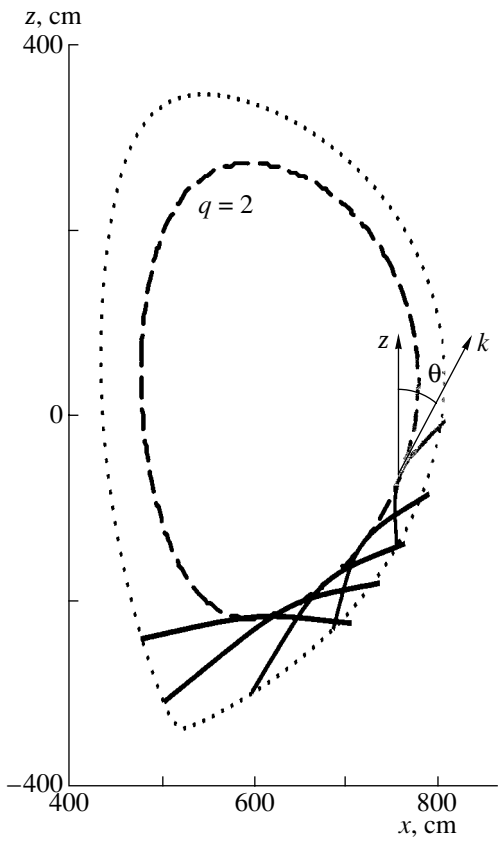

Fig. 7. Trajectories tangent to the $q = 2$ surface (which is shown with a dashed line) in the ECR region. The plasma boundary is depicted with dotted line. The angle $\theta = \arccos(k_z/|k|)$ is shown on one of the trajectories.

Let us consider a parallel beam with a small diameter (e.g., with $D = 1$ cm) in the ECR region. Such a beam complies with an actual focused beam near its waist (in Fig. 9, this region is enclosed by an oval contour). In this case, the applicability condition for the ray-tracing method consists, in fact, in that the beam should not broaden strongly, at least over the length of the absorption region ($z \approx \Delta l_r$). It is seen from formulas (16) that, in this case, the following condition must be satisfied:

$$\frac{4(\Delta l_r)^2}{k^2 D^4} \lesssim 1 \Rightarrow \Delta l_r \lesssim \frac{kD^2}{2}. \qquad (17)$$

Our estimates show that the length of the absorption region Δl_r is in the range from 5 to 8.5 cm;[6] i.e., for wavenumber of $k \approx 30$ cm^{-1} and a beam-waist diameter of $D \approx 1$ cm, condition (17) ($\Delta l_r \lesssim 15$ cm) can easily be satisfied.

[6] The absorption length about 8 cm is achieved for almost vertical rays, whereas for rays close to horizontal, the absorption length amounts to 5–6 cm.

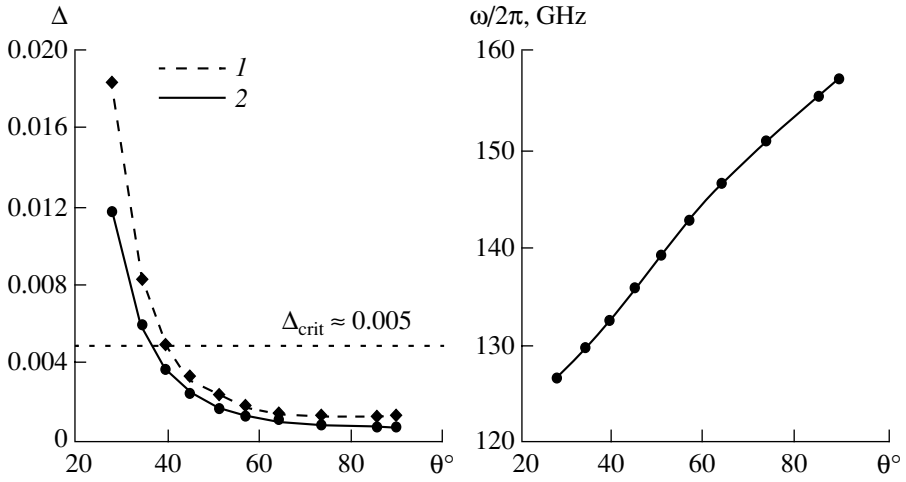

Fig. 8. Half-width of the power deposition region Δ as a function of the angle between the *z*-axis and the ray trajectory at the tangency point $\mathbf{r}_0$ for a test ray and a 1-cm-diameter beam at $N_\parallel \simeq \beta_T \simeq 0.1$ (on the left): (*1*) beam (D = 1 cm) and (*2*) test ray. The corresponding angular dependence of the microwave frequency is shown on the right.

Let us return to the discussion of Fig. 8. It is seen in the figure that as the angle θ decreases (the ray trajectories near the tangency point become closer to vertical), the width of the power deposition region increases. And vice versa, the width of the power deposition region is minimum for trajectories that are closer to horizontal. The reason is that the path length through the region where absorption is weak increases as the trajectory becomes closer to vertical. As a result, the optical depth $\tau \sim 1$ is accumulated as the ray crosses a distance that is longer than in the case of horizontal launching. In the latter case, the ray reaches the strong-absorption region after crossing the shortest distance and the optical depth τ is accumulated more rapidly.

Finally, the results obtained with the matched-frequency scheme (for the q = 2 magnetic surface and $N_\parallel \gtrsim \beta_T$ at the tangency point) allow us to conclude that for moderate deviations of the ray trajectory near the tangency point $\mathbf{r}_0$ from horizontal (our calculation show that, in this case, the angle θ takes on values in the range $40° \le \theta \le 90°$), the tangential launching ensures the highly-localized power deposition.

In conclusion of this section, we consider the fixed-frequency scheme. We chose the same tangency points $\mathbf{r}_0$ on the q = 2 magnetic surface as in Fig. 7. The calculated half-width of the power deposition region Δ is shown in Fig. 10a. We emphasize that the microwave frequency ω is fixed in this case. As a result, the $N_\parallel$ value satisfying condition (15) increases as the tangency point $\mathbf{r}_0$ shifts toward the greater values of x (or, equivalently, as the angle θ decreases; see Fig. 10b). The corresponding angular dependence of the optical depth is shown in Fig. 10c.

Hence, we can conclude that, in order to suppress the tearing mode with the use of the fixed-frequency scheme, we should restrict ourselves to trajectories satisfying inequalities $55° \le \theta \le 90°$ near the tangency point.

On the whole, based on the results numerical simulations, we can draw a general conclusion that, for the configuration of magnetic surfaces under consideration, the minimum width of the power deposition region is provided by the launching geometry in which a horizontal ray is tangent to the magnetic surface.[7]

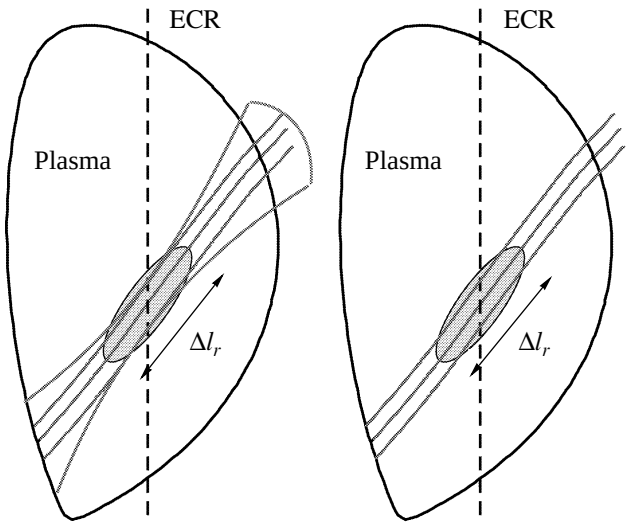

Fig. 9. Assessment of the role of diffraction: a real focused beam (on the left) and a model parallel beam (on the right).

[7] In this paper, we restrict ourselves to the consideration of only the lower part of the chosen magnetic surface. Results that can be obtained for the upper part are generally the same.

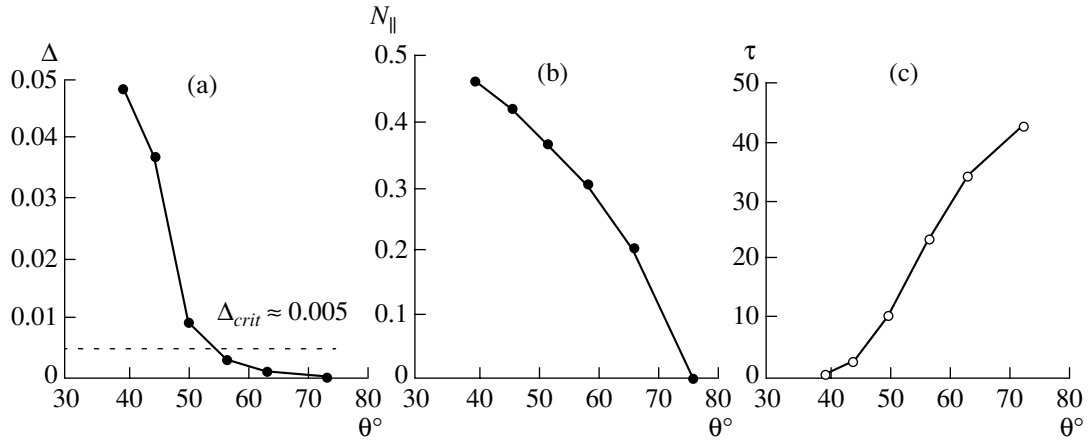

Fig. 10. Half-width of the power deposition region Δ, the longitudinal wavenumber $N_\parallel$, and the optical depth τ as functions of the angle θ between the *z*-axis and the ray trajectory at the tangency point for a fixed frequency $\omega/2\pi = 148.93$ GHz.

CONCLUSION

A numerical code taking into account the influence of the thermal effects on the ray trajectories has been developed. Computer simulations have demonstrated the possibility of minimizing the width of the power deposition region in the proposed launching scheme, in which the rays propagate at a tangent to the chosen magnetic surface in the ECR region. For the parameters of a large toroidal device, numerical simulations carried out for the case of a weakly relativistic plasma have shown that, with this launching geometry, it is possible to obtain a power deposition profile with a width of less than one centimeter. This meets both the possible requirements for experiments on the stabilization of tearing modes by noninductive current drive and the more stringent requirements for the plasma stabilization by ECR heating of a local plasma region. It is clear that this result can be refined by self-consistently taking into account the diffraction and scattering of the microwave beam.

ACKNOWLEDGMENTS

We thank E.V. Suvorov and A.A. Balakin for support and interest in this work. This work was supported in part by the Russian Foundation for Basic Research, project no. 00-02-17200.

APPENDIX

The weakly relativistic ray-tracing code described in this paper was tested by using analytical relationships for the absorption coefficients and the optical depth (see, e.g., [7]). A comparison of the calculated and analytical results is presented in Figs. 11–13.

Thus, for the transverse propagation across the magnetic field (the angle ϑ between the wave vector and the field **B** is close to π/2, so that the inequality $\beta_T \gg N_\parallel$ is satisfied), the O-mode absorption coefficient is described by the well-known expression

$$\frac{\mathrm{Im}\,k}{k_0}(\omega \longrightarrow s\omega_H) = \frac{2^{2-s}s^{2s-2}}{s!(2s+3)!!}\sqrt{\pi}qN^{2s-2}\beta_T^{2s-2}\zeta^{s+1.5}e^{-\zeta}, \quad (18)$$

where $\zeta = 2(s\omega_H - \omega)/s\omega_H\beta_T^2$, $N^2 = 1 - q/s^2$ is the refractive index, $q = s^2\omega_{pe}^2/\omega^2$, and *s* is the harmonic number. The calculated and analytical results are compared in Fig. 11.

Let us consider another example. In the "classical" interval of propagation angles

$$|\pi/2 - \vartheta| \gg \beta_T/N_\parallel, \quad (19)$$

in which the relativistic dependence of the electron gyrofrequency on the velocity can be neglected, the cyclotron absorption coefficients for the fundamental harmonics of the O- and X-modes can be represented in the form

$$\frac{\mathrm{Im}\,k_j}{k_0} = \beta_T\Phi_j(\vartheta, q)f(\zeta_j),$$

$$f(\zeta_j) = \frac{e^{\zeta_j^2}}{1 + 4/\pi\left(\int_0^{\zeta_j} e^{t^2}dt\right)^2},$$

$$\zeta_j = (\omega - s\omega_H)/N_j\beta_T\omega\cos\vartheta, \quad (20)$$

$$\Phi_j(\vartheta, q) = \frac{1}{4\sqrt{\pi}}\frac{1}{1 + K_j^2}\frac{\cos\vartheta}{q\sin^4\vartheta}$$

$$\times\left(2(1 - q\cos^2\vartheta) + K_j\cos\vartheta[2(1-q) + q\tan^2\vartheta]\right)^2,$$

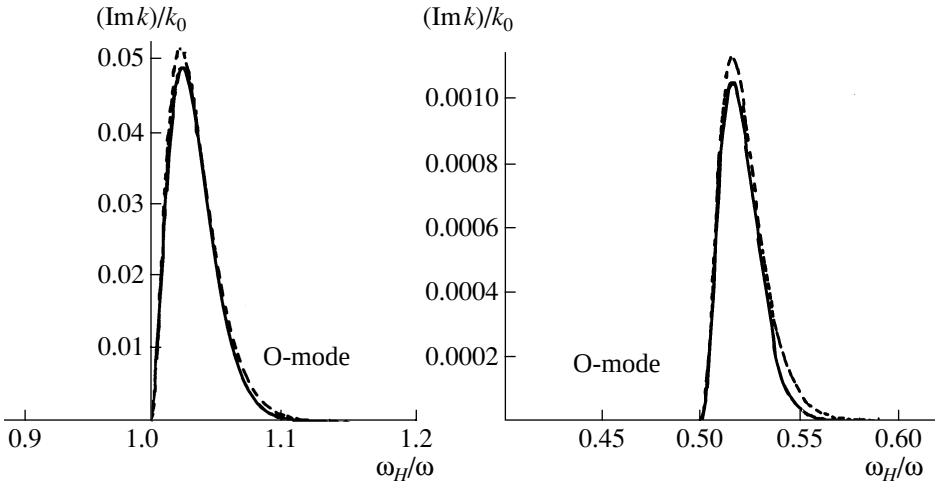

Fig. 11. Absorption coefficients Imk/k_0 calculated by formula (18) (dashed line) and by numerically solving the dispersion equation (solid line) in the case of transverse microwave propagation for the fundamental (on the left, $N_\parallel \approx 0.037$ and $\beta_T \approx 0.1$) and second (on the right, $N_\parallel \approx 0.038$ and $\beta_T \approx 0.1$) harmonics of the O-mode vs. parameter ω_H/ω at $\omega_{pe}^2/\omega^2 \simeq 0.3$.

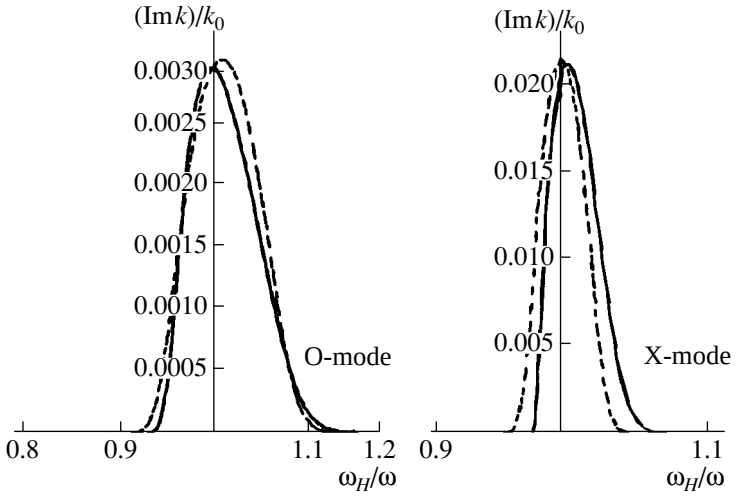

Fig. 12. Absorption coefficients calculated by formula (20) (dashed line) and by solving the dispersion equation (solid line) in the "classical" interval of angles for the fundamental harmonics of the O-mode (on the left, $N_\parallel \approx 0.53$ and $\beta_T \approx 0.044$) and X-mode (on the right, $N_\parallel \approx 0.22$ and $\beta_T \approx 0.044$) vs. parameter ω_H/ω at $\omega_{pe}^2/\omega^2 \simeq 0.3$.

where the refractive index N_j and the polarization coefficients K_j and Γ_j are defined by the well-known expressions for a cold plasma [21]:

$$N_j^2 = 1 - \frac{2v(1-v)}{2(1-v) - u\sin^2\vartheta \mp \sqrt{u^2\sin^4\vartheta + 4u(1-v)^2\cos^2\vartheta}},$$
$$K_j = \frac{2\sqrt{u}(1-v)\cos\vartheta}{u\sin^2\vartheta \pm \sqrt{u^2\sin^4\vartheta + 4u(1-v)^2\cos^2\vartheta}}, \quad (21)$$

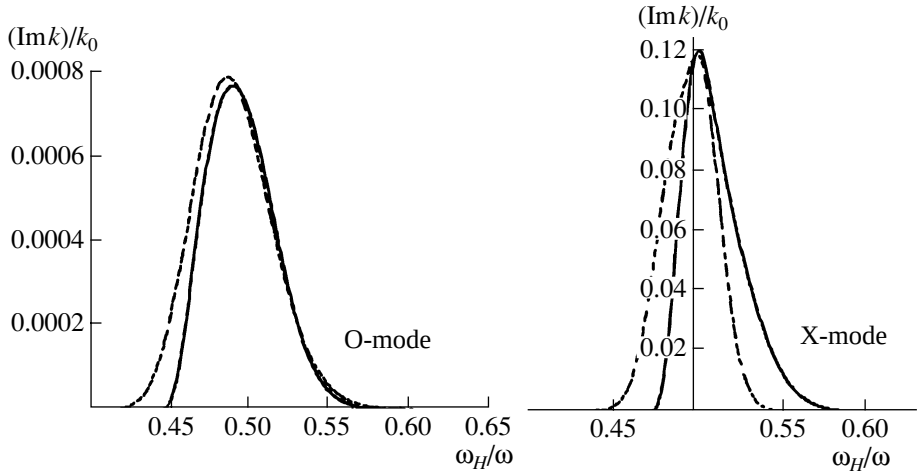

Fig. 13. Absorption coefficients calculated by formula (22) (dashed line) and by solving the dispersion equation (solid line) in the "classical" interval of angles for the second harmonics of the O-mode (on the left, $N_\| \approx 0.53$ and $\beta_T \approx 0.1$) and X-mode (on the right, $N_\| \approx 0.31$, $\beta_T \approx 0.1$) vs. parameter ω_H/ω at $\omega_{pe}^2/\omega^2 \simeq 0.3$.

$$\Gamma_j = \frac{v\sqrt{u}\sin\vartheta(1 + K_j\sqrt{u}\cos\vartheta}{1 - u - v + uv\cos^2\vartheta}.$$

Here, $u = \omega_H^2/\omega^2$, $v = \omega_{pe}^2/\omega^2$, the upper sign stands for the X-mode, and the lower sign stands for the O-mode.

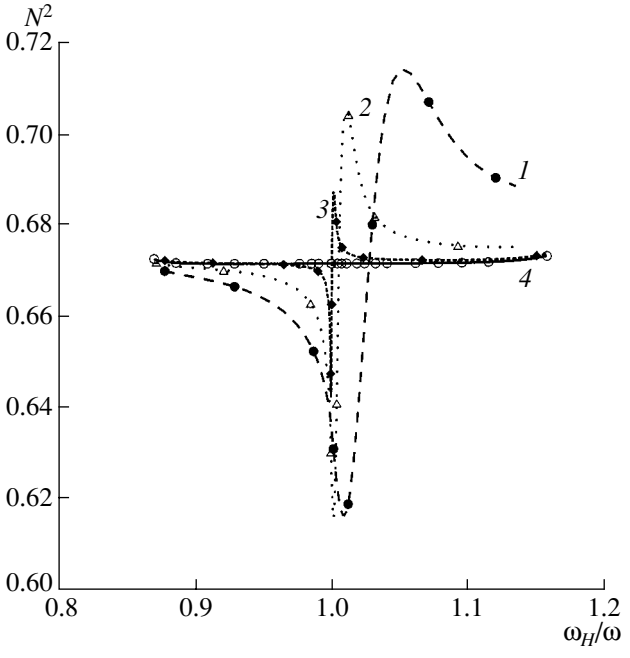

Fig. 14. Squared refractive index N^2 in the case of transverse propagation for the fundamental harmonic of the O-mode vs. parameter ω_H/ω at $\omega_{pe}^2/\omega^2 \simeq 0.3$ and different temperatures T_e: (*1*) 5, (*2*) 1, and (*3*) 0.1 keV. Curve *4* shows calculations in the cold-plasma approximation by formula (21).

Figure 12 compares the computation results with calculations by analytic formula (20). Note that the certain asymmetry of the absorption coefficient calculated from the dispersion relation (Fig. 12, solid curves) and the appreciable (in particular, for the second harmonic; see Fig. 13, solid curves) shift of the point at which absorption begins are caused by the contribution from relativistic effects that are ignored in formula (20). In particular, the beginning of absorption is determined by the condition of ECR cutoff in weakly relativistic approximation (15).

For the $s \geq 2$ harmonics in the angular range under consideration (see [7]), we have

$$\frac{\mathrm{Im}\,k_j}{k_0} = \sqrt{\pi}\frac{v\sin^{2s-2}\vartheta}{|\cos\vartheta|}\frac{s^{2s}}{s!2^{2s}}\beta_T^{2s-3}$$

$$\times N_j^{2s-4}\frac{(1 + K_j\cos\vartheta + \Gamma_j\sin\vartheta)^2}{1 + K_j^2}e^{-\zeta_j^2}. \qquad (22)$$

The results of comparison for the second harmonic are shown in Fig. 13.

Finally, Fig. 14 demonstrates the presence of resonant oscillations of the squared refractive index N^2 for the fundamental harmonic of the O-mode in the vicinity of the absorption region. Calculations were performed for different temperatures. The figure also shows the values of N^2 calculated in the cold-plasma approximation by formula (21). As could be expected, the difference from the results obtained with formula (21) is most pronounced near the ECR region and increases with increasing temperature.

REFERENCES

1. E. Westerhof, Nucl. Fusion **27**, 1929 (1987).
2. E. Westerhof, Nucl. Fusion **30**, 1143 (1990).

3. K. Hamamatsu and A. Fukuyama, Plasma Phys. Controlled Fusion **42**, 1309 (2000).
4. *ITER Physics Basis*, Nucl. Fusion **39** (12) (1999).
5. I. P. Shkarofsky, Phys. Fluids **9**, 561 (1986).
6. P. A. Robinson, J. Math. Phys. **27**, 1206 (1986).
7. V. V. Alikaev, A. G. Litvak, E. V. Suvorov, and A. A. Fraiman, *High-Frequency Plasma Heating*, Ed. by A. G. Litvak (Am. Inst. of Phys., New York, 1992), p. 1.
8. A. D. Piliya and V. A. Fedorov, *Reviews of Plasma Physivs*, Ed. by B. B Kadomtsev (Consultants Bureau, New York, 1987; Energoatomizdat, Moscow, 1984), Vol. 13.
9. E. Westerhof, in *Proceedings of the Joint Varenna–Lausanne International Workshop on Theory of Fusion Plasmas, Varenna, 1994*, p. 115.
10. E. Westerhof, Plasma Phys. Controlled Fusion **39**, 1015 (1997).
11. H. Bindslev, in *Proceedings of the 9th Joint Workshop on EC Emission and EC Heating, Borrego Springs, CA, 1995* (World Scientific, Singapore, 1995), p. 585.
12. E. Westerhof, in *Proceedings of the 3rd Carolus Magnus Summer School on Plasma Physics, Spa, Belgium, 1997*, p. 139.
13. I. P. Shkarofsky, G. Smit, L. D. Piarlstian, *et al.*, in *Proceedings of the 9th Joint Workshop on EC Emission and EC Heating, Borrego Springs, CA, 1995* (World Scientific, Singapore, 1995), p. 651.
14. M. D. Tokman, E. Westerhof, and M. A. Gavrilova, Plasma Phys. Controlled Fusion **42**, 91 (2000).
15. M. D. Tokman, E. Westerhof, and M. A. Gavrilova, Zh. Éksp. Teor. Fiz. **118**, 1319 (2000) [JETP **91**, 1141 (2000)].
16. N. J. Fisch, Rev. Mod. Phys. **59**, 175 (1987).
17. A. Yu. Kuyanov, A. A. Skovoroda, and M. D. Tokman, Plasma Phys. Controlled Fusion **39**, 277 (1997).
18. M. D. Tokman, in *Proceedings of the 9th Joint Workshop on EC Emission and EC Heating, Borrego Springs, CA, 1995* (World Scientific, Singapore, 1995).
19. G. V. Permitin and A. I. Smirnov, Zh. Éksp. Teor. Fiz. **109**, 736 (1996) [JETP **82**, 395 (1996)].
20. A. G. Peeters, Phys. Plasmas **3**, 4386 (1996).
21. V. L. Ginzburg, *The Propagation of Electromagnetic Waves in Plasmas* (Nauka, Moscow, 1967; Pergamon, Oxford, 1970).

Translated by N.F. Larionova

Plasma Physics Reports, Vol. 29, No. 1, 2003, pp. 65–77. Translated from Fizika Plazmy, Vol. 29, No. 1, 2003, pp. 72–84.

MAGNETOSPHERIC PLASMAS

Steady-State Axisymmetric Configurations of a Weakly Ionized Plasma in the Field of a Rotating Magnetized Spherical Body

A. O. Soldatkin and Yu. V. Chugunov

Institute of Applied Physics, Russian Academy of Sciences, ul. Ul'yanova 46, Nizhni Novgorod, 603950 Russia

Received May 14, 2002; in final form, August 21, 2002

Abstract—Self-consistent steady-state axisymmetric configurations of a plasma envelope with a uniform anisotropic conductivity around a rotating magnetized spherical body are considered. A set of electrodynamic and magnetohydrodynamic equations is analyzed under the assumption that the mass velocity of a moving weakly ionized plasma has only the azimuthal component. The equations describing the profile of the angular frequency of the rotating plasma envelope, the magnetic field, the conduction currents, and the plasma density distribution are solved in the limit of a strong anisotropy of the conductivity of a weakly ionized gas. The applicability of the results obtained to a qualitative interpretation of the phenomena occurring in the plasmaspheres of magnetized planets is discussed. © *2003 MAIK "Nauka/Interperiodica"*.

1. INTRODUCTION

The familiar problem of a unipolar inductor [1, 2] has recently attracted renewed interest in connection with the development of the theory of the rotating plasmaspheres of astrophysical objects such as neutron stars [3, 4] and magnetized planets [5–11]. In the plasmaspheres of neutron stars, a dominant role in the corotation of the plasma envelope is played by relativistic effects because at a certain magnetic field line, the corotational velocity may be close to the speed of light.

In the nonrelativistic models that are referred to as the models of the planetary electric generator [8, 9, 11], an important role is played by the nonrigid rotation of the plasma envelope (i.e., by the dependence of the angular rotation frequency on the coordinates). The nonrigid rotation gives rise to a number of phenomena that may be significant in considering the structures of the plasmaspheres of magnetized planets and other astrophysical objects. These are, on the one hand, electrodynamic phenomena associated with the generation of electric fields, electric currents, and magnetic field perturbations and, on the other hand, magnetohydrodynamic phenomena responsible for the establishment of the quasi-steady distributions of the field of the rotation velocities of an ionized medium, the distributions of the particle densities and particle temperatures, and the distributions of other parameters of the plasma envelope. In the general steady-state case, the problem reduces to solving a self-consistent set of hydrodynamic equations and the electrostatic equations for the current in a conducting medium with allowance for its motion. Among the factors responsible for the variety and complexity of the processes occurring in systems of this kind, there are the possible nonuniformity of the angular frequency distribution of a rotating medium, the existence of current structures, and the anisotropy of the conductivity of the medium.

In this paper, we solve a self-consistent problem of the steady-state axisymmetric rotation of a plasma envelope with a uniform conductivity around a magnetized spherical body. We assume that the conductivity of the envelope is anisotropic and consider a weakly ionized plasma. The corresponding set of electrodynamic and magnetohydrodynamic equations is analyzed under the assumption that the mass velocity of the moving plasma has only the azimuthal component. In the model chosen for further analysis, the conductivity of a weakly ionized gas is described under the assumption that its longitudinal component is governed by the magnetized electrons, whereas the ions are assumed to be unmagnetized. We look for a class of solutions that describe possible axisymmetric configurations of a rotating plasma envelope (the angular frequency distribution of the rotating envelope and the distributions of the plasma density, currents, and magnetic field perturbations over the height and azimuthal angle). The analytic solution obtained in this work, being of interest in its own right, may, on the one hand, provide additional information about the possible ways of finding some other solutions and, on the other hand, may be used as a starting point for a more adequate formulation of the problem in numerical modeling.

At the end of the paper, we discuss the possibility of using the results obtained to describe and interpret various phenomena occurring in the plasmaspheres of the Earth and other magnetized planets.

1063-780X/03/2901-0065$24.00 © 2003 MAIK "Nauka/Interperiodica"

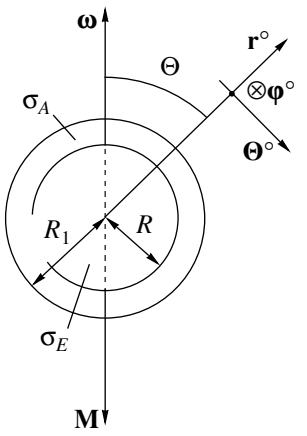

Fig. 1. Geometry of the system.

2. FORMULATION OF THE PROBLEM

We consider a plasma envelope that is corotating with a magnetized spherical body of radius R. In order to construct a simple model of the envelope, we make the following basic assumptions. We consider a steady-state ($\partial/\partial t = 0$) axisymmetric ($\partial/\partial\varphi = 0$) problem in which the mass velocity $\mathbf{V}$ of the moving medium has only the azimuthal component; hence, in spherical coordinates (r, Θ, φ) (Fig. 1), it can be expressed in terms of the angular rotation frequency ω:

$$\mathbf{V} = (0, 0, \omega r \sin\Theta).$$

The parameters of the plasma envelope, as well as the fields and the currents, can be described by Maxwell's equations and magnetohydrodynamic equations.

For simplicity, we assume that the medium consists of electrons, ions of one species, and neutrals, the corresponding densities being N_e, N_i, and N_n, respectively. We also assume that the plasma is weakly ionized:

$$N_e, N_i \ll N_n. \quad (1)$$

Under condition (1), the plasma electrons and ions should have an insignificant impact on the density distribution of neutral particles, which substantially simplifies the problem. However, condition (1) does not rule out the influence of charged particles on the velocity of the neutral plasma component in a steady state. It seems natural to assume that the velocities of the plasma electrons and ions in steady motion differ only slightly from the mass velocity:

$$\mathbf{u}_e = \mathbf{V} + \delta\mathbf{V}_e, \quad \mathbf{u}_i = \mathbf{V} + \delta\mathbf{V}_i, \quad \delta V_e, \delta V_i \ll V, \quad (2)$$

where $\mathbf{u}_e$ and $\mathbf{u}_i$ are the electron and ion velocities. Here and below, the subscripts e, i, and n refer to electrons, ions, and neutrals, respectively.

We introduce the density of the charged plasma particles, $\rho_p = M_i N_i + m_e N_e$. The viscosity coefficient is introduced as a sum of the dynamic viscosity coefficients of the electrons, ions, and neutrals: $\eta = \eta_e + \eta_i + \eta_n$. Then, using the equations of motion of the plasma components [12] and taking into account conditions (2), we can obtain the following analogue of the Navier–Stokes equation for the charged plasma component:[1]

$$\rho_p(\mathbf{V}\cdot\nabla)\mathbf{V} = -\nabla p_p + \rho_p\mathbf{g} + \eta\Delta\mathbf{V} + \frac{1}{c}\mathbf{j}\times\mathbf{B} + \rho'\left(\mathbf{E} + \frac{1}{c}\mathbf{V}\times\mathbf{B}\right), \quad (3)$$

where $\rho' = e(N_i - N_e)$ is the space charge density, $\mathbf{j} = e(N_i\delta\mathbf{V}_i - N_e\delta\mathbf{V}_e)$ is the conduction current density, $p_p = p_e + p_i$ is the pressure of the plasma electrons and ions, and c is the speed of light. Equation (3) takes into account the effects of the gravitational attraction of a spherical body on the plasma particles (the free-fall acceleration being $\mathbf{g}$), as well as the presence of the electric ($\mathbf{E}$) and magnetic ($\mathbf{B}$) fields. In what follows, the last term in Eq. (3), which is associated with the violation of plasma quasineutrality, will be omitted, because it is of the next order of smallness in relativistic effects as compared to Ampére's force. Since, at low altitudes (in comparison with the radius of the spherical body), the centrifugal force is much weaker than the gravitational force $\rho_p\mathbf{g}$, the first term in Eq. (3) can also be discarded. On the other hand, we stress that, in the plasma flow geometry under consideration, the viscous force $\eta\Delta\mathbf{V}$, which is orthogonal to both the gravitational and centrifugal forces, plays an important role and thus should be retained in the equation.

The Navier–Stokes equation should be supplemented with the equation of state and the heat balance equation. However, at this step, we are not considering heat sources corresponding to the sought-for plasma flow and close the set of equations by the condition that the mixed derivatives of the pressure be the same:

$$\frac{\partial^2 p_p}{\partial r\partial\Theta} = \frac{\partial^2 p_p}{\partial\Theta\partial r}. \quad (4)$$

This condition is valid under the above assumption that the pressure is isotropic. In turn, this assumption is justified under weak ionization condition (1), when the isotropy of the plasma pressure can be maintained by the neutral component, which plays the role of a thermostat in the approximation at hand.

The fields, currents, and charges satisfy Maxwell's equations

$$\nabla\cdot\mathbf{B} = 0, \quad \nabla\times\mathbf{B} = \frac{4\pi}{c}\mathbf{j}, \quad \nabla\cdot\mathbf{E} = 4\pi\rho', \quad \nabla\times\mathbf{E} = 0,$$

[1] It turns out that the viscosity coefficient in Eq. (3) is essentially determined by the neutral component. This reflects the effect of neutrals on plasma electrons and ions in a weakly ionized plasma under the assumption of a quasi-azimuthal motion of the plasma components.

which should be supplemented with the following familiar Ohm's law for a moving medium with an anisotropic conductivity [12]:

$$\mathbf{j} = \Sigma\left(\mathbf{E} + \frac{1}{c}[\mathbf{V}\times\mathbf{B}]\right), \quad (5)$$

where Σ is the conductivity tensor of the medium.

3. BASIC EQUATIONS

It is convenient to describe the magnetic field by the vector potential $\mathbf{A}$ in the Coulomb gauge:

$$\mathbf{B} = \nabla\times\mathbf{A}, \quad \nabla\cdot\mathbf{A} = 0.$$

The current density component j_φ is related to A_φ by

$$j_\varphi = -\frac{c}{4\pi r}\hat{\Lambda}(A_\varphi), \quad (6)$$

where $\hat{\Lambda} = \frac{\partial^2}{\partial r^2}r + \frac{1}{r}\frac{\partial}{\partial\Theta}\frac{1}{\sin\Theta}\frac{\partial}{\partial\Theta}\sin\Theta$ is a second-order differential operator.

Using Ohm's law (5), we can algebraically obtain the following local expression for the electric field in terms of the magnetic field, conduction current density, and mass velocity:

$$\mathbf{E} = \frac{\mathbf{j}}{\tilde{\sigma}_\perp} - \frac{1}{c}\mathbf{V}\times\mathbf{B} - \left(1-\frac{\tilde{\sigma}_\perp}{\sigma_\parallel}\right)\frac{\mathbf{j}\cdot\mathbf{B}}{\tilde{\sigma}_\perp B^2}\mathbf{B} - \frac{\sigma_H}{\sigma_\perp\tilde{\sigma}_\perp}\frac{\mathbf{B}\times\mathbf{j}}{B}.$$

Here, $\sigma_\parallel$, $\sigma_\perp$, and σ_H are, respectively, the longitudinal, transverse, and Hall conductivities, which all depend on the magnetic field strength. The quantity

$$\tilde{\sigma}_\perp = \sigma_\perp + \frac{\sigma_H^2}{\sigma_\perp}$$

is the effective Cowling conductivity. In the steady-state axisymmetric problem, the azimuthal component of the electric field is equal to zero, which yields the following algebraic relationship:

$$j_\varphi = \left(1-\frac{\tilde{\sigma}_\perp}{\sigma_\parallel}\right)\frac{\mathbf{j}\cdot\mathbf{B}}{B^2}B_\varphi + \frac{\sigma_H}{\sigma_\perp}\frac{[\mathbf{B}\times\mathbf{j}]_\varphi}{B}. \quad (7)$$

Combining Maxwell's equations, assuming that the Cowling conductivity $\tilde{\sigma}_\perp$ is constant,[2] and taking into account the expression for the electric field, we arrive at the equation

$$\nabla\times\left(\frac{1}{\tilde{\nu}}\mathbf{V}\times\mathbf{B} - \nabla\times\mathbf{B} + \left(1-\frac{\tilde{\sigma}_\perp}{\sigma_\parallel}\right)\frac{\mathbf{j}\cdot\mathbf{B}}{B^2}\mathbf{B} + \frac{\sigma_H}{\sigma_\perp}\frac{\mathbf{B}\times\mathbf{j}}{B}\right) = 0,$$

$$\tilde{\nu} = \frac{c^2}{4\pi\tilde{\sigma}_\perp},$$

where $\tilde{\nu}$ is the magnetic viscosity. The r and Θ components of this equation reduce to the condition $E_\varphi = 0$, which has already been used above. The φ component of the equation has the form

$$\frac{1}{\tilde{\nu}}\frac{\partial(\omega, r\sin\Theta A_\varphi)}{\partial(r,\Theta)} + \hat{\Lambda}(B_\varphi) = \frac{\partial}{\partial\Theta}\left(\left(1-\frac{\tilde{\sigma}_\perp}{\sigma_\parallel}\right)\frac{\mathbf{j}\cdot\mathbf{B}}{B^2}B_r + \frac{\sigma_H}{\sigma_\perp}\frac{[\mathbf{B}\times\mathbf{j}]_r}{B}\right) - \frac{\partial}{\partial r}\left(\left(1-\frac{\tilde{\sigma}_\perp}{\sigma_\parallel}\right)r\frac{\mathbf{j}\cdot\mathbf{B}}{B^2}B_\Theta + \frac{\sigma_H}{\sigma_\perp}r\frac{[\mathbf{B}\times\mathbf{j}]_\Theta}{B}\right), \quad (8)$$

where $\frac{\partial(U,V)}{\partial(r,\Theta)} = \frac{\partial U}{\partial r}\frac{\partial V}{\partial\Theta} - \frac{\partial U}{\partial\Theta}\frac{\partial V}{\partial r}$ is the Jacobian.

Let us consider Eq. (3). On the right-hand side of this equation, we omit the term that accounts for the centrifugal force. Then, turning to the above assumptions, we reduce the r and Θ components of the equation to the form

$$0 = -\frac{\partial p_p}{\partial r} + \rho_p g + \frac{1}{4\pi}\left(\frac{1}{r^2}\frac{\partial}{\partial r}(rA_\varphi)\hat{\Lambda}A_\varphi + \frac{1}{r}B_\varphi\frac{\partial}{\partial r}(rB_\varphi)\right),$$

$$0 = -\frac{1}{r}\frac{\partial p_p}{\partial\Theta} + \frac{1}{4\pi}\left(\frac{1}{r^2\sin\Theta}\frac{\partial}{\partial\Theta}(\sin\Theta A_\varphi)\hat{\Lambda}A_\varphi + \frac{1}{r\sin\Theta}B_\varphi\frac{\partial}{\partial\Theta}(\sin\Theta B_\varphi)\right).$$

Since the gravitational attractive force only has the radial component, it is natural to write the density in the form

$$\rho_p = \rho_p^{\text{bar}}(r) + \tilde{\rho}_p(r,\Theta),$$

where $\rho_p^{\text{bar}}(r)$ is the barometric density distribution at a constant plasma temperature T_p,

$$\rho_p^{\text{bar}} = \rho_1^{\text{bar}}\exp\left(\frac{R_1 - r}{H_p}\right), \quad H_p = 2\kappa T_p/gM_n,$$

and κ is Boltzmann's constant.

[2] In the limit of a strong anisotropy of the conductivity of an ionized gas (see below), the Cowling conductivity is equal to the longitudinal conductivity, which is, in turn, assumed to be constant.

Using condition (4), which implies that the mixed derivatives of the pressure are the same, we can easily obtain the following equation for the term $\tilde{\rho}_p(r, \Theta)$:

$$r\frac{\partial}{\partial r}\left(\frac{1}{r}\frac{\partial}{\partial\Theta}(\sin\Theta A_\varphi)\hat{\Lambda}A_\varphi\right) - \sin\Theta\frac{\partial}{\partial\Theta}\left(\frac{1}{r}\frac{\partial}{\partial r}(rA_\varphi)\hat{\Lambda}A_\varphi\right) - \frac{\partial(r\sin\Theta, B_\varphi^2)}{\partial(r, \Theta)} = 4\pi g r\sin\Theta\frac{\partial\tilde{\rho}_p}{\partial\Theta}. \quad (9)$$

The φ component of Eq. (3) has the form

$$\frac{\partial(r\sin\Theta B_\varphi, r\sin\Theta A_\varphi)}{\partial(r, \Theta)} + 4\pi\eta r^2\sin^2\Theta\hat{\Lambda}(\omega r\sin\Theta) = 0. \quad (10)$$

We thus arrive at the set of equations (6)–(10), which can be regarded as equations for the five unknown functions j_φ, A_φ, B_φ, ω, and $\tilde{\rho}_p$ because the meridional components of the magnetic field and conduction current are obtained by differentiating A_φ and B_φ, respectively. Hence, this set is closed and determines the unknown parameters of the plasma flow, magnetic field, and conduction current.

An analysis of Eqs. (6)–(10) shows that the current structure forming in the envelope distorts the magnetic self-field of the spherical body; in particular, it generates the magnetic component B_φ. Also, the anisotropy of the conductivity gives rise to the current component j_φ. As a result, the electrodynamic processes (the current and field generation) and the magnetohydrodynamic phenomena (the steady-state distributions of the angular frequency of the rotating envelope and the plasma density in it) are mutually coupled to each other.

It is convenient to switch from A_φ to the quantity Φ, which has the meaning of the magnetic flux through a spherical surface of radius r in the angular interval from 0 to Θ, and to introduce the quantity I, which is proportional to the total current through the same part of the surface:

$$\Phi = 2\pi r\sin\Theta A_\varphi, \quad I = 2r\sin\Theta B_\varphi.$$

In what follows, we will work in dimensionless variables $f = f^{\text{DIMENSIONAL}}/f_0$. The corresponding normalizing factors are the radius $r_0 = R$ of the spherical body, the angular rotation frequency $\omega_0 = \Omega_p$, the magnetic field strength $B_0 = |B(R, 0)|$ at the pole of the body, and the neutral density $r = R_1$ at the lower boundary ρ_0 of the plasma envelope. The remaining normalizing factors are expressed in terms of the factors just given: $\Phi_0 = \pi r_0^2 B_0$, $I_0 = r_0 B_0$, $j_0 = cB_0/4r_0$, and $E_0 = \omega_0 r_0 B_0/c$.

4. LIMIT OF A STRONG ANISOTROPY OF THE CONDUCTIVITY OF AN IONIZED GAS

The set of equations constructed under the basic simplifying assumptions turns out to be extremely complicated. Without additional assumptions limiting the applicability range of the sought-for solution, further analysis of the equations runs into serious difficulties.

In order to solve the equations, we develop the following model of the conductivity of an ionized gas. For simplicity, we assume that the electron and ion collision frequencies, ν_e and ν_i, are independent of altitude. We also make the following assumptions:

(i) the longitudinal conductivity $\sigma_\parallel$ is determined by the electrons, $\frac{m_e\nu_e}{M_i\nu_i} \ll 1$;

(ii) the electrons are magnetized, $\omega_{He} \gg \nu_e$;

(iii) the ions are unmagnetized, $\omega_{Hi} \ll \nu_i$; and

(iv) the following inequality is satisfied: $\omega_{He}\omega_{Hi} \ll \nu_e\nu_i$.

Here, the electron and ion gyrofrequencies, ω_{He} and ω_{Hi}, depend on the magnetic field. Accordingly, in this approximation, which will be referred to as the strongly anisotropic conductivity approximation, the expressions

$$\frac{\sigma_H}{\sigma_\perp}\frac{1}{B} = \frac{eB_0}{m_e c\nu_e} = \beta \gg 1,$$

$$\left(1 - \frac{\tilde{\sigma}_\perp}{\sigma_\parallel}\right)\frac{1}{B^2} = \frac{eB_0}{m_e c\nu_e}\frac{eB_0}{M_i c\nu_i} \ll 1$$

do not contain the magnetic field. This allows the equations to be substantially simplified:

$$j_\varphi = -\frac{1}{2\pi r}\hat{\Lambda}\left(\frac{\Phi}{r\sin\Theta}\right), \quad (11)$$

$$j_\varphi = -\frac{1}{4\pi}\frac{\beta}{r^3\sin^2\Theta}\frac{\partial(I, \Phi)}{\partial(r, \Theta)}, \quad (12)$$

$$\mathrm{Re}_M\frac{\partial(\omega, \Phi)}{\partial(r, \Theta)} + \hat{\Lambda}\left(\frac{I}{r\sin\Theta}\right) = \pi\beta\frac{\partial\left(\frac{j_\varphi}{r\sin\Theta}, \Phi\right)}{\partial(r, \Theta)} + \frac{\beta I}{r^3\sin^3\Theta}\frac{\partial(r\sin\Theta, I)}{\partial(r, \Theta)}, \quad (13)$$

$$G\frac{\partial\tilde{\rho}_p}{\partial\Theta} = 2\pi\frac{\partial\left(\Phi, \frac{j_\varphi}{r\sin\Theta}\right)}{\partial(r, \Theta)} - \frac{\partial\left(r\sin\Theta, \frac{I^2}{r^3\sin^3\Theta}\right)}{\partial(r, \Theta)}, \quad (14)$$

$$\frac{\partial(I, \Phi)}{\partial(r, \Theta)} + \chi r^2\sin^2\Theta\hat{\Lambda}(\omega r\sin\Theta) = 0. \quad (15)$$

The simplified set of equations involves the following dimensionless parameters: the magnetic Reynolds number $\mathrm{Re}_M = \frac{\omega_0 r_0^2}{\tilde{\nu}}$, the Hall parameter $\beta = \frac{eB_0}{m_e c \nu_e}$, the gravitational parameter $G = \frac{16\pi r_0 \rho_0 g}{B_0^2}$, and the viscosity parameter $\chi = \frac{16\pi}{B_0^2}\eta\omega_0$.

The Hall parameter is the ratio of the electron gyrofrequency to the electron collision frequency and thus characterizes the anisotropy of the conductivity. In the model of conductivity developed here, the transverse conductivity $\sigma_\perp(B_0)$, the Hall conductivity $\sigma_H(B_0)$, and the Cowling conductivity $\tilde{\sigma}_\perp(B_0)$ at the magnetic field strength B_0 are related to the longitudinal conductivity by the formulas

$$\sigma_\perp(B_0) = \frac{\sigma_\parallel}{\beta^2}, \quad \sigma_H(B_0) = \frac{\sigma_\parallel}{\beta}, \quad \tilde{\sigma}_\perp(B_0) = \sigma_\parallel. \quad (16)$$

The gravitational parameter is the ratio of the characteristic potential energy density of the medium in the gravitational field of a spherical body to the magnetic field energy density. The parameter χ, which will be called the viscosity parameter of the medium, is proportional to the hydrodynamic viscosity coefficient and determines the ratio of the work done by the viscous force in one period of rotation to the magnetic field energy within the envelope. Formally, the parameter χ can be expressed in terms of the interaction parameter S (known from the theory of MHD generators [13, 14]), the magnetic Reynolds number, and the Reynolds number Re obtained from dimensionality considerations:

$$\chi = \frac{4}{S}\frac{\mathrm{Re}_M}{\mathrm{Re}},$$

where $S = \frac{\tilde{\sigma}_\perp B_0^2}{c^2 \rho_0 \omega_0}$ and $\mathrm{Re} = \frac{\rho_0 \omega_0 r_0^2}{\eta}$. The interaction parameter S is the ratio of the internal force from the magnetic field to the kinetic gas pressure.

The approach used here has much in common with the method based on the Grad–Shafranov equation [1] and can be regarded as a generalization of this method to the case of a viscous plasma in a gravitational field (in a geometry with the corresponding symmetries).

In the conductivity model in question, the current density component j_φ is nonzero, and, accordingly, the related magnetic field perturbations come into play only in a plasma flow with nonzero hydrodynamic viscosity. This circumstance signifies that it is important to describe the processes occurring in a plasma envelope in a self-consistent manner, by allowing for both electrodynamic and magnetohydrodynamic forces.

In the approximation at hand, the set of equations has a first integral that relates the angular frequency ω of a rotating plasma envelope and the magnetic flux Φ to the known solution Ψ to the equation $\hat{\Lambda}(\Psi) = 0$. Combining Eqs. (11), (12), and (15), one can obtain

$$\hat{\Lambda}\left(\frac{\Phi}{r\sin\Theta} + \frac{\beta\chi}{2}\omega r\sin\Theta\right) = 0,$$

$$\frac{\Phi}{r\sin\Theta} + \frac{\beta\chi}{2}\omega r\sin\Theta = \Psi(r, \Theta).$$

5. LINEARIZATION OF EQUATIONS AND THEIR FURTHER SIMPLIFICATION

We linearize the set of equations assuming that the magnetic flux Φ is a sum of the unperturbed flux Φ_H of the magnetic self-field of a spherical body and the small perturbation Φ_1:

$$\Phi = \Phi_H + \Phi_1, \text{ where } \hat{\Lambda}\left(\frac{\Phi_H}{r\sin\Theta}\right) = 0,$$

$$|\Phi_1| \ll |\Phi_H|, \quad \left|\frac{\partial\Phi_1}{\partial r}\right| \ll \left|\frac{\partial\Phi_H}{\partial r}\right|, \quad \left|\frac{\partial\Phi_1}{\partial\Theta}\right| \ll \left|\frac{\partial\Phi_H}{\partial\Theta}\right|.$$

We also assume that the quantity I (or, in other words, the magnetic field component B_φ) is a small perturbation such that in Eq. (13), the terms quadratic in I and the term $\hat{\Lambda}(I/r\sin\Theta)$ can be neglected. The conditions for this neglect will be discussed below.

The set of equations simplified by this linearization procedure has an additional first integral that relates ω to j_φ through an arbitrary function $\Omega(\Phi_H)$ of the unperturbed magnetic flux:

$$\omega = \frac{\pi\beta}{\mathrm{Re}_M}\frac{j_\varphi}{r\sin\Theta} + \Omega(\Phi_H), \quad (17)$$

in which case the simplified set of equations takes the form

$$4\frac{\mathrm{Re}_M}{\beta^2\chi} r j_\varphi = \hat{\Lambda} j_\varphi + \frac{1}{\pi\beta}\hat{\Lambda}(r\sin\Theta\Omega(\Phi_H)), \quad (18)$$

$$\frac{\partial(I, \Phi_H)}{\partial(r, \Theta)} = -\frac{4\pi}{\beta} r^3 \sin^2\Theta j_\varphi, \quad (19)$$

$$\omega = \frac{\pi\beta}{\mathrm{Re}_M}\frac{j_\varphi}{r\sin\Theta} + \Omega(\Phi_H), \quad (20)$$

$$\frac{2\pi}{G}\frac{\partial\left(\Phi_H, \frac{j_\varphi}{r\sin\Theta}\right)}{\partial(r, \Theta)} = \frac{\partial\tilde{\rho}_p}{\partial\Theta}, \quad (21)$$

$$\frac{\Phi_H + \Phi_1}{r\sin\Theta} + \frac{\beta\chi}{2}\omega r\sin\Theta = \Psi(r, \Theta). \quad (22)$$

These equations contain two arbitrary functions, $\Omega(\Phi_H)$ and $\Psi(r, \Theta)$. Clearly, the sought-for quantities j_φ, I, ω, $\tilde{\rho}_p$, and Φ_1 corresponding to the chosen functions $\Omega(\Phi_H)$ and $\Psi(r, \Theta)$ can easily be determined from Eqs. (18)–(22), respectively.

The solution is largely determined by the form of the arbitrary functions. Below, we will choose their particular forms and, in this sense, will obtain a particular solution to the linearized problem. For simplicity, we assume that the function $\Omega(\Phi_H)$ is constant and choose the value of this constant from the conditions at infinitely large values of r. Under the assumptions $j_\varphi \xrightarrow[r\to\infty]{} 0$ and $\omega \xrightarrow[r\to\infty]{} \omega_\infty$, Eq. (20) yields $\Omega(\Phi_H) \xrightarrow[r\to\infty]{} \omega_\infty$. Thus, we fix the function

$$\Omega(\Phi_H) = \omega_\infty. \tag{23}$$

Note that since $\hat{\Lambda}(\Phi_H/r\sin\Theta) = 0$ and $\hat{\Lambda}(r\sin\Theta) = 0$, the combinations $\Phi_H/r\sin\Theta$ and $\omega_\infty r\sin\Theta$ in Eq. (22) can be included in Ψ. As a result, we obtain

$$\frac{\Phi_1}{r\sin\Theta} + \frac{\beta\chi}{2}(\omega - \omega_\infty)r\sin\Theta = \Psi_1(r, \Theta).$$

Since the quantities Φ_1 and $\omega - \omega_\infty$ are small perturbations, we can set $\Psi_1(r, \Theta) = 0$ by choosing

$$\Psi(r, \Theta) = \frac{\Phi_H}{r\sin\Theta} + \omega_\infty r\sin\Theta. \tag{24}$$

Under condition (23), the solution to Eq. (18) has the form

$$j_\varphi = \frac{\exp(-\varepsilon r)}{\varepsilon r}\sum_{n=1}^{\infty}\left[\sum_{k=0}^{n}\frac{b_k^n}{(\varepsilon r)^k}\right]\frac{\partial P_n(\cos\Theta)}{\partial(\cos\Theta)}\sin\Theta, \tag{25}$$

where $b_{k+1}^n = \dfrac{n(n+1) - k(k+1)}{2(k+1)}b_k^n$, $k = 0, 1, \ldots, n$;

P_n are Legendre polynomials; and the coefficients b_k^n are connected through a recurrence relation. Using expression (25), the integrals of the equations, and the equations themselves, we can determine the remaining sought-for quantities:

$$I = \hat{I}(\Phi_H)$$

$$-\frac{4\pi}{\beta}\int_R^r\left\{\left(\frac{\partial\Phi_H(r, \Theta)}{\partial\Theta}\right)^{-1} r^3\sin^2\Theta j_\varphi(r, \Theta)\right\}dr, \tag{26}$$

$$\omega = \omega_\infty + \frac{\pi\beta}{\mathrm{Re}_M}\frac{\exp(-\varepsilon r)}{\varepsilon r^2}\sum_{n=1}^{\infty}\left[\sum_{k=0}^{n}\frac{b_k^n}{(\varepsilon r)^k}\right]\frac{\partial P_n(\cos\Theta)}{\partial(\cos\Theta)}, \tag{27}$$

$$\tilde{\rho}_p = \tilde{P}(r) + \frac{2\pi}{G}\int_0^\Theta\frac{\partial\left(\Phi_H(r, \Theta'), \dfrac{j_\varphi(r, \Theta')}{r\sin\Theta'}\right)}{\partial(r, \Theta')}d\Theta', \tag{28}$$

$$\Phi_1 = -\frac{2\pi}{\varepsilon^3}\exp(-\varepsilon r)$$

$$\times\sum_{n=1}^{\infty}\left[\sum_{k=0}^{n}\frac{b_k^n}{(\varepsilon r)^k}\right]\frac{\partial P_n(\cos\Theta)}{\partial(\cos\Theta)}\sin^2\Theta, \tag{29}$$

where $\tilde{P}(r)$ and $\hat{I}(\Phi_H)$ are arbitrary functions of their arguments. The integrand in expression (26) should be written as a function of r and Φ_H, in which case the integration should be carried out only over r.

An important point is that the expressions contain the dimensionless parameter

$$\varepsilon = \sqrt{4\frac{\mathrm{Re}_M}{\beta^2\chi}} = \frac{r_0 B_0}{c}\sqrt{\frac{\sigma_\parallel}{\beta^2\eta}}, \tag{30}$$

which determines the characteristic dimension $\delta h = r_0/\varepsilon$ of the region where the plasma rotation in the envelope is nonrigid and where the azimuthal current j_φ flows and the perturbations of the plasma density and magnetic field are localized.[3]

The particular form of the solution is determined by the boundary conditions. It is clear that based on the symmetry of j_φ with respect to $\Theta = \pi/2$ (i.e., to the equatorial plane), the solutions may be divided into two classes: symmetric solutions, constructed from harmonics with odd numbers n, and antisymmetric solutions, constructed from harmonics with even numbers n. For a prescribed form of the unperturbed magnetic flux Φ_H, each class of solutions is characterized by a certain symmetry of the physical quantities. Let us consider the symmetry properties of Eqs. (18)–(22) with arbitrary functions chosen in forms (23) and (24). One can see that the following possible changes of variables leave the set of equations invariant:

$$\Theta \to \pi - \Theta, \quad j_\varphi \to j_\varphi, \quad \Phi_H \to \Phi_H,$$
$$\omega \to \omega, \quad \Phi_1 \to \Phi_1, \quad \tilde{\rho}_p \to \tilde{\rho}_p, \quad I \to -I;$$
$$\Theta \to \pi - \Theta, \quad j_\varphi \to j_\varphi, \quad \Phi_H \to -\Phi_H,$$
$$\omega \to \omega, \quad \Phi_1 \to \Phi_1, \quad \tilde{\rho}_p \to -\tilde{\rho}_p, \quad I \to I;$$
$$\Theta \to \pi - \Theta, \quad j_\varphi \to -j_\varphi, \quad \Phi_H \to \Phi_H,$$
$$\omega \to -\omega, \quad \Phi_1 \to -\Phi_1, \quad \tilde{\rho}_p \to -\tilde{\rho}_p, \quad I \to I;$$
$$\Theta \to \pi - \Theta, \quad j_\varphi \to -j_\varphi, \quad \Phi_H \to -\Phi_H,$$
$$\omega \to -\omega, \quad \Phi_1 \to -\Phi_1, \quad \tilde{\rho}_p \to \tilde{\rho}_p, \quad I \to -I.$$

[3] Using the first of relationships (16), we can rewrite expression (30) as $\delta h B_0 c^{-1}\sqrt{\sigma_\perp(B_0)\eta^{-1}}$. Then, we can see that the characteristic scale on which the plasma flow is nonuniform follows from the condition that the Hartman parameter corresponding to the conductivity $\sigma_\perp(B_0)$ be equal to unity [1]. In turn, this condition can be interpreted as reflecting the balance between the magnetic force acting on the medium and the viscous forces in the medium in the established equilibrium state.

Regardless of the form of j_φ, the symmetry of Φ_H with respect to the equator is of the same kind as the symmetry of the angular frequency distribution ω and magnetic flux perturbation Φ_1. At the same time, the symmetries of the distributions of the density $\tilde{\rho}_p$ and quantity I with respect to the equatorial plane are determined by the form of the unperturbed magnetic flux: when j_φ and Φ_H are symmetric with respect to the equator, the function $\tilde{\rho}_p$ is symmetric, while the function I is antisymmetric.

We point out the following important consequence of the symmetry conditions in our problem. For symmetric distributions of j_φ and Φ_H, the distributions of the angular frequency and density $\tilde{\rho}_p$ may remain symmetric during nonrigid rotations even under appropriate boundary conditions only if the distribution of I is antisymmetric with respect to the equator, in which case the azimuthal component B_φ of the magnetic field should be antisymmetric. In this case, it is necessary to impose the condition $B_\varphi = 0$ in the equatorial plane; or to introduce an external current that flows, e.g., in the equatorial plane and closes the current system under consideration [15]

$$(j_{\text{ext}})_r = \frac{1}{\pi r} B_\varphi \delta\left(\Theta - \frac{\pi}{2}\right)$$

(introducing this current goes beyond the scope of magnetohydrodynamic description); or to choose another appropriate form of the function $\hat{I}(\Phi_H)$.

6. THE SIMPLEST SYMMETRIC SOLUTION

As an example of the simplest solution, we consider a symmetric solution constructed solely from the $n = 1$ harmonic. One can readily see that under the above conditions $j_\varphi \xrightarrow[r\to\infty]{} 0$ and $\omega \xrightarrow[r\to\infty]{} \omega_\infty$, this solution corresponds to the boundary condition

$$\omega(R_1, \Theta) = \omega_1.$$

It is also necessary to impose the additional condition $B_\varphi(r, 0) = B_\varphi(r, \pi/2) = B_\varphi(r, \pi) = 0$ in order to not go beyond the limits of hydrodynamic description, i.e., not to introduce the external localized radial current that closes the current system under consideration.

The geometry of the configuration in question is illustrated in Fig. 1. Supposing that all of the above assumptions are satisfied in the region $r > R_1$, we consider the solution only in this region and impose the corresponding conditions at its boundary $r = R_1$. We can consider the region $r > R_1$ separately, neglecting the interaction between a plasma envelope and a spherical body and assuming that the following condition is satisfied: $\sigma_A \ll \sigma_E \ll \sigma_\parallel$, where σ_A is the conductivity of the isotropic interlayer and σ_E is the conductivity of the body. The corrections to the solution that come from the current system in the body should be proportional to the ratio of the conductivities of the ball and of the envelope. Under the conditions in question, these corrections are certainly small.

We adopt a dipole field as an unperturbed magnetic field; moreover, to be specific, we assume that the magnetic moment **M** of the spherical body and the vector of its angular rotation velocity are oppositely directed (Fig. 1). Then, the unperturbed magnetic flux has the form

$$\Phi_H = -\frac{\sin^2\Theta}{r}.$$

We consider the simplest symmetric solution under the assumption that the localization parameter is large ($\varepsilon \gg 1$), because it is the assumption that is consistent with the applicability range of the solution:

$$\omega = \omega_\infty + (\omega_1 - \omega_\infty)\frac{R_1^2}{r^2}\exp(\varepsilon(R_1 - r)),$$

$$j_\varphi = \frac{(\omega_1 - \omega_\infty)\mathrm{Re}_M}{\pi\beta}\frac{R_1^2}{r}\exp(\varepsilon(R_1 - r))\sin\Theta,$$

$$\Phi = -\frac{\sin^2\Theta}{r} - (\omega_1 - \omega_\infty)\frac{\beta\chi}{2}R_1^2\exp(\varepsilon(R_1 - r))\sin^2\Theta.$$

We determine the function I in the upper and lower hemispheres separately, by choosing the arbitrary function $\hat{I}(\Phi_H)$ in such a way that the current density is finite everywhere and the function I itself vanishes at $\Theta = \pi/2$:

$$I = (\omega_1 - \omega_\infty)\chi\varepsilon^2 R_1^2 r^4 \exp(\varepsilon(R_1 - r))$$

$$\times\left(-\cos\Theta \pm \varepsilon\int_r^{\frac{r}{\sin^2\Theta}}\sqrt{1 - \frac{r'\sin^2\Theta}{r}}\frac{r'^4}{r^4}\frac{1 - \dfrac{3}{\varepsilon r'} - \dfrac{3}{(\varepsilon r')^2}}{1 + \dfrac{1}{\varepsilon r}}\right.$$

$$\left.\times\exp(\varepsilon(r - r'))dr'\right).$$

Here and below, the plus sign refers to the upper hemisphere ($0 < \Theta < \pi/2$) and the minus sign refers to the lower hemisphere ($\pi/2 < \Theta < \pi$). It is easy to show that at small angles Θ, the solution I so constructed is proportional to Θ^2; hence, taking into account the antisymmetry of the function I, we see that the condition $B_\varphi(r, 0) = B_\varphi(r, \pi) = 0$ is satisfied.

The meridional component of the magnetic field and the meridional current density are determined by

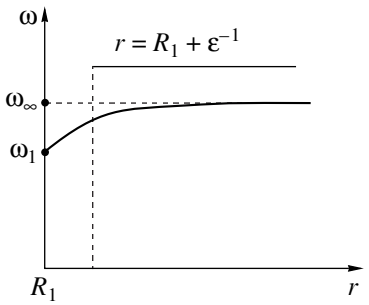

Fig. 2. Simplest symmetric solution to the linearized problem for $\mathbf{M} \uparrow\downarrow \boldsymbol{\omega}$ and $\omega_\infty > \omega_1$. The distributions of the angular frequency of a rotating plasma envelope are shown.

differentiating the magnetic flux:

$$B_r = -\frac{1}{2r^2}\frac{\partial \Phi}{\partial(\cos\Theta)}, \quad B_\Theta = -\frac{1}{2r\sin\Theta}\frac{\partial \Phi}{\partial r},$$

$$j_r = -\frac{1}{2\pi r^2}\frac{\partial I}{\partial(\cos\Theta)}, \quad j_\Theta = -\frac{1}{2\pi r\sin\Theta}\frac{\partial I}{\partial r}.$$

The plasma density component $\tilde{\rho}_p$ is obtained by integration:

$$\tilde{\rho}_p = -(\omega_1 - \omega_\infty)\frac{2\mathrm{Re}_M \varepsilon}{\beta G}\frac{R_1^2}{r^3}\exp(\varepsilon(R_1 - r))\sin^2\Theta + \tilde{P}(r).$$

Since we have incorporated the plasma density component that depends only on r into the barometric density distribution $\rho_p^{\mathrm{bar}}(r)$, we can set the free function equal to zero, $\tilde{P}(r) = 0$, taking into account, in particular, the boundary condition

$$\rho_p \xrightarrow[r\to\infty]{} 0.$$

In this case, the plasma density has the form

$$\rho_p = \rho_1^{\mathrm{bar}}\exp\left(\frac{R_1 - r}{H_p}\right) + \tilde{\rho}_1\frac{R_1^3}{r^3}\exp(\varepsilon(R_1 - r))\sin^2\Theta,$$

$$\tilde{\rho}_1 = (\omega_\infty - \omega_1)\frac{2\mathrm{Re}_M \varepsilon}{\beta G R_1}.$$

This expression implies that if the magnetic moment of the body is directed opposite to the angular velocity of the rotating envelope, then, for $H_p < 1/\varepsilon$, the conditions $\rho_p > 0$ and $\rho_p \xrightarrow[r\to\infty]{} 0$ can be satisfied simultaneously only when $\omega_\infty > \omega_1$, which, in turn, indicates that the plasma envelope should undergo super-rotation, i.e., the upper layers of the envelope should rotate at higher angular speeds than the lower layers. Depending on the ratio between the parameters H_p and $1/\varepsilon$, the rotation in the chosen altitude range is dominated either by a spherically symmetric barometric density distribution or by electromagnetic forces, which are accounted for by the second term in the expression for the plasma density. In the latter case, we have $\rho_p > 0$; consequently, the quantity $\tilde{\rho}_1$ should be positive. The amplitude ρ_1^{bar} of the barometric density distribution is determined by external factors, e.g., by ionization sources in the chosen altitude range.

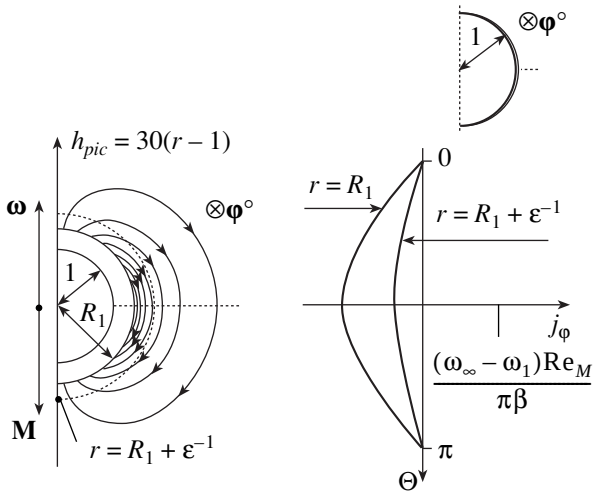

Fig. 3. Simplest symmetric solution to the linearized problem for $\mathbf{M} \uparrow\downarrow \boldsymbol{\omega}$ and $\omega_\infty > \omega_1$. The lines of the meridional component of the perturbed dipole magnetic field and the profiles $j_\varphi(R_1, \Theta)$ and $j_\varphi(R_1 + \varepsilon^{-1}, \Theta)$ of the azimuthal component of the conduction current are shown.

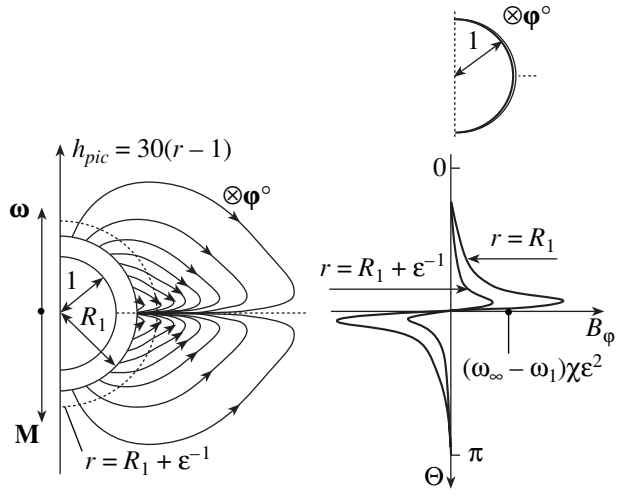

Fig. 4. Simplest symmetric solution to the linearized problem for $\mathbf{M} \uparrow\downarrow \boldsymbol{\omega}$ and $\omega_\infty > \omega_1$. The lines of the meridional component of the conduction current and the profiles $B_\varphi(R_1, \Theta)$ and $B_\varphi(R_1 + \varepsilon^{-1}, \Theta)$ of the azimuthal component of the magnetic field shown are shown.

The results obtained are illustrated in Figs. 2–5. For definiteness, the plots were calculated for the following parameter values, which are consistent with the applicability range of the solution and refer to altitudes of 80 to 100 km in the Earth's ionosphere:

$$R_1 = 1.00125, \quad \mathrm{Re}_M = 40, \quad \beta = 90, \quad \chi = 2 \times 10^{-6},$$
$$G = 42000, \quad \omega_\infty = 1.4, \quad \omega_1 = 1. \tag{31}$$

Figure 2 shows the angular frequency profile. The angular frequency distribution is spherically symmetric; in accordance with the above analysis, it is necessary that $\omega_\infty > \omega_1$. At distances of about several δh, the angular rotation frequency becomes constant. Note that, at these distances, the corresponding kinetic energy density $\rho_p \omega^2 r^2/2$ exponentially decreases to zero.

Figure 3 shows the pattern of the lines of the meridional component of the perturbed magnetic field and the profiles of the azimuthal current component j_φ at constant r (the direction of the φ-axis is indicated).[4] In the case $\varepsilon \gg 1$, which we are considering here, the meridional component of the magnetic field perturbation is strongly localized, unlike the unperturbed dipole magnetic field of a spherical body. The figure displays two patterns of the lines of the meridional component of the magnetic field perturbation: shown on the left are the lines in the region $r > 1$ on a scale enlarged by a factor of 30 in the r direction, and the inset in the upper right corner of the figure shows the lines on an ordinary radial scale. The dashed line in the larger scale image indicates the position of the boundary $r = R_1 + \varepsilon^{-1}$. The current with the density j_φ is seen to form a jet, which is slightly localized in the angular coordinate and in which, at $\mathbf{M} \uparrow\downarrow \boldsymbol{\omega}$ and $\omega_\infty > \omega_1$, the current flows in the direction opposite to that of the mass velocity of the moving medium. A comparison between the profiles of the azimuthal component of the conduction current density, $j_\varphi(R_1, \Theta)$ and $j_\varphi(R_1 + \varepsilon^{-1}, \Theta)$, illustrates how the azimuthal current density distribution changes with altitude.

Calculation of the total azimuthal current density in the system for $\varepsilon \gg 1$ yields

$$I_\varphi^{\mathrm{sum}} = \int_{R_1}^{\infty} dr \int_0^{\pi} r j_\varphi d\Theta \approx \frac{(\omega_\infty - \omega_1)\sqrt{\chi \mathrm{Re}_M}}{\pi}. \tag{32}$$

Figure 4 shows the structure of the lines of the meridional component of the conduction current density and the profiles $B_\varphi(R_1, \Theta)$ and $B_\varphi(R_1 + \varepsilon^{-1}, \Theta)$ of the azimuthal component of the perturbed magnetic field. The figure displays two patterns of the lines of the meridional component of the conduction current: shown on the left are the lines in the region $r > 1$ on a scale enlarged by a factor of 30 in the r direction, and the inset in the upper right corner of the figure shows the lines on an ordinary radial scale. The dashed line in the larger scale image indicates the position of the boundary $r = R_1 + \varepsilon^{-1}$.

[4] The conduction current in the form of a delta function at the origin of the coordinates, which is generated by the dipole component of the magnetic field perturbation, is not shown in the figure.

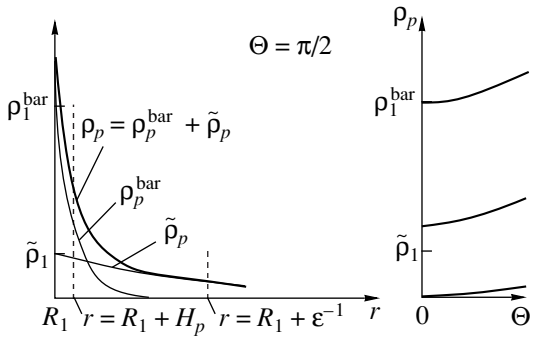

Fig. 5. Simplest symmetric solution to the linearized problem for $\mathbf{M} \uparrow\downarrow \boldsymbol{\omega}$ and $\omega_\infty > \omega_1$. The density distribution ρ_p of the charged plasma component in the equatorial plane at $\rho_1^{\mathrm{bar}} = 4\tilde{\rho}_p$ and the boundaries $r = R_1 + H_p$ and $r = R_1 + \varepsilon^{-1}$ (on the left) and the corresponding density profiles $\rho_p(R_1, \Theta)$, $\rho_p(R_1 + H_p, \Theta)$, and $\rho_p(R_1 + \varepsilon^{-1}, \Theta)$ of the charged plasma component (on the right) are shown.

We can see that the azimuthal component of the magnetic field is localized near the equatorial plane. The localization results from an intense quasi-radial current that flows in the equatorial plane and forms a closed circuit between the current loops in the upper and lower hemispheres. The reasons for the onset of this current are twofold. On the one hand, in the case in question, specifically, in the strongly anisotropic conductivity approximation ($\beta \gg 1$), in which the longitudinal conductivity is much higher than the transverse and Hall conductivities, the current should flow along the magnetic field. On the other hand, in the system under consideration, the current cannot flow along the magnetic field lines in the equatorial plane because of the symmetry properties of the problem: the current loops in the upper and lower hemispheres should be closed in a circuit through the equatorial plane. Because of these two circumstances, the current lines should concentrate in the equatorial region, in which the current should flow perpendicular to the magnetic field lines. In [5], such considerations led us to the suggestion that the generation of electric fields and currents in a system in which the conductivity of a plasma envelope is anisotropic can be described at a qualitative level by using an isotropic conductivity profile corresponding to a transverse conductivity in an actual anisotropic envelope, because it is the transverse conductivity of the medium that ensures the closing of the current loops. The present analysis of the solution in the case of a highly anisotropic conductivity of the medium shows that this suggestion appears to be justified. First,

it is the transverse conductivity that enters into the expression for the parameter ε, which determines the form of the solution. Second, let us consider the amplitude j_m^A of the meridional conduction-current density component, which has been calculated above. We introduce the dimensionless coefficient $\Delta = |\omega_\infty - \omega_1|$ (characterizing the degree to which the rotation of the plasma envelope is nonrigid) and write the amplitude j_m^A in dimensional form:

$$j_m^A = j_0 \frac{\Delta \chi \varepsilon^2 R_1^2}{2\pi} = \frac{\Delta}{2} E_0 \sigma_\perp(B_0). \quad (33)$$

From this expression, we can see that, in the system under discussion, the transverse conductivity indeed predominates in the meridional current, which was considered in [5].

It is also of interest to consider the amplitude j_φ^A of the meridional current density. In dimensional form, we obtain

$$j_\varphi^A = j_0 \frac{\Delta \mathrm{Re}_M R_1}{\pi \beta} = \Delta E_0 \sigma_H(B_0) \quad (34)$$

and, consequently, arrive at the relationship

$$\frac{j_m^A}{j_\varphi^A} = \frac{1}{2\beta} \ll 1,$$

which indicates that the meridional current is far less intense than the azimuthal current. The expression for the total current I_m^{sum} circulating in meridional loops is fairly difficult to analyze. However, based on the above relationship for the ratio of the amplitudes of the total currents, we can conclude that the following condition is satisfied:

$$I_m^{\mathrm{sum}} \sim I_\varphi^{\mathrm{sum}}/\beta \ll I_\varphi^{\mathrm{sum}}.$$

The question then arises of how to close the magnetic field lines and how to form closed current loops in the upper and lower hemispheres. In principle, it might be possible to consider a layer $r < R_1$ with isotropic conductivity, to find a solution for this layer, and to join it with the solution for the outer layer using the conditions at the boundary between the layers. However, since the inhomogeneous problem is very difficult to solve, we restrict ourselves to considering only one layer, assuming that it is, in principle, possible to close the current system and magnetic field lines through the lower lying layers.

The left half of Fig. 5 shows the density distribution ρ_p of charged plasma particles in the equatorial plane (at $\Theta = \pi/2$). For definiteness, we present the distribution calculated for $\rho_1^{\mathrm{bar}} = 4\tilde{\rho}_p$. The positions of the boundaries $r = R_1 + H_p$ and $r = R_1 + \varepsilon^{-1}$ are indicated by the dashed lines. We can assert that at distances from the boundary $r = R_1$ that are several times longer than H_p, the quantity ρ_1^{bar} plays a minor role. The right half of Fig. 5 shows the density profiles $\rho_p(R_1, \Theta)$, $\rho_p(R_1 + H_p, \Theta)$, and $\rho_p(R_1 + \varepsilon^{-1}, \Theta)$ of the charged plasma component. One can see that the spherically symmetric part of the density distribution decreases fairly rapidly.

To conclude this section, we present the expression for the total power of Ohmic losses as a function of the integral of the product $\mathbf{j} \cdot (\mathbf{E} + c^{-1}[\mathbf{V} \times \mathbf{B}])$. In dimensional form, the expression is as follows:

$$Q = \frac{2\Delta}{3} E_0 j_m^A 4\pi r_0^2 \delta h. \quad (35)$$

The fact that the quantity $4\pi r_0^2 \delta h$ is the volume of a narrow spherical layer of thickness δh clarifies the physical meaning of expression (35).

The electric field and current are generated at the expense of the energy of rotation of a central body. The formulation of the steady-state problem implies that this energy is infinitely high, in which case it is necessary that the energy of Ohmic losses during the time interval T under consideration be less than the energy K_E of rotation of a spherical body: $QT \ll K_E$. The amount by which the effect in question changes the angular frequency Ω_P of the rotating body during the time T is easy to estimate:

$$\delta\Omega_P \approx \Omega_P \frac{1}{2} \frac{QT}{K_E}.$$

7. APPLICABILITY CONDITIONS OF THE SOLUTION OBTAINED

In the problem as formulated, an important assumption is that the medium is weakly ionized; this corresponds to the condition $\rho_p \ll \rho_n$. Of course, for $H_n < 1/\varepsilon$, the density of the neutral component decreases more rapidly with increasing altitude than does the density of the charged plasma component; hence, this condition is satisfied only in a certain altitude range. However, under the conditions

$$\rho_1^{\mathrm{bar}}, \tilde{\rho}_1 \ll 1, \quad (36)$$

the altitude range over which the medium remains weakly ionized can be considered to be sufficiently large.

Above, we have analyzed the conditions underlying the conductivity model and imposed restrictions on the ratios of the collision frequencies to the electron and ion gyrofrequencies. By substituting the above solution to the simplified set of equations (18)–(22) into the set of equations (11)–(15), we can show that the solution is valid under the following conditions:

$$\varepsilon \gg 1, \quad (37)$$

$$\frac{\varepsilon}{\beta^2} \ll \frac{1}{8\pi}, \tag{38}$$

$$\Delta\sqrt{\chi \mathrm{Re}_M} \ll 1. \tag{39}$$

In other words, inequalities (37)–(39) are applicability conditions for the above procedures of linearizing and simplifying the set of equations (11)–(15). Condition (37) implies that the perturbations are strongly localized, and condition (38) indicates that the conductivity should be highly anisotropic. Finally, condition (39) can be regarded as providing upper limits on the viscosity of the medium and the kinetic energy density in it in comparison, respectively, with the magnetic viscosity and with the magnetic field energy at a given degree to which the rotation of a envelope in the plasmasphere is nonrigid ($\Delta = |\omega_\infty - \omega_1|$).

Clearly, the applicability conditions for the solutions constructed from any harmonics of j_φ that are symmetric with respect to the equator do not differ from the above applicability conditions for the solution constructed solely from the $n = 1$ harmonic. The reason for this is twofold: first, for $\varepsilon \gg 1$, the radial parts of the solutions depend only weakly on the harmonic number n, and, second, in the equatorial region, all symmetric solutions behave in the same manner.

In contrast, near the equator, the behavior of the solutions that are antisymmetric in j_φ differs radically from that of the symmetric solutions. Thus, in an antisymmetric solution, the meridional component of the magnetic field perturbation is antisymmetric; i.e., the radial magnetic field component in the equatorial plane is nonzero. On the other hand, in this plane, the unperturbed magnetic field does not have a radial component. Consequently, for a solution antisymmetric in j_φ, it is, in principle, impossible to satisfy one of the conditions used in the linearization procedure, namely, the condition that the magnetic field perturbation near the equatorial plane is small. Hence, it is clear that the equatorial region in a narrow angular range should be described by the nonlinear equations.

8. APPLICABILITY OF THE RESULTS OBTAINED TO A DESCRIPTION OF THE PLASMASPHERES OF MAGNETIZED PLANETS

Above, we have obtained a particular solution to the self-consistent set of equations describing the steady-state axisymmetric configurations of a plasma envelope with an anisotropic conductivity in the field of a rotating spherical body. We have developed a model of the conductivity of the envelope and have imposed a number of conditions on the parameters of the problem. In this section, we consider the possibility of applying the results obtained from the model to a description of the plasmaspheres of magnetized planets.

The description of a real plasmasphere by the above model of the steady-state corotation of a magnetized spherical body and a plasma envelope should be carefully applied to a direct comparison of the calculated results with experimental data. Being intrinsically nonuniform and unsteady, real systems are subject to numerous effects that were not taken into account in the model. On the other hand, the analysis of greatly simplified models often makes it possible to reveal the regular features of the processes in question, to obtain the averaged values of some parameters, and to qualitatively explain some of the global physical effects. Although we are making no claim that our model yields results exactly corresponding to the experimental data, we think that the solution derived can provide a basis for understanding a number of important problems in the physics of the plasmaspheres of magnetized planets. It is in this context that we will test our model against experiment.

We begin by noting that the steady-state approximation is unlikely to cause fundamental errors in a description of the plasmaspheric phenomena we are considering in this section. When the illumination of the envelope changes in the course of rotation, the only parameters that change to any essential degree are the local electrodynamic and thermodynamic parameters, first of all, the conductivity of the plasma envelope. Applying the steady-state model to the analysis of different conditions should give information about the processes that can occur in a given range of longitudes at different times. On the other hand, the above simplifying assumption that the particle collision frequencies and conductivity are both uniform is more relevant for comparing theory with experiment. Thus, for Earth conditions, formula (30) formally implies that the localization parameter ε depends strongly on altitude. Hence, the results obtained above may serve merely to provide a qualitative interpretation of the actual phenomena, as will be done in this section.

In the Earth conditions, our model of conductivity applies to the ionospheric layer at altitudes of 80 to 100 km. The longitudinal conductivity in this layer is approximately equal to

$$\sigma_\parallel (90\ \mathrm{km}) \approx 10^{-2}\ \mathrm{S/m}.$$

By performing calculations for the experimental data averaged over time, the Earth's surface, and the height of the ionospheric layer under consideration, we can see that parameter values (31) satisfy all of the above assumptions. Using these values, we can find, first, the values of the normalizing factors, $r_0 = R \approx 6.4 \times 10^6$ m, $\omega_0 = \Omega_p \approx 7.3 \times 10^{-5}$ s^{-1}, $B_0 \approx 6.0 \times 10^{-5}$ T, $\Phi_0 \approx 8.0 \times 10^9$ T m^2, $I_0 \approx 4.0 \times 10^2$ T m, $j_0 \approx 2.4 \times 10^{-5}$ A/m^2, $E_0 \approx 3.0 \times 10^{-2}$ V/m, and $\rho_0 \approx 10^{-6}$ kg/m^3, and, second, the unperturbed magnetic field (6.0×10^{-5} T), the meridional perturbation of the magnetic field (6.0×10^{-8} T), the azimuthal component of the magnetic field (3.6×10^{-6} T), the meridional current density (3.0×10^{-8} A/m^2), the azimuthal current density ($1.3 \times$

10^{-6} A/m^2), and the density $\tilde{\rho}_p$ of the charged plasma component ($\tilde{\rho}_1 \approx 8 \times 10^{-10}$ kg/m^3). The total current flowing in the azimuthal jet is $I_\varphi^{\text{sum}} = 1.0 \times 10^6$ A, the total current in the meridional loop is $I_m^{\text{sum}} \sim 1.1 \times 10^5$ A, and the total loss power is about $Q \sim 10$ GW. The width of the layer in which the perturbations are localized is $\delta h = r_0 \varepsilon^{-1} \approx 64$ km. It is of interest to note that, for these parameter values, the interaction parameter S is on the order of unity. This indicates that, if we treat a planetary envelope moving in a magnetic field as an MHD generator, then, under the conditions in question, the energy of motion of a medium is efficiently converted into electromagnetic energy.

The estimated relative slowing of the angular frequency of the Earth's rotation in one year due to the electric currents circulating in the ionosphere is negligibly small, $\delta\Omega_p/\Omega_p \sim 4 \times 10^{-13}$. Therefore, the assumption of the steady-state rotation of a plasma envelope is valid to a very high degree of accuracy. On the other hand, the Earth's rotation is actually slowed; for certain values of the parameters of the model, the rate of slowing over long time intervals may be relatively high.

Let us consider the most important results of those obtained from the analysis of the problem in the context of their possible application to explaining the actual phenomena in plasmaspheres.

(i) We have shown that the characteristic spatial scale δh, which appears in the approximation under discussion, is much smaller than the radius of a spherical body (planet). This scale determines the dimension of the envelope in which the plasma rotation is nonrigid and in which the azimuthal current j_φ, the meridional current, the perturbations of the dipole magnetic field, and the charged plasma component are all localized. The application of this result to Earth conditions is restricted by the fact that the nonuniformity of the conductivity is not taken into account in the model; hence, formally, the scale δh depends on altitude and, moreover, the amount by which δh changes can be smaller than its magnitude. Nevertheless, it is clear that the processes responsible for the peculiar skin effect when the conduction current and magnetic field perturbations are localized (see the small-scale insets in Figs. 3 and 4) should operate in actual plasmaspheres.

(ii) It has been established from measurements of the deceleration of satellites in the Earth's atmosphere [16] that, in a fairly wide range of azimuthal angles in the Earth conditions, the angular frequency of the rotating plasma envelope coincides with the angular frequency Ω_E of the Earth's rotation in the near-surface layer at altitudes below 150 km and increases linearly to $1.4\Omega_E$ at altitudes of 150 to 350 km. Super-rotation was also recorded in the atmospheres of Venus, Jupiter, and Saturn. To explain the causes of this phenomenon, a number of hypotheses have been advanced. As a rule, the super-rotation of a planetary envelope is attributed to unsteady processes driven by the nonuniform heating of the planet by solar radiation [17, 18]. However, there is, as yet, no final explanation for the super-rotation and, in particular, no satisfactory agreement between the calculated results and experimental data. Consequently, the fact that the above self-consistent model demonstrates the possibility of a steady-state super-rotation of a viscous plasma envelope of a planet appears to be important. The nonrigid rotation of a conducting envelope in a magnetic field results in the generation of a meridional conduction current at the expense of the unipolar induction effect [5–7]. The balance between the Ampére's force, the pressure gradient, the gravitational force, and the viscous forces self-consistently governs the density distribution of the charged plasma component. It has been found that, for the given configuration of the planetary magnetic field ($\mathbf{M} \uparrow\downarrow \boldsymbol{\omega}$), it is just in the case of super-rotation that the charged-particle density profile decreases with increasing altitude. Hence, we have shown that the super-rotation of a plasma envelope can be largely explained as being due to the action of electromagnetic forces.

(iii) Among the phenomena known to occur in the equatorial region of the Earth's plasmasphere is the equatorial electrojet. Measurements of the magnetic field perturbations [19–21] revealed a fairly intense conduction current flowing along the geomagnetic equator.[5] The maximum current density on the order of 10^{-5} A/m^2 is reached at altitudes of about 105 km, the half-height and half-width of the current density distribution being about 10 and 300 km, respectively. Therefore, the total current can be roughly estimated as 4×10^4 A. The parameters of the equatorial electrojet undergo substantial daily and seasonal oscillations. The current density distribution with these mean parameters is established in the daytime, in which case the current is flowing eastward. At night, a very weak current is sometimes recorded that flows in the opposite (westward) direction [20]. It is clear that, in constructing a systematic theory of the equatorial electrojet, it is necessary to take into account the effect revealed by solving the steady-state problem, specifically, the generation of the azimuthal current component at the expense of the unipolar induction phenomenon. At least, in the Earth's ionosphere, the altitude interval where the applicability conditions for the calculated distribution of the azimuthal current density are satisfied coincides with the altitude interval where the azimuthal current is observed to be intense and the calculated current amplitudes may be comparable with those measured experimentally.

(iv) Explanations offered for the structure of the meridional current in the ionospheric E layer were primarily based on the dynamo theory [12, 22]. The existence of an additional mechanism for generating the

[5] This concerns the periods of normal geomagnetic activity.

meridional current in the plasmasphere—a planetary electric generator produced by the unipolar induction effect because of the nonrigid rotation of a plasma envelope in the magnetic field of the planet—was justified in recent papers [8–11]. The electric field and conduction current estimated in [5] from the latitude- and longitude-averaged values of the conductivity at different altitudes were found to be of the same order as the conductivity values known in the physics of the Earth's ionosphere. In this context, it is important to note that the estimate obtained in [5] for the total current in the loop (10^5 A) coincides with the total meridional current I_m^{sum} calculated from our model, which self-consistently takes into account the unipolar induction effect. Hence, we emphasize that self-consistent and non-self-consistent descriptions provide estimates of the same order of magnitude. On the other hand, the calculated total power of Ohmic losses, $Q \sim 10$ GW, is on the order of the estimated power (5 GW) of such a source of the electric field as the ionospheric dynamo [23].

Hence, although it cannot be claimed that our model yields results exactly corresponding to the experimental data, we can state that the planetary rotation mechanism for generating the electric field and conduction current plays an important role in the electrodynamics of the Earth's plasmasphere.

ACKNOWLEDGMENTS

This work was supported in part by the Russian Academy of Sciences (under the "Astronomy" program), the Council of the Federal Program "Government Support of the Leading Scientific Schools" (project no. 00-15-96674), and the Russian Foundation for Basic Research (project no. 02-02-17111).

REFERENCES

1. L. D. Landau and E. M. Lifshitz, *Electrodynamics of Continuous Media* (Gostekhizdat, Moscow, 1953; Pergamon, New York, 1984).
2. I. E. Tamm, *Principles of Theory of Electricity* (Nauka, Moscow, 1989), p. 442.
3. V. S. Beskin, A. V. Gurevich, and Ya. N. Istomin, Zh. Éksp. Teor. Fiz. **85**, 401 (1983).
4. V. S. Beskin, A. V. Gurevich, and Ya. N. Istomin, *Physics of the Pulsar Magnetosphere* (Cambridge University Press, Cambridge, 1993).
5. A. O. Soldatkin and Yu. V. Chugunov, Izv. Vyssh. Uchebn. Zaved., Radiofiz. **44**, 778 (2001).
6. A. O. Soldatkin and Yu. V. Chugunov, Izv. Vyssh. Uchebn. Zaved., Radiofiz. **43**, 483 (2000).
7. A. O. Soldatkin and Yu. V. Chugunov, Izv. Vyssh. Uchebn. Zaved., Radiofiz. **43**, 595 (2000).
8. D. E. Malov and Yu. V. Chugunov, Izv. Vyssh. Uchebn. Zaved., Radiofiz. **40**, 232 (1997).
9. P. A. Bespalov and Yu. V. Chugunov, Izv. Vyssh. Uchebn. Zaved., Radiofiz. **40**, 138 (1997).
10. P. A. Bespalov, Yu. V. Chugunov, and S. S. Davydenko, J. Atmos. Terr. Phys. **16**, 69 (1996).
11. P. A. Bespalov, Yu. V. Chugunov, and S. S. Davydenko, J. Atmos. Terr. Phys. **58**, 605 (1996).
12. B. N. Gershman, *Dynamics of Ionospheric Plasma* (Nauka, Moscow, 1974), p. 47.
13. N. A. Krall and A. W. Trivelpiece, *Principles of Plasma Physics* (Academic, New York, 1973; Mir, Moscow, 1975).
14. A. V. Nedospasov, Usp. Fiz. Nauk **123**, 333 (1977) [Sov. Phys. Usp. **20**, 861 (1977)].
15. P. A. Bespalov and Yu. V. Chugunov, Planet. Space Sci. **32**, 365 (1984).
16. C. W. Allen, *Astrophysical Quantities* (Athlone, London, 1973; Inostrannaya Literatura, Moscow, 1960).
17. W. Kundt, Planet. Space Sci. **31**, 1339 (1983).
18. M. N. Izakov, Astron. Vestn. **35**, 275 (2001).
19. T. N. Davis, K. Burrows, and J. D. Stolarik, J. Geophys. Res. **72**, 1845 (1967).
20. N. C. Maynard, J. Geophys. Res. **72**, 1863 (1967).
21. V. Doumouya, J. Vassal, Y. Cohen, *et al.*, Ann. Geophys. (Germany) **16**, 658 (1998).
22. S. Kato, *Dynamics of the Upper Atmosphere* (Center for Academic Publication, Tokio, 1980), p. 165.
23. H. Volland, Phys. Scr. **18**, 289 (1987).

Translated by O.E. Khadin

Plasma Physics Reports, Vol. 29, No. 1, 2003, pp. 78–81. Translated from Fizika Plazmy, Vol. 29, No. 1, 2003, pp. 85–89.

NONLINEAR PHENOMENA

Waves of States in an Electron Beam with a Distributed Virtual Cathode

A. G. Lymar'

Kharkov Institute of Physics and Technology, National Science Center
Akademicheskaya ul. 1, Kharkov, 61108 Ukraine

Received July 31, 2002

Abstract—Results are presented from computer simulations of the dynamics of an electron beam injected into the drift space between two parallel conducting planes. The specific features of the competitive coexistence of states with and without a virtual cathode are investigated. © *2003 MAIK "Nauka/Interperiodica".*

In the past decade, the virtual cathode (VC), first described in [1, 2], has been addressed in the literature as a possible cause for the appearance of accelerated ions in high-current electron-beam devices [3]; it has also attracted interest in connection with practical applications. Thus, in [4] a device was described in which record ion accelerating gradients of 40 MeV/m were attained with the help of a VC in a high-current electron beam. A number of different types of vircators (high-power VC-based microwave oscillators) have been proposed (see, e.g., [5]). However, the implementation of VCs encounters difficulties because VC physics is still poorly understood even at a qualitative level.

For both of the above examples of VC implementation, it is of interest to study the competitive coexistence of states with and without a virtual emitter. This process was observed for the first time in [6], where a virtual emitter was produced in an ion beam.[1]

In this paper, the specific features of the coexistence of different states of a high-current charged-particle beam are investigated numerically. A schematic of the model device is shown in Fig. 1.

Electrons are accelerated in the gap between cathode *1* and grid *2* and then enter the drift space between the grid and collector *3*. The potential difference between the cathode and the grid is U_k; the grid and the collector are short-circuited.

According to the theory of [1, 2], the beam state in the drift space between the grid and the collector is determined by the dimensionless quantity $J = J_{inj}/J_d$, where J_{inj} is the injected current density and

$$J_d = \frac{4}{9}\varepsilon_0\sqrt{\frac{2e}{m}}\frac{U_k^{3/2}}{(y_1 - y_0)^2}.$$

As J increases from zero to $J \le 8$, all the electrons injected into the drift space cross it and are absorbed by the collector. At $J = 8$, the beam undergoes an irreversible transition into a state in which a fraction of the injected electrons return to the grid as if they were emitted by a cathode located in the drift space. This state is referred to as the state with a VC. After the state with a VC has appeared, it exists in the range $J > 4$. At $J = 4$, the state with a VC is irreversibly converted into a state without a VC.[2]

It follows from the above-mentioned that there is a hysteresis of states. For each value of J in the hysteresis interval ($J_{\min} < J < 8$), the beam can exist in a state either with or without a VC, depending on the previous history. Each of these states is stable against small perturbations.

So far, we have considered the behavior of a system that is uniform in the x and z directions. Let now assume that, in a system that is in one of the possible states with $J_{\min} < J < 8$, the quantity J changes at some instant over a certain interval $x_l < x < x_r$ so that the beam in this interval passes over to another possible state, and, after the transition has occurred, the quantity J takes its previous value. As a result, in neighboring regions, the system can occur in two different states, which can simultaneously occur at the given value of J. Since each of these states itself is stable, far from boundary between these states, the system behaves as if there were no boundary at all. Therefore, all the changes can only happen near the boundary as a result of "the competition of the stabilities of the neighboring states."

The results of computer simulations presented below demonstrate how the system shown in Fig. 1 evolves in the drift space from the two neighboring states.

[1] If the state of a charged-particle beam of any kind is analogous to a VC in an electron beam, then it is natural to call it a "virtual emitter."

[2] Numerical simulations of the state with a VC [7] show that the theoretical predictions of [1, 2] should be refined because the state with a VC is oscillating; as a result, the VC disappears at $4 < J_{\min} \simeq 5.8$.

1063-780X/03/2901-0078$24.00

The simulations were performed by the particle-in-cell method. The particles moved within a rectangular domain. The numbers of meshes along the axes were certain powers of 2, the typical values being 1024 meshes along the x-axis and 128 meshes along the y-axis. The potential was calculated by means of the fast Fourier transform. The initial conditions were chosen such that, in the planes $x = x_0$ and $x = x_1$, the x-component of the electric field was zero; i.e., there was an even periodicity along the x-axis with a period of $2(x_1 - x_0)$. The particles were injected at each time step with an initial velocity directed along the y-axis at each mesh point of the x-axis. The initial velocity and the time step were equal to unity. It was assumed that the magnetic field applied along the y-axis was sufficiently strong for the x-component of the particle velocity to be neglected. The equations of motion were nonrelativistic. It was also assumed that the particles arriving at the grid or the collector were absorbed there.

Numerical simulations show that it is possible to form a system consisting of two neighboring states, as was described above. However, the computation time can substantially be reduced by preparing the initial state as follows:

(i) First, by calculating the particle motion in a one-dimensional drift space (the system is uniform along the x-axis), a state with a certain value of $J = J_{calc} < 8$ from the hysteresis region of states is determined. After a steady state has been established, this state (i.e., the coordinates and velocities of all the particles in the gap) is stored in the computer memory.

(ii) Then, with the help of the same program, the calculations for $J > 8$ are performed. After the formation of a VC in the gap, J is gradually decreased to J_{calc} and retains this value until the oscillatory mode is established. A certain instantaneous state of this mode is also stored.

(iii) A part of the spatial period ($x_0 < x < x_g$) is filled with particles whose coordinates and velocities correspond to the state with a VC, and the remaining part of the period ($x_g < x < x_1$) is filled with particles whose coordinates and the velocities correspond to a state without a VC. Then, two-dimensional simulations with such initial conditions are performed.

Figure 2 illustrates the results of one-dimensional simulations. The figure presents the given time dependences of J and the calculated time dependences of the potential at the midplane of the drift space (at $y_c = y_0 + (y_1 - y_0)/2$). In case (a), we have $J_{calc} = 6 < 8$, and no VC is formed. In case (b), for a certain time in the beginning of the process, we have $J = 8.5 > 8$. After the formation of a VC, J is gradually reduced to $J_{calc} = 6$; in this case, the VC is conserved.

Figure 3 shows the time evolution of the boundary between the states with and without a VC for different values of the injected current density. Each curve in the figure presents the spatial profile of the potential in the midplane of the drift space at some instance.

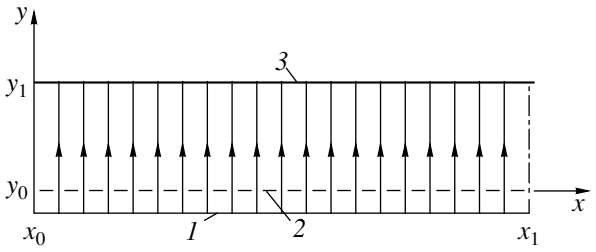

Fig. 1. Schematic of the modeled device: (*1*) cathode, (*2*) grid, and (*3*) collector.

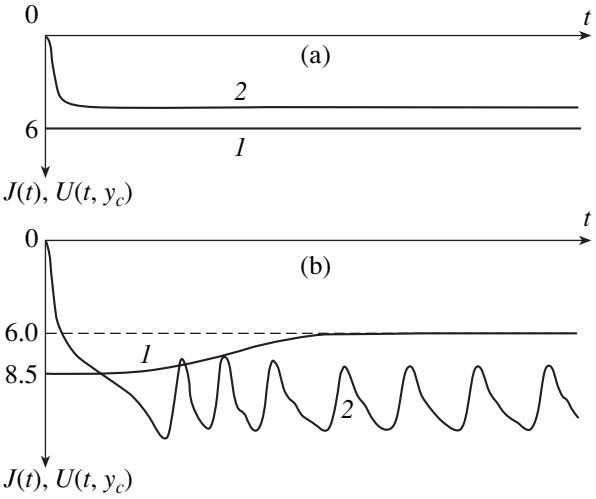

Fig. 2. Functions (*1*) $J(t)$ and (*2*) $U(t, y_c)$: (a) no state with a VC and (b) a state with a VC is formed.

Figure 3a illustrates the process of absorption of a state without a VC by a state with a VC, Fig. 3b corresponds to an essentially fixed boundary between the states, and Fig. 3c demonstrate the absorption of a state with a VC by a state without a VC. For case (c), the value of $(x_1 - x_0)$ was chosen to be 2048, which was twice as long as for cases (a) and (b).

In case (c), the character of oscillations in the state with a VC changes qualitatively as time elapses. The period of oscillations becomes shorter, and their amplitude decreases. We can assume that, in this case, we observe one more state with a VC, which was described in [8, 9]. In this state, which is referred to as the high-frequency VC (HFVC) mode [8], the amplitude of oscillations is lower and the frequency is three times higher than those in the usual low-frequency VC (LFVC) mode. In [8], the HFVC state arose when the space charge in the drift space dropped rapidly due to the sharp decrease in the injection current. In our case, the appearance of an HFVC state can be provoked by

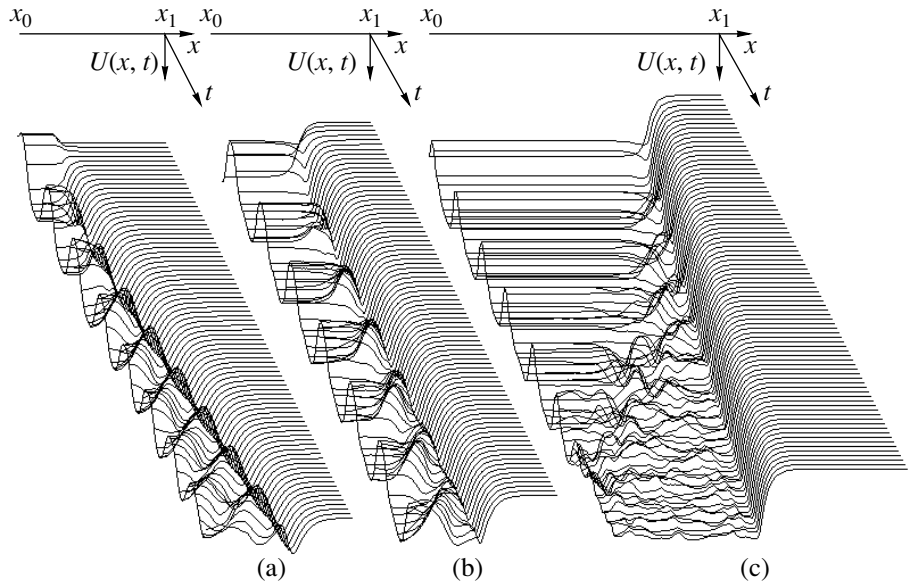

Fig. 3. Electric potential in the midplane of the drift space as a function of x and t for different values of the injection current density: J = (a) 7.88, (b) 7.4, and (c) 5.85; the number of injection cycles for plots (a), (b), and (c) is 4096, 4096, and 8192, respectively.

the drop in the space charge that takes place near the boundary between the states with an LFVC and without a VC. It can be seen in Fig. 3c that, after the formation of an HFVC state, all of the three states (the HFVC state; absorbing the LFVC state; and the state without a VC, absorbing the HFVC state) coexist for a certain period of time.

In view of the occurrence of an HFVC state, it is of interest to examine its interaction with an LFVC state and a state without a VC.

One-dimensional simulations show that the HFVC state transforms into the LFVC state if the velocities of the injected particles are varied by the law

$$V_i = 1 + A\sin(3.14n/T),$$

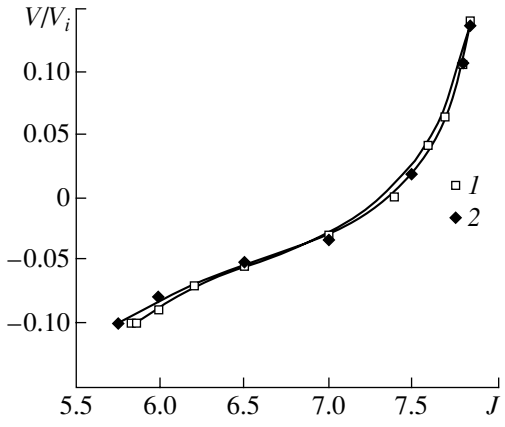

Fig. 4. The propagation velocity of the boundary between different states vs. injected current density: (*1*) states with an LFVC and without a VC and (*2*) states with an HFVC and without a VC.

where n is the number of the injected particle. The values of A and T can be rather arbitrary. In our calculations, we set $A = 0.009$ and $T = 5$. After the formation of an HFVC, the value of A was gradually decreased to zero. If, in this case, the HFVC state is conserved, we can conclude that the HFVC can exist at this value of the injection current. The results obtained show that the HFVC state can only exist within the above hysteresis range of the injection current densities (at $J_{\min} < J < 8$).

We have also performed two-dimensional simulations of the evolution of a system consisting of states with an HFVC and without a VC, as well as a system consisting of an LFVC and an HFVC state.

Figure 4 shows the quantity V/V_i (where V is the velocity of the boundary between the states and $V_i = 1$ is the particle injection velocity) as a function of the injection current density J (the positive boundary velocity corresponds to the direction of propagation from left to right). It can be seen from the figure that the dependence of the boundary velocity on J for a system consisting of states with an LFVC and without a VC is almost the same as for a system consisting of states with an HFVC and without a VC. The evolution of a system consisting of states with an HFVC and without a VC for $J = 7.85$ is shown in Fig. 5a.

In the interaction between the LFVC and HFVC states, the former state is absorbed in the entire hysteresis range of the injection current densities. The lower J, the higher the absorption rate, which, however, is rather difficult to estimate because there is no pronounced boundary between these states. The evolution of an LFVC–HFVC system for $J = 6.0$ is shown in Fig. 5b.

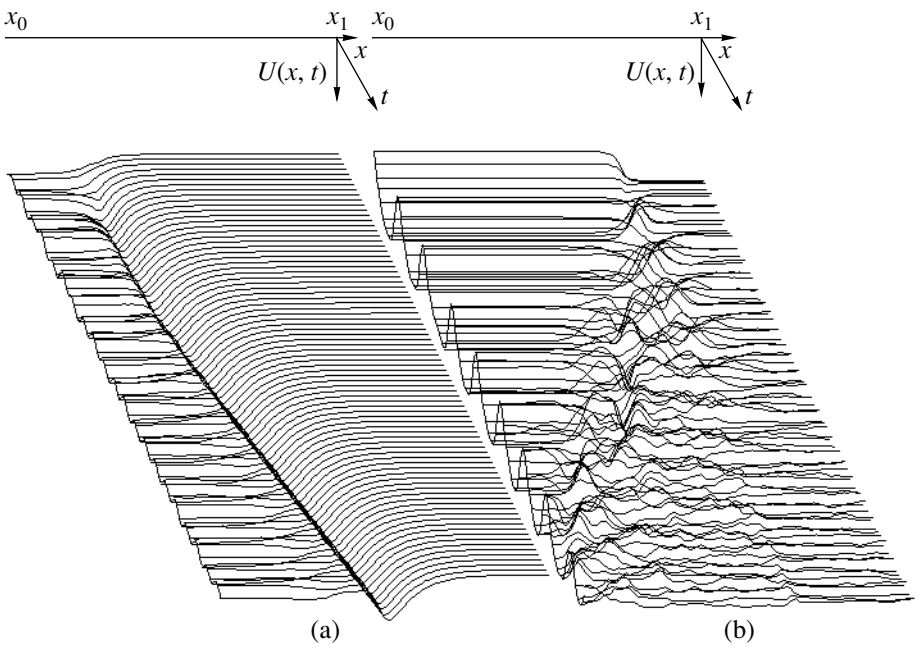

Fig. 5. Electric potential in the midplane of the drift space as a function of x and t for different values of the injection current density and different interacting states: (a) $J = 7.85$ (states with an HFVC and without a VC; the number of the injection cycles is 4096) and (b) $J = 6.0$ (states with an LFVC and HFVC; the number of the injection cycles is 8192).

The main results of this study can be summarized as follows:

(i) The competitive coexistence of states with an LFVC and without a VC, first observed and qualitatively described in [6], has been confirmed.

(ii) The possibility of a competitive coexistence of the states with an HFVC and without a VC, as well as the states with an HFVC and an LFVC, has been demonstrated.

(iii) It has been found that, as time elapses, a third state can occur at the boundary of the competing states and one more boundary between the states can appear. First, the states with an LFVC and without a VC compete; then, between these states, an HFVC state appears and, accordingly, the boundaries between the LFVC and HFVC states and the boundary between the states with an HFVC and without a VC arise.

(iv) Some quantitative characteristics of the change of states have been determined.

One of the possible applications of electric fields arising at a moving boundary between the states with and without a VC is collective ion acceleration [10]. If we assume that protons can be accelerated to the maximum wave velocity obtained in the present study, then the proton energy will be 20 times higher than the energy of the injected electrons. Approximately the same values were obtained in the best experiments on the collective acceleration of ions in high-current electron beams [4, 11].

We note that the distribution of the electric potential at the boundary between the states with an HFVC and without a VC (see Fig. 5a) allows ion acceleration for any propagation direction of the boundary.

REFERENCES

1. V. R. Bursian and V. I. Pavlov, Zh. Russ. Fiz.-Khim. Ob. **55**, 71 (1923).
2. C. E. Fay, A. L. Samuel, and W. Shockley, Bell Syst. Tech. J. **17** (1), 49 (1938).
3. V. G. Gapanovich and A. A. Kolomenskiĭ, Izv. Vyssh. Uchebn. Zaved., Fiz., No. 10, 59 (1979).
4. P. G. O'Shea, W. W. Destler, J. Rodgers, and Z. Segalov, Appl. Phys. Lett. **49**, 1696 (1986).
5. V. D. Selemir, B. V. Alekhin, V. E. Vatrunin, *et al.*, Fiz. Plazmy **20**, 689 (1994) [Plasma Phys. Rep. **20**, 621 (1994)].
6. A. G. Lymar', A. V. Zvyagintsev, and N. A. Khizhnyak, Preprint No. 88-1 (Kharkov Inst. of Physics and Technology, Kharkov, 1988).
7. C. K. Birdsall and W. B. Bridges, J. Appl. Phys. **32**, 2611 (1961).
8. C. K. Birdsall and W. B. Bridges, J. Appl. Phys. **34**, 2946 (1963).
9. A. P. Priverzentsev, N. I. Sablin, and G. P. Fomenko, Radiotekh. Élektron. (Moscow) **34**, 659 (1989).
10. A. G. Lymar', V. V. Belikov, A. V. Zvyagintsev, *et al.*, Otkrytiya Izobret., No. 36, 290 (1990).
11. J. S. Luse and H. L. Sahlin, IEEE Trans. Nucl. Sci. **20**, 336 (1973).

Translated by A.S. Sakharov

Plasma Physics Reports, Vol. 29, No. 1, 2003, pp. 82–91. Translated from Fizika Plazmy, Vol. 29, No. 1, 2003, pp. 90–100.

LOW-TEMPERATURE PLASMA

Comparison of the AC Barrier Corona with DC Positive and Negative Coronas and Barrier Discharge

Yu. S. Akishev, A. V. Dem'yanov, V. B. Karal'nik, A. E. Monich, and N. I. Trushkin

Troitsk Institute of Innovation and Fusion Research, State Scientific Center of the Russian Federation, Troitsk, Moscow oblast, 142190 Russia

Received May 23, 2002

Abstract—Results are presented from experimental studies of ac corona discharges between a point electrode and a dielectric-coated plate in nitrogen, argon, helium, and air in the voltage frequency range $f = 50$ Hz–50 kHz. The characteristic features of this type of discharge are compared with the well-known features of dc positive and negative coronas and a barrier discharge between plane electrodes. It is shown that the presence of a dielectric barrier on the plane electrode significantly changes the electric characteristics and spatial structure of the corona, whereas the main phases of the discharge evolution remain unchanged as the voltage increases. With a point electrode, the breakdown voltage of the barrier corona decreases substantially as compared to the breakdown voltage of a barrier discharge with plane electrodes. This leads to softer conditions for the streamer formation in a barrier corona, which becomes more stable against spark generation. *© 2003 MAIK "Nauka/Interperiodica".*

1. INTRODUCTION

Low-current ac discharges between a point (or an edge) and a dielectric-coated plane are widely used in practice, e.g., to modify dielectric surfaces [1]. Typically, the interelectrode distance and applied-voltage frequency do not exceed several millimeters and tens of kilohertz, respectively. Under these conditions, the characteristic time of the ion drift between electrodes is short as compared to the half-period of the ac voltage; as a result, in every half-period, the gap gets filled with space charge and a quasi-steady corona discharge forms in the gap.

This type of discharge will be referred to as an ac barrier corona (BC), because it combines the features of the familiar barrier and corona discharges. Indeed, the dielectric layer on the plane electrode is a barrier for the conduction current, as is the case in a usual barrier discharge [2], whereas the point leads to the formation of a positive or negative corona in the gap during the corresponding periods of the applied voltage.

Although various BC modifications have long been applied in technology, the physics of this type of discharge is still poorly understood. From the physical standpoint, it is of interest to distinguish between the features of the barrier and corona discharges that are present in BC and those characteristic of BCs only. In this context, it is expedient to briefly remind the basic properties of a barrier discharge between plane electrodes and dc positive and negative coronas in the point–plane geometry.

The barrier discharge is an ac discharge between two closely spaced ($d \le 3$ mm) metal plates, of which at least one is coated with a dielectric. Depending on the amplitude of the applied voltage, two main modes of the barrier discharge can be distinguished: a diffuse mode and a streamer mode.

In narrow gaps (with lengths of $d \le 1$ mm) at voltages only slightly exceeding the Townsend breakdown voltage (i.e., at very low initial currents), the barrier discharge is uniform in the transverse (with respect to the current) direction [3–6]. This mode is referred to as a diffuse mode. In recent years, it has been established that the diffuse mode corresponds to a glow discharge in the highly subnormal and hampered regime, in which the current density at electrodes is low compared to the normal current density in a glow discharge and the cathode layer occupies the entire interelectrode gap.

As the amplitude of the applied voltage increases, the degree to which the glow cathode layer is subnormal becomes smaller; as a result, at a certain voltage amplitude, the cathode-layer thickness d_c becomes smaller than d. Under these conditions, the glow discharge is no longer hampered, but it still remains subnormal. It is well known [7] that the subnormal cathode layer has a negative differential resistance and is unstable against transverse perturbations and that the instability growth rate increases with increasing deviation from the normal regime. For this reason, the subnormal cathode layer in nitrogen or air contracts into current spots and the diffuse mode transforms into the streamer one. In this mode, in every half-period of the applied voltage, the discharge gap gets filled with many fine unsteady current filaments (streamers), which are randomly distributed in space. Near the barrier surface, each streamer branches out, covering a small area with a diameter no larger than the interelectrode distance.

1063-780X/03/2901-0082$24.00

Note that in a barrier discharge in helium, the deviation from the normal regime of the cathode layer is much smaller than in the case of nitrogen or air; therefore, the diffuse mode in He can also occur at $d_c < d$. However, the negative dynamic resistance of the subnormal cathode layer results in regular pulsations of the current in each half-period, although the barrier discharge remains uniform in the transverse direction [6]. Since the barrier-discharge current is proportional to the frequency and amplitude of the applied voltage, the diffuse mode is limited to low frequencies and small amplitudes slightly exceeding the Townsend breakdown voltage.

In this study, we are only interested in dc corona discharges excited on point electrodes (with a radius of curvature of $r_0 \le 0.5$ mm) and in gaps a few centimeters in length ($d \le 30$ mm). We begin with a *positive corona*. The discharge in a point–plane gap (the point being at a positive potential) becomes visible even at voltages U lower than the corona ignition voltage U_*. The value of U_* is determined from the condition for a self-sustained corona [8–10]: $\int_0^d \alpha(x)dx \simeq \ln\frac{1}{\gamma}$, where α is the ionization multiplication constant for an electron avalanche and γ is the effective coefficient of secondary electron generation by various processes (including volume photoionization, surface photoemission, and surface emission caused by positive ions and metastable particles). Up to the ignition voltage, the positive corona is unstable and exists in a bursty regime [9], in which rare and random individual bursts on the point occur, giving rise to fine and weak streamers originating from the point.

After ignition ($U \ge U_*$), the positive corona usually remains in the diffuse mode, in which the point is covered with a uniform glow [11–13] (actually, it is pulsed [14]) and the average corona current increases as the discharge voltage squared. Typically, the diffuse mode of the positive corona in all gases exists at low currents (lower than several tens of microamperes); as the current increases, rather regular and intense streamers arise in the gap. As U increases, the streamer repetition rate rises to several tens of kilohertz and the amplitude of the related current spikes increases to several tens of milliamperes [15]. As the voltage increases further, the streamer mode transforms into a spark.

In a *negative corona*, no bursts are observed as the applied voltage approaches U_*, and the evolution of the corona after ignition (at $U \ge U_*$) depends on the sort of gas. In electronegative gases (air), the negative diffuse corona occurs in a pulsed mode (the so-called Trichel pulses [9], whose repetition rate increases linearly with the average corona current). At characteristic currents of $I \approx 130 \pm 10$ μA, the pulsed mode changes abruptly to a steady-state mode, which occurs at currents of up to $I \approx 200$–250 μA.

The streamer mode does not occur in a negative corona; therefore, without special measures for discharge stabilization (the use of a gas flow, resistive anode, etc.), the diffuse corona transforms into a spark. Stabilization can substantially increase the spark threshold; in this case, an intermediate mode between the diffuse corona and the spark (a steady-state diffuse glow discharge [16], in which the interelectrode gap is filled with plasma) can occur.

In electropositive gases (N_2, He, and Ar), the ignition voltage of the negative corona is substantially higher than the sustaining voltage. For this reason, after ignition, the corona current jumps to a steady-state level of several hundred of microamperes, which is determined by the current–voltage characteristic of the discharge and by the ballast resistance in the external circuit. At such currents, the corona is diffuse and does not pulsate. The current range of the diffuse mode in electropositive gases is significantly wider than that in electronegative gases and extends up to several milliamperes. For example, with gaps of about 15 mm, the negative diffuse corona in N_2, Ar, or He transforms into a spark at currents of up to 10 mA. An interesting feature of the negative corona in electropositive gases is that the corona possesses a hysteresis; i.e., after ignition, the voltage can be reduced to a level below U_* without corona quenching. It is in this range that the pulsed mode of a negative corona in N_2, Ar, or He occurs [17].

Thus, the diffuse mode of a barrier discharge is observed only in short gaps. In contrast, the diffuse mode of a corona discharge is observed in longer gaps, because the current density at the plane electrode increases sharply for small values of d; as a result, the corona transforms into a spark at very low currents. The streamer mode is predominant for both the barrier discharge and a positive corona. The streamer branching on the electrode surface is insignificant. In a negative corona, the streamer mode is absent.

In this paper, in order to determine the position of the ac BC among the above discharges, we compare the features of BC in the point–plane geometry with those of a barrier discharge in a plane gap and steady-state (positive and negative) coronas in a point–plane gap.

2. EXPERIMENT

Experiments with an ac BC were carried out in a $150 \times 150 \times 50$-mm organic-glass discharge chamber with a point and a plane electrode mounted in it (Fig. 1). The point electrode was nearly paraboloidal in shape with a radius of curvature $r \approx 0.1$ mm. The interelectrode distance was varied within the range $d = 1.5$–30 mm. The plane electrode was a 100-mm-diameter metal disk. To avoid edge effects and provide a monotonically decreasing electric field at the boundary of the disk, its edges were rounded to a Rogowski profile. The metal surface was entirely covered with a polymer

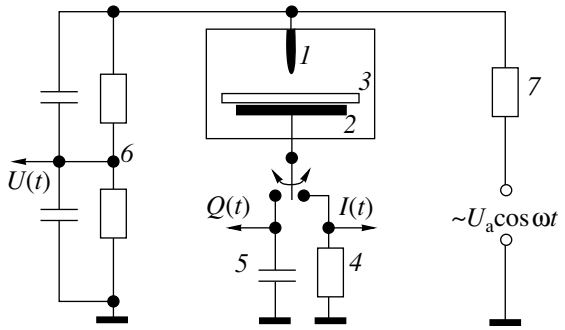

Fig. 1. Experimental setup for studying BCs: (*1*) point electrode, (*2*) plane electrode, (*3*) dielectric barrier (polymer film), (*4*) low-inductance current shunt, (*5*) capacitor for measuring the charge carried across the discharge gap, (*6*) voltage divider, and (*7*) ballast resistor.

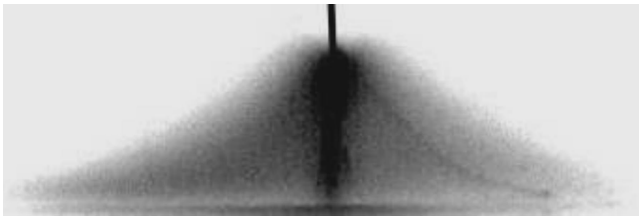

Fig. 2. Photograph of a BC in Ar (side view). The barrier is a polyethylene film, $d = 6$ mm, $f = 400$ Hz, and $U_a = 3.5$ kV.

(polyethylene, polypropylene, teflon, etc.) film with a thickness of 15–75 μm, which was 30–100 times smaller than the thickness of the dielectric coating in usual barrier discharges. Such a small film thickness ensured the large specific capacity of the barrier and, accordingly, the high current density in the BC as compared to usual barrier discharges, all other parameters being the same. In some experiments, we used a plane resistive electrode with an isotropic resistivity.

In experiments, we used ambient air, high-purity 99.999% nitrogen, 99.99% argon, and 99.99% helium. All of the experiments were performed at atmospheric pressure; for air, additional experiments were carried out at a reduced pressure ($P = 380$ torr). Before the experiments, the gas-discharge chamber was evacuated to a pressure of $P = 10^{-3}$ torr and then was filled with a working gas. To ensure the certificate gas purity, the experiments were carried out with slow gas circulation through the discharge chamber.

The sinusoidal electric voltage was applied to the point electrode from a generator through a ballast resistor with $R_b = 300$ kΩ. Two types of high-voltage generators were used in the experiments. In one of them, the frequency f and the voltage amplitude U_a were smoothly varied from 50 Hz to 50 kHz and from 0 to 4.5 kV, respectively. Higher voltages (up to 35 kV) were produced by the second generator—a 3NOM-35/1 transformer operating at a fixed frequency of $f = 50$ Hz. The shape and amplitude of the discharge voltage were recorded with a compensated voltage divider, the signal from which was fed to a storage oscillograph. The rms voltage was measured by an S-96 electrostatic voltmeter. The shape and amplitude of the discharge current were recorded with the help of a low-inductance current shunt. The charge carried through the discharge gap during one half-period and the active discharge power (i.e., the electric power deposited in the discharge) were determined from the charge–voltage characteristic (CVC) of the barrier corona. The discharge was photographed with an Olympus E-100RS digital camera.

3. EXPERIMENTAL RESULTS

3.1. Visual Observations of a BC

We begin with the description of visual observations demonstrating the evident distinctions of BC from a barrier discharge or usual corona. It is well known [18] that the current channel of a usual point–plane corona broadens away from the point. The effective radius (at a level of 0.5) of the current channel increases with distance and can be approximated by the function $R \sim R_W(x/d)^{1/2}$ (where x is the distance from the point and $R_W \simeq 0.7d$ is the Warburg radius); i.e., the current channel of a usual corona is convex. At the plane electrode, the corona current is concentrated within a circle of radius R_W. In the first approximation, the Warburg radius is independent of the mode (diffuse or streamer) and polarity of the corona.

It turns out, however, that in the case of BC, the simple relation $R_W \simeq 0.7d$ between its longitudinal and transverse sizes is only applicable for the diffuse mode (i.e., at small amplitudes of the applied voltage U_a) and is inapplicable for the streamer mode. The reason is that the BC streamers (which begin to be generated at the point electrode at voltages lower than those in a barrier discharge) behave in a different manner than in a barrier discharge or usual corona. After reaching the barrier, the BC streamers intensely branch out on its surface (especially in the case of electropositive gases) and propagate ("slip") along the dielectric surface over a long (in comparison with d) distance from the discharge axis.

In the presence of a barrier, not only does the area occupied by a BC on the plane electrode increase substantially, but also the shape of the current channel in the discharge gap is modified. Instead of being convex, the time-averaged BC current channel is concave, which is clearly seen in the photograph of a BC in argon (side view) presented in Fig. 2. It follows from this figure that the visual BC radius near the plane electrode is approximately equal to $1.5d$, which is more than twice as large as the Warburg radius R_W.

The broadening of the current channel at the barrier depends on the BC mode and the sort of gas. The broad-

ening is strongest for argon, in which case the surface streamers readily branch out and propagate over a long distance from the discharge axis. At large voltage amplitudes U_a, the radius of the region occupied by surface streamers amounts to several tens of d. The next in this line are helium and nitrogen. BCs in air broaden only slightly; in this case, like in usual barrier discharges, the branching surface streamers propagate over a distance no longer than d.

The experiment has shown that in electropositive gases, the visual BC radius R_c at the dielectric barrier increases with increasing U_a (Fig. 3) and does not depend on the interelectrode distance d. In contrast, for air, this radius behaves as the Warburg radius of a usual corona; i.e., it depends only slightly on U_a and increases with increasing gap length d.

The increase in the BC area due to the spread of streamers over the dielectric surface prevents (or strongly hampers) an increase in the average current density through the barrier as the total BC current increases. For example, in the case of argon, the average current density remains at a level of 20–30 $\mu A/cm^2$. This feature distinguishes BC from a usual corona, in which the average current density usually increases with increasing total current.

In a usual corona, the increase in the average current density at the metal plate leads to the onset of instability and the conversion of the corona into a spark. In BC, the spread of the streamers impedes the formation of a spark and, thus, allows one to substantially extend the BC current range. For example, in electropositive gases at gap lengths of $d \simeq 1$–10 mm, it is possible to obtain the average BC currents through the point electrode as high as 2–3 mA without spark generation. (In these experiments, the maximum attainable current was limited not by the processes on the point electrode, but by the properties of the polymer film, which undergone thermal destruction at high currents.)

The above currents are tens of times higher than the threshold current for spark generation in a usual positive corona and are several times higher than those in a negative corona at the same value of d. The difference between the threshold currents for spark generation in BC and usual corona is most pronounced at small d. Thus, at small gap lengths ($d \leq 3$ mm), the streamer mode of a dc positive corona in argon cannot be realized at all, because after breakdown the discharge transforms immediately into a spark, whereas BC exists up to currents of several milliamperes without transformating into a spark.

3.2. Waveforms of the BC Current

It is well known that the waveforms of the barrier discharge current are the same for both half-periods. Figures 4 and 5 illustrate the typical oscillograms of the BC current for different gases and discharge modes. It can be seen that the waveforms of the BC current are

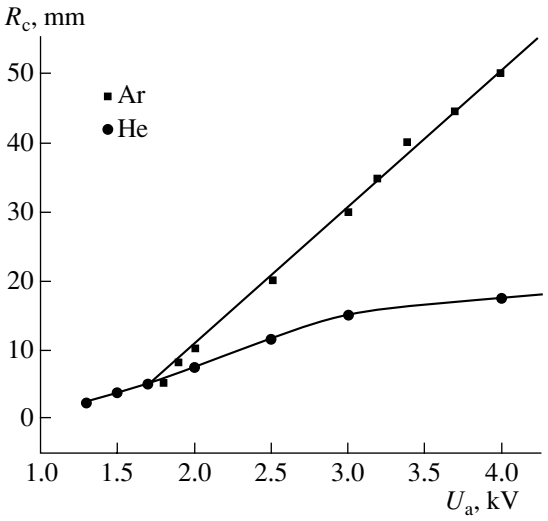

Fig. 3. Visual BC radius at the barrier surface vs. amplitude of the applied voltage for $d = 1.5$ mm; $f = 0.4$ kHz for a BC in He and $f = 1$ kHz for a BC in Ar.

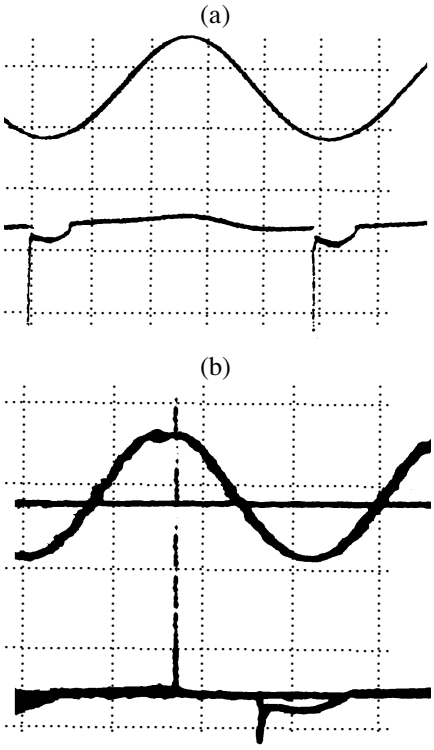

Fig. 4. Oscillograms of the voltage (upper curves) and current (lower curves) in different BC modes: (a) the diffuse mode in both half-periods (Ar, $d = 6$ mm, $f = 400$ Hz, the current scale is 0.1 mA/division, the voltage scale is 4 kV/division, and the time scale is 0.5 ms/division) and (b) the diffuse mode in the negative half-period and the streamer mode in the positive half-period (N_2, $d = 1.5$ mm, $f = 3$ kHz, the current scale is 2 mA/division, the voltage scale is 4 kV/division, and the time scale is 0.1 ms/division).

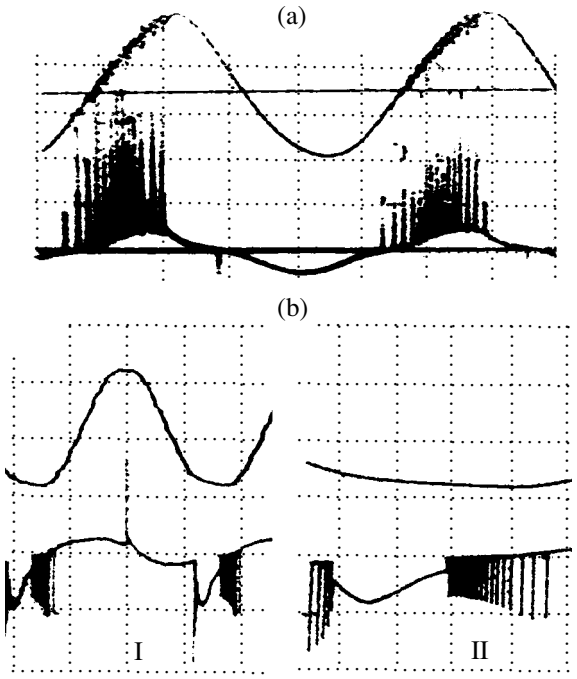

Fig. 5. Oscillograms of the voltage (upper curves) and current (lower curves) in the diffuse BC mode in the negative half-period and the streamer mode in the positive half-period: (a) He, d = 1.5 mm, f = 1 kHz, the current scale is 4 mA/division, the voltage scale is 2 kV/division, and the time scale is 0.2 ms/division and (b) air, P = 380 torr, d = 5 mm, f = 3 kHz, the current scale is 0.4 mA/division, and the voltage scale is 4 kV/division (the time scales on oscillograms I and II are 100 and 20 μs/division, respectively).

asymmetric, which indicates that the BC properties are different in the positive and negative half-periods. Therefore, it is expedient to describe the BC evolution with increasing U_a for each half-period individually.

In the positive half-period, BCs in all gases exist in diffuse and streamer modes that are similar to those of usual positive coronas. The diffuse mode is characterized by the absence of spikes in the current oscillogram (Fig. 4a); this mode occurs in a narrow range of the initial currents (no higher than tens of microamperes). The main BC mode is the streamer mode, which is observed visually as a variety of unsteady branching streamers, which spread randomly over the dielectric surface. In the current oscillograms, this mode manifests itself by spikes with amplitudes of tens (or even hundreds) of milliamperes (Fig. 4b). The number of spikes during one half-period increases with increasing voltage amplitude. At a fixed value of U_a, the number of spikes depends on the sort of gas. The number of spikes is maximum for a BC in helium (Fig. 5a), which correlates with the observed high density of the surface streamers in this gas.

In the negative half-period, BCs in all gases and at all currents exist only in the diffuse mode, which is confirmed by the fact that there are no large-amplitude spikes in the current oscillograms. The absence of streamers in BC corresponds to a similar property of a usual negative corona, in which the streamer mode is not observed.

The current spike at the beginning of the negative half-period is related to the formation of a glow cathode layer on the point electrode. The amplitude of this spike is much smaller than the amplitudes of the current spikes related to the streamer generation in the positive half-period. The initial spike is followed by the current minimum, whose depth decreases with increasing frequency. Then, a quasisteady diffuse mode is established, which, for small BC radii, is similar to usual negative coronas (Fig. 5b).

Seemingly, at large voltage amplitudes U_a (i.e., in the presence of widely spread streamers in the positive half-period), the BC conductivity in the negative half-period is no longer provided by the space charge of the corona discharge. In our opinion, in this case, the conductivity is provided by a decaying plasma produced by the surface streamers in the preceding positive half-period.

In BCs, as in usual low-current negative coronas, high-frequency current pulses (Trichel pulses) are observed at the beginning and the end of each negative half-period. Characteristically, the amplitude of the Trichel pulses in a BC is greater than in a usual negative corona with the same point radius. In this respect, a BC is similar to a negative point–plane corona with a resistive anode, for which the amplitude of Trichel pulses is also larger as compared to a usual corona with a metal anode [19].

A sequence of regular current spikes was also observed in argon. The repetition rate of regular pulses in N_2 and He is rather low as compared to the ac voltage frequency f [19]; that is why such pulses were absent in experiments carried out at $f \geq 1$ kHz.

3.3. Charge and Energy Characteristics of BC

The charge Q carried across the BC gap during one half-period can be determined from the discharge CVC. Typical CVCs at low and high average currents (or at large and small voltage amplitudes U_a) are shown in Figs. 6a and 6b, respectively. The charge Q is equal to the CVC spread along the abscissa. It can be seen from these figures that, at small U_a, the CVC is smooth and symmetric, which corresponds to the diffuse BC mode for both half-periods. At large voltage amplitudes, the CVC remains smooth in the negative half-period and has many spikes in the positive half-period, which corresponds to the diffuse BC mode in the negative half-period and to the streamer mode in the positive half-period. The charge Q increases with increasing U_a and depends weakly on f (Fig. 7).

A comparison of the current oscillograms and the CVCs shows that the range of the voltage amplitudes at

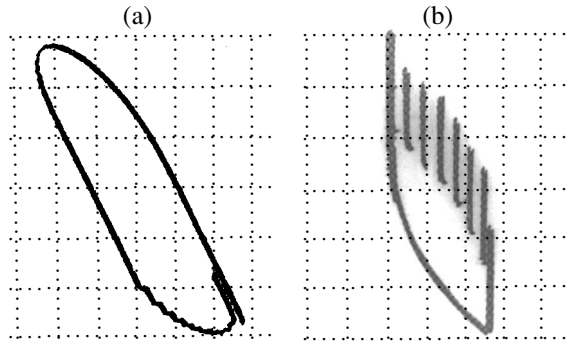

Fig. 6. Charge–voltage characteristics of a BC at $f = 0.4$ kHz in different modes: (a) diffuse mode in both half-periods, the voltage amplitude $U_a = 3$ kV, $d = 6$ mm, the vertical scale is 1 kV/division, and the horizontal scale is 1 nC/division and (b) diffuse mode in the negative half-period and the streamer mode in the positive half-period, $U_a = 3$ kV, $d = 1.5$ mm, the vertical scale is 1 kV/division, and the horizontal scale is 200 nC/division.

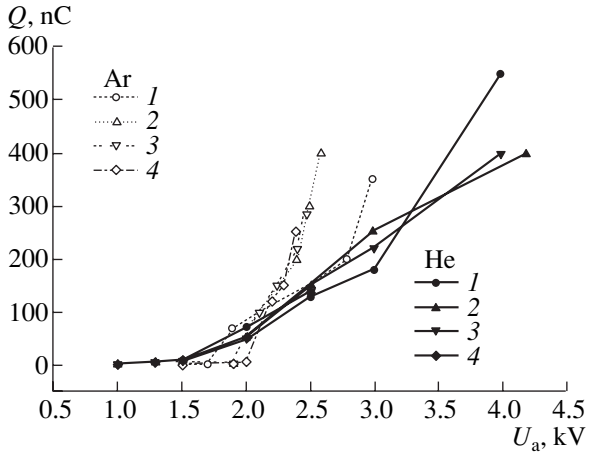

Fig. 7. Charge carried across the BC discharge gap vs. amplitude of the applied voltage for $d = 1.5$ mm and $F =$ (*1*) 0.4, (*2*) 1, (*3*) 3, and (*4*) 10 kHz. Open symbols correspond to Ar, and closed symbols correspond to He.

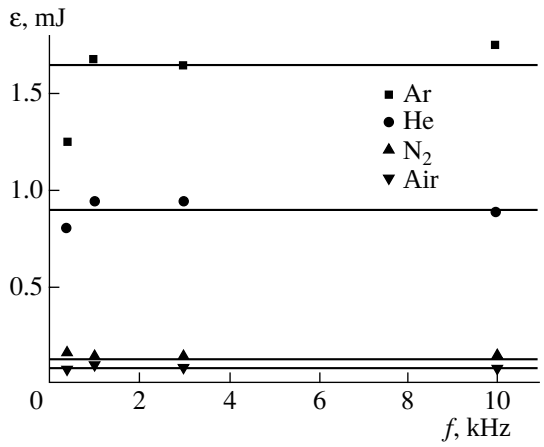

Fig. 8. Energy ε deposited in a discharge per one period vs. frequency f of the applied voltage for $d_{ac} = 1.5$ mm and $U_a =$ 2.5 kV (Ar, He), 4 kV (N_2), and 4.6 kV (air). The barrier is a polyethylene film.

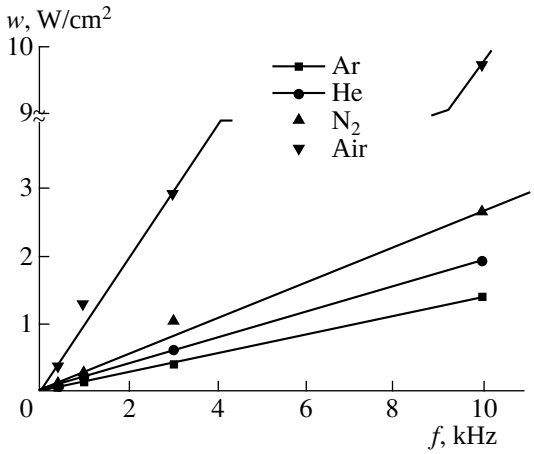

Fig. 9. Power density w released on the barrier surface (polyethylene film) vs. frequency f of the applied voltage for $d_{ac} = 1.5$ mm and $U_a = 2.5$ kV (Ar, He), 4 kV (N_2), and 4.6 kV (air).

which the carried charge does not exceed the value $Q \leq 10$ nC corresponds to a diffuse BC, whereas the voltage range corresponding to the larger values of Q and large derivatives $\partial Q/\partial U_a$ is related to the streamer BC mode in the positive half-periods. The density of streamers on the barrier surface is also of great importance. Thus, although the visual radii of BCs in He and Ar at large voltage amplitudes U_a differ strongly, the carried charges Q in these discharges are nearly the same, which can be attributed to the higher density of the surface streamers in He.

The area enclosed by the CVC on the (Q, U) plane determines the energy ε released by a BC during one half-period. The experiments show that, at a fixed voltage amplitude U_a, the value of ε depends strongly on the sort of gas and depends only slightly on the voltage frequency f (Fig. 8). The value of ε is maximum for argon and minimum for air. In a streamer BC, the bulk of the Joule energy is released near the surface (this is particularly true for BCs at small d). The average power density released in a BC near and on the surface, $w = \varepsilon f/S_c$, depends on the voltage frequency. Indeed, since the visual corona area S_c in each gas is primarily a func-

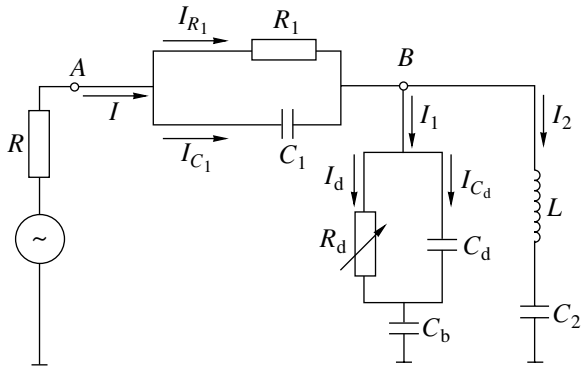

Fig. 10. Equivalent electric circuit used in numerical simulations: R is the internal resistance of the generator, R_1 = 300 kΩ is the ballast resistance, R_d is the nonlinear BC resistance, C_1 = 30 pF and C_2 = 75 pF are the parasitic capacitances of the external circuit, C_d = 2 pF is the capacitance of the BC discharge gap, C_b is the barrier capacitance, and L is the parasitic inductance.

tion of U_a (Fig. 3), an increase in the frequency at a fixed voltage amplitude should lead to a liner increase in w, which is observed in the experiment (Fig. 9).

An analysis of the dependence of the visual BC radius at the plane electrode on the sort of gas leads to interesting results. Thus, although the value of ε for a strongly broadened BC in argon is maximum as compared to other gases, the surface power density in this gas is minimum. In contrast, in air, the value of ε is minimum; however, the surface power density at a given voltage frequency is maximum, because, in this gas, the BC broadens only slightly.

4. NUMERICAL RESULTS

Numerical simulations of a BC were performed in an electric-circuit model in which the discharge gap was assumed to be a nonlinear resistance with given (see below) current–voltage characteristics for the positive and negative half-periods. The equivalent electric circuit including a BC is shown in Fig. 10. The BC usually occupies only a fraction of the full area of the dielectric-coated plane electrode. Depending on experimental conditions, the capacitance of the part of the dielectric barrier through which the current flows is relatively low and amounts to several tens or hundreds of picofarads. In this case, it is important to take into account the parasitic capacitances of various elements of the external circuit (between the generator output and the corona point and between the point and ground), which are of the same order of magnitude. These parasitic capacitances cause (both in simulations and experiments) current peaks with amplitudes that far exceed the average current value. The parasitic inductance of the circuit ($L \le 100$ nH) and the internal resistance of the voltage generator were also taken into account.

The equivalent circuit was described by the standard set of Kirchhoff's equations describing to the balance of currents and voltages for different subcircuits:

$$U(t) = IR + U_{R1} + U_d^{\pm}(I_d) + U_b,$$
$$I = I_1 + I_2 \equiv dq_b/dt + dq_{C2}/dt,$$

where $U(t)$ is the generator output voltage; I is the total circuit current; R is the internal resistance of the generator; $U_{R1} = q_{C1}/C_1$ is the voltage across the ballast resistor R_1, which depends on the charge q_{C1} on the parasitic capacitance C_1 (between points A and B); $U_d^{\pm}$ is the voltage across the BC gap in the positive and negative half-periods; I_d is the conduction current across the BC gap; $U_b = q_b/C_b$ is the barrier voltage; q_b is the barrier charge; C_b is the barrier capacitance; and q_{C2} is the charge on the parasitic capacitance C_2 (between point B and the ground).

The other equations are

$$LdI_2/dt + q_{C2}/C_2 = q_d/C_d + q_b/C_b,$$
$$dq_{Cd}/dt = I_{Cd} = I_1 - I_d,$$
$$dq_{C1}/dt = I - q_{C1}/R_1C_1,$$

where C_d is the capacitance of the discharge gap.

Simulations were performed for the following two cases. The first case corresponds to the voltage amplitudes at which the visual BC radius only slightly exceeds the length of the interelectrode gap. This situation is more typical of BCs in nitrogen and air. In this case, we assumed that the barrier capacitance was independent of the amplitude of the applied voltage. Taking into account the above properties of BCs, we assumed that the BC current–voltage characteristics in the diffuse modes of the positive and negative half-periods were described by parabolic dependences similar to those for usual positive and negative coronas:

$$I_d^{\pm} = k^{\pm}U_d(U_d - U_0^{\pm}),$$

where k is the dimensional factor depending on the mobilities of the current carriers and on the length of the discharge gap. For He, Ar, and N_2, the current of the positive corona is carried by ions, whereas the current of the negative corona is carried by electrons; i.e., $k^+ \ll k^-$. For air, we have $k^+ \simeq k^-$, because the current in the positive and negative coronas is carried by positive and negative ions, respectively.

For the positive half-period, U_0^+ coincides with the corona ignition voltage U_*; for the negative half-period, we take $U_0^- < U_*$ in the case of electropositive gases and $U_0^- \simeq U_*$ in the case of air. We also took into account the effect of streamers that arose in the positive

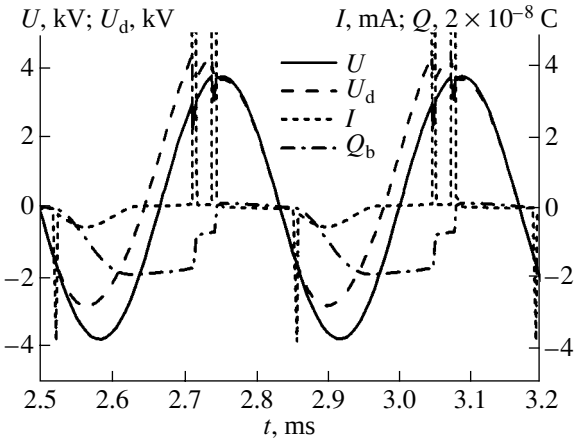

Fig. 11. Results of numerical simulations of a BC in N_2: the voltage across the gas gap U_d, the current I, and the charge Q_b on the barrier at a sinusoidal applied voltage U. The barrier capacitance is 25 pF, d = 1.5 mm, and f = 3 kHz. The amplitudes of the two current spikes in the positive half-period are ~70 mA.

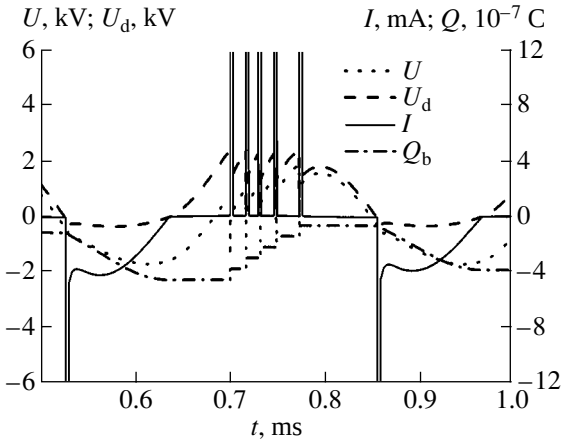

Fig. 12. Results of numerical simulations of a broadened BC in Ar: the voltage across the gas gap U_d, the current I, and the charge Q_b on the barrier at a sinusoidal applied voltage U. The barrier capacitance is C_b = 260 pF, d = 1.5 mm, and f = 3 kHz.

half-period starting from a certain voltage $U_s > U_*$. These streamers shunted the gap; as a result, the voltage across the gap decreased abruptly to $U_1^+ \ll U_s$. The values of U_0^+, U_0^-, U_s, and U_* were determined from the experiment.

The second case corresponds to a strongly broadened streamer BC ($R_c \gg d$). This type of corona occurs in helium and argon. In this case, the visual BC radius increases with increasing amplitude of the applied voltage; as a result, the barrier capacitance also increases with U_a:

$$C_b \sim S_c \simeq \theta R_c^2(U_a),$$

where S_c is the effective BC area, which is not equal to the visual area πR_c^2; θ is the fitting factor, taking into account the density of the streamers filling a circle with the visual radius R_c; and the dependence $R_c(U_a)$ is taken from the experiment.

The positive half-period of a strongly broadened BC was calculated in the same way as in the previous case, but with allowance for the dependence of the barrier capacitance on the applied voltage, $C_b = C_b(U_a)$. It was assumed that the conductivity of the gap $\sigma_-(t)$ in the negative half-period was provided by the plasma created by the surface streamers in the preceding half-period, rather than by the space charge of the negative corona. By the time at which the glow cathode layer is formed (a spike in the current oscillogram), the residual conductivity of the recombining plasma remains at a level of

$$\sigma_-(T/2) \simeq e\mu_e n_e \simeq 2e\mu_e/\beta T,$$

where e, μ_e, and n_e are the electron charge, electron mobility, and electron density, respectively; T is the period of the applied ac voltage; and $\beta \simeq 10^{-7}$ cm^3/s is the electron–ion dissociative recombination coefficient. It was assumed that, after the breakdown of the cathode layer, the plasma conductivity in the gap increased again due to ionization:

$$\sigma_-(t) \simeq \sigma_-(T/2)\exp(\alpha(U_d(t) - U_*)),$$

where α is the dimensional factor characterizing the intensity of ionization and t is the time counted from the breakdown of the cathode layer. Then, we have

$$I_d(t) \simeq \sigma_-(t)E(t)S_c \simeq \sigma_-(t)U_d(t)S_c/d.$$

The set of differential equations as formulated is stiff because of the substantial difference between the values of the parameters characterizing the electric circuit. For this reason, the set of equations was solved by the Gear method.

The typical results of numerical simulations are presented in Figs. 11–13. In spite of a rather simplified numerical model, the calculated curves reflect all the main experimental results. The simulations show one more interesting property of BCs in N_2, Ar, and He that distinguishes them from usual barrier discharges. It turns out that a nonzero negative charge is always maintained at the dielectric barrier in a BC (Fig. 11). The average value of this charge increases with increasing amplitude of the applied voltage. The physical reason why the equilibrium between; the positive and negative half-periods of BCs in electropositive gases is established due to an excess of a negative charge on the barrier is the strong difference of the BC properties in these

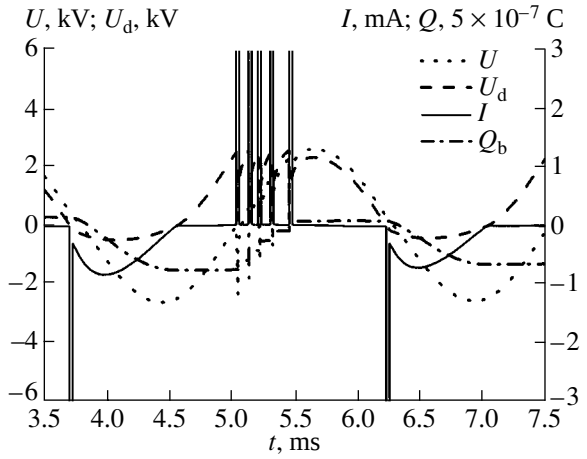

Fig. 13. Results of numerical simulations of a broadened BC in Ar: the voltage across the gas gap U_d, the current I, and the charge Q_b on the barrier at a sinusoidal applied voltage U. The barrier capacitance is C_b = 145 pF, d = 1.5 mm, and f = 400 Hz.

half-periods, in which we have $k^+ \ll k^-$ and $U_s > U_* > U_0^-$.

Keeping in mind this BC property and also the fact that BCs are widely used to modify surfaces, we note that the negative charge present on the surface can additionally activate it (see, e.g., [20]). This circumstance may be very important and must be taken into consideration when choosing the BC modes, as well as when analyzing the properties of dielectric surfaces modified with the help of BCs.

Simulations of a strongly broadened BC (with a corona radius of $R_c \simeq 6d$) in argon show that the number of the current spikes in the positive half-period increases with increasing amplitude of the applied voltage, as is observed in the experiment (Figs. 12, 13). The charge Q_s carried by streamers during each current spike is nearly constant ($Q_s \simeq (7.6 \pm 0.2) \times 10^{-8}$ C) and depends only slightly on the applied voltage frequency. A satisfactory agreement of the calculated current waveforms with the experimental ones was achieved for the degree of the barrier filling by the streamers θ = 0.6. In the negative half-period, the agreement between calculations and experiment was achieved by assuming the residual density of the decaying plasma to be at a level on the order of 10^9–10^{10} cm^{-3}, depending primarily on the voltage frequency.

5. CONCLUSIONS

(i) A BC occurs at lower voltages as compared to the barrier discharge and exists up to currents that far exceed the current of a usual corona discharge in the point–plane geometry.

(ii) In the positive half-period of the applied voltage, the BC exists in two modes: the diffuse mode and the streamer mode. In the negative half-period, the BC exists in the diffuse mode only.

(iii) The BC has asymmetric current profiles in the positive and negative half-periods, which distinguishes this type of discharge from usual barrier discharges.

(iv) The BC in electropositive gases occurs with an excess of negative charge on the barrier, which is atypical of usual barrier discharges.

(v) Unlike usual barrier and corona discharges, the BC spreads from the point over the dielectric surface. The BC spreading is more pronounced in electropositive gases, in which the surface streamers branch out intensely and propagate along the dielectric over large distances.

(vi) In air, the branching of the surface streamers is less pronounced; hence, we can conclude that in the positive and negative half-periods, the BC is similar in properties to usual dc positive and negative coronas.

(vii) In the diffuse modes of the positive and negative half-periods, BCs in N_2, Ar, and He are similar in properties to usual dc positive and negative coronas.

(viii) The limiting currents for the conversion of BC streamers into a spark exceed the currents at which a steady-state corona in the point–plane geometry converts into a spark. This fact indicates that a necessary condition for the conversion of a positive streamer into a spark is the formation of a current spot on the cathode.

In conclusion, we note that the results obtained shed light on the fundamental properties of BCs in the diffuse and streamer modes in various gases. The results obtained provide a general idea of the background against which ionization instabilities develop. Therefore, this paper is a necessary step in studying the mechanisms for generation of streamers near a positively charged point and their propagation in a discharge gap and over a dielectric surface, as well as the mechanisms for conversion of streamers into a spark.

ACKNOWLEDGMENTS

We thank A.P. Napartovich and E.M. Bazelyan for fruitful discussions of the results obtained. This work was supported by the Russian Foundation for Basic Research, project no. 02-02-16913.

REFERENCES

1. U. Kogelschatz, in *Proceedings of the International Symposium on High-Pressure Low-Temperature Plasma Chemistry, Greifswald, 2000*, Vol. 1, p. 1.
2. B. Eliasson and U. Kogelschatz, IEEE Trans. Plasma. Sci **19**, 309 (1991).
3. R. Bartnikas, IEEE Trans. Electr. Insul. **6**, 63 (1971).
4. S. Okazaki, M. Kogoma, M. Uehara, and Y. Kimura, J. Phys. D **26**, 889 (1993).

5. F. Massines, R. Messaourdi, and C. Mayoux, Plasmas Polym. **3**, 43 (1998).
6. Yu. S. Akishev, M. E. Grushin, V. B. Karal'nik, and N. I. Trushkin, Fiz. Plazmy **27**, 550 (2001) [Plasma Phys. Rep. **27**, 520 (2001)].
7. A. Engel, *Ionized Gases* (Clarendon, Oxford, 1955; Fizmatgiz, Moscow, 1959).
8. N. A. Kaptsov, *Electronics* (Gostekhteorizdat, Moscow, 1953).
9. L. B. Loeb, *Electrical Coronas* (Univ. of California Press, Berkeley, 1965).
10. I. P. Vereshchagin, *Corona Discharge in Apparatuses of Electron–Ion Technology* (Énergoatomizdat, Moscow, 1985).
11. W. Hermstein, Arch. Elektrotech. (Berlin) **45** (4), 279 (1960).
12. G. Buchet and M. Goldman, in *Proceedings of the 9th International Conference on Phenomena in Ionized Gases, Bucharest, 1969*, p. 291.
13. H. I. Korge, Uch. Zap. Tartu Gos. Univ., No. 479, 107 (1979).
14. Yu. S. Akishev, M. E. Grushin, A. A. Deryugin, *et al.*, J. Phys. D **32**, 2399 (1999).
15. Yu. S. Akishev, V. B. Karal'nik, and N. I. Trushkin, Proc. of SPIE **4460,** 26 (2002).
16. Yu. S. Akishev, M. E. Grushin, I. V. Kochetov, *et al.*, Fiz. Plazmy **26**, 172 (2000) [Plasma Phys. Rep. **26**, 157 (2000)].
17. Yu. S. Akishev, M. E. Grushin, A. A. Deryugin, *et al.*, Fiz. Plazmy **25**, 941 (1999) [Plasma Phys. Rep. **25**, 867 (1999)].
18. R. S. Sigmond, J. Appl. Phys. **53**, 891 (1982).
19. Yu. S. Akishev, M. E. Grushin, V. B. Karal'nik, and N. I. Trushkin, Fiz. Plazmy **27**, 563 (2001) [Plasma Phys. Rep. **27**, 532 (2001)].
20. A. B. Gil'man, A. I. Drachev, A. A. Kuznetsov, *et al.*, Khim. Vys. Energ. **30**, 373 (1996).

Translated by N.F. Larionova

Plasma Physics Reports, Vol. 29, No. 1, 2003, pp. 92–95. Translated from Fizika Plazmy, Vol. 29, No. 1, 2003, pp. 101–104.

COMMENTS

The Problem of Obtaining Exact Solutions to the Equations for an Intense Charged-Particle Beam and an Analysis of the Paper by N.D. Naumov "Self-Similar Motion of Charged Particles"

V. A. Syrovoy

All-Russia Electrotechnical Institute, Krasnokazarmennaya ul. 12, Moscow, 111250 Russia

Received February 14, 2002

Abstract—The novelty and correctness of the paper by N.D. Naumov "Self-Similar Motion of Charged Particles," Fiz. Plazmy **19**, 1406 (1993) [Sov. J. Plasma Phys. **19**, 738 (1993)] are discussed. © *2003 MAIK "Nauka/Interperiodica".*

The construction of the most complete class of exact solutions to the hydrodynamic equations for an intense charged-particle beam is an integral part of the problem of developing adequate mathematical models in the optics of dense particle flows. The main application of this branch of physics is in microwave electronics (including plasma microwave electronics [1]), high-current accelerators, high-voltage switches, technological systems, etc. In order to check the correctness of the approximate and numerical models, it is necessary to store a collection of test problems in such a way that it would possess all distinctive properties of the general formulation of the problem. These properties, which cannot be adequately described by a particular solution, include the following: nonsteady and relativistic effects, nonuniform current extraction from a curved emitter, a nonuniform external magnetic field, long curvilinear space trajectories, the presence of an ion background, etc. In this context, it is relevant to search for and interpret exact solutions that are described by ordinary differential equations, no matter how exotic the result obtained may be or whether it can ever be applied in practice.

An attempt to contribute to the problem under discussion was made by Naumov [2] by way of looking for and describing the self-similar motion of charged particles in nonsteady nonrelativistic flows. In the present note, the current state of the problem is briefly reviewed and the contribution of paper [2] to the problem is analyzed.

To begin with, it should be noted that the concept of exact solutions acquired a new meaning when Ovsyannikov [3, 4] introduced the notion of invariant solution (H-solution). The complete family of invariant solutions is constructed by analyzing the group properties of the initial partial differential equations.[1] The self-similarity property was found to have much deeper roots than the concepts of similarity and dimensionality [5] and is closely related to the invariance of a system (possibly dimensionless) under the group of transformations generated by dilatations. Self-similar solutions are a particular (but important) subclass of invariant solutions. Naumov [2] rightly noted that "among self-similar motions, there is motion such that the velocities are proportional to the distance from the center of symmetry." However, the converse is not true: the motion with such a property is not necessarily self-similar. The erroneous interpretation of self-similar motion led Naumov [2] to the conclusion that it is possible to speak of the self-similarity property in the problem about a thin curvilinear ribbon-shaped beam [6], for which the sought-for solution is expressed through the linear fragment of the Taylor expansion about the coordinate normal to the curved beam axis.

That new things are well-forgotten old things is true in high fashion, but not in natural sciences. In research on the construction and interpretation of exact solutions to the equations for the beam, the following results were obtained before the paper by Naumov [2] had been published.

In [7], H-solutions were studied for a steady-state nonrelativistic planar flow. The objectives of that paper were to reveal the functional form of the solutions with which it is possible to convert the basic partial differential equations into a set of ordinary differential equations, to give the first physical interpretation of the solutions obtained, and to determine how the solutions known from the literature are related to the group properties of the equations for the beam. In [8], an analysis was made of steady-state beams, including relativistic beams in 3D-space. H-solutions corresponding to nonsteady-state beams were studied in [9]. The objective of [10] was to investigate the possibility of constructing new exact solutions from the familiar solutions under transformations involving arbitrary functions of time;

[1] Concerning the application of this method in many branches of mathematical physics, see L. V. Ovsyannikov and N. Kh. Ibragimov, *General Mechanics* (VINITI, Moscow, 1975), Vol. 2.

1063-780X/03/2901-0092$24.00 © 2003 MAIK "Nauka/Interperiodica"

these transformations mean a transition to a noninertial frame of reference whose origin moves arbitrarily in space at a nonrelativistic velocity. It was shown that these transformations leave invariant not only the hydrodynamic equations for the beam but also the Vlasov equations. The case of an immobile ion background and a multicomponent flow consisting of several charged-particle species was investigated in [11]. Paper [12] was devoted to interpreting some steady-state flows, including relativistic conical flows of Brillouin type, for which it was possible to express the solutions in elementary functions. In Chapter 2 of [13], the results obtained in [7–12] were summarized in the tables that present the functional forms of H-solutions.

Paper [14] provided an analysis of the results obtained in the theory of generalized non-steady-state single-component flows. H-solutions for a non-steady-state beam that are invariant under transformations with arbitrary functions of time were analyzed in [15], and steady solutions that are invariant under the same transformations but with exponential functions of time (instead of arbitrary functions) were examined in [16]. The group properties of a two-dimensional non-steady-state solenoidal beam equations were considered in [17].

Invariant solutions for two-dimensional steady-state relativistic and nonrelativistic flows were interpreted in [18, 19], and invariant solutions for non-steady-state relativistic flows were interpreted in [20]. A careful analysis of relativistic and nonrelativistic conical flows of Brillouin type was given in [21].

In [22], a geometrized theory of dense beams [23] was used to estimate the results obtained in theoretical studies of single-component flows, in which attempts were made to describe an arbitrary flow in space by an ordinary differential equation for the potential of the generalized momentum by choosing the coordinate system in a special way.

The above review of the studies on the subject shows that the problem of constructing as complete as possible sets of exact solutions has been analyzed in great detail (in the cited papers, one can find a full list of the solutions reported in the literature). However, these studies do not exhaust the subject. First, a large number of exact solutions (especially nonsteady ones) have not yet been interpreted, or, in other words, the corresponding sets of ordinary equations have not yet been examined in detail. Second, there has been no study of the problems of constructing partially invariant solutions [4][2] or of the group properties of the systems consistent with H-solutions of ranks 3 and 2 (3- and 2-rank solutions satisfy partial differential equations, in which the number of independent variables is one or two less than in the original three-dimensional time-dependent set).

However, it is still unknown how some of the solutions reported in the literature are related to the group properties of the beam equations. These solutions may be divided into two groups. The first group includes the solutions for planar ($\partial/\partial z = 0$) potential solenoidal flows, which are constructed by using a complex formalism [17, 25–28]. The solutions of the second group are associated with the concept of degenerate flows [29] and generalized Brillouin flows [30–32].[3]

Researchers interested in the problem under discussion must work in the directions outlined above and must take into account the results obtained previously.

Let us analyze the results obtained in [2] in the context of the above brief review. The paper by Naumov begins by considering one-dimensional non-steady-state flows, which, to the best of my knowledge, were first studied in [33]. The remark that planar and axisymmetric flows can be expanded in the z direction using Galilean transformations refers to a very particular case in which transformations with arbitrary functions of time [10, 13, 15] are applied with respect to the z-axis under the assumption of a uniform magnetic field.

The functional form of solution determined by formulas (5) in [2],

$$\mathbf{v} = \mathbf{R}V(t), \quad \varphi = R^2\Phi(t), \quad \rho = \rho(t), \quad \mathbf{H} = \mathbf{H}(t), \tag{1}$$

was given in [9]; the new result is the integrals that describe the radial and azimuthal velocity components (here, R, ψ, and z are cylindrical coordinates).

The solution to the problem of the motion of an elliptically shaped beam in a magnetic field in the case of uniform deformation of the beam cross section [34] is not a self-similar one but belongs to the class of H-solutions of rank 3, which are invariant under transformations with arbitrary functions of time [15].

The last of the solutions considered in [2] is also non-self-similar and is interpreted as describing oscillations of a spherical bunch in a Penning trap. However, this solution is a particular case of an H-solution of rank 3, whose functional form was presented in [15] and which is described by the formulas [2]

$$u = \frac{\dot{R}}{R}x + Cy, \quad v = -Cx + \frac{\dot{R}}{R}y,$$
$$w = \frac{\dot{R}}{R}z, \quad C = \frac{1}{2}H_z = \text{const}, \tag{2}$$
$$\varphi = \varphi_{11}(x^2 + y^2) + \varphi_{33}z^2, \quad \rho = \frac{\rho_0}{R^3},$$

[2] In [24], the investigation of partially invariant solutions to the equations for a steady-state beam in space yielded versions of solutions with an nonharmonic vector potential; this indicates that, within the beam, there are currents that are not associated with it.

[3] Deserving special consideration are exact solutions constructed in a paper by A. V. Malykhin and O. A. Ollo, Radiotekh. Élektron. (Moscow) **35**, 1928 (1990), by systematically applying the Lagrange formalism.

$$R = R(t), \quad \rho_0 = \text{const}.$$

Here, x, y, and z are Cartesian coordinates and u, v, and w are the velocity components in these coordinates. The formulas are written in terms of dimensionless variables that make it possible to remove all physical constants from consideration.

The interpretation given in [2] appears questionable. To illustrate this, it is necessary to describe solution (2) more carefully than it was done in [2]. Substituting formulas (2) into the equations for the beam yields the self-consistent potential

$$\varphi = \frac{1}{6}(\rho + C^2)(x^2 + y^2) + \frac{1}{6}(\rho - 2C^2)z^2, \qquad (3)$$

which is a sum of the Laplace potential φ_L of the Penning type and the potential φ_s of the spherically symmetric field of a space charge:

$$\varphi_L = \frac{1}{6}C^2(x^2 + y^2 - 2z^2), \quad \varphi_s = \frac{1}{6}\rho(x^2 + y^2 + z^2). \quad (4)$$

The interpretation given in [2] would be correct if the particles distributed initially over a sphere were always to lie on a sphere whose radius changes with time. Let us show that this is not the case.

Formulas (2) for the velocity components are valid only under the assumption that the particle coordinates undergo a uniform deformation:

$$x = \alpha x_0 + \beta y_0, \quad y = \mu x_0 + \nu y_0, \quad z = \kappa z_0, \qquad (5)$$

where x_0, y_0, and z_0 are the initial Cartesian coordinates and α, β, μ, ν, and κ are time-dependent trajectory functions. In order to obtain the velocity components u, v, and w, it is necessary to take the time derivative of relationships (5) and to express the initial coordinates x_0, y_0, and z_0 in terms of x, y, and z using relationships (5)

$$u = \frac{1}{\delta}[(\dot\alpha\nu - \dot\beta\mu)x + (\dot\beta\alpha - \dot\alpha\beta)y], \quad \delta = \alpha\nu - \beta\mu,$$
$$v = \frac{1}{\delta}[(\dot\mu\nu - \dot\nu\mu)x + (\dot\nu\alpha - \dot\mu\beta)y], \quad w = \frac{\dot\kappa}{\kappa}z. \qquad (6)$$

A comparison of these velocity components with those given by formulas (2) yields the following four equations for the four trajectory functions, which thus are completely determined by the function $R(t)$ and constant C in formulas (2)

$$\frac{\dot\alpha\nu - \dot\beta\mu}{\delta} = \frac{\dot\nu\alpha - \dot\mu\beta}{\delta} = \frac{\dot R}{R},$$
$$\frac{\dot\beta\alpha - \dot\alpha\beta}{\delta} = \frac{\dot\nu\mu - \dot\mu\nu}{\delta} = C, \quad \kappa = R. \qquad (7)$$

It is easy to see that, under uniform deformation (5), the unit sphere $x_0^2 + y_0^2 + z_0^2 = 1$ transforms into an object described by

$$(\nu^2 + \mu^2)x^2 + (\beta^2 + \alpha^2)y^2 - 2(\beta\nu + \alpha\mu)xy + \frac{\delta^2}{\kappa^2}z^2 = \delta^2. \qquad (8)$$

In order for the object to remain a sphere, the following three conditions should be satisfied:

$$\beta\nu + \alpha\mu = 0, \quad \nu^2 + \mu^2 = \beta^2 + \alpha^2 = \delta^2/\kappa^2. \qquad (9)$$

However, we have no free functions to satisfy these conditions. Consequently, the object that initially was a sphere becomes an ellipsoid, which clearly contradicts formulas (4).

In order to remove this contradiction, it is necessary to abandon the assumption of a spherical bunch of finite radius. The variations in the density of an electron flow described by solution (2) are such that the particles originally distributed over the sphere start moving along the surface of an ellipsoid without breaking the spherical symmetry of the potential of an infinite uniform beam.

To conclude, note that paper [2] does not provide new exact solutions and its contribution to the subject is twofold: first, the investigation of self-similar solutions (1), possessing cylindrical symmetry [see formulas (5) in that paper], and, second, the integration of the equations describing solution (2). However, the physical meaning of these results should be revised in the above manner. As for the first contribution, the integrals in the equations of motion are written out and a qualitative analysis of the solution is given. The incompleteness of the study by Naumov [2] is partially compensated for by the data obtained from numerical calculations relevant to this solution (in particular, for the case with a neutralizing background) [35].

REFERENCES

1. L. A. Mitin, V. I. Perevodchikov, M. A. Zav'yalov, *et al.*, Fiz. Plazmy **20**, 733 (1994) [Plasma Phys. Rep. **20**, 662 (1994)].
2. N. D. Naumov, Fiz. Plasmy **19**, 1406 (1993) [Plasma Phys. Rep. **19**, 738 (1993)].
3. L. V. Ovsyannikov, Dokl. Akad. Nauk SSSR **118**, 439 (1958).
4. L. V. Ovsiannikov, *Group Analysis of Differential Equations* (Nauka, Novosibirsk, 1962; Academic, New York, 1982).
5. L. I. Sedov, *Similarity and Dimensional Methods in Mechanics* (Fizmatgiz, Moscow, 1987; Academic, New York, 1959).
6. N. D. Naumov, Radiotekh. Élektron. (Moscow) **45**, 1384 (2000) [J. Commun. Technol. Electron. **45**, 1252 (2000)].

7. V. A. Syrovoy, Zh. Prikl. Mekh. Tekh. Fiz., No. 4, 10 (1962).
8. V. A. Syrovoy, Zh. Prikl. Mekh. Tekh. Fiz., No. 3, 26 (1963).
9. V. A. Syrovoy, Zh. Prikl. Mekh. Tekh. Fiz., No. 1, 3 (1964).
10. V. A. Syrovoy, Zh. Prikl. Mekh. Tekh. Fiz., No. 3, 56 (1965).
11. V. A. Syrovoy, Zh. Prikl. Mekh. Tekh. Fiz., No. 5, 9 (1965).
12. V. A. Syrovoy, Zh. Prikl. Mekh. Tekh. Fiz., No. 6, 3 (1965).
13. V. A. Syrovoy, Doctoral Dissertation in Physics and Mathematics (Moscow, 1971).
14. V. N. Danilov and V. A. Syrovoy, Zh. Tekh. Fiz. **47**, 2210 (1977).
15. V. A. Syrovoy, Radiotekh. Élektron. (Moscow) **29**, 2430 (1984).
16. V. A. Syrovoy, Radiotekh. Élektron. (Moscow) **30**, 367 (1985).
17. V. A. Syrovoy, Izv. Vyssh. Uchebn. Zaved., Radiofiz. **27**, 635 (1984).
18. A. V. Vashkovskiĭ, E. A. Soluyanova, V. A. Syrovoy, and Sh. E. Tsimring, Radiotekh. Élektron. (Moscow) **31**, 783 (1986).
19. A. V. Vashkovskiĭ, V. A. Syrovoy, and Sh. E. Tsimring, Radiotekh. Élektron. (Moscow) **41**, 350 (1996) [J. Commun. Technol. Electron. **41**, 279 (1996)].
20. A. V. Vashkovskiĭ and V. A. Syrovoy, Radiotekh. Élektron. (Moscow) **36**, 392 (1991) [Sov. J. Commun. Technol. Electron. **36** (16), 69 (1991)].
21. A. V. Vashkovskiĭ and V. A. Syrovoy, Izv. Vyssh. Uchebn. Zaved., Radiofiz. **34**, 837 (1991).
22. V. A. Syrovoy, Izv. Vyssh. Uchebn. Zaved., Radiofiz. **33**, 1391 (1990).
23. V. A. Syrovoy, Radiotekh. Élektron. (Moscow) **44**, 645 (1999) [J. Commun. Technol. Electron. **44**, 601 (1999)].
24. O. P. Germanovich and V. P. Chervonnykh, Zh. Tekh. Fiz. **50**, 1160 (1980) [Sov. Phys. Tech. Phys. **25**, 665 (1980)].
25. P. T. Kirstein, J. Electr. Contr. **4** (5), 425 (1958).
26. S. N. Ogorodnikov, Izv. Vyssh. Uchebn. Zaved., Radiofiz. **12**, 1577 (1969).
27. S. N. Ogorodnikov, Zh. Tekh. Fiz. **42**, 1348 (1972) [Sov. Phys. Tech. Phys. **17**, 1076 (1972)].
28. S. N. Ogorodnikov, Zh. Tekh. Fiz. **43**, 1311 (1973) [Sov. Phys. Tech. Phys. **18**, 834 (1973)].
29. V. N. Danilov, Zh. Prikl. Mekh. Tekh. Fiz., No. 1, 3 (1968).
30. V. N. Danilov, Radiotekh. Élektron. (Moscow) **8**, 1892 (1963).
31. V. N. Danilov, Radiotekh. Élektron. (Moscow) **8**, 2046 (1963).
32. V. N. Danilov, Radiotekh. Élektron. (Moscow) **11**, 1994 (1966).
33. O. P. Beguchev, Zh. Tekh. Fiz. **26**, 1483 (1956).
34. V. A. Levin, Zh. Prikl. Mekh. Tekh. Fiz., No. 2, 122 (1967).
35. N. D. Naumov, Radiotekh. Élektron. (Moscow) **39**, 1179 (1994).

Translated by G.V. Shepekina